Understanding of infrared heating for thermoforming of semi-crystalline thermoplastics

Sinan Boztepe

Université Fédérale
Toulouse Midi-Pyrénées

THÈSE

En vue de l'obtention du

DOCTORAT DE L'UNIVERSITÉ DE TOULOUSE

Délivré par :

IMT - École Nationale Supérieure des Mines d'Albi-Carmaux

Présentée et soutenue par :
Sinan BOZTEPE

le 14 décembre 2018

Titre :

Understanding of infrared heating for thermoforming of semi-crystalline thermoplastics

---

École doctorale et discipline ou spécialité :
ED MEGEP : Génie mécanique, mécanique des matériaux

Unité de recherche :
Institut Clément Ader, UMR CNRS 5312, IMT Mines Albi

Directeurs de Thèse :
Fabrice SCHMIDT, Professeur, IMT Mines Albi
Yannick LE MAOULT, Professeur, IMT Mines Albi

Jury :

Dominique BAILLIS, Professeur des Universités, INSA Lyon, Présidente
Christophe LE NILIOT, Professeur des Universités, Polytech Marseille, Rapporteur
Vincent SOBOTKA, Professeur des Universités, Polytech Nantes, Rapporteur
Olivier DE ALMEIDA, Maître-assistant, IMT Mines Albi, Examinateur
Gary MENARY, Maître de Conférences, Queens University of Belfast, Examinateur
Christian GERLACH, Chargé de Recherche, Procter & Gamble, Invité

This thesis is dedicated to my grandfather, Kâzim Ercan.

Je dédie cette thèse à mon grand-père, Kâzim Ercan.

Bu tez, dedem Kâzim Ercan'a adanmıştır.

Our true mentor in life is science.

Dans la vie, notre véritable guide est la science.

Hayatta en hakiki mürşit ilimdir.

Mustafa Kemal Ataturk (1881 – 1938)

Henri De la Beche (1832) – (Source: http://collection.sciencemuseum.org.uk)

Any road that doesn't follow science, ends in darkness.

Tout chemin qui ne suit pas la science mène à l'obscurantisme

İlimden gidilmeyen yolun sonu karanlıktır.

Haji Bektash Veli (1209 – 1271)

Acknowledgements

I would like to express my sincere gratitude to my research advisors Olivier de Almeida, Yannick Le Maoult and Fabrice Schmidt for their guidance and continuous support throughout this thesis. During my research, they did not only give me scientific advice but they each taught me how to be a true researcher and how to improve my critical reasoning, communication skills and collaborative work. I therefore enjoyed being guided by them and also being part of their team.

I also gratefully acknowledge my supervisor from our industrial partner Procter & Gamble Co., Christian Gerlach, for his guidance and frequent communications throughout my Ph.D.

My sincere thanks also go to Dr. Rémi Gilblas, for his suggestions and assistance starting from the beginning of my thesis. I will never forget our brainstorming sessions which greatly helped me to achieve my goals during my experimental research. I enjoyed all the moments not only discussing about science, but also cheering our daily lives in a kind and friendly attitude.

I would also like to acknowledge Mr. Christophe Escape from Procédés, Matériaux et Energie Solaire (PROMES) - CNRS laboratory for his technical support and assistance with the several spectroscopic analyses presented in this research.

I acknowledge and give special thanks to my colleagues: Théo Baumard, Dr. Sylvain Corveleyn, Abdelmagid El Bakali, Benjamin Javaudin, Sabrine Jlassi and Dr. Céline Vicard. I would also like to acknowledge the technical staff and research engineers of Institut Clément Ader namely, Sabine Le Roux, Aurélien Mazzoni, Dr. Mehdi Salem and Karine Vieillevigne for their technical support.

Last but not least, I would like to thank my wife, Marion Boztepe, and my brother, Ercan Boztepe, for motivating me everytime and supporting me spiritually throughout my life in any case and condition.

CONTENTS

LIST OF FIGURES

LIST OF TABLES

NOMENCLATURE

The symbols used in this thesis are listed here in two sub-sections, namely Latin and Greek symbols. The abbreviations are presented at the end of this section. The symbols and abbreviations are given in alphabetical order.

Latin Symbols

A_λ	Attenuated fraction of spectral energy	[-]
BRDF	Bidirectional Reflectance Distribution Function	[sr^-]
BSDF	Bidirectional Scatter Distribution Function	[sr^-]
BTDF	Bidirectional Transmittance Distribution Function	[sr^-]
c_o	Speed of the light in vacuum / non-participating medium	[km/h]
c_{air}	Speed of light in air	[km/h]
c_{medium}	Speed of light in a participating medium	[km/h]
C_p	Specific heat capacity	[J/(kgK)]
$C_{p,}^{apparent}$	Apparent heat capacity	[J/(kgK)]
$C_{p,}^{apparent}(T)$	Temperature-dependent apparent heat capacity	[J/(kgK)]
D	Diameter	[mm, μm]
D_p	Optical penetration depth	[μm]
D_λ	Spectral scattering coefficient	[m^{-1}]
dS	Infinitesimal distance along radiation propagation	[m]
E	Irradiance or total emissive power of real body	[W/m^2]
E`	Storage modulus	[Pa]
E_b	Blackbody irradiance	[W/m^2]
E_λ	Hemispherical spectral emissive power	[$W/(m^2\mu m)$]
$E_\lambda(\theta)$	Directional spectral emissive power of real body	[$W/(m^2\mu m)$]
$E_{\lambda b}$	Hemispherical spectral emissive power of black body	[$W/(m^2\mu m)$]
$E_{\lambda b}(\theta)$	Directional spectral emissive power of black body	[$W/(m^2\mu m)$]
G	Grain size	[μm]
Gr	Grashof number	[-]
h	Heat transfer coefficient	[$W/(m^2K)$]
I_λ	Spectral intensity	[$W/(m^2\mu m.sr)$]

$I_{\lambda b}$	Spectral intensity of black body radiation	[W/(m^{2}μm.sr)]
J	Double objective function	[-]
k	Thermal conductivity	[W/(mK)]
k (T)	Temperature-dependent thermal conductivity	[W/(mK)]
l_∞	Crystalline lamella of infinite thickness	[nm]
l_c	Lamellae thickness	[nm]
M	Total mass of crystalline phase	[mg]
n_{air}	Refractive index of air	[-]
$n_{amorphous}$, $n_{crystalline}$	Refractive indexes of amorphous and crystalline phase	[-]
n_{medium}	Refractive index of medium	[-]
Nu	Nusselt number	[-]
P_i	Incident laser power	[W]
P_s	Scattered laser power	[W]
r	Radius of a spherical scatterer	[nm, μm]
Re	Reynolds number	[-]
$R_{numerical}$	Numerically-computed reflectance	[-]
$R_\lambda^{i,\cap}$	Directional-hemispherical reflectance	[-]
$R_\lambda^{i,\cap}(T)$	Temperature-dependent directional-hemispherical reflectance	[-]
R_λ	Reflected fraction of spectral energy	[-]
$R_\lambda^{\cap,\, i}$	Hemispherical-directional reflectance	[-]
$R_\lambda^{i,r}$	Directional-directional reflectance	[-]
S	Trajectory of the propagated radiation	[-]
T_m^o	Equilibrium melting temperature	[K]
T	Temperature	[K]
t	Time step	[-]
T_{actual}	Actual temperature	[K]
T_{bb}	Temperature of black body	[K]
$T_{crystallization}$	Crystallization temperature	[K]
T_g	Glass transition temperature	[K]
T_{lamp}	Temperature of IR lamp	[K]
T_m	Melting temperature	[K]
$T_{numerical}$	Numerically-computed transmittance	[-]
T_s	Softening temperature	[K]
T_{set}	Set temperature of the heating stage	[K]

$T_\lambda^{i,\cap}$	Directional-hemispherical transmittance	[-]
$T_\lambda^{i,\cap}(T)$	Temperature-dependent directional-hemispherical transmittance	[-]
$T_\lambda^{i,r}$	Directional-directional transmittance	[-]
$T_\lambda^{i,r}(T)$	Temperature-dependent directional-directional transmittance	[-]
UI_{bb}	Isothermal unit	[-]
X_c	Degree of crystallinity	[-]
$\bar{V}$	Specific volume	[m^3/kg]
ΔH_m	Enthalpy of fusion	[J/g]
ΔH^o_m	Enthalpy of fusion for hypothetical 100% crystalline polymer	[J/g]
Δn	Relative refractive index	[-]
ΔT	Temperature difference	[K, ^oC]
$\Delta T_{cooling}$	Supercooling	[K]
$\nabla.q_r$	Radiative source term	[W/m^3]
$\nabla.q_r(T)$	Temperature-dependent radiative source term	[W/m^3]

Greek Symbols

α	Normalizing ratio	[-]
β_λ	Spectral extinction coefficient	[m^{-1}]
$\beta_\lambda(T)$	Temperature-dependent spectral extinction coefficient	[m^{-1}]
$\overline{\beta}(T)$	Integrated temperature-dependent extinction coefficient	[m^{-1}]
$\varepsilon(T)$	Total emissivity of real body at a temperature of T	[-]
ε_{PET}	Total emissivity of PET	[-]
ε_λ	Spectral emissivity	[-]
κ_λ	Spectral absorption coefficient	[m^{-1}]
$\overline{\kappa}(T)$	Integrated absorption coefficient	[m^{-1}]
λ	Wavelength	[μm]
λ_m	Wavelength of propagated radiation in a medium	[μm]
λ_{max}	Wavelength of the maximum emitted power of real or black body	[μm]
ξ	Shape parameter	[-]
$\overline{\rho}$	Integrated reflectivity	[-]
$\rho_{amorphous}$, $\rho_{crystalline}$	Densities of amorphous and crystalline phases	[kg/m^3]
ρ_{global}	Global density	[kg/m^3]
σ_e	Surface energy of the basal surface of the crystalline lamella	[J/m^2]

φ	Azimuth angle	[°]
ϕ_λ	Scattering phase function	[-]
Φ_λ^{i}	Incident light flux	[W/(m^{2}μm)]
Φ_λ^{r}	Reflected light flux	[W/(m^{2}μm)]
$\Phi_\lambda^{s\text{-}back}$	Back-scattered light flux	[W/(m^{2}μm)]
$\Phi_\lambda^{s\text{-}forward}$	Forward-scattered light flux	[W/(m^{2}μm)]
Φ_λ^{t}	Directly transmitted light flux	[W/(m^{2}μm)]
Ω	Solid angle	[sr]
θ_i	Incident polar angle	[°]
θ_s	Scattering polar angle	[°]

Abbreviations

AFM	Atomic force microscopy
AN	Annealed
CFD	Computational fluid dynamics
C-H	Carbon-hydrogen
DSC	Differential scanning calorimetry
EMW	Electromagnetic wave
FEM	Finite element modeling
FTIR	Fourier-transform infrared
He-Ne	Helium-neon
HDPE	High density polyethylene
hrs	Hours
IR	Infrared
ISBM	Injection-stretch blow molding
iPP	Isotactic polypropylene
LTW	Laser transmission welding
PbS	Lead sulfide
LED	Light emitting diode
LLDPE	Linear low-density polyethylene
LN_2	Liquid nitrogen
LW	Long-wave
LMT	Lorenz-Mie theory
LDPE	Low-density polyethylene

MDF	Medium-density fiberboard
HgCdTe	Mercury cadmium telluride
MIR	Middle-infrared
MW	Middle-wave
MC	Monte Carlo
MALS	Multiple angle light scattering
NBP	Narrow bandpass
NIR	Near-infrared
POM	Polarized optical microscope
PA 6	Polyamide 6
PA 11	Polyamide 11
PA 12	Polyamide 12
PET	Poly (ethylene terephthalate)
PC	Polycarbonate
PCA	Polycrystalline Al_2O_3
PMMA	Polymethyl methacrylate
PP	Polypropylene
$KMnO_4$	Potassium permanganate
QC	Quenched
RTE	Radiative Transfer Equation
RDG	Rayleigh-Debye-Gans
rps	Revolution per second
SEM	Scanning electron microscopy
SC	Slow-cooled
SALS	Small angle light scattering
SAN	Acrylonitrile resin
SAXS	Small angle X-ray scattering
SQP	Sequential Quadratic Programming
TCR	Thermal contact resistance
TC	Thermocouple
TEM	Transmission electron microscopy
UV	Ultraviolet
VIS	Visible

This page intentionally left blank.

Chapter 1

INTRODUCTION

1.1. Problem Statement and Motivation

Today, thermoplastics and thermoplastic composites are promising candidates for manufacturing highly cost-effective and environmental-friendly components in terms of rapid forming and recyclability. High volume production of thermoplastic-based products is the interest of a broad range of industries including: aerospace, automotive, packaging, building & construction, etc. The packaging industry holds the largest market share of thermoplastic-based products, which is followed by building & construction and automotive & aerospace sectors [1]. For the high-volume productions, the right way of processing is crucial for manufacturing the right product.

Thermoforming processes, such as thermostamping [2,3], vacuum forming [4], stretch-blow molding [3], laser transmission welding (LTW) [5] are widely used for high volume production of thermoplastic-based products. Thermoforming of thermoplastics and their composites are performed adopting a combined heating and forming stages at which the preform is heated prior to the forming to improve formability by softening the polymer, as illustrated in Figure 1.1. Semi-crystalline thermoplastics can be softened enough around their melting range since their crystalline phase keeps material in rubbery elastic state until it melts [6]. Hence, the thermoforming window of semi-crystalline thermoplastics are relatively narrower than amorphous thermoplastics. Consequently, semi-crystalline polymers are generally thermoformed at semi-molten state.

Radiative heating is commonly used for thermoforming process of thermoplastics since polymers usually have low thermal conductivity and semi-transparent media. The major advantage of radiation heating is that a portion of the radiative energy penetrates into the bulk polymer medium where high heat flux densities can be used to decrease the heating time without causing thermal damage to the polymer surface [6]. Different radiation sources are used for thermoforming or welding processes of thermoplastics where either polychromatic or monochromatic radiation sources such as infrared (IR), light emitting diode (LED) or lasers are commonly used. In contrast to laser heating applications, IR radiation is emitted at a spectral range which varies regarding to the power and temperature of an IR emitter. Absorption of radiation in polymer media occurs in IR range by excitation of vibrations in molecules [5], so that heat generation happens. Regardless the type of radiative heating, the main objective of the heating stage is to obtain a proper temperature field in the polymer media with rapid heating. Because, the temperature-dependent viscoelastic properties of thermoplastic polymers have great effect on material flow behavior and forming mechanics [7]. Hence, the final temperature state at the end of the heating stage plays significant role for achieving successful forming with respect to the quality of a thermoformed part. Considering the relatively narrow thermoforming window of semi-crystalline

thermoplastics, accurate temperature control and close monitoring of temperature field gain further importance. This thesis therefore focuses on understanding of IR heating of semi-crystalline thermoplastics which aims to analyze the driven mechanisms for IR radiation transport in such type of polymer media. In addition, the thesis proposes a predictive model for radiation heat transfer in semi-crystalline polymers.

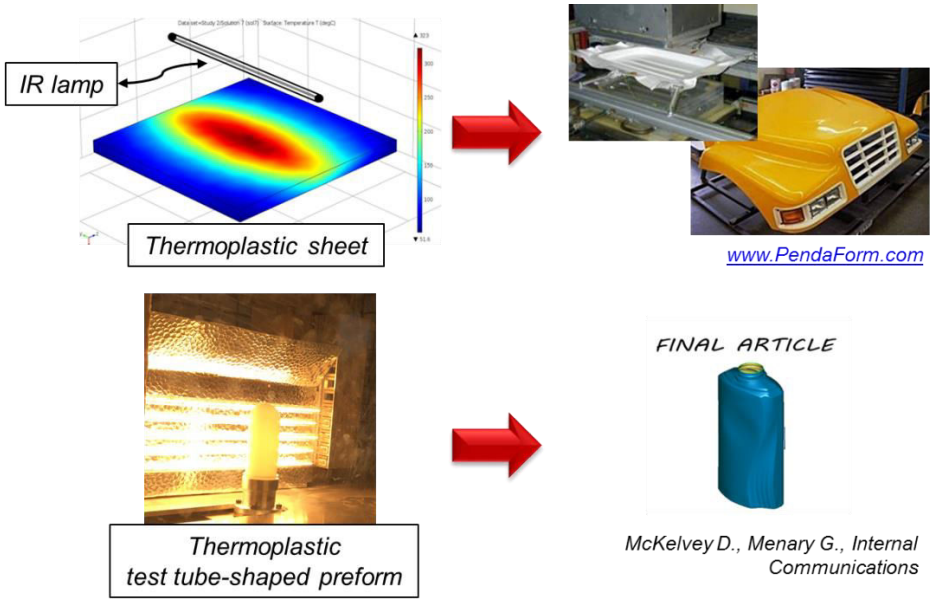

FIGURE 1.1. Overview of the various type of thermoforming processes of thermoplastics.

In this research project, the IR heating problem of semi-crystalline thermoplastics was handled studying high density (HDPE) polyethylene. This research project is supported by Procter & Gamble, a consumer goods company, whose one of the focus areas is packaging industry. Focusing back again the packaging industry, it is known that the market share of polyethylene family -including HDPE, low-density (LDPE) and linear low-density (LLDPE) polyethylene- is around two third of the total thermoplastic shares in Europe, as reported in 2001 [1]. This research work presented here aims to address the role of crystalline structure on radiation heat transfer in unfilled semi-crystalline thermoplastics. In the frame of this research, the developed experimental-numerical approaches can thus be adopted for radiative heating of any type of unfilled semi-crystalline thermoplastics.

1.2. IR heating of semi-crystalline thermoplastics

1.2.1. The coupled relation between the crystalline structure and optical properties of semi crystalline thermoplastics

As mentioned in the previous section, radiation absorption in IR range is mainly governed by excitation of molecules in a radiatively heated material. This fact has a direct relation with the optical properties of the radiatively heated materials in terms of their absorption bands, which was studied extensively for PE [8,9]. Whereas, the location of radiation absorption is related to how radiation travels inside of polymer medium. The key fact here is the crystalline structure of semi-crystalline thermoplastics as it introduces an optically heterogeneous medium. The term -optically heterogeneous medium- represents the optical discontinuities due to the amorphous and crystalline phases of such type of polymers, which eventually causes optical scattering in their medium. Considering the radiation transport and its absorption in semi-crystalline polymer media, the coupled relation between their crystalline structure and optical properties is required to be understood adequately. The relation between the crystalline structure and optical properties of semi-crystalline thermoplastics received a notable attention in the past including wide range of thermoplastics [10–15], at which this relation was mainly analyzed at room temperature. The focus was mainly on understanding the crystallite formations or units causing optical scattering, whereas uncertainties still remain about the scatterer characteristics in unfilled semi-crystalline polymers, including their size and shape.

Considering IR heating of semi-crystalline polymers, the crystalline structure likely causes a twofold effect: Firstly, as mentioned above, there is an ambiguity about the scatterer characteristics of crystalline phase causing optical scattering. Hence, the determination of spatial distribution of scattered radiation and the location of absorption inside of a semi-crystalline medium is still complex. Secondly, the crystalline phase, particularly lamellar morphology, evolves under heating which may potentially cause a change in the scatterer characteristics, and thus optical scattering and optical properties of the medium. This problem should not be confused with the radiation heat transfer in doped [16,17] or short fiber filled [18] thermoplastics as, the scatterer characteristics -which is related to the size of doped or filled particles- potentially do not change under heating. For the heating of unfilled PE starting from room temperature, it is likely to happen that phase transitions between amorphous and crystalline phases start to occur since its melting range can extend down as far as room temperature. In return, thinner crystallites -which are thermodynamically less stable than thicker crystals- melt at lower temperatures, earlier than the thicker ones [19,20]. The potential evolution of optical scattering in unfilled semi-crystalline polymers under heating was experimentally analyzed in literature, where the temperature-dependent optical properties of semi-crystalline polymers was studied [21–24]. A remarkable change in the optical properties of semi-

crystalline thermoplastics under heating, especially close to melting range, was demonstrated. Those studies was typically focused on laser assisted forming processes [21–23], thus the effect of temperature-dependent optical scattering and optical properties were mainly studied at monochromatic wavelengths.

Considering that an IR source emits polychromatic radiation, the spectral dependence of optical scattering is also required to be considered. In other words, in the spectral range of the emitted radiation, the optical scattering behavior in a semi-crystalline medium may change as a function of each wavelength. Hence, for the case of IR heating, the temperature dependent optical scattering and optical properties of unfilled semi-crystalline thermoplastics are required to be analyzed in the spectral range of emitted radiation.

1.2.2. Radiation transport in semi-crystalline thermoplastics and radiation heat transfer modeling

Predictive models are crucial for accurate temperature control and to obtain proper temperature field at the end of IR heating stage of semi-crystalline thermoplastics. Regarding to the optical-morphological relations discussed above, the relation between their crystalline structure and optical properties is the key to develop a radiation heat transfer model including both the potential change in radiation transport in semi-crystalline polymer media and, the evolutions of optical scattering under heating.

Most of the radiative heat transfer models developed for IR heating or laser assisted forming processes of thermoplastics are based on optically homogeneous medium assumption. As shown schematically in Figure 1.2, the emitted radiation from an IR source (or lamp) strikes polymer surface and, it either reflects or penetrates into the polymer medium. Assuming an optically homogeneous medium, the radiation attenuation decreases exponentially in the medium following Beer-Lambert Law, which was adopted extensively for radiative heating of both amorphous and low-crystalline thermoplastics [21–23,25]. Based on this assumption, radiation heat transfer in amorphous and low-crystalline polymers was well-explained and accurately modeled. However, this assumption may be ill-defined for highly crystalline polymers as, it may not adequately explain how radiation propagates and, is absorbed under heating condition. In that sense, the question arises here about how radiation transport in the optically heterongenous medium of unfilled semi-crystalline polymers can be modeled accurately under heating condition.

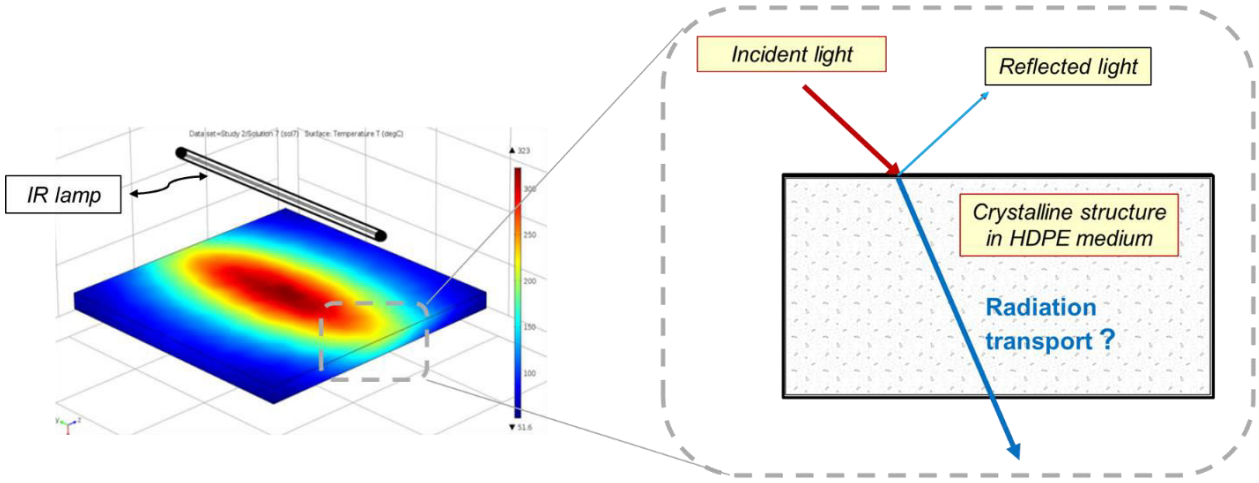

FIGURE 1.2. A schematic illustration of the problem for radiation transport in semi-crystalline medium.

In terms of modeling the radiation heat transfer in optically heterogeneous media, numerous examples exist in literature [16,26,27], which allows to predict the spatial distribution of the scattered light intensity accurately. However, radiation heat transfer models that predicts radiation physics in optically heterogeneous media can be computationally costly, especially if the spectral complexity of radiation source or the geometrical complexity of a heated component is involved [28]. Thus, it is likely difficult to implement such predictive models in practical purposes unless the heated product is at small scales or in simple geometry, unlike the thermoforming processes of thermoplastic-based components at macroscale.

In addition, focusing back again the crystalline morphology-optical scattering relations, scatterer characteristics in unfilled semi-crystalline polymers remain uncertain. This may be solved adopting inverse analyses where experimental characterization of spatial distribution of scattered light in a polymer medium can be fitted to light scattering theories [29]. Thanks to this strategy, and under an assumption of an arbitrary or spherical shape of scatterer, the equivalent scatterer size in semi-crystalline polymer medium can be proposed. The spectral dependency of optical scattering behavior may then be estimated considering the spectral range of emitted IR radiation and, used as input for IR heating modeling.

Beyond this fact, the complexity of the radiation transport problem in unfilled semi-crystalline polymers mainly increases due to potential evolution of scatterer characteristics under heating, induced by amorphous-crystalline phase transitions. In that case, temperature-dependent optical properties and angular optical scattering of polymer media may be required to analyze. Such analyses, including angular optical scattering in PE, was experimentally analyzed at monochromatic wavelength and, the evolution of spatial distribution of scatter light was shown in [11]. Again, knowing that IR radiation is emitted in a spectral range, modeling optical scattering in such an evolving medium may introduce a remarkable

uncertainty in terms of predicting radiation transport and scattering path. Because it could theoretically be a function of the equivalent scatterer that evolves under heating and the spectral range of IR radiation.

Modeling of IR heating of highly crystalline polymers thus remains challenging due the physical background of crystalline morphology-optical properties relations. Hence, simplifying the modeling approach based on the temperature-dependent optical characteristics in semi-crystalline thermoplastics may be the key. Thanks to this, the change in the radiation absorption capacity of the heterogeneous polymer media under heating could be taken into account at macroscale, without computing the scattering path and the location of absorbed energy at microscale. Consequently, the underlying physics of radiation transport and absorption in semi-crystalline polymer media may be adequately approximated without computing radiation transport at microscale, which may offer cost-effective numerical solutions. Whereas, it is of prime importance to understand how accurate temperature field prediction can be obtained adopting this simplification. This approach is required to be analyzed in terms of the temperature tolerance of relatively narrow thermoforming window of semi-crystalline thermoplastics.

1.3. Outline of the thesis

In this thesis, the main focus is on understanding IR heating of semi-crystalline thermoplastics to propose a combined experimental-numerical approach to both characterize the thermal radiation absorption capacity of semi-crystalline polymer media and to model radiation heat transfer to predict 3D temperature field. The research work described herein aims to analyze experimentally the coupled relation between crystalline structure - optical properties of semi - crystalline HDPE. The morphological - optical analyses were analyzed at room temperature and under heating condition to address: *what crystallite formations cause optical scattering in semi-crystalline polymer media and how their coupled relation evolves under heating condition?* Based on the characterization of thermal radiation absorption capacity, which is parametrized as thermo-optical properties, a temperature - dependent numerical model was developed. In terms of assessing the modeling accuracy, an experimental methodology was proposed for non-invasive surface temperature measurements via IR thermography on the semi-transparent HDPE medium.

Concerning the connections between the chapters in terms of the adopting similar analyses and methodologies, some of the theoretical essentials and scientific backgrounds are recalled in each related chapter. In order to bridge the crystalline morphology - optical properties and optical scattering behavior, a significant difference in the analyzed morphology was aimed to be introduced adopting another type of PE polymer: LLDPE. For all the various type morphological – optical analyses presented in this thesis, both the type of PE was used for performing comparative analyses. Unless otherwise indicated or cited

from literature, in the whole part of the following chapters, HDPE and LLDPE are named as PE-1 and PE-2, respectively. The core of the thesis and the focus of the chapters are schematically outlined in Figure 1.3. This thesis compromises four main chapters:

Chapter 2 presents literature review considering optical scattering-crystalline morphology relations in semi-crystalline polymers and radiation heat transfer modeling in optically heterogeneous polymer media. The chapter initially introduces main theoretical essentials for IR radiation physics. The studies proposing crystallite formations that cause optical scattering in various type of unfilled semi-crystalline thermoplastics were reviewed. The experimental-theoretical approaches for estimating the crystalline morphology-optical scattering relation in semi-crystalline polymers were discussed. At the end, radiation heat transfer modeling approaches developed for semi-crystalline or doped thermoplastic media were presented.

Chapter 3 aims to bridge optical - morphological characteristics of PE at room temperature, based on comparative experimental measurements on both HDPE and LLDPE. For this purpose, morphology-dependent optical scattering in PE medium was investigated performing successive spectroscopic – calorimetric – microscopic analyses. Thanks to the analyses, the role of crystalline structure on the optical properties of PE and the spectral dependence of optical scattering was highlighted. The morphology-dependence of the total scattered light was estimated in forward and backward directions. The analyses extended considering the spatial distribution of scattered light intensity at 632.8 nm and, the relation between spatial distribution of scattered light and PE morphology was investigated. The crystalline formations or size of morphological units in PE medium causing optical scattering was questioned.

Chapter 4 focuses on the evolutions in the crystalline morphology and optical characteristics of HDPE and LLDPE under heating. The temperature-dependent behavior in the optical properties of HDPE and LLDPE was experimentally analyzed. The experimental calorimetric - optical studies presented in this chapter aims to correlate the temperature-dependent transmittance characteristics to the lamellae melting in PE medium. Thanks to this step, most probable lamellar crystal size that melts and induces remarkable change in the optical scattering behavior in PE medium under heating was addressed. The temperature-dependent spectroscopic measurements enabled to determine the temperature-dependent thermo-optical properties of HDPE, over the temperature range between room temperature up to melting range of HDPE.

In *Chapter 5*, a novel combined numerical-experimental approach is proposed for IR heating of semi-crystalline thermoplastics. Radiation heat transfer model was developed considering the simplification of radiation transport in the optically heterogeneous medium of PE under heating. The temperature-

dependent thermo-optical properties characterized in *Chapter 4*, was adopted in this chapter as, *radiation absorption parameter* for radiation heat transfer modeling of HDPE. In addition, an experimental method was proposed concerning non-invasive surface temperature measurements on semi-transparent PE via IR thermography. The accuracy of the numerical model was assessed performing numerical-experimental IR heating studies using different IR heating setup. At last, the morphology-dependent thermal radiation absorption capacity in HDPE and LLDPE medium and radiative heating behavior relations were qualitatively analyzed.

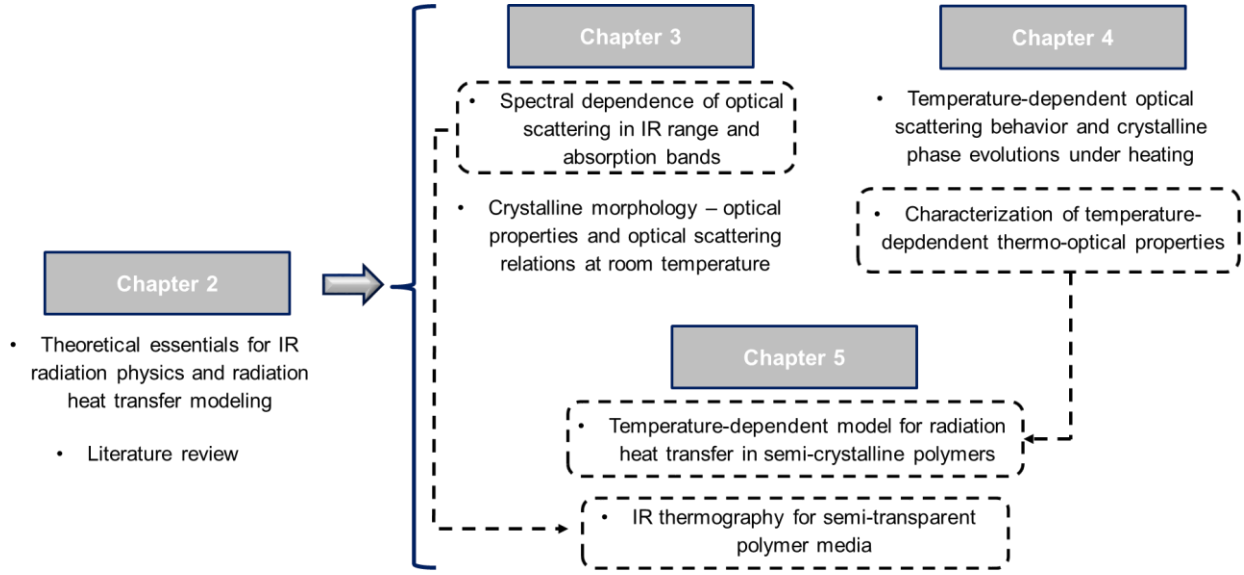

FIGURE 1.3. Outline of the thesis and the motivations of the chapters.

The last chapter of the thesis, *Chapter 6,* summarizes the key conclusions of the whole study and provides recommendations for future work. In addition, considering the underlying physics of the complete problem focused here, a discussion is presented for broadening the applicability of the experimental-numerical approaches proposed in this thesis for radiative heating of any type of unfilled semi-crystalline thermoplastics.

References

[1] Biron M. Thermoplastics and Thermoplastic Composites: Technical Information for Plastics Users. Elsevier; 2007.

[2] Boisse P. Advances in Composites Manufacturing and Process Design. Woodhead Publishing; 2015.

[3] Heat Transfer in Polymer Composite Materials: Forming Processes, Ed: Nicolas Boyard, John Wiley & Sons, 2016.

[4] Burkhardt Gert, Hüsgen Ulrich, Kalwa Matthias, Pötsch Gerhard, Schwenzer Claus. Plastics Processing, 1. Processing of Thermoplastics. Ullmanns Encycl Ind Chem 2011. doi:10.1002/14356007.a20_663.pub2.

[5] Poprawe R. Tailored Light 2: Laser Application Technology. Springer Science & Business Media; 2011.

[6] Klein R. Laser Welding of Plastics. John Wiley & Sons; 2012.

[7] Bhattacharyya D. Composite Sheet Forming. Elsevier; 1997.

[8] Gulmine J., Janissek P., Heise H., Akcelrud L. Polyethylene characterization by FTIR. Polym Test 2002;21:557–63. doi:10.1016/S0142-9418(01)00124-6.

[9] Kossack W, Papadopoulos P, Parkinson M, Prades F, Kremer F. IR transition moment orientational analysis on semi-crystalline polyethylene films. Polymer 2011;52:6061–5. doi:10.1016/j.polymer.2011.10.051.

[10] Fratini CM. Study of the Morphology and Optical Properties of Propylene/Ethylene Copolymer Films 2006.

[11] Keane JJ, Stein RS. The scattering of light from thin polymer films. II. Scattering from polyethylene. J Polym Sci Part Polym Chem 1956;20:327–350.

[12] Wang L, Kamal MR, Rey AD. Light transmission and haze of polyethylene blown thin films. Polym Eng Sci 2001;41:358–372.

[13] Denis A, Dargent E, Lebaudy PH, Grenet J, Vautier C. Dependence on the spectral scattering coefficient on crystallinity into semicrystalline polyester. J Appl Polym Sci 1996;62:1211–8.

[14] Hakoume D, Dombrovsky LA, Delaunay D, Rousseau B. Spectroscopic diagnostics of morphological changes arising in thermal processing of polypropylene. Appl Opt 2014;53:2702. doi:10.1364/AO.53.002702.

[15] Kolesov I, Mileva D, Androsch R. Mechanical behavior and optical transparency of polyamide 6 of different morphology formed by variation of the pathway of crystallization. Polym Bull 2014;71:581–93. doi:10.1007/s00289-013-1079-9.

[16] Ilie M, Kneip J-C, Matteï S, Nichici A, Roze C, Girasole T. Laser beam scattering effects in non-absorbent inhomogenous polymers. Opt Lasers Eng 2007;45:405–12. doi:10.1016/j.optlaseng.2006.07.004.

[17] Mamuschkin V, Roesner A, Aden M. Laser Transmission Welding of White Thermoplastics with Adapted Wavelengths. Phys Procedia 2013;41:172–9. doi:10.1016/j.phpro.2013.03.067.

[18] Hohmann M, Devrient M, Klämpfl F, Roth S, Schmidt M. Simulation of Light Propagation within Glass Fiber Filled Thermoplastics for Laser Transmission Welding. Phys Procedia 2014;56:1198–207. doi:10.1016/j.phpro.2014.08.035.

[19] Wlochowicz A, Eder M. Distribution of lamella thicknesses in isothermally crystallized polypropylene and polyethylene by differential scanning calorimetry. Polymer 1984;25:1268–1270.

[20] Peacock AJ. Handbook of polyethylene: structures, properties, and applications. New York: Marcel Dekker; 2000.

[21] Keller B, Pfeifer R, Su W-N, Eyerer P. Temperature Dependent Optical Properties of Polymers as a Basis for Laser Process Modeling ,1998.

[22] Becker F, Potente H. A step towards understanding the heating phase of laser transmission welding in polymers. Polym Eng Sci 2002;42:365–374.

[23] Geiger M, Frick T, Schmidt M. Optical properties of plastics and their role for the modelling of the laser transmission welding process. Prod Eng 2009;3:49–55. doi:10.1007/s11740-008-0141-1.
[24] Hawkins SW, Richards RB. Light transmission and the formation and decay of spherulites in polythene. J Polym Sci Part Polym Chem 1949;4:515–22.
[25] Schmidt F. Modelling of infrared heating of thermoplastic sheet used in thermoforming process. J Mater Process Technol 2003;143–144:225–31. doi:10.1016/S0924-0136(03)00291-7.
[26] Apetz R, Bruggen MPB. Transparent Alumina: A Light-Scattering Model. J Am Ceram Soc 2003;86:480–6. doi:10.1111/j.1151-2916.2003.tb03325.x.
[27] Berrocal E, Sedarsky DL, Paciaroni ME, Meglinski IV, Linne MA. Laser light scattering in turbid media Part I: Experimental and simulated results for the spatial intensity distribution. Opt Express 2007;15:10649–65. doi:10.1364/OE.15.010649.
[28] Humphrey A, Harman T, Berzins M, Smith P. A scalable algorithm for radiative heat transfer using reverse monte carlo ray tracing. Int. Conf. High Perform. Comput., Springer; 2015, p. 212–230.
[29] Agrawal BM, Mengüç MP. Forward and inverse analysis of single and multiple scattering of collimated radiation in an axisymmetric system. Int J Heat Mass Transf 1991;34:633–47. doi:10.1016/0017-9310(91)90112-R.

This page intentionally left blank.

Chapter 2

IR HEATING ASSISTED THERMOFORMING PROCESS OF SEMI-CRYSTALLINE THERMOPLASTICS

2.1. Overview of IR heating for thermoforming process of semi-crystalline thermoplastics

As aforementioned, IR radiation heat transfer is widely used for various type of thermoforming processes of thermoplastics such as vacuum forming [1], injection-stretch blow molding (ISBM) [2]. Bulk, or unfilled, polymers usually have low thermal conductivity where also some of them, such as PE, PET, are semi-transparent [2,4,5] which makes radiation heating as promising method to heat such medium efficiently for rapid forming processes. More specifically, the key benefit of radiation heating is that a significant amount of the radiative energy penetrates into the bulk polymer medium thanks to their semi-transparency where high heat flux densities can be used to decrease the heating time without causing thermal damage to the polymer surface [1].

Thermoforming window - which is the suitable temperature range for a successful forming process - of amorphous thermoplastics is wider than semi-crystalline thermoplastics [6]. Amorphous thermoplastics are driven into rubbery state above their glass transition temperature (T_g) that provides relatively large thermoforming window between their T_g and softening (T_s) temperature. Conversely, semi-crystalline thermoplastics can be softened enough around their melting range which causes a narrow thermoforming window. Above T_g of such type of polymers, their semi-crystalline phase still stands that keeps the material in tough-elastic state until crystals melt down in melting range [1,7]. More closely, thermoforming window range of semi-crystalline polymers is related to the fraction of their crystalline phase. In general, the fraction of crystalline phase can be parametrized as degree of crystallinity (X_c (%)). It is known that, regarding to cooling conditions, X_c of PET may reach up to 30% [8,9] whereas this ratio may reach up to 80% for HDPE [10]. In Figure 2.1, the softening behavior of two different semi-crystalline thermoplastics and their thermoforming window are schematically displayed. A low crystalline poly (ethylene terephthalate) (PET) is compared with the highly crystalline PE. As it is seen, the storage moduli (E`) of both materials changes differently under heating condition that causes to change materials softening behavior and therefore their thermoforming window are different. Therefore, the typical processing range for PET is relatively larger than highly crystalline polymers, such as HPDE, where such type of PE are thermoformed when it is in semi-molten state.

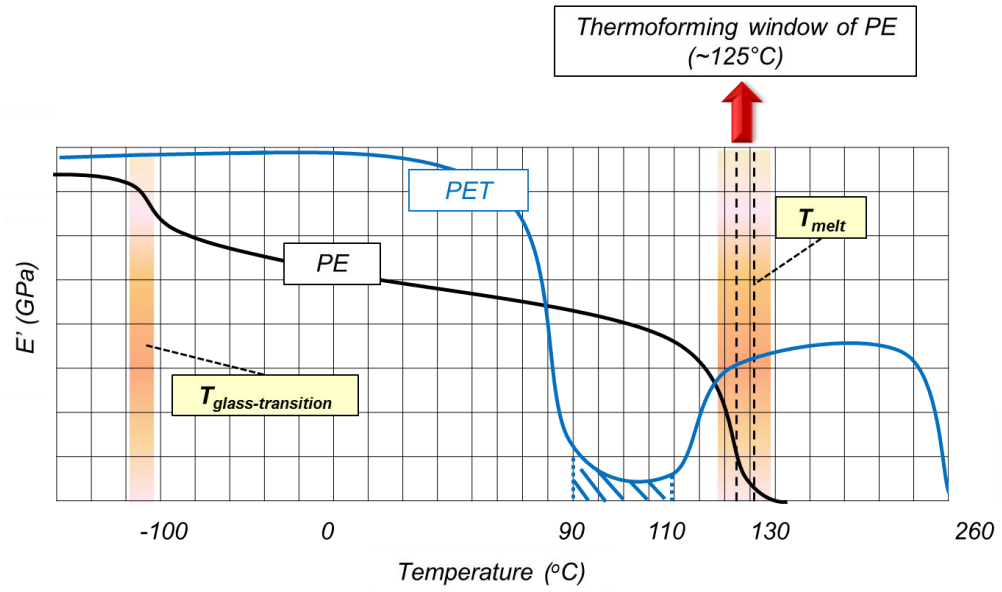

FIGURE 2.1. Comparison between the softening behavior of low crystalline PET and highly crystalline PE.

Since temperature-dependent rheology of polymer affects forming mechanics, and thus final product quality [11], it is crucially important to have an extensive knowledge on the temperature distribution at the end of IR heating stage. As a consequence, more accurate temperature control and close monitoring of temperature state is required for achieving a successful forming on highly crystalline thermoplastics.

2.2. Radiation physics of IR heating

Radiation transport phenomena can be explained theoretically based on two different point of views of electromagnetic wave (EMW) theory and, quantum theory which is yet quite complex for radiation applications in engineering [12,13]. According to electromagnetic wave theory radiation propagates in the form of transverse waves where they oscillate perpendicular to direction of propagation. Maxwell's equations can accurately describe the propagation of electromagnetic waves where interference and polarization of propagated radiation takes a prominent role. Nevertheless, in many engineering problems related to radiation heat transfer, polarization and interference of radiation propagation may be assumed negligible in comparison to its directional and spectral complications if the conditions mentioned below are satisfied [12]:

- The wavelength of the propagated radiation is much smaller than the size of an object where the radiation propagates into.

- The distance for a radiative transfer between two interacting objects is several times larger than the wavelength of propagated radiation.

As long as the those conditions are valid, which is the case in the current study as well, the radiation energy can be defined as photons or light particles and, the radiation transport can be expressed adopting ray tracing methods and geometrical optics approximations [12].

2.2.1. Directional and spectral distribution of emitted radiation

Considering the directional dependency of a radiation source, is it known that an ideal radiation source is theoretically emits maximum amount of radiative energy where the emitted energy is independent of direction. Such an ideal body is called as *black body* in theory [12,14]. The spectral intensity (I_λ), which represents the level of radiative energy propagating in any direction, is uniform for the spectral intensity of a black body ($I_{\lambda b}$). The independent behavior in $I_{\lambda b}$ is schematically illustrated in Figure 2.2 in terms of the same level I_λ obtained in any direction.

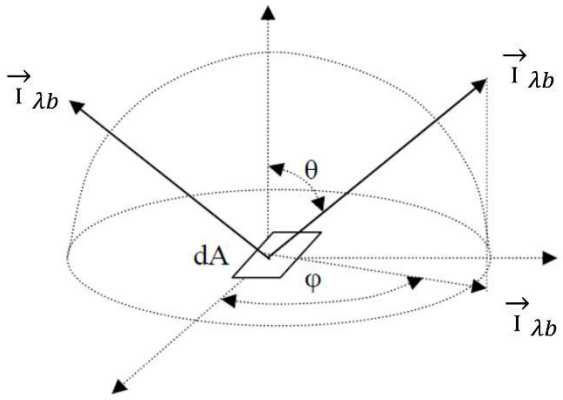

FIGURE 2.2. Direction-independent intensity of emitted radiation from a Lambertian source.

As the emitted black body intensity is uniform in all directions, the notation that represents azimuth angle (φ) may be omitted and the relation between $I_{\lambda b}$ and the directional spectral emissive power of black body ($E_{\lambda b}(\theta)$) can be formulized as in Equation 2.1, known as Lambert's Cosine Law:

$$E_{\lambda b}(\varphi, \theta) = E_{\lambda b}(\theta) = I_{\lambda b}(\theta) \cos\theta \tag{2.1}$$

Considering the relation illustrated in Figure 2.2, the hemispherical spectral emissive power of a black body ($E_{\lambda b}$ ($W/m^2\mu m$)), which physically defines all the emitted spectral intensity through an entire hemisphere, is the integration of the intensity all over the solid angles of the hemisphere (Equation 2.2):

$$E_{\lambda b} d\lambda = I_{\lambda b} d\lambda \int_{\phi=0}^{2\pi} \int_{\theta=0}^{\frac{\pi}{2}} cos\,\theta\, sin\,\theta\, d\theta d\varphi = I_{\lambda b} \pi d\lambda \quad (2.2)$$

where the spectral distribution of $E_{\lambda b}$ can be explained using the Planck's Law [12]:

$$E_{\lambda b}(T) = \pi I_{\lambda b}(T) = \frac{2\pi h c_0^2}{n^2 \lambda^5 [\exp(\frac{h c_0}{n k_B \lambda T}) - 1]} = \frac{2\pi C_1}{n^2 \lambda^5 [\exp(\frac{C_2}{n \lambda T}) - 1]} \quad (2.3)$$

In Equation 2.3, n represents the refractive index of medium where radiation transport occurs. Assuming that radiation transport is in *non-participating medium*, n can be considered as 1 [12,14]. Theoretically, n is the ratio between the speed of the light in vacuum, or non-participating medium, (c_o) and, the reduced speed of light in a *participating medium* (c_{medium}) of greater density. Hence, radiation transport formulized in Equation 2.3 considers n as unity, which is also independent of wavelength in this condition. Otherwise wavelength dependency of n needs to be introduced for the case of radiation transport in a participating medium. λ is the variable representing wavelength of the emitted black body radiation power at a temperature, T. In addition, the parametric constants of Planck's Law and the derived parameters between those constants, such as C_1 and C_2 appeared in Equation 2.3, can be found in Annex A1.1. Regarding the temperature of a black body (T_{bb}), the spectral range of $E_{\lambda b}$ at each corresponding T_{bb} level can be calculated using the relation in Equation 2.3. The calculated spectral distribution of $E_{\lambda b}$ considering T_{bb} between 400 - 3000K are presented in Figure 2.3. At it is seen in the figure, the spectral range of the $E_{\lambda b}$ shifts towards to smaller wavelengths once temperature increases. In the similar manner, there is also an inverse relation between T_{bb} and the wavelength at which the maximum emitted power of a black body occurs (λ_{max}). The Wien's displacement Law founds that the product of λ_{max} and T_{bb} is constant as 2897.8 μmK [12,14]. This relation is not only valid for black body, but also for any real body. Using the Wien's displacement law, the λ_{max} of an emitting body can be obtained from Equation 2.4, based on the knowledge of its temperature:

$$\lambda_{max} T = 2897.8 \mu m K \quad (2.4)$$

At any temperature, the spectral range of 95.6 % of the overall emitted power of any type of body can be theoretically found between $\lambda_{max}/2$ and $5\lambda_{max}$ [2,14]. Considering that temperature of a typical IR lamp used for ISBM processes of polymers is set around 2000 - 2800K, the spectral range of its E_λ should be around roughly 0.55- 7.2 μm. In reality, the radiation emitting sources are far from being black body where their emittance efficiency is much lower than a black body. The spectral emissivity of such a real

body (ε_λ), which is the ratio between its hemispherical spectral emissive power (E_λ) to the $E_{\lambda b}$, can be determined using Equation 2.5:

$$\varepsilon_\lambda(T) = \frac{E_\lambda(T)}{E_{\lambda b}(T)} \tag{2.5}$$

If we assume a greybody, which theoretically shows no spectral dependency in its ε_λ (T), the overall emitted radiation of its E_λ (T) should be lowered by the factor of ε_λ (T). Nevertheless, its spectral distribution and λ_{max} does not change, as also illustrated in Figure 2.3. Here, the E_λ (T) of a grey body at a temperature (T_{gb}) of 2400K was calculated assuming a constant ε_λ as 0.27. The solid and dashed black lines in the figure represent the E_λ (T) of the black and grey bodies at a temperature of 2400K. The shift between their values over wavelength is seen. Obviously, the lower the emissivity of a real body the lower radiative power could be emitted. As also seen Figure 2.3, the overall emitted radiation increases with an increase in T_{bb}. In addition, the spectral ranges of typical radiation bands, namely visible (VIS), near (NIR) and middle- infrared (MIR) bands are displayed in the figure below.

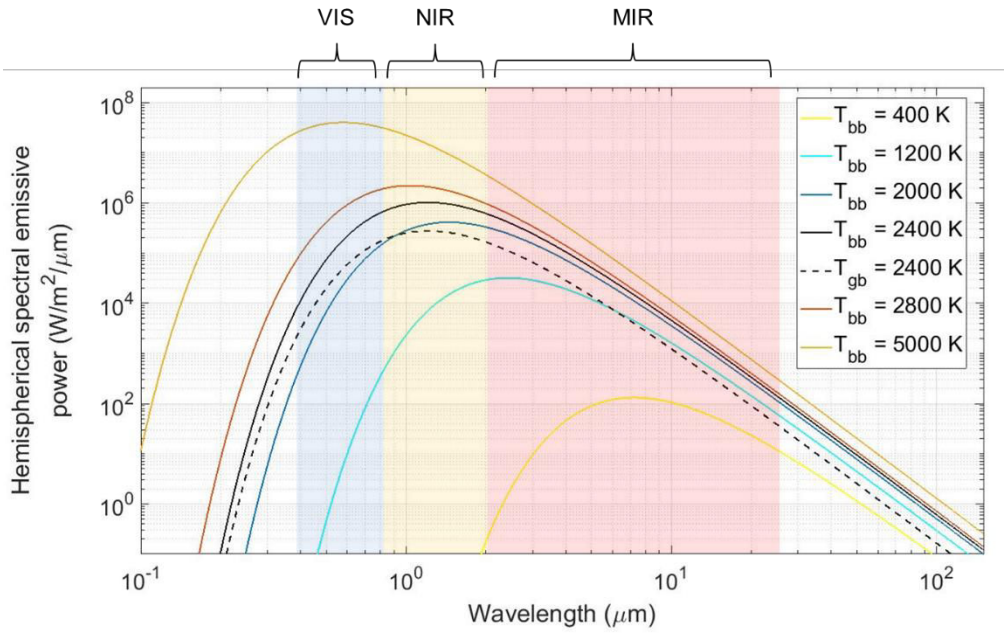

FIGURE 2.3. $E_{\lambda b}$ (T) as a function of temperature and its comparison to E_λ of a grey body at 2400K.

The overall emitted power, namely total emissive power of black body or black body irradiance (E_b), can be determined integrating of $E_{\lambda b}$ on the overall spectrum, which can also be calculated using Stefan-

Boltzmann Law (Equation 2.6). Regarding to this law the black body emissive power increases once T_{bb}.by the fourth power:

$$E_b = \int_0^\infty E_{\lambda b}(T)\, d\lambda = \sigma T^4 \tag{2.6}$$

Based on the relation defined in Equation 2.6, the total emissivity ε (T), also named mean emissivity, of a real body at a temperature of T can be determined, as stated in Equation 2.7:

$$\varepsilon(T) = \frac{E(T)}{E_b(T)} = \frac{\int_0^\infty \varepsilon_\lambda(T) E_{\lambda b}(T) d\lambda}{\sigma T^4} \tag{2.7}$$

Considering a case of IR heating with a halogen lamp, the spectral dependence of the emitted power from a tungsten of the lamp was studied in detail in [9] where the spectral-dependence of the tungsten coil was also approximated using Hagen- Rubens Law [12]. As later discussed by Le Maoult and Schmidt [2], ε_λ (T) of the tungsten coil varies strongly for the wavelengths smaller than 2.6 μm especially lower than 1 μm which is in close agreement with the earlier studies performed for the ε_λ (T) tungsten [15,16]. In addition, they reported that ε (T) of a halogen lamp at 2470K is 0.27. The temperature of the lamp (T_{lamp}) is the calculated value based on its nominal power, which was reported in [17,18]. Besides of halogen lamps, quartz tube or ceramic lamps are also typical IR emitters used for thermoforming [2]. Andrieu et al. [17] analyzed the temperature of quartz tube and ceramic lamps when they are at nominal power. They showed that temperature of ceramic and quartz tube emitter is around 740K and 1150K, respectively. Similar value was stressed earlier in [18] for quartz tube. The experimental studies on the characteristics of IR emitter was extended further in [17], at which a comparative analysis was performed considering energy efficiency, geometrical design features and spectrum of emitted radiation. They measured irradiance (E (W/m^2)) on an identical 600*600mm surface, which was positioned 15 cm away from the tested IR emitters. The measurements were carried out using a flux meter in the spectrum between 0.6 and 15 μm. In Figure 2.4, the geometrical details of halogen (a), ceramic (b) and quartz tube (c) IR emitters are displayed. As shown in Figure 2.4 (a), halogen lamps can be designed with and without ceramic reflector coated on the backside of the lamp. Thanks to this step, the potential emitted radiation towards to back direction of the lamp may reflect and thus may be received by heated geometry. In Figure 2.4 (d), radiation transport between IR heating unit and a heated polymer is schematically displayed. The typical length of halogen lamp and the diameter of its tungsten coil is around 300 mm [18,19] and 2 mm [19], respectively; where also the tungsten is enclosed by quartz tube with a diameter around 10mm.

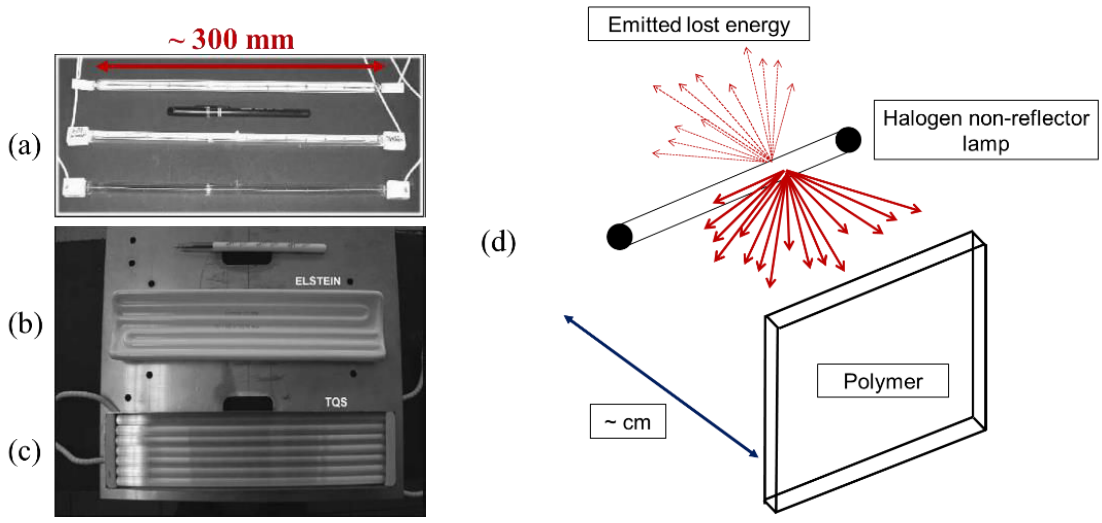

FIGURE 2.4. Typical halogen (a), ceramic (b) and quartz tube (c) IR emitters [18], and the schematical illustration of IR heating performed using a halogen non-reflector lamp (d).

Table 2.1 presents the radiative characteristics of IR emitters at their nominal power calculated in [17] based on E measurements. Using the E values, the emitted power that is received by the identical 600*600mm^2 surface was calculated for each tested IR emitter. Based on the effective nominal power of each lamp and the received power at the identical surface, energy efficiency of the IR emitters was determined. The effective nominal power here represents the fraction of power that is potentially transferred to the heated geometry. In other words, for example, a halogen non-reflector emitter (without coated with ceramic reflector) was used for the E measurements. Considering that the emitted energy is equally distributed from the tungsten wire of the halogen lamp, 50% of the emitted energy may be lost since it may be emitted to the inverse directions to the heated geometry. Therefore, the effective nominal power of halogen lamp is determined as half of its nominal power (500W). The same approach was applied to the other tested IR emitters based on their geometrical design features. As distinctively seen in the table below, the spectrum of emitted radiation from a halogen lamp is at much shorter wavelengths, which lies in VIS and NIR ranges. The comparative analyses revealed in [17] clearly points out the importance of IR lamps selection in terms of various thermoforming process parameters, such as energy efficiency, heating time, process setup, and as well as, optical properties of participating polymer medium. This point will be discussed further in the following sections, and also in Chapter 5 considering radiation heat transfer modeling of PE.

IR emitter type	Quartz Tube	Ceramic	Halogen
Emitted power received by the identical surface (W)	234	208	117
Nominal effective power (W)	600	480	250
Energy efficiency (%)	39.0	43.3	46.8
T_{lamp} at nominal power (K)	1150	740	2470
Spectral range of emitted radiation (µm)	1.25 – 12.5	1.5 - 15	0.6 - 6

TABLE 2.1. Overview of radiative characteristics of IR emitters used for thermoforming processes [17].

Beyond the characteristics of emitted energy from a real body, the radiation sources may not follow both the directional and spectral independent behavior whereas one of the conditions may be satisfied. For instance, radiation sources that follow Equation 2.1 are called as Lambertian source. The directional dependency of halogen, quartz tube or ceramic lamps IR heaters was also investigated in detail in [17]. Their experimental analyses showed the significant difference in the directional-dependency of I_λ emitted by various type of IR emitter (Figure 2.5). As shown in the figure, the emittance from the ceramic lamps (Elstein FSR and HTS) and Quartz tube (TQS FS H2) are strongly directional-dependent, while a halogen (Philips) lamp follows Lambertian's Cosine Law closely. This behavior may be critical in terms of modeling the emitted radiation from a specific IR lamp.

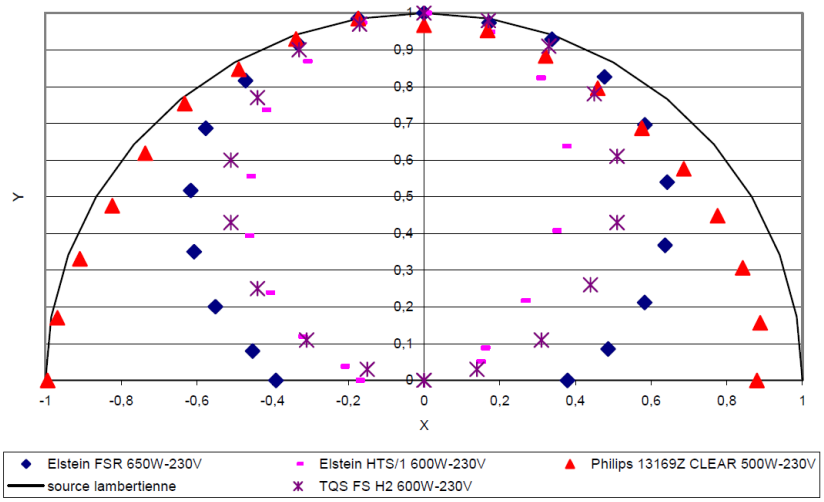

FIGURE 2.5. Experimental analyses on the directional dependency of emitted power ($E_\lambda(\theta)$) from the various types of IR lamps [17].

In Equation 2.3, the emitted radiation of a black body was formulized considering a non-participating medium. In general speaking, the air medium may be considered as non-participating, except for some radiation heat transfer problems such as in atmospheric studies [12,20]. Considering the IR heating or laser assisted thermoforming processes, the traveled distance of radiation energy into an air medium - in other words the distance between a heated polymer and radiation source- is way shorter, which is in order of centimeters as shown in Figure 2.4 (d). Therefore, the air between the radiation source and the heated polymer may be assumed as *non-participating* for thermoforming processes and its refractive index (n_{air}) can be assumed as 1.

2.2.2. Radiation transport in participating medium

Considering a radiation propagated in a participating medium its intensity may alter due to interactions with the medium where it travels through [14]. The physical meaning of radiation transport in participating medium is that the intensity of a propagated radiation in a certain direction attenuates due to scattering or absorption of some fraction of radiative energy by the medium which eventually leads generation of heat in the medium. An incident radiation that arrives on a participating medium surface may either be reflected from the surface or, transmitted and attenuated inside of the medium. Regarding the conservation of energy, the ratio of reflected (R_λ), attenuated (A_λ) and transmitted (T_λ) radiation energy traveling through a participating medium can be stated as unity, as presented in Equation 2.8. It should be noted that the physically measured R_λ and T_λ are also named as *reflectance* and *transmittance* in literature [21,22]:

$$1 = A_\lambda + R_\lambda + T_\lambda \tag{2.8}$$

The terms R_λ and T_λ are given here only represents the total fraction of reflected and transmitted radiation without including any directional information. Theoretically, the fraction of incident light propagates in a certain direction and, transmitted through a participating medium in certain direction is named as directional-directional transmittance ($T_\lambda^{\,i,r}$). Regarding to the characteristics of a participating medium, the incident light propagates in certain direction may scatter inside of participating medium where the transmitted light through the medium can be considered in all directions of a theoretically assumed hemisphere. The fraction of transmitted light in such way is named as directional-hemispherical transmittance ($T_\lambda^{\,i,\cap}$). Simply, both for transmitted or reflected radiation, the former and the latter directional notation represents the considered angle, or all the angles in an entire hemisphere, of the radiation which is generally defined just before and after a radiation interaction with a participating surface or a bulk medium. In accordance with this rule, regarding the surface characteristics of the medium in terms of surface irregularities, the incident light may be either reflected specularly ($R_\lambda^{i,r}$) or

diffusively ($R_\lambda^{i,\cap}$) where the ratio between $R_\lambda^{i,r}$ and $R_\lambda^{i,\cap}$ changes as a function of surface roughness [21,23]. The remaining amount of radiation travels through the medium where its direction may change regarding the relative refractive index (Δn) between the two media where radiation travels from one to the another one. Based on Snell–Descartes Law; the change in the direction of transmitted radiation can be defined. Assuming that incident radiation travels through an air and a participating polymer medium the, the Snell–Descartes law can be written as in Equation 2.9:

$$n_{air}.\,sin\theta_{air} = n_{polymer}.\,sin\theta_{polymer} \tag{2.9}$$

where $n_{polymer}$ represents the polymer medium's refractive index. The schematic illustration of specular and diffuse reflection on a participating medium is presented in Figure 2.6.

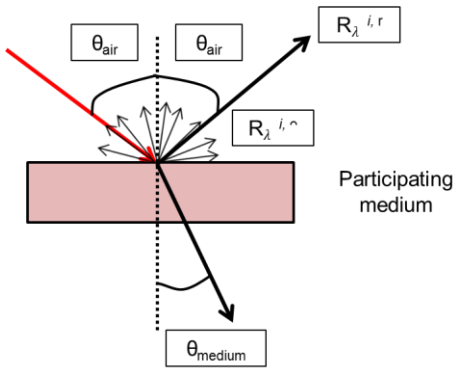

FIGURE 2.6. Specular and diffuse reflections of incident radiation that arrives on the surface of a participating medium and changes its direction due to refractive index difference.

In the given direction of the transmitted radiation inside of the participating medium, its intensity can be theoretically defined considering all the scattering, absorption and emission phenomena alongside that propagation direction. In theory, the definition for the energy balance of radiation energy in the participating medium is called as Radiative Transfer Equation (RTE). The integro-differential form of RTE can be stated mathematically as below [12,14]:

$$\frac{dI_\lambda}{dS} = -\beta_\lambda(S)\,I_\lambda(S) + \kappa_\lambda(S)\,I_{\lambda b}(S) + \frac{D_\lambda}{4\pi}\int_{\Omega_i=0}^{4\pi} I_\lambda(S,\Omega_i)\,\phi_\lambda(\Omega,\Omega_i)\,d\Omega_i \quad \text{with;} \quad \beta_\lambda = \kappa_\lambda + D_\lambda \tag{2.10}$$

The change in radiative energy after a small path increment (dS) along the radiative propagation direction of S and solid angle (Ω) can be calculated based on RTE. The first term in the formula stands for the radiation loss due to both absorption and scattering effects where spectral extinction coefficient

(β_λ) is the sum of both spectral absorption (κ_λ) and scattering (D_λ) coefficients. The second term accounts the radiation gain due to self-emission of along the S direction which is function of $I_{\lambda b}$. It should be noted here that the first term based on β_λ reflects the total attenuation that occurs in the given direction, while only the term, κ_λ accounts for the attenuated energy that is absorbed by the medium and converted into heat. The amount of energy scattered in that direction is represented by the D_λ, which only results attenuation in the intensity [7,12,14]. The third term represents the radiation gain caused by in-scattering phenomena where scattering phase function (ϕ_λ) describes the probability of directional distribution of the scattered radiation. Such type of participating medium is called as *optically heterogeneous* where the calculation of heat generation may be complex, as the optical scattering characteristics needs to be known to describe the spatial change in the propagated radiation. This point will be explained further in Section 2.1.1 regarding to experimental theoretical calculations of spatial distribution of scattered light.

Considering a cold and optically homogeneous medium, the second and the third terms of RTE may be neglected, respectively. Based on these assumptions the RTE can be greatly simplified at which the derived formula is stated as Beer-Lambert Law [2,3,7,12,14] (Equation 2.11):

$$I_\lambda(S) = I_\lambda(0).exp^{-\beta_\lambda.S} \tag{2.11}$$

The law thus explains the radiation attenuation inside of an optically homogeneous medium as a function of exponential decrease where the heat generation in the direction of propagated radiation can be described accurately. The radiation transport inside of a homogeneous and heterogeneous media was schematically illustrated in Figure 2.7 (a) and (b). In addition, radiation attenuation in homogeneous medium regarding the Beer-lambert law is shown in Figure 2.7 (a).

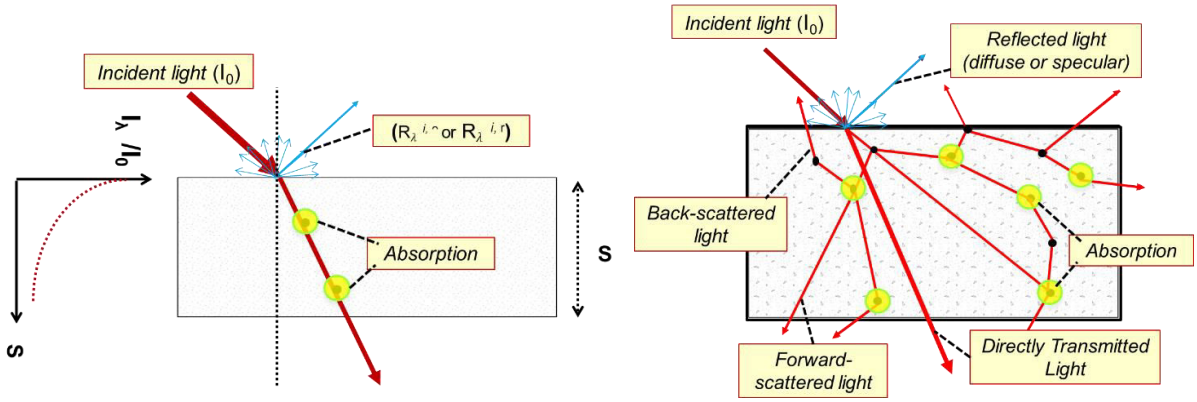

(a) (b)

FIGURE 2.7. Schematically illustrated radiation transport in optically homogeneous (a) and heterogeneous media (b).

Considering that internal heat generation inside of a medium depends on only absorption characteristics, divergence of radiant flux vector ($\nabla \cdot q_r$) - called as *radiative source term* – at the depth "S" gives the local energy source (Equation 2.12):

$$\nabla \cdot q_r(S) = \int_0^{\infty} -\kappa_\lambda I_\lambda(0) e^{-\kappa_\lambda S} d\lambda \tag{2.12}$$

The reciprocal of κ_λ, which is the parameter indicating how strong radiation is absorbed and attenuated in the medium, is called as optical penetration depth (D_p (m)). Thus, it physically represents the depth where radiation propagated inside of a participating medium extinct. In a participating medium which has a temperature at T, its integrated absorption coefficient ($\overline{\kappa}(T)$ (m^{-1})) can be calculated and D_p can be determined for the corresponding medium temperature (Equation 2.13):

$$\overline{\kappa}(T) = \frac{\int_{\lambda_1}^{\lambda_2} \kappa_\lambda . I_\lambda^o(T) d\lambda}{\int_{\lambda_1}^{\lambda_2} I_\lambda^o(T) d\lambda} \qquad \text{with; } D_p = \frac{1}{\overline{\kappa}(T)} \tag{2.13}$$

In terms radiation heat transfer modeling in PE medium, the computation of ($\nabla \cdot q_r$) is one of the key factors to achieve an accurate estimation of temperature field distributions as it is the parameter that defines how strong the medium absorb energy and thus convert into heat. Here, in Equation 2.12, ($\nabla \cdot q_r$) was shown as a function of only κ_λ assuming a non-scattering homogeneous medium. As shown in Equation 2.10, radiation attenuation in an optically heterogeneous medium is related to both scattering and absorption characteristics, which is parametrized as β_λ. Regarding the optical scattering behavior inside of PE medium, this parameter may change which eventually results a change in the computed ($\nabla \cdot q_r$) values. This point will be discussed further in Chapter 3 and 5.

2.3. Crystalline structure and optical scattering relations in semi-crystalline thermoplastics

It is known that the presence of crystalline structure in semi-crystalline polymers introduces an optically heterogeneous medium due to mismatch between the refractive indices of amorphous ($n_{amorphous}$) and crystalline ($n_{crystalline}$) phases. The coupled relation between the crystalline structure and optical scattering characteristics of various type of semi-crystalline polymer has been extensively studied in literature, such as PE [23–27], PET [8]; polypropylene (PP) [28–33] and polyamide 6 (PA 6) [34]. It should be noted that most of the studies found in literature were focusing on the different type of

engineering problems or physical characterizations of semi-crystalline polymers rather than using such relation for determining thermo-optical properties which can be used as input for the models to solve RTE. Either way, the studies that analyze the relation between the crystalline structure and optical characteristics is fundamental for determining crystalline morphology-dependent optical scattering behavior. Thanks to this, morphology-dependent ϕ_λ and the thermo-optical properties of semi-crystalline polymers may be determined and used as numerical input inside of a radiation heat transfer model.

The earliest studies on the crystalline structure – optical scattering relations in semi-crystalline polymers, particularly PE, was performed by the research group of University of Massachusetts [24–26] who employed light scattering techniques extensively to understand the morphology-dependent multiple angle light scattering (MALS) behavior in PE. In [24], PE was analyzed under unpolarized light at 546 nm where they reported that the scatterer size, so called scattering unit, in heterogeneous PE medium is between the order of hundreds of angstrom and order of microns. This range reflects a size of scatterer larger than individual crystallites (or lamallae) and smaller than spherulites. In addition, spectral-dependence of the calculated turbidity was reported for the measurements performed at 25°C in the spectral range between 350 to 950 nm. Interestingly, an inverse relation between turbidity and wavelength was observed in this range. In [25], a scattering model was proposed for PE which was combined with experimental angular light scattering tests performed using both unpolarized and polarized lights. They revealed that the average size of scatterer inside of PE medium changes under varying temperature due to the change in lamellar structures. It was concluded that the average size of scatterer, called as scattering unit in [25], is not a simple crystal, but an aggregate containing some amorphous material.

In the last decades, Denis et al. [8] studied semi-crystalline PET to characterize thermo-optical properties of the polymer to use as a numerical input in IR heating assisted thermoforming process modeling. Their study experimentally analyzed the spectral-dependent optical scattering behavior in PET as a function of variation in its crystalline structure which was identified as X_c employing calorimetric DSC measurements. The spectroscopic analyses covered the spectral range between 0.4 and 2.4 μm. An interesting analysis from their study was presented in Figure 2.8. In the figure, the monochromatic diffusion coefficient (m^{-1}) and depth (mm) represent the experimentally calculated D_λ and the sample thickness, respectively. Based on the DSC analyses, they reported that the X_c reduces once the depth through the material increases where it was also mentioned that the X_c was up to 30%. Therefore, it was concluded that increase in the diffusion coefficient is strongly affected by increase in the crystallinity if the wavelength is lower than 1 μm (region 1) whereas diffusion coefficient is independent of wavelengths greater than 1.4 μm (region 3). However, no further explanation was given considering the variation in the diffusion coefficient for the same degree of crystallinity. Indeed, their experimental result that is

displayed in Figure 2.8 clearly points out the strong variation in diffusion coefficient considering same level of crystallinity at an identical depth. Especially, this variation is more significant close to the sample surface (e.g depth=0 -320 μm) at zone of the highest X_c was obtained. In addition, considering the variation through the depth, it was observed that size of spherulites remained unchanged, which may be attributed to a scatterer size smaller than spherulites. Nevertheless, no such remark was stresses out.

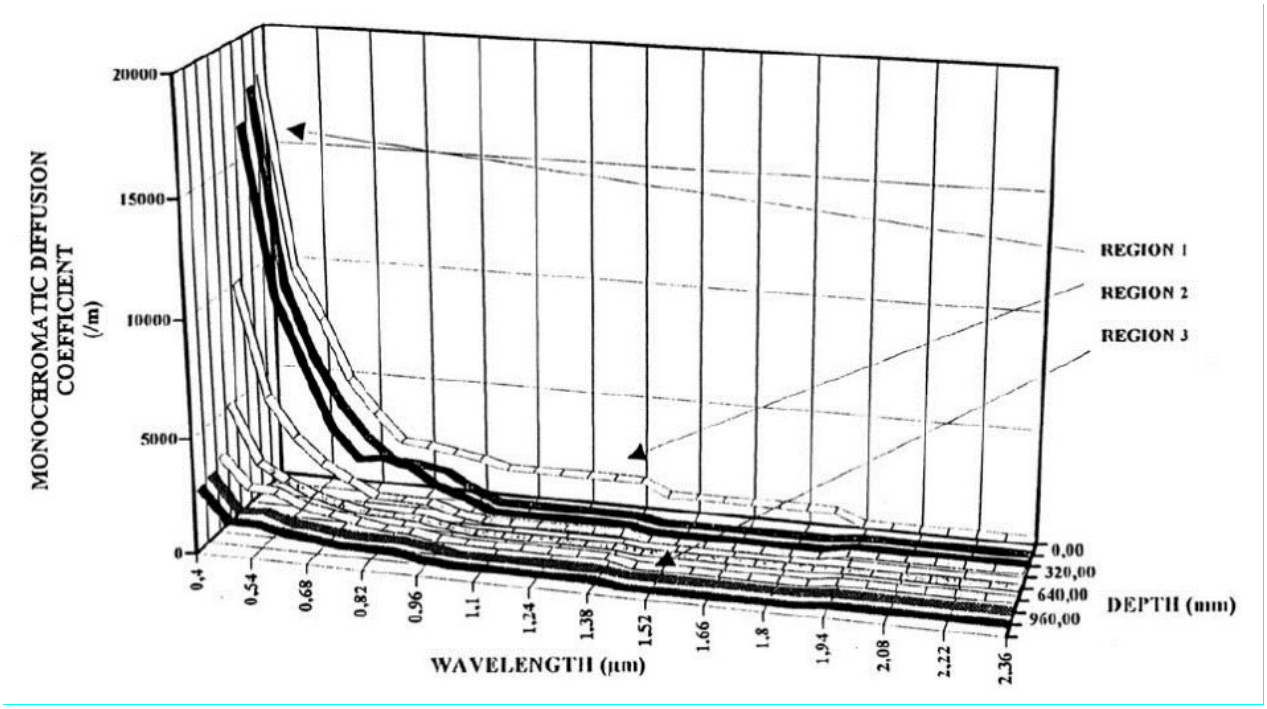

FIGURE 2.8. Variation of monochromatic diffusion coefficient (representing D_λ) of PET calculated at $0.4\ \mu m < \lambda < 2.36\ \mu m$ [8].

In terms of semi-crystalline polymers that have relatively have higher X_c than PET, the study conducted by De Santis et al [28] can be one of the examples. In [28], the relation between crystalline phase and the optical properties of recycled isotactic polypropylene (iPP) was analyzed. The opacity of PP, which was determined based on the reflectance measurements, was correlated to the spherulite size performing microscopic examinations under polarized microscope. Their study showed that spherulites are the responsible to change opacity in semi-crystalline iPP. In addition, it was experimentally observed that the opacity gets stronger once spherulite size increases. In a similar manner, Radusch et al. [29] also studied the optical scattering behavior-crystalline morphology relations in iPP regarding the combined experimental analyses with transmittance measurements and microcoscopic examinations. The variation in the spherulite size and lamellae thicknesses of both isothermally and non-isothermally melt-crystallized iPP was obtained using polarized optical (POM) and atomic force microscope (AFM), respectively. The

microscopic examinations were correlated to the transmittance measurements performed using Fourier-transform infrared (FTIR) spectroscopy at the spectral range between 380 and 750 nm. It was concluded in their study that the change in the lamellae thickness (l_c) of different iPP, which was varied between 10 to 35 nm, does not cause a change in the transmittance characteristics while it was dramatically reduced by an increase in spherulite size considering the range of 0 and 100 μm. In Figure 2.9 (a), the relation between the obtained spherulite size and transmittance characteristics of isothermally melt-crystallized iPP was presented. Similarly, no effect of X_c on the light transmittance measurements was reported. This point was supported by the work of Androsch et al. [34] that studies optical scattering behavior of the cold-crystallized at 413K and melt-crystallized PA 6 samples cooled at different rates. Based on AFM and POM analyses and transmittance measurements in VIS range (400-850 nm), it was stressed that the transmittance of melt-crystallized sample cooled at 0.5 K/min is considerably lower than the cold-crystallized PA 6 samples at which both the samples have the same X_c (around 40%). In addition to this, no spherulite formation was observed in the cold-crystallized samples regarding the POM examinations. Although, it was also stated in [34] that the size of spherulites and thickness of lamellae decreases under high supercooling conditions, it was only assumed that the dramatic change in transmittance of melt-crystallized samples are due to spherulites. This point may be needed to be supported by further calorimetric and microscopic examinations to obtain information about the lamellae thickness in response to the cooling rates applied on the melt-crystallized samples. Such complementary analyses beside of optical transmittance measurements was performed by Fratini et al. on the morphology-dependent optical scattering characteristics of PE [23]. Different from the concluding remarks revealed in [29], their study [23] supported the point that lamellae are also responsible for optical scattering. The role of spherulites on the optical characteristics was found similar to [29], as displayed in Figure 2.9 (b). It should be noted that the term -transparency- in Figure 2.9 (b) represents the transmitted light in a very narrow angular range, which can thus be close to $T_\lambda^{i,r}$.

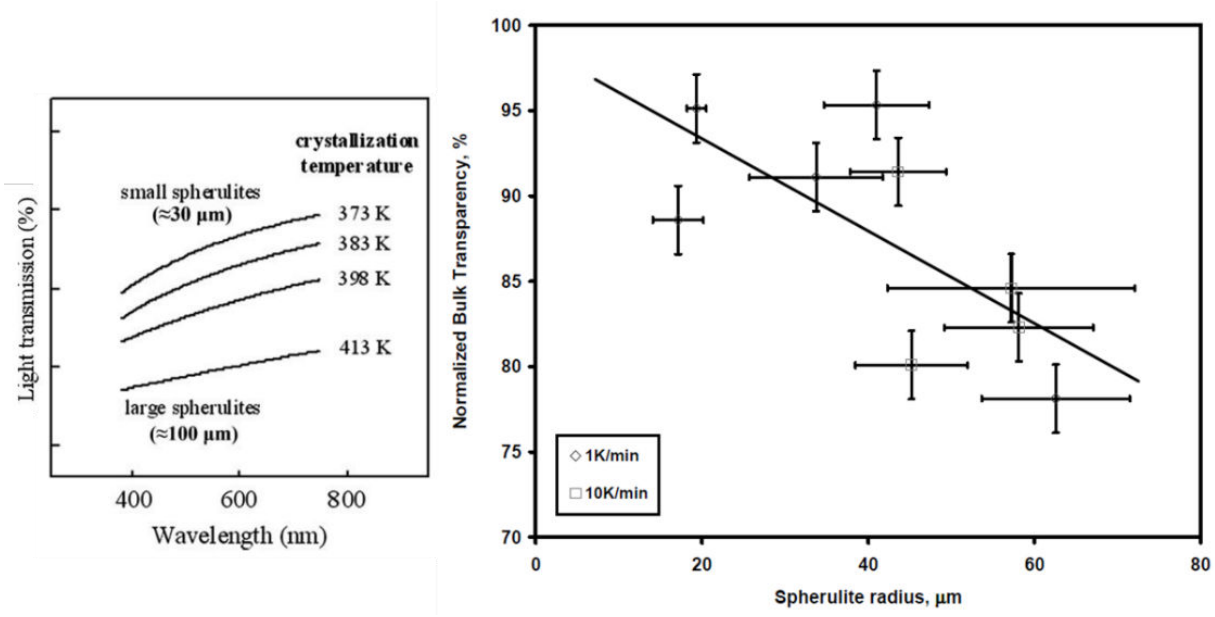

(a) (b)

FIGURE 2.9. Transmittance - crystalline morphology relations of isothermally melt-crystallized PP at various crystallization temperatures [29] (a) and, the PE cooled at both 1 K/min and 10 K/min [23] (b).

In addition to the analyses between spherulite size and transparency, the compression molded PE films were melt-crystallized at 1°C/min and were subsequently annealed at 140°C for 48 hours and then cooled to room temperature. The POM and small angle light scattering (SALS) tests confirmed there was no change in the spherulite size of those samples after annealing treatment. Conversely, lamellae thickening was observed through the AFM analyses and the transparency measurements showed how the transparency of PE reduces due to lamellae thickening that occurred during annealing. Figure 2.10 (a), POM examinations that shows no change in spherulite size of PE samples during annealing was presented. In Figure 2.10 (b), the transmittance measurements on those samples, and H_v scattering patterns obtained from SALS measurements presented. It should be mentioned here that the term - haze – is defined as the percentage of transmitted light that passes from a sample and deviates from the incident beam by more than 2.5°[23,27]. The detailed explanations on the transparency, haze and clarity can be found in the ASTM standards [35,36].

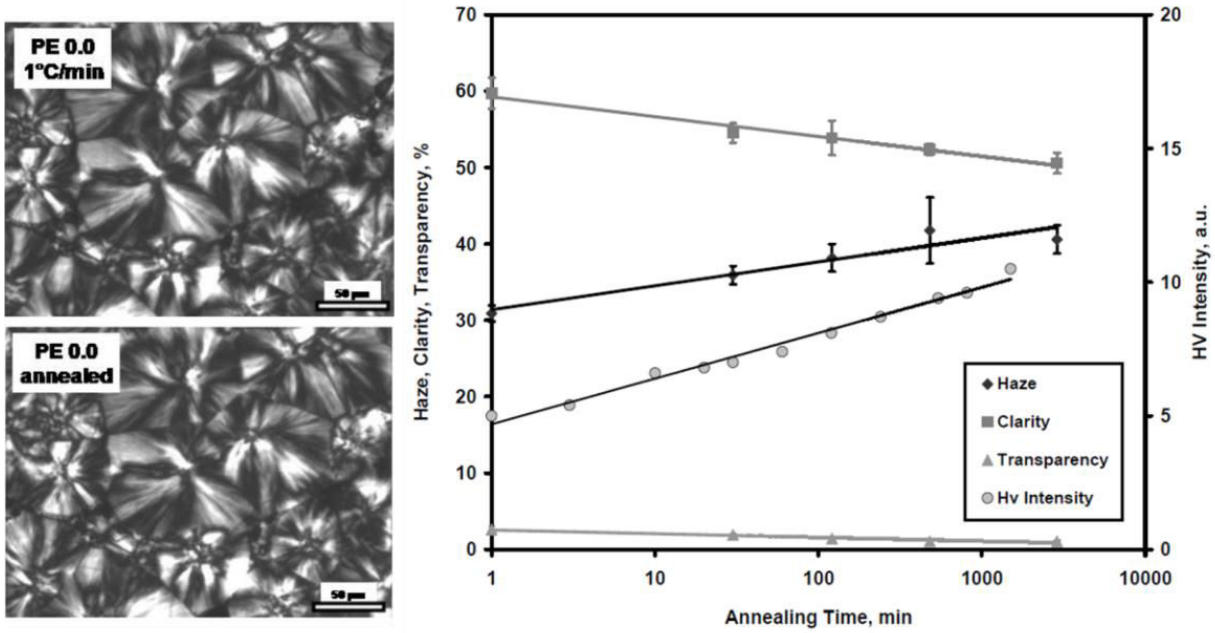

(a) (b)

FIGURE 2.10. Unchanged spherulite size of PE obtained before and after annealing (a), and its optical characteristics during annealing (b) [23].

Recently, Hakoume et al. [33] also studied the relation between the morphology and optical scattering behavior in PP where they revealed the spectral dependence similar to the remarks in [8]. It was proposed in [33] that optical scattering may happen due to spherulitic substructures, like lamallaes, similar to the point stressed in [24]. This was done adopting various processing temperatures from 40°C to 120°C for introducing different levels of crystallinity and morphologies in PP. The optical characteristics of all the fabricated samples were determined for VIS and NIR ranges. The experimentally calculated scattering coefficient was compared to the numerical computation that was built based on Lorenz-Mie theory (LMT) and the results were in good agreement. It was observed that optical scattering becomes weaker by increase in wavelength in NIR range. Their analyses was extended in [30] and the spectroscopic experimental analyses were performed in MIR range. Their analyses showed that optical scattering behavior that is effective in visible and NIR range while it becomes negligible in MIR Range. The similar tendency observed in their both studies was explained by the fact that the size of scattering particles becomes much smaller in comparison to radiation wavelength increased through MIR range. Therefore, it was concluded that the lamellae structures are responsible for the optical scattering behavior in unfilled semi-crystalline PP. Similar to the methodology adopted in [33], the morphology-dependent optical scattering relation in PE and PP was analyzed in [31,32] by performing light transmittance measurements

under crystallization. In [32], the time-dependent light attenuation was measured using He-Ne laser at 635 nm, and it was compared to the crystallization isotherms obtained by dilatometric measurements and small angle X-ray scattering (SAXS) analyses. The obtained trend from the time-dependent experimental analyses was correlated to the predicted light attenuation values. The predicted light attenuation was calculated adopting several optical scattering theories, namely Rayleigh, Rayleigh-Debye-Gans (RDG) and LMT. Their study showed that the earlier stages of crystallization where the growth of each individual spherulite was seen fall in the range of RDG scattering. Related to this observation, it was stressed that the dominating scatterer size, called as scattering object in their work, lies around 100 nm to 10 μm. It should be noted at this point that the scatterer was assumed as perfectly sphere. Similar experimental-theoretical comparisons was performed by Wang et al. [27] for LDPE and LLDPE where they experimentally analyzed surface and bulk morphology of PE and determined its transmittance characteristics in terms of haze. LMT was adopted for calculating the forward-scattered light intensity assuming that scatterers in PE medium are isotropic spherulites and scattering occurs only once in the medium. The obtained experimental and theoretical comparisons on the measured and calculated haze values showed a close agreement whereas underestimation was observed for all the theoretically calculated values. Although, no explanation was given about spectral range of the transmittance tests, we believe that the tests were done using at 550 nm, since it was mentioned that the theoretical scattering calculations were carried out at this wavelength.

The discussed points so far show the effect of crystalline morphology on the transmittance characteristics of semi-crystalline polymers. Apart from its effect on the transmittance caused by internal scattering in bulk medium of polymer, it was shown in literature that variation on crystalline structure also affects the reflectance characteristics of semi-crystalline polymers, which is also named as surface haze (scattering) in literature [23,27,37,38]. As mentioned in previous section, the reflectance of light from the surface is strongly related to surface irregularities, or surface roughness. It was stressed in [37,38] that crystalline formations close to the surface of the thin PE films may induce surface irregularities, where they showed the correlation between crystalline structure and surface haze. Sukhadia et al. [38] analyzed this relation on LLDPE and found the major part of total scattering was due to surface scattering in 25 μm films. In [37], a similar analysis was conducted using LDPE and HDPE, where also it was revealed that the percentage of surface haze is significant for the thin films, typically thinner than 50 μm, which is in agreement with the results of [38]. Considering that relatively thick PE films are studied in this research, the effect of crystalline structure on the reflectance characteristics was assumed negligible in comparison to its effect on transmittance. Overview of all the literature reviewed in this

section and, the main concluding remarks on the size of scatterer inside of unfilled semi-crystalline thermoplastics are summarized in Table 2.2.

	Semi-crystalline polymer type	**PE (HDPE/LDPE/LLDPE)**	**PET**	**PP**	**PA 6**
$T_\lambda^{i,r}$ and / or $T_\lambda^{i,c}$	**Bulk scattering - crystalline morphology relation studied in**	[23–25,27,39]	[8]	[28–33]	[34]
	Experimental methodology	FTIR/ SALS / POM / AFM [23] MALS test / FTIR[24–26] AFM / MALS test / FTIR[27]	FTIR / DSC (X_c)	FTIR/ POM [28,30,33] FTIR/ POM / AFM [28] Dilatometry / Laser Transmission [31,32]	FTIR/ POM & AFM
	Spectral range (µm)	0.546 and, 350 to 950 nm [24] 300nm [25] 0.55 [27]	0.4 - 2.4	0.38 - 0.75 [28] 0.635 [31,32] 0.67 - 1.1 [30,33] 0.67 - 16.7 [30,33]	0.4 - 0.85
	Proposed crystalline structure for optical scattering	Lamallaes [23,26] Between lamallaes and spherulites [24] Lamellaes and Spherulites [25] Spherulites [27]	X_c - D_λ relation was established	Spherulites [27, 28] Lamallaes [30,33] Spherulites and Lamallaes [31,32]	Spherulites / Lamallaes
	Proposed scatterer size	From order of 10nm to order of µm [24]	-	100nm - 10µm [31]	-
$R_\lambda^{i,c}$	**Surface scattering - crystalline morphology relation studied in**	[23,27,37,38]	-	-	-

TABLE 2.2. Summary of the literature review on the crystalline morphology - optical scattering relations in semi-crystalline thermoplastics.

2.3.1. Spatial distribution of optical scattering and scattering phase function characterizations

In previous section, the change in the optical scattering effect in relation to crystalline morphology of various type semi-crystalline polymers was discussed. It is obvious there is an ambiguity in terms of scatterer characteristics, where some studies support the point that spherulites are mainly responsible for scattering while some other put more emphasis on the role of lamellae for such scattering behavior. Furthermore, the experimental transmittance measurements stressed in the previous section demonstrates how extinction characteristics of polymer medium changes with a change in crystalline structure, however the spatial distribution of the scattered light may be not highlighted. In literature, it has been also found that adoption of well-known optical scattering theories combined with experimental MALS tests may provide a complete analysis to fulfill the two points mentioned above [24,40,41]. Thanks to an adopted scattering theory, the size of scatterer in semi-crystalline polymers may be proposed and potential light scattering profile, which theoretically represents ϕ_λ, may be predicted. The widely adopted scattering theories such as LMT, Rayleigh and RDG were originally developed calculating the scattering parameters and scattering profile of a heterogeneous medium considering a perfectly spherical scatterer [12]. Although new models were proposed later on considering scatterers with arbitrary shape [12,20], the calculation of such scattering models are quite complex which will not be discussed further in this thesis.

Under the assumption of a spherical shape for scatterers, a dimensionless scaling parameter called as shape parameter (ξ) defines how light scattering profile changes regarding the wavelength of the radiation in the medium (λ_m), refractive index of medium (n_{medium}) and size of the scatterer, defined as its radius (r) here (Equation 2.14). Using the equation below, the scattering phase function - ϕ_λ- can be calculated adopting an optical scattering theory. Regarding the value of ξ, different scattering theories may be taken into account. For instance, LMT addresses the general problem so that it can be used for both small and great scatterer sizes. However, Rayleigh theory may be convenient to predict ϕ_λ only when scatterer size is much smaller than λ_m, or simply with ξ <0.1 [12].

$$\xi = \frac{2\pi r}{\lambda_m} \text{ with } \lambda_m = \frac{\lambda_o}{n_{medium}} \tag{2.14}$$

In Figure 2.11 (a), schematic drawing of the ϕ_λ regarding to several theoretical values of ξ is illustrated. The change in the forward and back scattered portion of radiation and its relation to ξ is seen. In the case of isotropic scattering, ϕ_λ is equal to 1 where the scattered radiation is uniform for all the directions. Figure 2.11 (b), a typical test setup of MALS test is seen where both forward and back-scattered light can be detected at varying polar angle (θ_s). In general speaking, the tests are done using a

monochromatic laser light at the wavelength in VIS or NIR range. Regarding the angular resolution and range of such testing device both the back-scattered and forward-scattered angular light intensity distribution may be measured. Following an inverse methodology, a theoretically calculated ϕ_λ can be compared to the experimentally obtained light scattering profile through the MALS tests. Such an inverse approach was already adopted for semi-crystalline PE [24] and non-polymeric materials [40,41] where the scattered light intensity distributions.

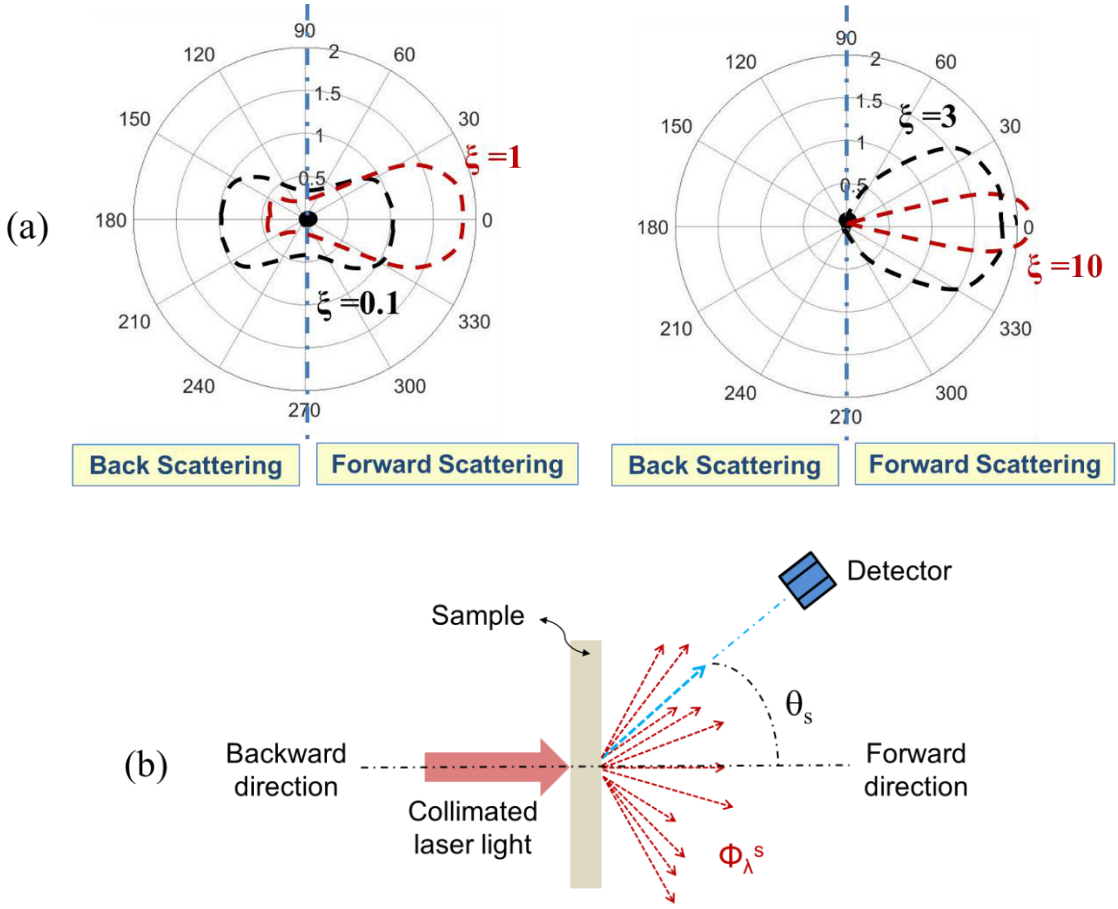

FIGURE 2.11. Spatial distribution of light scattering as a function of the size of a spherical scatterer (a) and, typical MALS test for measuring the spatial distribution of scattered light intensity (b).

Again, one of the earliest efforts was given by Keane et al. [24], for also measuring light scattering profile of PE. In their study, the experimental angle-dependent light scattering intensity was measured using a monochromatic light at 546 nm for the angles between 10° to 65°. The experimental measurements were compared to the calculated light scattering profile adopting Debye-Bueche scattering theory and the size of scatterer inside of PE medium was found between 200 and 300 nm. Therefore; as mentioned at the beginning of the previous section briefly, it was concluded that the size of scatterer in

PE is larger than individual crystallites (or lamallaes) and smaller than spherulites. More interestingly; MALS tests were performed under varying temperature until 110°. In order to stabilize the microstructure structure, or prevent potential reorganizations under varying temperature, PE is allowed to crystallize for long time where it was slowly cooled and annealed applying several isothermal steps around 100°C, before performing the MALS tests. It was clearly observed that angular behavior of light scattering distributions under varying temperature does not change, whereas scattered light intensity becomes weaker which creates a shift in the measured intensity at each angle. Such a temperature dependent optical scattering behavior may be one of the key factors for radiation heat transfer modeling of unfilled semi-crystalline polymer media.

Berrocal et al. [42] studied scattering behavior investigations on monodisperse polystyrene spheres in distilled water medium performing MALS tests while the scattered light intensity was only measured at 1.5° and 8.5°. The scattering characteristics was analyzed at 800 nm and the two-dimensional distribution of light intensity is recorded experimentally and compared to the computations performed adopting LMT combined with Monte Carlo (MC) simulations. The experimental-theoretical comparisons were done considering different scatterer size and concentrations and a close agreement was found between the experiments and theory. The interesting point in their study was that an empirical approach was proposed modifying Beer-Lambert Law which considers multiple scattering of radiation through an optically heterogeneous medium. This effect was considered in Beer-Lambert law introducing an additional term for the amount of multiple scattered radiation that was determined based on the MC simulations.

The scattering models discussed in this section so far dealt with heterogeneous media consisting of isotropic or monodisperse scatterers. However, this may not be the case for semi-crystalline PE medium. Based on the studies stressed here, the scatterer size inside of PE may not be a single spherulite size or lamellae thickness so that a monosize scatterer may not be taken into account. Similar to this fact, Apetz et al. [41] investigated the scattering behavior in polycrystalline Al_2O_3 (PCA). Optical heterogeneity in PCA medium was investigated considering bulk irregularities due to both porosity and crystal size. The angular scattered light intensity of the material was experimentally obtained at 550 nm. The scattering profiles of PCA samples prepared with different crystal size were measured using an in-plane rotated detector up to a scattering angle of +/- 60° around the sample. In Figure 2.12 (a), the scattering profile of the PCA samples which have crystal size -called as grain size (G) in their study- of 0.5 and 2 μm are presented. As it is seen in the figure, the normalized light scattering intensity distribution per scattering angle shows less pronounced forward-scattering at larger angles with an increase in the crystal size, which is in accordance with the theoretical ξ - ϕ_λ relations as shown in Figure 2.11 (a). The scattering model was developed adopting RDG theory where initially monosize scatterer was considered for the polycrystalline

medium. Using RDG theory, an equivalent β_λ was proposed and used for inverse computations of $T_\lambda^{i,r}$. In Figure 2.12 (b), the computed $T_\lambda^{i,r}$, called here as *real in-line transmittance*, and its comparison to the experimental measurements are seen. As it is seen in the figure, their model predicted the experimental transmittance measurement very closely while it slightly deviates for shorter wavelengths. This was explained by negligence of the crystal size population distributions. Their further analyses in [41] included crystal size distributions in the scattering model which resulted that scattering profile in PCA can be perfectly predicted adopting the difference in the size of crystals.

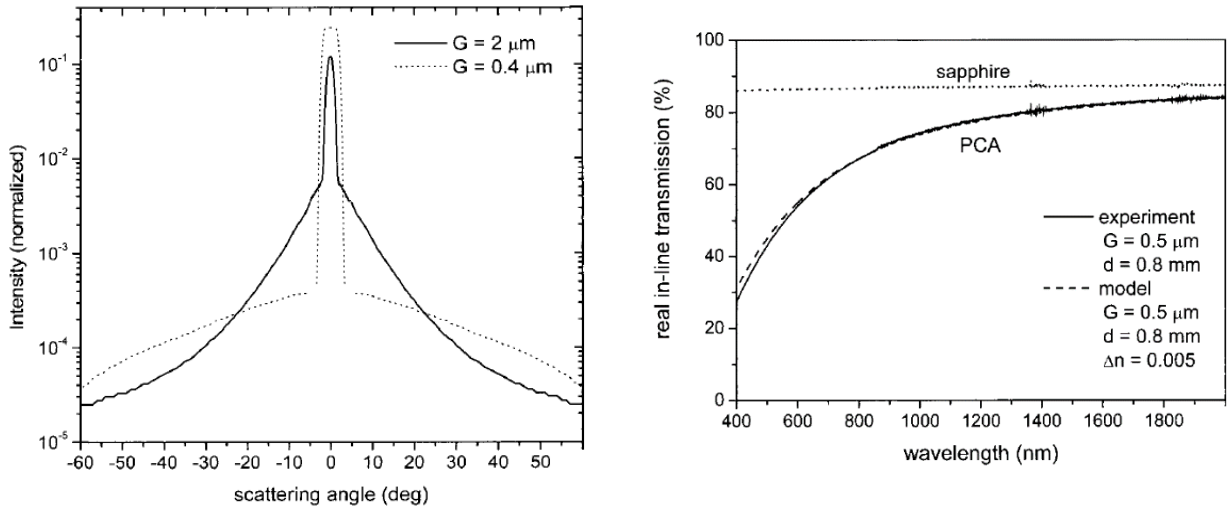

(a) (b)

FIGURE 2.12. Measured scattering profiles of PCA samples with different crystal sizes (G=0.4 and 2 μm) (a) and, the comparison between the measured and computed $T_\lambda^{i,r}$ using RDG theory (b) [41].

In addition, the effect of pore sizes on the optical scattering behavior was modeled adopting LMT theory. It was stressed that light scattering becomes close to be isotropic when the pores become smaller so that the light is isotropically scattered in backward and forward directions. In theory, this behavior is known as Rayleigh scattering where ξ equals to 0.1 for unpolarized scattered light [12,43]. The adopted approach assumed a purely scattering medium in which the optical free path – or scattering distance – is higher than the sample thickness. Regarding to the relation between optical free path and the sample thickness, it was also assumed a single scattering phenomenon. The single scattering may be adopted for radiation heat transfer in PE medium whereas, the spectroscopic analyses in fairly large spectral range shows negligence of absorption may not be possible [4,5]. In addition, equivalent size of scatterer -which may represent an averaged value for scatterer size population distributions- in PE medium may help to simplify the problem, similar to the one revealed in [41] using a monosize scatterer (Figure 2.12 (b)).

2.4. Phase Transitions in semi-crystalline thermoplastics under heating: A bridge between crystalline morphology and optical properties

2.4.1. Temperature dependency in thermo-optical properties of semi-crystalline polymers

As crystalline structure strongly affects the optical properties of semi crystalline polymers, in particular transmittance characteristics, it is likely to happen that transmittance of light alters under varying temperatures. In other words, any potential change in crystalline structure may induce a change in the role of scatterer inside of polymer medium which eventually leads to have an evolving scattering profile inside of medium.

This fact attracted many researchers and, one of the earliest studies was performed by Hawkins et al. [44] on the temperature-dependent transmittance of PE. Their experimental analyses showed how transmittance behavior in 1 mm thick PE sheet changes under subsequent heating and cooling conditions, especially after the temperatures greater than 75°C. It was stressed that the melting of crystallites; which was claimed whose size are in order of 10 nm, causes such a change in the transmittance levels and, spherulites remain until the last and largest crystallites melts. In addition, it was pointed out the transmittance behavior of PE showed no reversibility under heating and cooling hysteresis. The transmittance measurements obtained in this study was called as transparency however; no information was given about the wavelength of the measurements. Based on the further explanations in the testing apparatus of the study, we believe that the transmittance measurements was close to $T_{\lambda}^{i,r}$. Keane et al. [24] studied the temperature-dependent scattering characteristics of PE films, parametrized as *turbidity* in their study, obtained under subsequent cooling and heating steps. The turbidity presented here, which theoretically reflects D_{λ}, was calculated based on the exponential decrease in transmittance measurements, as shown in Equation 2.11. The increasing and decreasing trends in the calculated turbidity during heating-cooling hysteresis showed non-reversible behavior, which were in close agreement with [44]. In addition, it was clearly shown that the scattering properties of 50 to 300 μm thick PE films start to change after 80°C where also the change becomes more significant after 110°C measured at monochromatic light at 546 nm which was attributed to melting of crystallites in the corresponding temperature range.

In the last decades, Keller et al. [45] also gave an effort to explain temperature-dependency in absorption characteristics of various semi-crystalline polymers which was eventually used as numerical input for laser processing modeling. In their study, it was experimentally proven that D_p , which physically represents how strong radiation energy attenuates into medium (Equation 2.13), of polyamide

11 (PA 11) and PET at λ=.10.6 μm. Becker et al. [46] proposed temperature-dependent optical properties for semi-crystalline PP, named as "effective absorption constant". However, the temperature dependency in absorption characteristics of PP was modeled based on the temperature-dependent density profile of the polymer in the corresponding temperature range, so that it lacks the physical background due to no experimental characterization on its optical properties was performed. Recently, Geiger et al. [47] analyzed the temperature-dependent absorption characteristics of various type of amorphous and semi-crystalline polymers. They measured $T_\lambda^{i,\cap}$ and $R_\lambda^{i,\cap}$ of all the studied polymers for λ=940 nm where the measurements were taken under cooling condition. Their comparative analysis clearly showed how the calculated monochromatic absorption coefficient ($\kappa_{\lambda=940\ nm}$) of semi-crystalline polymer reduces dramatically when the temperature it close to their melting range while no temperature dependency was observed for the tested amorphous polymers. In Figure 2.13, the temperature-dependent $\kappa_{\lambda=940\ nm}$ of all the tested amorphous polymers (a) - namely polycarbonate (PC), acrylonitrile resin (SAN) and polymethyl methacrylate (PMMA) – and the semi-crystalline polymers (b) are displayed. The analyses in [47] were extended later on in [48], for temperature dependent absorption behavior of polyamide 12 (PA 12) and PP was under subsequently applied heating and cooling conditions. The $T_\lambda^{i,\cap}$ and $R_\lambda^{i,\cap}$ measurements again were performed between room and the melting temperature of polymers where a collimated thulium fiber laser at 1.94 μm was used. In a similar manner, a dramatic decrease in the absorption characteristics of both the semi-crystalline polymer was observed.

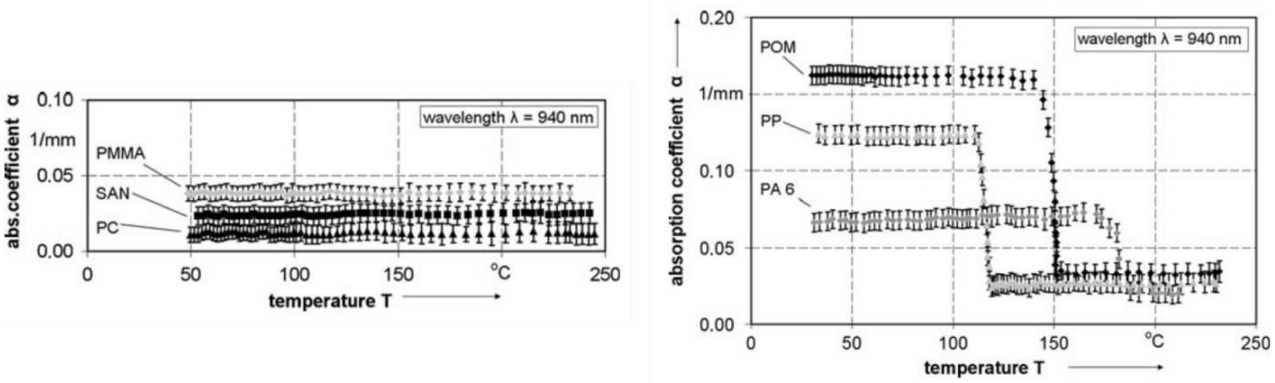

(a) (b)

FIGURE 2.13. Comparison between the measured temperature-dependent absorption characteristics of amorphous (a) and semi-crystalline polymers (b) at 940 nm [47].

The studies presented here, shows how optical scattering becomes weaker under varying temperature; especially changes significantly at the temperatures close to the melting range of various semi-crystalline polymers. Since optical scattering becomes weaker under varying temperature, the distance that radiation

travels through the polymer medium may be reduced due to an increase in the directly transmitted light inside of such optically heterogeneous media. In reverse, once optical scattering is strong at low temperatures far from melting range, the radiation path may be prolonged which results an increase in the total amount radiation, as stressed in [3,47].

2.4.2. Crystalline structure evolution in semi-crystalline polymers under heating and partial melting

The studies on temperature-dependent optical properties of various semi-crystalline polymer was discussed in the previous section. The major outcome of those studies is on the change in the optical characteristics, potentially due to the fact that scattering becomes weaker under varying temperature. Especially, this change becomes significant for the temperature ranges close to the melting range of different type of semi-crystalline polymer.

Crystalline morphology in melt-crystallized semi-crystalline polymers typically relies on various chemical and physical factors such as; cooling speed, molecular weight, degree of polymer chain branching, thermal history etc. [10,49,50] where a polymer in complete molten state generally follows nucleation, primary and second crystallization phases [10,50]. Considering PE, once the primary crystallization starts X_c increases rapidly in parallel to lateral growth of lamellae which eventually form spherulitic crystal structures [10,49]. The l_c of PE, theoretically the dimension that represents c-axis, [10,49,50] also changes due to the several chemical and physical factors explained above. As the aim of this research is to understand crystalline structure evolution under IR heating, crystallization kinetics – morphology relations will not be discussed. Whereas, it is worth to note that phase transitions that occurs in semi-crystalline polymer under heating starts to melt lamellae structures [10,51]. This fact may be required to be checked at a closer look, as the change in the optical characteristics of semi-crystalline polymers was mostly reported at temperatures somewhat below the melting of spherulites. Considering heating of PE, starting from room temperature, it is likely to happen that phase transitions start to occur as its melting range can extend down as far as room temperature, in return it may include very thin lamellae structures [10]. Regarding the Gibbs Free energy, it is known that thinner crystallites -which are thermodynamically less stable than thicker crystals - melt at lower temperatures than the thicker ones because they have a higher surface-to-volume ratio and hence a relatively greater contribution from the interfacial free energy term [10,52]. In order to obtain information about lamellae structures, various microscopic techniques such as AFM, SAXS and transmission electron microscopy (TEM) are used [53,54]. Apart from these techniques, differential scanning calorimetry (DSC) analyses may offer a simple and quick approach to predict most probable l_c in the semi-crystalline polymers based on Gibbs-Thomson equation:

$$T_m = T_m^0(1 - \frac{2\sigma_e}{\Delta H_m l_c}) \tag{2.15}$$

where T_m is the observed melting temperature for crystalline lamellae with l_c. T_m^0 is the equilibrium melting temperature of the crystalline lamella of infinite thickness (l_∞) and σ_e is the surface energy of the basal surface of the crystalline lamella, and it is associated with the energy of chain folding during the crystallization process. The last term in the formula - ΔH_m - represents the enthalpy of fusion per unit volume of lamellae thickness. The values of T_m^0, σ_e and ΔH_m was found as 414.5 K [50,55], $70*10^{-3}$J/m^2 [55] and $288*10^6$ J/m^3 [52,55] for PE. It should be mentioned here that the Gibbs-Thomson equation is valid only for lamellae whose lateral dimensions are much larger than their thickness, which is generally the case in semi-crystalline PE [50,54] , which was also reported for PE considering that lateral growth of lamellae is much larger than c-axis [10,49]. Assuming that at a given temperature the rate of heat consumption is proportional to the mass fraction of most probable l_c, it was proposed in [52] and [55] that it would be possible to obtain most probable l_c population rather than an estimating the most probable single crystal thickness. Alberola et al. [55], mathematically formulized this hypothesis and modified Gibbs-Thomson equation, which led to the formula presented in Equation 2.16. The derivations between the Equation 2.15 and 2.16 can be found in Annex A.1.2.

$$\frac{1}{M}\frac{dM}{dL} = \frac{dE}{dT}\frac{(T_m^0 - T_m)^2}{2\sigma_e T_m} \tag{2.16}$$

where M represents the mass of crystalline phase. Considering a certain temperature between T and T+ dT under heating, dM is the fraction of the crystalline phase which has a thickness in the range L and L+dL that melts between the corresponding temperature range which eventually consumes energy with dE/dT that can be registered by the DSC endotherm.

In literature, the l_c population of various type of branched and quasi-linear PE, such as LLDPE [56,57] and HDPE [52,54–56,58] respectively, was extensively analyzed. Those analyses showed that l_c population generally varies in the range between 5 to 30 nm where also it was revealed that cooling conditions may greatly affect the l_c populations in term of size and population distributions. For instance, Hallman et al.[56], investigated l_c populations in LLDPE and HDPE where a different crystalline morphology was prepared cooling samples under slow-cooling, quenching and annealing conditions. It was revealed that l_c population distributions are unimodal whereas annealing causes to have bi-modal distributions. In addition, it was observed that l_c population of HDPE that was between the range around 5 and 25 nm while the range was smaller for LLDPE with a range between 5 to 15 nm. Similar finding was

reported by [54] for HDPE where the range of its l_c population was mainly between 10 to 30 nm. They also showed how a clear shift in the population range occurs by annealing the material at 120 and 130°C. The effect of cooling and annealing PE at isothermal temperature steps on the l_c population was also investigated by [55] for HDPE. Similar to the results in [56], the change in the population distribution from unimodal to bi-modal was observed for the samples quenched and annealed at different isothermal temperature steps between 100 and 130°C. Although most of the analyses were in close agreement, it was stressed in literature that the calorimetric measurements performed by DSC should be carried out using a certain heating rate otherwise Gibbs-Thomson relation fails to estimate l_c [50,52,54]. At relatively low heating rates where reorganization of polymer chains is feasible, the melting temperature increases with decreasing heating rate. This increase is attributed to crystal thickening and/or crystal perfection [50,54] under heating. On the other hand; the thermal shift of the melting temperature with increasing heating rate may be seen which is attributed to superheating [50]. In [54], seven heating rates were adopted between 1K/min - 64K/min and, the l_c distributions were estimated using Equation 2.16. The estimated lamellar crystal populations were compared to l_c distributions obtained via TEM examinations. Regarding to close agreement between the adopted methods, it was concluded that heating between 8 - 16 K/min is the most suitable heating rate for HDPE to avoid both thermal shift and reorganization effects. Similarly, the heating rate between 10 - 20 K/min [52] and 5-20 K/min [57] were proposed for avoiding such errors to determine l_c populations of HDPE.

The knowledge about the size of crystals that melt down at a certain temperature may be a key to develop a relation between crystalline morphology and optical scattering evolutions in PE under heating. Thanks to melting endotherm that can be obtained via DSC measurements, temperature of most probable single crystal melting which has a certain thickness can be predicted adopting the Gibbs-Thomson relation. The Figure 2.14 (a) shows the relation between melting temperatures, T_m in the figure, and the reciprocal of the most probable single l_c in PE [51]. Here, the x axis shows the reciprocal of l_c value. Similarly study the change in l_c population was analyzed in [53] under heating, including combined TEM examinations and SAXS measurements on HDPE. In Figure 2.14 (b) the crystalline structure evolutions in HDPE was presented obtained between room temperature (RT here) and 130°C. As it is seen in the figure, the l_c population of HDPE shifts to greater values of l_c due to melting of thinner crystals earlier than the thicker ones under heating condition, which was confirmed through the TEM -SAXS comparisons registered at different temperature steps.

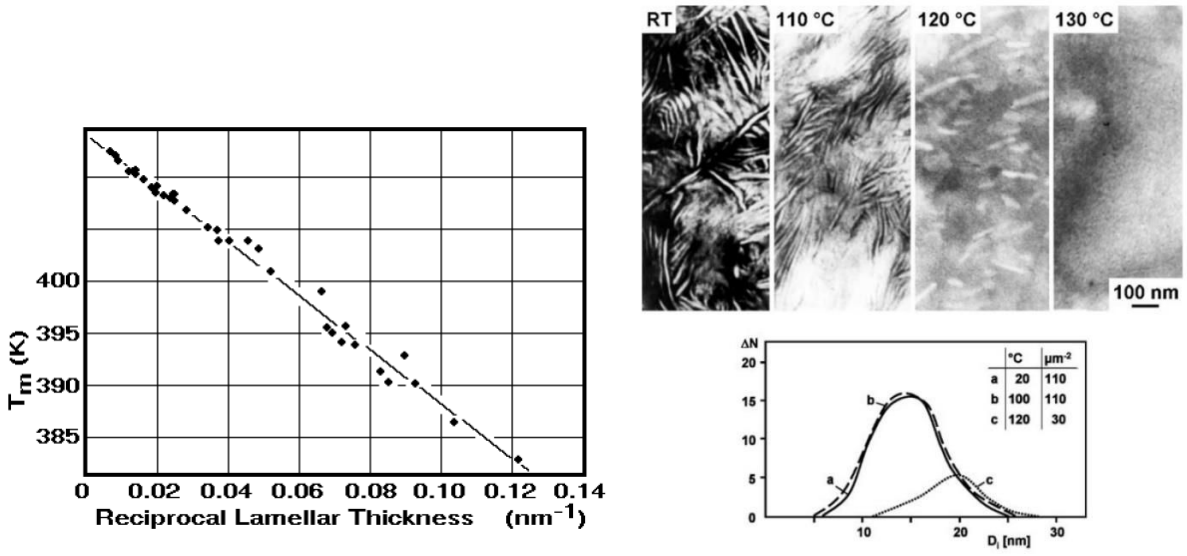

(a) (b)

FIGURE 2.14. The calculated melting temperature of a most probable l_c [51] (a) and, the evolution of l_c observed under heating condition [53] (b).

The reviewed literature on the calorimetric approach to predict l_c distributions in PE polymer are summarized in Table 2.3. In the table, the potential l_c distributions are presented based on the maximum range of the l_c distributions reported in each study considering various type of cooling conditions for two types of PE. In addition, their population distribution mode is given.

PE type	**HDPE**	**LLDPE**
Heating rate	10 K/min [52,56–58] 1 - 64 K/min [54] 8 K/min [55]	10 K/min [56,57]
Maximum range of l_c distributions	10 - 30 nm [54] 5 - 40 nm [55] 5 - 30 nm [56,58] 20 - 100 nm [52,57]	7 - 13 nm [56] 5 - 20nm [57]
Type of crystal population distributions	Unimodal distribution [52,54,56–58] Unimodal and bimodal distribution [55]	Bimodal distribution [56,57]

TABLE 2.3. Overview of the reviewed literature on the l_c population distributions of PE polymers calculated based on Gibbs-Thomson equation.

2.5. Overview of the numerical approaches for radiation heat transfer modeling in thermoforming processes

Most of the radiative heat transfer models developed for IR heating and laser-assisted thermoforming of thermoplastics are based on optically homogeneous medium assumption where the radiation attenuation in polymer medium is computed based on Beer-Lambert Law [18,19,45–47,59–63], shown in Equation 2.11. The process simulations developed in those studies were mostly focusing on radiation transport either in amorphous or low crystalline polymers. However, it may be an ill-defined assumption for modeling radiation transport in PE medium due to strong optical scattering, as presented in Section 2.3.

In our research group, Cosson et al. [19] developed an algorithm - named as RAYHEAT - that computes radiative source term for the case of IR heating. The algorithm is a MATLAB-based code that simulates radiation using geometrical optics that is based on ray tracing method. Therefore, spectral and directional dependencies of the emitted radiation from an IR lamp were considered. Although, there are other modeling approaches for radiation transport in participating media, it was revealed by Jensen et al. [64] that ray tracing is one of the most accurate methods in comparison to the other approaches. In RAYHEAT, the change in the direction of a propagated radiation was only assumed at the surface of a heated medium. Therefore, radiation attenuation in a medium is modeled adopting Beer - Lambert Law where optical scattering is neglected. The accuracy of the algorithm was demonstrated in [19,63] considering low crystalline PET at which optically homogeneous medium can be assumed. Detailed information on the computation algorithm and the theoretical background RAYHEAT can be found in Annex A.1.3. The schematic illustrations presented in Annex A1.3 were reproduced from [19,63]. Another model proposed by Chen et al. [62] for radiation heat transfer in LTW. The developed model -so called direct-scattered model- takes into account the laser beam scattering in unfilled semi-crystalline PA 6. The scattering characteristics were considered in β_λ. And, radiation attenuation was assumed adopting -so called modified Bouguer- Lambert Law in the study- where β_λ was introduced. Although directional change of incident laser beam due to optical scattering was considered in the study, it was limited in terms of directional-dependency. To simplify the model, it was only assumed a forward-scattered light and back-scattering was neglected. In addition, the angular distribution of scattered laser beam was modeled based on a statistical distribution function. Hence, neither experimental analysis on the angular distributions of scattered light in PA 6 was performed nor optical scattering theory was adopted to determine a scatterer-size-dependent ϕ_λ for PA 6. Apart from that, LTW process models proposed in [45–47] took into account optical scattering caused by crystalline structure of various semi-crystalline polymers including the temperature dependency in their optical properties. However, the directional

change in the scattered radiation was not considered so that the models were built based on optically homogeneous medium. By this way, the evolution of optically scattering in polymer medium under varying temperature was considered without modeling spatial distribution of propagated radiation.

The numerical model developed in [59] was based on homogeneous medium assumption with Beer-Lambert Law for CO_2 laser welding simulations of semi-crystalline HDPE, LDPE and PP. Interestingly; their model was closely fitted to the experimentally characterized optical properties of both LDPE and HDPE. Although, the model based on optically homogeneous medium may not be enough to explain radiation transport in highly crystalline PE, the accurate prediction of the model may be explained by the fact that optical scattering may not be effective any longer after certain wavelengths. More specifically, the scatterer size may be negligibly small in comparison to the wavelength of CO_2 laser (λ = 10.6 μm). Similar point was discussed in [30] for PP where the optical scattering becomes negligible at wavelengths in MIR range. This point is crucial for establishing an accurate optical scattering model, as already pointed out in Section 2.1.2.

2.5.1. Radiation Heat Transfer modeling in optically heterogeneous polymer medium

Although, there is a redundant source on thermoforming process simulations based on optically homogeneous medium assumption, there is much less sources found for IR heating or laser assisted thermoforming process simulations where most of them were conducted in the last decades. One of the earliest studies known in the field was performed by [65] where they discussed the two and four flux models for predicting absorption and transmittance values in optically heterogeneous plastic medium. Based on the experimental-theoretical comparisons combined with critical analyses for modeling radiation transport in non-scattering and scattering polymer media, they proposed that four-flux model can be used to predict radiation transport in absorbing and scattering medium of semi-crystalline polymers.

In terms of IR heating assisted thermoforming process simulations, the multiple works performed by the research group at University of Rouen [8,66] may be the first ones for developing IR heating model that considers the optical scattering in PET. In addition, the model took into account the change in the direction of radiation propagation due to optical scattering so that ϕ_λ was determined adopting four-flux model [66]. And, RTE was solved considering cold and optically heterogeneous medium assumptions, hence self-emission of PET was ignored. In their study, it was thought that degree of crystallinity was the main factor that causes scattering behavior in PET during cold-crystallization under IR heating. Those analyses were extended by Denis et al. [8] where different levels of crystallinity and its effect on the optical scattering characteristics of PET was experimentally analyzed. Based on the analyses, an

empirical law was established between the degree of crystallinity and the D_λ of PET. Similar modeling approach was adopted by [22] for LTW process modeling for particle doped amorphous PC at using a diode laser at 968 nm. The four-flux model was implemented to compute the scattered laser light beam intensity distributions at welding surface. The angular distribution of scatter light was included in the model calculating ϕ_λ. Thanks to the experimental spectroscopic measurements, $T_\lambda^{i,r}$, $T_\lambda^{i,\cap}$ and $R_\lambda^{i,\cap}$ was obtained and, κ_λ and D_λ were calculated. The process simulations to compute the spatial distribution of laser light at welding surface was done using a commercial ray-tracing based software, ZEMAX. Their numerical results helped to optimize LTW process in terms of weld seam quality which was also analyzed in the work.

Another modeling approach was proposed by Ilie et al. [67,68] for a similar LTW processing of particle doped amorphous PMMA using a laser at 940 nm. In their study, an assessment on the weldability of thermoplastics was performed concerning the laser beam profile at the interface between the two welded components. In [67], PMMA charged with fused silica were studied and the radiation heat transfer was modeled considering a purely scattering medium where absorption was neglected. Monte Carlo method was adopted to compute the change in the direction of propagated radiation caused by the scattering. The scattering characteristics and ϕ_λ was calculated based on LMT that enables to explain scattering behavior based on the spectral characteristics of propagated radiation and morphological features (dimensions) of scatterer. Physically, these parameters provide information on how strong a particle causes an optical scattering. Background of LMT and the formulas for the scattering characteristics presented here can be found in [12,67]. Based on this theory, the scatterer – the charged particles in the studied material- were assumed perfectly spherical and mono-sized. In the current research, as the scatterer is related to the crystalline structure, scatterer size may vary considering crystalline-phase formation. Therefore, granulometry of the scatterer may be determined rather than adopting a mono-sized one in this research. The proposed numerical model in their study was validated performing experimental analyses in [67,68]. These validations showed that LMT coupled with Monte Carlo method predict optical scattering of radiation and laser beam profile on the interface of the welded components. However, slight overestimation in the radiation intensity was observed at the interface of the welded components which may be attributed to the neglected absorption in the particle-charged PMMA medium since LMT was restricted to non-absorbing scattering medium [12,20]. Therefore instead of using LMT under assumption of negligible absorption, a modified LMT considering a scattering in absorbing medium may be adopted as developed in [20]. In Figure 2.15 (a) and (b), the computed scattering behavior was analyzed as a function of transmitted laser beam radius and radiation intensity at the interface of the welded components respectively. In both figures, the computed scattered radiation was

analyzed as function of both the diameter of the charged particle and Δn that is defined between 1.1 and 1.9. As also displayed in the figure, up to a certain size of particle diameter, optical scattering dramatically increases causing an increase in laser beam radius (a) and decrease in the laser intensity (b) at the same time. Related to this, it was revealed that further increase in particle size causes to change in scattering direction and forward-scattering increases where it was also reported that scattering effect may be ignored for the particles that is much smaller than radiation wavelength.

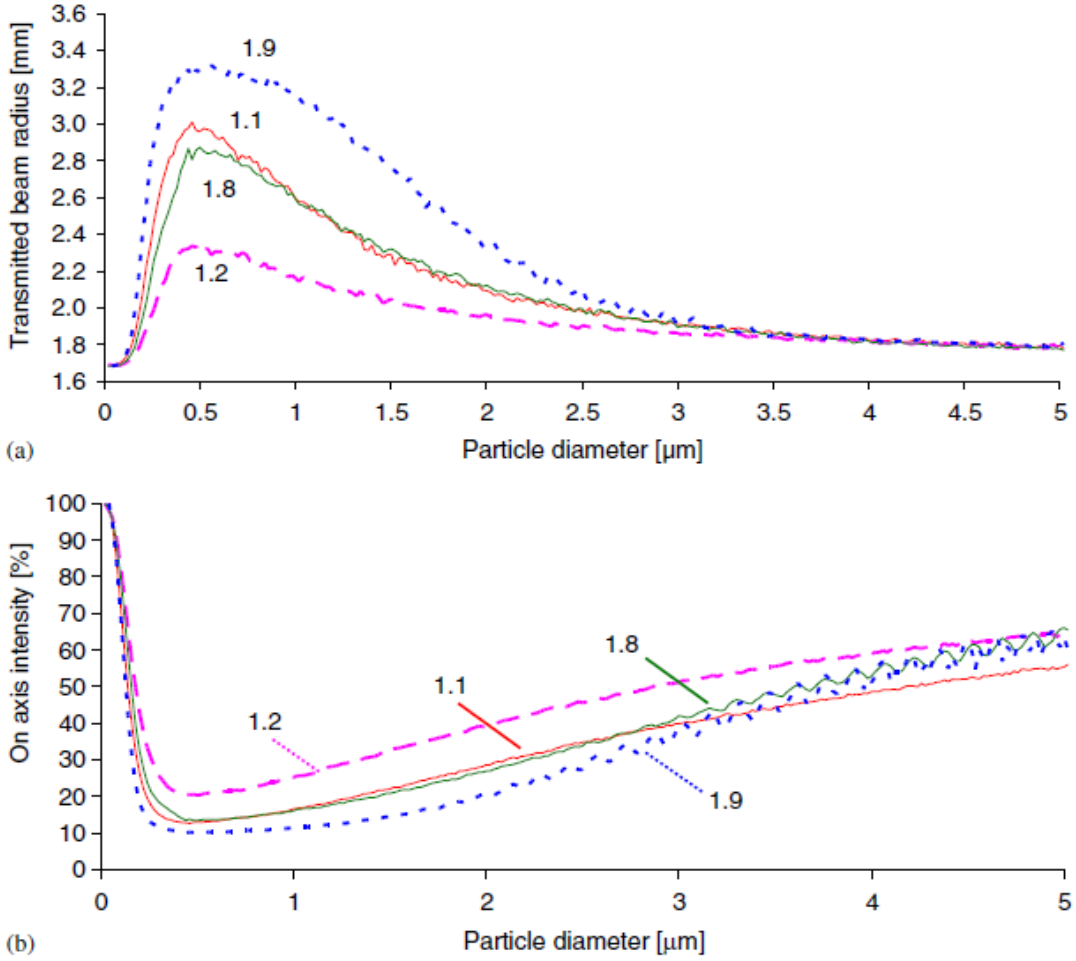

FIGURE 2.15. Variation in the computed radius of the transmitted laser beam profile (a) and its on-axis intensity (b) as functions of the filled particle diameter and relative refractive index in PMMA [67].

In table 2.4, the overview of the reviewed literature in this section was summarized in terms of radiation heat transfer modeling approach used for thermoforming processes of thermoplastics. As aforementioned, the main issue is related to optical heterogeneity in semi-crystalline polymers, whereas particle doped amorphous polymer may be also considered within the context of the same problem.

Nevertheless, this may be relatively an easier for address optical scattering behavior as the size of scatterer is known, which is not the case for unfilled semi-crystalline thermoplastics.

		Participating medium assumption	
		Optically homogeneous	**Optically heterogeneous**
Polymer type / medium		PS [18,60], PET [19,45,63] PA 6 [62], PA 11 [45], PP [46,47,59], HDPE / LDPE [59], PVC [61]	Particle doped PC [22] Particle doped PMMA [67,68], PET [8,66]
Radiation source - wavelength	**IR heating**	0.6 - 6 [18,19,63]	0.6 - 6 [8], 0.7 - 14 [66]
	Laser	Diode: 940nm [47,62], 808nm [61] CO_2 : 10.6 μm [45,59,60]	Diode: 968nm [22] 808nm [67], 940nm [68]
Modeling approach		Temperature dependent absorption behavior [45–47] Beer-Lambert law: Absorption behavior characterized at room temperature [18,19,59–61,63] Modified Bouguer- Lambert Law: Forward scattering considered based on statistical distribution [62]	Two-flux [65] Four-flux [22,65,66] LMT - Monte Carlo [67,68]

TABLE 2.4. Overview of reviewed literature on the radiation heat transfer modeling of thermoplastics.

2.6. Summary

In order to build a predictive radiation heat transfer model for IR heating stage of PE polymer, literature was reviewed including the theory of IR radiation physics and the performed studies on IR heating. Considering the well-known RTE, the necessity to take into account optical scattering in the optically heterogeneous medium of highly crystalline PE was stressed reviewing the studies on the coupled effect between crystalline structure and optical properties of semi-crystalline polymers.

The literature review shows that the coupled relation between optical scattering - crystalline morphology may be neglected for low crystalline thermoplastics. This assumption is further critized for radiation heat transfer models developed for such polymers like PET. However, for highly crystalline polymers, such as linear PE, assumption of optically homogeneous medium may be ill defined since crystalline phase causes significant optical scattering especially in VIS and NIR ranges, as discussed here based on various studies. In literature, the discussion for the scatterer size inside of semi-crystalline

polymer media mainly focuses around the spherulites and their substructures, lamellae. Microscopic or calorimetric analyses can help to identify spherulite and lamellae characteristics. Angular distribution of scattering profile related to the analyzed crystalline morphology may be the key for identifying scatterer size, as proposed in literature. In that point; multiple angle scattering analyses combined with optical scattering theories can provide theoretical-experimental comparisons, to propose a size of scatterer size related to crystalline morphology. Eventually, such information can be used for phase function definitions that may allow to solve RTE for modeling radiation heat transfer in optically heterogeneous polymer media. On the other hand, it was experimentally demonstrated that the thermo-optical behavior of semi-crystalline polymers changes dramatically close to melting range where also some change is seen between room temperature and this range. It is widely accepted that such evolution occurs due to melting of lamellar crystals. Adopting well-known crystal melting hypothesis known as Gibbs Thomson the information about lamellae size can be obtained and correlated to the temperature-dependent optical characteristics of polymer.

The studies that propose a radiation heat transfer models built for optically heterogeneous medium of polymers was mostly dedicated for laser-assisted thermoforming processes. Hence, the optical scattering characteristics of semi-crystalline or doped particle polymer media were analyzed and modeled considering a specific wavelength since laser light is monochromatic. As pointed out several times in Section 2.1 and 2.3, the optical scattering is spectral-dependent. As a consequence, in contrast to laser heating applications, the radiation emitted by an IR source and transferred through a polymer medium is not monochromatic, but in a range, which introduces a complexity in terms of modeling of optical scattering, as the scattering behavior may change in the spectral range of emitted radiation.

References

[1] G. Burkhardt, U. Hüsgen, M. Kalwa, G. Pötsch, C. Schwenzer, Plastics Processing, 1. Processing of Thermoplastics, in: Ullmanns Encycl. Ind. Chem., Wiley-VCH Verlag GmbH & Co. KGaA, 2000.

[2] Y. Le Maoult, F. Schmidt, Infrared Radiation Applied to Polymer Processes, in: N. Boyard (Ed.), Heat Transf. Polym. Compos. Mater., John Wiley & Sons, Inc., 2016: pp. 385–423.

[3] R. Poprawe, ed., Tailored Light 2, Springer Berlin Heidelberg, Berlin, Heidelberg, 2011.

[4] P.T. Tsilingiris, Comparative evaluation of the infrared transmission of polymer films, Energy Convers. Manag. 44 (2003) 2839–2856.

[5] T. Okada, R. Ishige, S. Ando, Analysis of thermal radiation properties of polyimide and polymeric materials based on atr-ir spectroscopy, J. Photopolym. Sci. Technol. 29 (2016) 251–254.

[6] M. Kutz, Applied Plastics Engineering Handbook: Processing and Materials, William Andrew, 2011.

[7] R. Klein, Laser Welding of Plastics: Materials, Processes and Industrial Applications, Wiley-VCH Verlag GmbH & Co. KGaA, Weinheim, Germany, 2011.

[8] A. Denis, E. Dargent, P.H. Lebaudy, J. Grenet, C. Vautier, Dependence on the spectral scattering coefficient on crystallinity into semicrystalline polyester, J. Appl. Polym. Sci. 62 (1996) 1211–1218.

[9] S. Monteix, Y. Le Maoult, F. Schmidt, Modélisation du chauffage convecto-radiatif de préformes en P.E.T.,. Thèse de Doctorat, Ecole des Mines de Paris, 2001.

[10] A.J. Peacock, Handbook of polyethylene: structures, properties, and applications, Marcel Dekker, New York, 2000.

[11] J.K. Lee, T.L. Virkler, C.E. Scott, Influence of initial sheet temperature on ABS thermoforming, Polym. Eng. Sci. 41 (2001) 1830–1844.

[12] J.R. Howell, M.P. Menguc, R. Siegel, Thermal Radiation Heat Transfer, 6th Edition, CRC Press, 2015.

[13] H.D. Baehr, K. Stephan, Heat and Mass Transfer, Springer Science & Business Media, 2013.

[14] M.F. Modest, Radiative Heat Transfer, Second Edition, 2 edition, Academic Press, Amsterdam ; Boston, 2003.

[15] R.D. Larrabee, The spectral emissivity and optical properties of tungsten, (1957). http://dspace.mit.edu/handle/1721.1/4755

[16] J.C. De Vos, A new determination of the emissivity of tungsten ribbon, Physica. 20 (1954) 690–714.

[17] S. Andrieu, Y. Le Maoult, F. Schmidt, Étude expérimentale et numérique du chauffage infrarouge de plaques thermoplastiques pour le thermoformage, Paris, ENMP, 2005.

[18] F. Schmidt, Modelling of infrared heating of thermoplastic sheet used in thermoforming process, J. Mater. Process. Technol. 143–144 (2003) 225–231.

[19] B. Cosson, F. Schmidt, Y. Le Maoult, M. Bordival, Infrared heating stage simulation of semi-transparent media (PET) using ray tracing method, Int. J. Mater. Form. 4 (2011) 1–10.

[20] J.R. Frisvad, N.J. Christensen, H.W. Jensen, Computing the scattering properties of participating media using Lorenz-Mie theory, ACM Trans. Graph. 26 (2007) 60.

[21] M. Bass, Optical Society of America, eds., Handbook of optics, 2nd ed, McGraw-Hill, New York, 1995.

[22] V. Mamuschkin, A. Roesner, M. Aden, Laser Transmission Welding of White Thermoplastics with Adapted Wavelengths, Phys. Procedia. 41 (2013) 172–179.
[23] C.M. Fratini, Study of the Morphology and Optical Properties of Propylene/Ethylene Copolymer Films, (2006). https://vtechworks.lib.vt.edu/handle/10919/27211 (accessed January 17, 2017).
[24] J.J. Keane, R.S. Stein, The scattering of light from thin polymer films. II. Scattering from polyethylene, J. Polym. Sci. Part Polym. Chem. 20 (1956) 327–350.
[25] F.H. Norris, R.S. Stein, The scattering of light from thin polymer films. IV. Scattering from oriented polymers, J. Polym. Sci. Part Polym. Chem. 27 (1958) 87–114.
[26] R.S. Stein, J.J. Keane, F.H. Norris, F.A. Bettelheim, P.R. Wilson, Some light-scattering studies of the texture of crystalline polymers, Ann. N. Y. Acad. Sci. 83 (2006) 37–59.
[27] L. Wang, M.R. Kamal, A.D. Rey, Light transmission and haze of polyethylene blown thin films, Polym. Eng. Sci. 41 (2001) 358–372.
[28] F. De Santis, R. Pantani, Optical Properties of Polypropylene upon Recycling, Sci. World J. 2013 (2013) 1–7.
[29] Q. Zia, R. Androsch, H.-J. Radusch, Effect of the structure at the micrometer and nanometer scales on the light transmission of isotactic polypropylene, J. Appl. Polym. Sci. 117 (2010) 1013–1020.
[30] D. Hakoume, L.A. Dombrovsky, D. Delaunay, B. Rousseau, Effect of Processing Temperature on Radiative Properties of Polypropylene and Heat Transfer in the Pure and Glassfibre Reinforced Polymer, in: Begellhouse, 2014.
[31] J. Fritsch, W. Stille, G. Strobl, Investigation of polymer crystallization kinetics with time dependent light attenuation measurements, Colloid Polym. Sci. 284 (2006) 620–626.
[32] B. Heck, T. Kawai, G. Strobl, Time dependent light attenuation measurements used in studies of the kinetics of polymer crystallization, Polymer. 47 (2006) 5538–5543.
[33] D. Hakoume, L.A. Dombrovsky, D. Delaunay, B. Rousseau, Spectroscopic diagnostics of morphological changes arising in thermal processing of polypropylene, Appl. Opt. 53 (2014) 2702.
[34] I. Kolesov, D. Mileva, R. Androsch, Mechanical behavior and optical transparency of polyamide 6 of different morphology formed by variation of the pathway of crystallization, Polym. Bull. 71 (2014) 581–593.
[35] ASTM International, ASTM D1746-15, Standard Test Method for Transparency of Plastic Sheeting, West Conshohocken PA. (2015).
[36] ASTM International, ASTM D1003-13, Standard Test Method for Haze and Luminous Transmittance of Transparent Plastics, West Conshohocken PA. (2013).
[37] R. Patel, V. Ratta, P. Saavedra, J. Li, Surface haze and surface morphology of blown film compositions, J. Plast. Film Sheeting. 21 (2005) 217–231.
[38] A.M. Sukhadia, D.C. Rohlfing, M.B. Johnson, G.L. Wilkes, A comprehensive investigation of the origins of surface roughness and haze in polyethylene blown films, J. Appl. Polym. Sci. 85 (2002) 2396–2411.
[39] R.S. Stein, R. Prud'Homme, Origin of polyethylene transparency, J. Polym. Sci. Part C Polym. Lett. 9 (1971) 595–598.
[40] B.M. Agarwal, M.P. Menguc, Forward and inverse analysis of single and multiple, (n.d.).
[41] R. Apetz, M.P.B. Bruggen, Transparent Alumina: A Light-Scattering Model, J. Am. Ceram. Soc. 86 (2003) 480–486.

[42] E. Berrocal, D.L. Sedarsky, M.E. Paciaroni, I.V. Meglinski, M.A. Linne, Laser light scattering in turbid media Part I: Experimental and simulated results for the spatial intensity distribution, Opt. Express. 15 (2007) 10649–10665.
[43] C.F. Bohren, D.R. Huffman, Absorption and Scattering of Light by Small Particles, John Wiley & Sons, 2008.
[44] S.W. Hawkins, R.B. Richards, Light transmission and the formation and decay of spherulites in polythene, J. Polym. Sci. Part Polym. Chem. 4 (1949) 515–522.
[45] B Keller, R. Pfeifer, W.-N. Su, P. Eyerer, Temperature Dependent Optical Properties of Polymers as a Basis for Laser Process Modeling, (n.d.).
[46] F. Becker, H. Potente, A step towards understanding the heating phase of laser transmission welding in polymers, Polym. Eng. Sci. 42 (2002) 365–374.
[47] M. Geiger, T. Frick, M. Schmidt, Optical properties of plastics and their role for the modelling of the laser transmission welding process, Prod. Eng. 3 (2009) 49–55.
[48] T. Laumer, T. Stichel, T. Bock, P. Amend, M. Schmidt, Characterization of temperature-dependent optical material properties of polymer powders, in: 2015: p. 160001.
[49] U.W. Gedde, A. Mattozzi, Polyethylene Morphology, in: A.-C. Albertsson (Ed.), Long Term Prop. Polyolefins, Springer Berlin Heidelberg, Berlin, Heidelberg, 2004: pp. 29–74.
[50] G. Reiter, G.R. Strobl, eds., Progress in understanding of polymer crystallization, Springer, Berlin ; New York, 2007.
[51] B. Wunderlich, Thermal analysis of polymeric materials, Springer, Berlin, 2005.
[52] A. Wlochowicz, M. Eder, Distribution of lamella thicknesses in isothermally crystallized polypropylene and polyethylene by differential scanning calorimetry, Polymer. 25 (1984) 1268–1270.
[53] Electron Microscopy of Polymers, Springer Berlin Heidelberg, Berlin, Heidelberg, 2008.
[54] H. Zhou, G.L. Wilkes, Comparison of lamellar thickness and its distribution determined from d.s.c., SAXS, TEM and AFM for high-density polyethylene films having a stacked lamellar morphology, Polymer. 38 (1997) 5735–5747.
[55] N. Alberola, J.Y. Cavaille, J. Perez, Mechanical spectrometry of alpha relaxations of high-density polyethylene, J. Polym. Sci. Part B Polym. Phys. 28 (1990) 569–586.
[56] R.L. Hallman Jr, The Effect of Processing Parameters on Barrier Properties of Polymers, (2013).
[57] L. Feng, M.R. Kamal, Distributions of Crystal Size from DSC Melting Traces for Polyethylenes, Can. J. Chem. Eng. 82 (2008) 1239–1251.
[58] S.-Y. Lee, S.-Y. Park, H.-S. Song, Lamellar crystalline structure of hard elastic HDPE films and its influence on microporous membrane formation, Polymer. 47 (2006) 3540–3547.
[59] J.M.P. Coelho, M.A. Abreu, F. Carvalho Rodrigues, Methodologies for determining thermoplastic films optical parameters at 10.6 μm laser wavelength, Polym. Test. 23 (2004) 307–312.
[60] Y. Kurosaki, T. Matayoshi, Study of controllability of melt depth in infrared laser penetration welding of thermoplastics, in: ANTEC-Conf. Proc.-, Citeseer, 2004: pp. 1222–1226.
[61] J.D. Van de Ven, A.G. Erdman, Laser Transmission Welding of Thermoplastics—Part I: Temperature and Pressure Modeling, J. Manuf. Sci. Eng. 129 (2007) 849.
[62] M. Chen, Gap bridging in laser transmission welding of thermoplastics, (2009). http://qspace.library.queensu.ca/handle/1974/5220 (accessed October 15, 2015).

[63] M. Bordival, F.M. Schmidt, Y. Le Maoult, B. Cosson, B. Plantamura, A ray tracing method to simulate the infrared heating of semi-transparent thermoplastics, Int. J. Mater. Form. 3 (2010) 809–812.

[64] K.A. Jensen, J.-F. Ripoll, A.A. Wray, D. Joseph, M. El Hafi, On various modeling approaches to radiative heat transfer in pool fires, Combust. Flame. 148 (2007) 263–279.

[65] R.C. Progelhof, J.L. Throne, Predicting radiant energy transmission through polymer sheets, Polym. Eng. Sci. 14 (1974) 760–763.

[66] P. Lebaudy, J.M. Saiter, J. Grenet, C. Vautier, Temperature distribution in poly (ethylene terephthalate) plate undergoing heat treatment. Diffusion influence: 1. Theoretical approach, Polymer. 33 (1992) 1887–1892.

[67] M. Ilie, J.-C. Kneip, S. Matteï, A. Nichici, C. Roze, T. Girasole, Laser beam scattering effects in non-absorbent inhomogenous polymers, Opt. Lasers Eng. 45 (2007) 405–412.

[68] M. Ilie, D. Grevey, S. Mattei, E. Cicala, V. Stoica, Diode laser welding of ABS: Experiments and process modeling, Opt. Laser Technol. 41 (2009) 608–614.

This page intentionally left blank.

Chapter 3

MORPHOLOGY-DEPENDENT OPTICAL PROPERTIES OF SEMI-CRYSTALLINE THERMOPLASTICS

3.1. Introduction

In this chapter, the morphology dependent optical properties of PE are analyzed bridging the crystalline structure to its transmittance, reflectance characteristics and optical scattering behavior. As discussed in Chapter 2, the reviewed literature shows the strong coupling between crystalline structure – optical characteristics of various types of semi-crystalline thermoplastics. In this research, different types of PE, namely HDPE and LLDPE are used for analyzing this relation in-depth in order to understand the role of crystalline morphology on the optical characteristics adequately. Thus, the experimental methodology proposed here could be used for analyzing the optical behavior of any type of unfilled semi-crystalline thermoplastics. In this thesis, HDPE and LLDPE are named as PE-1 and PE-2, respectively.

At first part of the chapter, the crystalline structure of PE is discussed briefly based on literature and, its morphological characteristics in relation to crystallization behavior are highlighted. Afterwards, the experimental methodology adopted for the analyses is presented including sample preparations and optical, calorimetric and microscopic examinations. This is followed by discussions on the experimental analyses. Thanks to the calorimetric analyses, lamellar morphology of PE was predicted based on Gibbs Thomson approach, where also its spherulitic structures was examined using microscopic techniques. The optical properties of PE were obtained using FTIR measurements and the spatial distribution of optical scattering was analyzed based on MALS tests performed at 632.8 nm. As an overview, this chapter aims to answer three main points to bridge the crystalline morphology to optical properties of PE at room temperature:

- *What is the role of crystalline structure on the optical properties of PE? In the case of strong optical scattering in PE medium due to its morphology, what is the spectral dependence of optical scattering in VIS, NIR and MIR ranges?*

- *What are the crystalline formations or morphological units that are responsible for optical scattering in PE medium?*

- *What is the relation between spatial distribution of scattered light and PE morphology? How scattering behavior changes in forward and backward directions in relation to the morphology?*

3.2. Crystalline structure of polyethylene

Polyethylene morphology has been intensively studied in literature considering its crystallization [1,2] and melting behavior [2–7]. As discussed before, crystallization behavior of PE is out of the scope of the thesis. However, basic understanding on the effect of crystallization behavior of PE on its morphological

features is necessary to develop an experimental methodology to bridge its crystalline structure to the optical characteristics. In this section, a broad overview about PE crystalline morphology including its lamellae structures, spherulitic superstructures and, their formations in relation to polymer chain structure and different cooling conditions is given.

As aforementioned, crystalline morphology in melt-crystallized PE typically relies on various chemical and physical factors such as; cooling speed, molecular weight, degree of polymer chain branching, thermal history [1,2,5]. Regarding to earliest studies conducted on the crystallization behavior of PE [8–10], it was experimentally demonstrated that crystallites form based on *chain-folding principle*. More specifically, regular folding of polymer chains form stacks of crystal lamellae with amorphous region sandwiched between adjacent lamellar crystals, as firstly reported by Kobayashi et al [10] for melt-crystallized PE. In the case of crystallization from the melt, PE crystallization generally encompasses two distinct processes, namely crystallite initiation and crystallite growth nucleation [2]. At very beginning, formation (or initiation) of new crystallites occurs, which is called primary nucleation. This step is followed by crystal growth and secondary nucleation processes that occur simultaneously. Crystal growth is the process of adding of new chain stems to the existing crystallites, whereas secondary nucleation refers to new lamellar formations from the surface of the existing ones. Crystal growth mechanism itself can also be categorized in primary and secondary crystallizations. During the simultaneous secondary nucleation and primary crystallization X_c increases rapidly in parallel to lateral growth of lamellae [1,2,5] and growing of spherulitic superstructures. The laterally grown lamellas are usually organized in spherical superstructures, called *spherulites* [2,5]. The longitudinal axis of lamellas refers to the crystallographic b-axis which mainly lies along the spherulite radii [2,5]. The concurrent growth of spherulites continue until impingement with the neighboring spherulites occurs where basically non-spherulitic superstructures may form. As coined by Bassett et al [11] , *axialites* - which represents another crystal superstructure which does not show a spherical symmetry – are also seen in PE. In Figure 3.1, spherulitic structure of PE and its subspherulitic crystallite formations, such as dominant and subsidiary lamellas, and the crystallographic axes are schematically shown. The terms, dominant and subsidiary lamellas in Fig 3.1, are introduced by Bassett et al [12], which represents relatively thicker and thinner chain folding which is caused by several chemical factors such as molar mass, length of molecules and their branch content etc.[5,13]. The l_c in PE, which is represented by the crystallographic c-axis [1,5], is perpendicular to lateral grown axis of lamellas (b-axis), and thus to spherulite radii. (Figure 3.1).

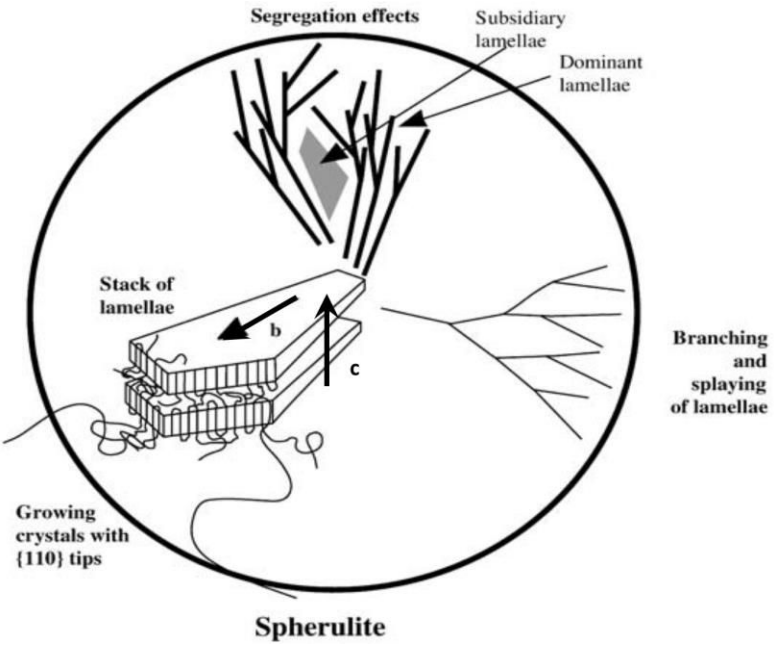

FIGURE 3.1. Spherulitic superstructures and stacked order of lamellar crystals [5].

The length of folded chain, which is parametrized here as l_c, reflects the distribution of crystallizable sequence lengths on the linear segment of polymer chains. In case of higher degree of chain branching, the growth of lamellar crystallites in c-axis is thus restricted. To summarize, the higher the degree of branching, the smaller the averaged value of l_c in PE [2]. In addition, the length of folded chain is highly sensitive to temperature variations under cooling, as reported extensively in literature for melt-crystallized PE [4,14–17] As shown clearly by Barham et al [17], the initial fold length, or l_c, is inversely proportional to the supercooling ($\Delta T_{cooling}$), which defines the temperature difference between T_m^0 and the temperature at which crystallization occurs ($T_{crystallization}$). The Figure 3.2 (a) shows this inverse relation between the initial fold length and the temperature relations obtained from melt-crystallized PE [17]. In addition, as the crystal thickening is quite slow [18], there is a linear relation between time and the growth of chain-folding crystallites. In Figure 3.2 (b), the study on the relation between the time of chain folding growth at several isothermal temperature steps are displayed [19]. The crystal thickening behavior applying isothermal crystallization below T_m^0 is called annealing. Regarding to the isothermal temperature, if there is sufficient mobility in the folded-chain crystal, it then enables annealing process which results thickening of lamellar crystals.[3]. The mobility in the folded-chain is related to a sliding diffusion where it tends to move along the c-axis via chain sliding diffusion to attain a thermodynamically more stable crystal [7]. But, as shown in Fig 3.2 (a) and (b), such a perfectly stable crystal can be obtained under very low $\Delta T_{cooling}$ under very long time. Regardless the degree of chain branching, annealing of polyethylene is

accelerated by an increase in the isothermal crystallization temperature. In this behavior, the key factor is the increased polymer chain mobility at higher temperatures.

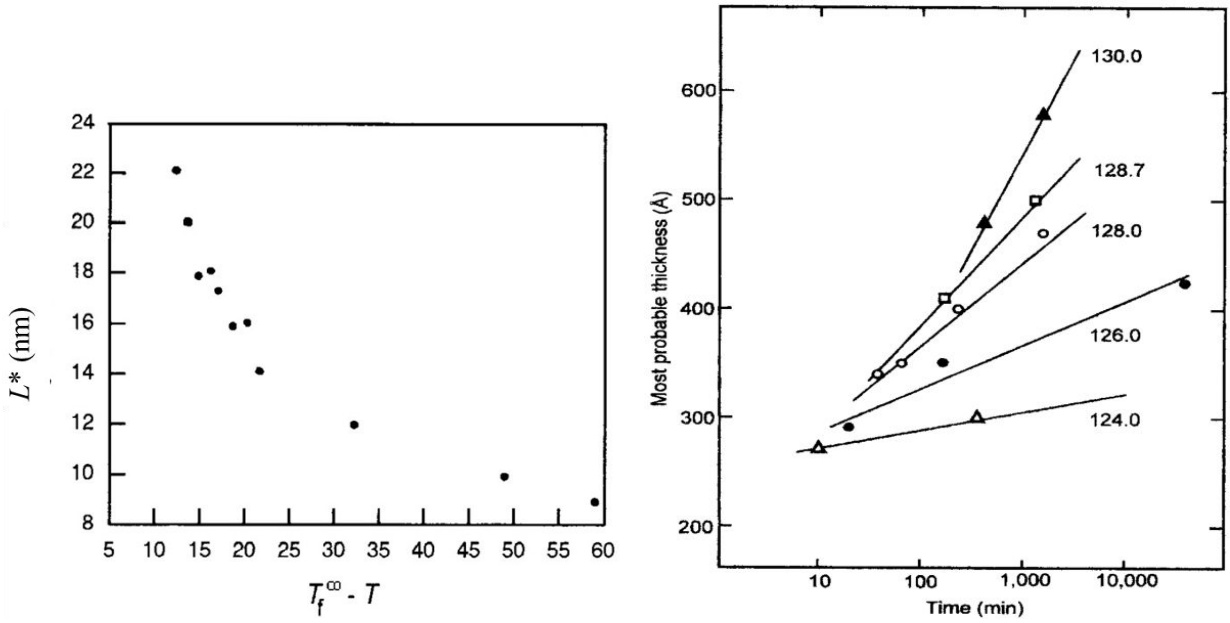

(a) (b)

FIGURE 3.2. The effect of supercooling (a) [17], isothermal time and crystallization temperatures (b) [19] on the lamellae thickening in PE.

Regarding to widely-accepted behavior shown in Fig3.2 (a), thinner crystals form at lower temperatures. However, PE continues to crystallize even at room temperature, although crystallite formation is much slower due to lower chain mobility at lower temperatures. In such case secondary crystallization occurs at which several type of crystallite growth may be seen such as, thickening of preexisting crystallites, annealing of lamellae to relieve crystal defects; or thin and poorly ordered crystals created from the amorphous material that lies in interlamellar zones [20]. Secondary crystallization may also happen concurrently with nucleation and crystal growth at high temperatures whereas, only secondary crystallization is seen at lower temperatures due to lower chain mobility. In last decades, the studies performed using synchrotron enabled to understand secondary crystallization better. Some studies on melt-crystallized PE [21,22] and PET [22] already showed the insertion of thin crystals in interlamellar regions during secondary crystallization. In [22], in contrast to the behavior observed in PET, it was reported that the mode of secondary crystallization in PE was thickening of preexisting crystallites. It should be noted here that isothermal crystallization temperature was 125°C in [22], in contrast to the non-isothermal crystallization studied in [21], at a cooling rate of 1 K/min starting from 160°C down to 40°C.

Different conclusions from these studies may be plausible since the length of folded-chain is strongly related to crystallization temperature, and thus chain mobility as stressed above.

3.3. Experimental analyses on the morphology-dependent optical properties of polyethylene

3.3.1. Materials

As aforementioned, the optical-morphological analyses presented in this chapter were done using two types of PE. HDPE and LLDPE were named here as PE-1 and PE-2, respectively. It is known that the polymer chain structure of HDPE is mainly unbranched with low number of flaws or branches, which can be considered as linear PE [2]. Conversely, LLDPE has highly branched polymer chain structure, mainly consisting of short branches. In comparison to linear PE, such a branched composition induces lower amount of crystals in an equivalent volume where also potential lamellae thickening is also mitigated due to branching in the polymer chains, as discussed in the previous section. In this research project, the PE-1 represents the type of polymer which is used for the IR-heating assisted thermoforming processes. The key reason here for using two types of PE is to introduce significant difference in PE morphology in terms of crystalline structure and level of crystallinity. Thanks to this, comparative analyses between the PE polymers in different morphologies can be done to bridge the crystalline structure to the optical properties and optical scattering behavior of PE.

3.3.2. Sample preparations and introduction of different morphological state

The experimental analyses on the morphological and optical characteristics of PE-1 and PE-2 were performed adopting different comparative analyses. Characterizations of optical properties of the PE polymers were done preparing samples in the form of thin films. The calorimetric and microscopic examinations on the morphology of the polymers were done using small samples that were cut from the thin films. For each comparative analysis, several groups of samples in different thickness, morphology, and/or PE polymer type were prepared. The overview of the studied samples in each corresponding analysis is presented in the results and discussions (Section 3.4).

Although all the PE-1 and PE-2 samples were prepared differently in terms of thickness and cooling conditions, an identical preparation procedure was followed for preparation of the thin film samples. The PE-1 and PE-2 polymers in the form of pellets were injection molded and square plates with dimensions of 78x78x2.2 mm were fabricated. The main reason to fabricate samples via injection molding is to obtain void free samples as the void formations may affect the optical properties of polymers, as reported in [23]. The injected plates and compressed for obtaining thin film samples with controlled thickness. The

compression procedure was started by heating the samples up to 180 °C and holding the polymer at that temperature for 5 min to melt crystalline phase completely. The samples were then compressed up to the desired thickness and the adopted cooling condition was applied. The samples were cooled down under three different cooling conditions: free convection in still air (slow-cooled), quenching in liquid nitrogen (LN_2) and annealed applying thermal fractionation by isothermal stepwise cooling. Thanks to different cooling conditions, different groups of samples were prepared with the identical PE polymer and thickness, but with different crystalline structure. For the sake of clarity in this chapter, the slow-cooled, quenched and annealed samples are called as *SC*, *QC* and *AN*, respectively.

The *QC* samples were quenched immediately after opening the heating chamber whereas the SC samples were left in the opened heating chamber during cooling to room temperature. The cooling rate of the *SC* samples were registered by the thermocouple of the heating chamber positioned just below the samples, while *QC* samples could not be determined. The cooling curve of the SC samples are presented in Annex A.2.1. The annealing process of PE-1 and PE-2 polymers were done following different isothermal stepwise cooling. The isothermal temperature levels were secured in the heating chamber where the temperature can be controlled and registered thanks to the thermocouple of the heating chamber. Considering the effect of degree of chain branching, the highest (or first) isothermal step was chosen slightly lower for relatively more branched PE-2 polymer than the one chosen for PE-1. The isothermal cooling steps of PE-1 and PE-2 samples are presented in Table 3.1. In the table, the isothermal temperature steps of PE-1 and PE-2, and the waiting time for each step are given. Between each consecutive isothermal step, it was observed that the decrease and stabilization in temperature occur between 7-9 minutes, which reflects cooling rate varies between 1-2 K/min. The stepwise cooling curves of PE-1 and PE-2 are presented in Annex A.2.2.

Polymer type	**PE-1**	**PE-2**	**Waiting time (min)**
Isothermal temperature steps (°C)	130, 125, 120, 115	120, 115	10
	110, 105, 100, 95, 90		15
	80, 70, 60, 50, 40		25

TABLE 3.1. Stepwise cooling procedure applied for annealing of PE-1 and PE-2 samples.

3.3.2.1. Film thickness measurements

Sample thicknesses were measured using a caliper where also intra-film and inter-film thickness variation was checked performing eddy current thickness measurements using Isoscope FMP10 high-

precision probe (Fischer ©). The thickness measurements of all the prepared samples showed that the intrafilm thickness variation is around +/- 20 μm whereas interfilm thickness variation was slightly higher, around +/- 30 μm. More than 40 PE-1 and PE-2 film samples were prepared using that procedure, it was observed that compression process is repeatable.

3.3.3. Characterization of crystalline morphology of polyethylene

3.3.3.1. Calorimetric analyses and prediction of lamellar morphology

The calorimetric analyses of PE-1 and PE-2 samples were carried out using a double-furnace, power compensated DSC (PerkinElmer DSC 8000). The DSC is equipped with a LN_2 cooling unit (intra cooler). The measurements were done under N_2 purge gas with a flow rate of 20 ml/min. For each DSC analysis, a piece of material with a mass of 3 mg (+/-0.1 mg) was cut from the compressed thin films and sealed into standard aluminum sample pan. The heating scan was performed either 10 K/min or 20 K/min at a temperature range of -50°C to 180°C. These heating rates were chosen regarding the literature on the calorimetric analyses of PE under different heating rate. As discussed in detail in Section 2.4.2, most of the studies on PE suggested that ideal heating rate range is between 10-20 K/min. Wunderlich [24] showed further analyses considering the relation between different heating rates where it was revealed that zero entropy production of PE is mostly around 20 K/min indicating that no evolution may happen in its crystalline phase.

Thanks to the DSC analyses, both the amount of crystals, which is parametrized as X_c, and the lamellar morphology of PE-1 and PE-2 was investigated. X_c was defined based on the ratio between the ΔH_m of the sample and the enthalpy of fusion of 100% crystalline PE (ΔH^o_m), as shown in Equation 3.1. The melting endotherm of each sample was determined integrating the melting peak with a baseline drawn between around 25°C and 150°C. ΔH^o_m of PE was adopted from literature, as 288 J/g [15]:

$$X_c(\%) = \frac{\Delta H_m}{\Delta H_m^0}(\%) \tag{3.1}$$

The crystallinity and peak melting temperature were evaluated using the first heating scan before deleting the thermal history of the differently cooled PE samples so that their lamellar morphology and X_c in relation to cooling condition was obtained. The prediction of lamellar thickness was done adopting Equation 2.16. As presented in detail Chapter 2, the equation was derived based on Gibbs-Thomson equation, which enables to predict most probable l_c population distribution rather than an estimation of the most probable single crystal thickness from Gibbs-Thomson approach.

3.3.3.2. Chemical etching of polyethylene surface and microscopic examinations

The microscopic examinations were carried out cutting small samples from the prepared thin PE-1 and PE-2 films. In order to observe the crystalline phase, a well-known surface treatment technique, namely permanganic chemical etching developed by Bassett et al [25], was applied to the samples prior to the microscopic examinations. Basically, the chemical etching treats the surface of interest to improve textural contrast of crystalline phase. In other words, the etching enables chemical digestion of the non-crystalline zones of the cut surface so that amorphous material of the cut surface can be removed and, the underlying spherulitic structure or lamellar organization can be seen [2,5,13]. Since T_g of PE is in the range between -100°C and -130°C [2], cutting on PE surface at room temperature alters the crystalline phase texture by smearing its soft surface [2]. In order to avoid deformation - and thus preserve the crystalline phase texture - on the cut surface, it is required to cut samples when PE is close to be brittle around T_g. In this study, the samples were cryomicrotomed at -80°C and successful cut surfaces were obtained. Similar temperatures just above T_g was adopted in literature for PE [26,27] and, clean texture of crystalline phase was obtained.

The permanganic etching solution was prepared with 1% weight/volume of potassium permanganate ($KMnO_4$) in a mixture of 10 volumes of concentrated sulphuric acid, 4 volumes of 85% orthophosphoric acid, and 1 volume of distilled water, as applied in [27–29]. The samples were etched for 2 hours then rinsed with distilled water and cleaned in ultrasonic batch for 3 minutes. The samples were then dried at room temperature before the microscopic analyses. The crystalline structure of PE was examined employing a scanning electron microscope (SEM) (Nova NanoSEM 450 / 650). The power of the electron beam was chosen at 5keV in order to minimize the radiation damage on the polymer surface which potentially causes to deteriorate the texture of crystalline phase in a very short time [6].

3.3.4. Characterization of optical properties of polyethylene

3.3.4.1. Spectroscopic analyses

As reviewed in Chapter 2, the physical meanings of T_λ and R_λ are the ratio of the total amount of transmitted (Φ_λ^t) and reflected (Φ_λ^r) radiative flux over incident flux (Φ_λ^i). The optical characteristics of PE-1 and PE-2 were analyzed including their $R_\lambda^{i,\cap}$ and transmittance properties measured in two different configurations, $T_\lambda^{i,r}$ and $T_\lambda^{i,\cap}$. The spectroscopic measurements were carried out in the spectral range of 0.25 - 25 µm, which lies in VIS (0.4-0.8), NIR (0.8-2µm) and MIR (2-25µm) [30]. The $T_\lambda^{i,r}$ tests were done using a FTIR spectrometer (Bruker Vertex 70) whereas, $T_\lambda^{i,\cap}$ and $R_\lambda^{i,\cap}$ tests were done using two different spectrometers, namely Bruker Vertex 70 and Perkin Elmer 950. The reason to use two different spectrometers was about the limitation in the spectral range of the integrating sphere used in Bruker

Vertex 70 in VIS range. This limitation is due to the reflectance characteristics of different sphere coating materials typically used in optical metrology. Here, the integrating spheres of Bruker Vertex 70 and Perkin Elmer 950 are infragold and spectralon-coated, respectively. It is known that spectralon has reflectance up to 95% between 0.25 and 2.5 µm, while infragold has such high reflectance values beyond 2 µm [31]. The optical measurements done via Bruker Vertex 70 were carried out in our laboratory, while the tests done with the latter spectrometer were realized in Procédés, Matériaux et Energie Solaire (PROMES) – CNRS laboratory.

The overview of the test setups used for $T_\lambda^{i,r}$, $T_\lambda^{i,\cap}$ and $R_\lambda^{i,\cap}$ measurements are schematically displayed in Figure 3.3 (a), (b) and (c), respectively. Both the $T_\lambda^{i,\cap}$ and $R_\lambda^{i,\cap}$ tests were performed mounting an integrating sphere on the spectrometers, where the sample position was changed regarding to measurement type.

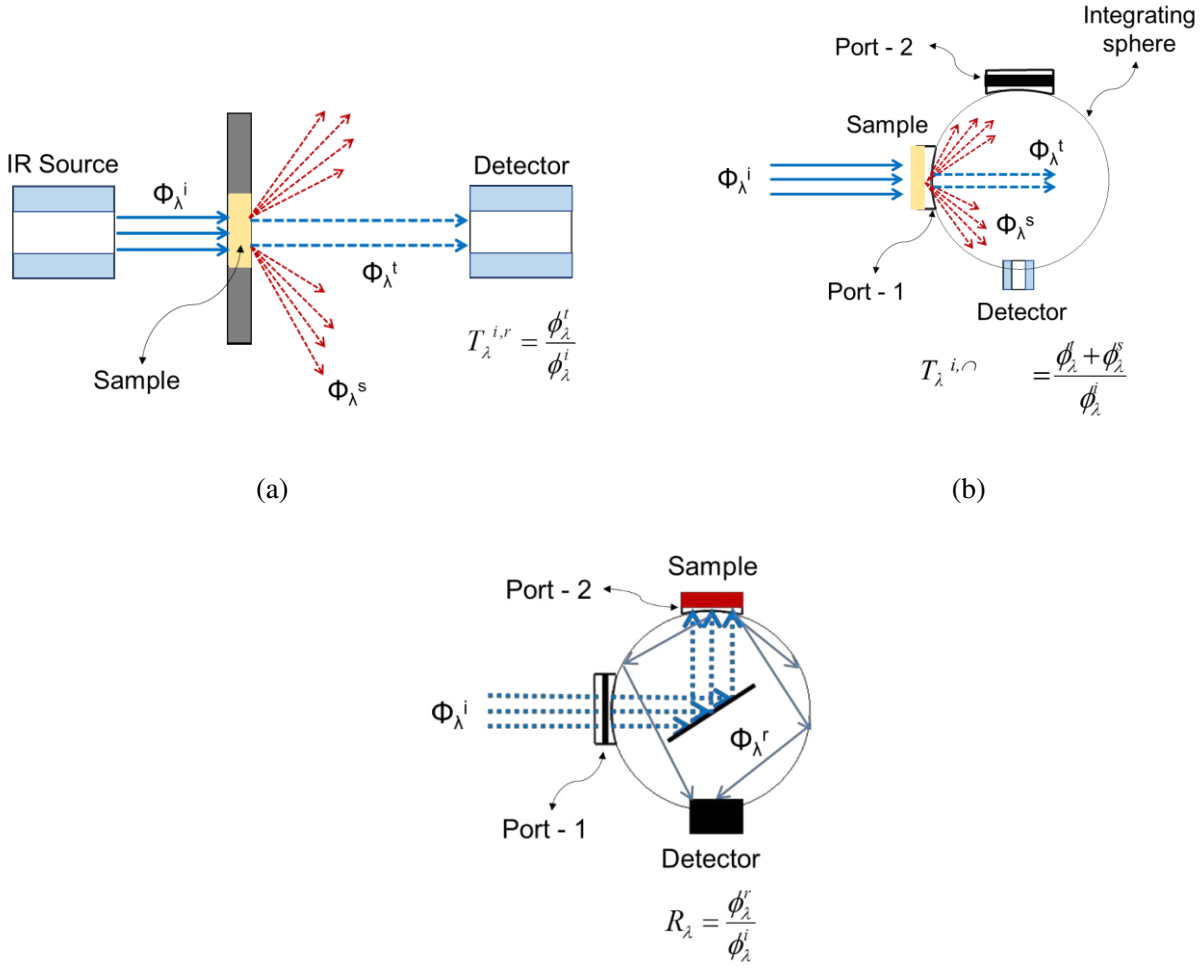

FIGURE 3.3. Overview of the test setups for $T_\lambda^{i,r}$ (a), $T_\lambda^{i,\cap}$ (b) and $R_\lambda^{i,\cap}$ (c) measurements.

As displayed in Figure 3.3 (b) and (c), for the $T_\lambda^{i,\cap}$ and $R_\lambda^{i,\cap}$ measurements, the samples were positioned at the entrance port (Port-1) and the side port (Port-2) of the integrating sphere, respectively. Considering an optically heterogeneous medium, Φ_λ^i may be either directly transmitted or scattered. Hence, as shown in Figure 3.3 (b), $T_\lambda^{i,\cap}$ tests performed with integrating sphere enable to detect both the forward-scattered ($\Phi_\lambda^{s\text{-}forward}$) and directly transmitted - Φ_λ^t - light fluxes which travel through such a heterogeneous medium. It should also be noted here that some amount of the radiative flux may also be back-scattered ($\Phi_\lambda^{s\text{-}back}$) inside of the heterogeneous medium and may not enter the integrating sphere [32]. In contrast to the $T_\lambda^{i,\cap}$ tests, only Φ_λ^t may be detected for the $T_\lambda^{i,r}$ measurements on an optically heterogeneous medium. Although Apetz el al. [33] reported that $\Phi_\lambda^{s\text{-}forward}$ in small angles may also be detected by the detector of spectrometer, this may be relatively small in comparison to the amount of Φ_λ^t and, it is therefore neglected in this study.

In addition, if multiple internal scattering is considered in an optically heterogeneous medium, it may then be required to take into account that the scattered light inside of the medium may come back into the direction of the incident light. In other words, the light may be scattered multiple times inside of the medium due to the optical heterogeneity and some amount of the scattered light may be back to the direction of the incident light and detected by the spectrometer. This phenomenon is known as radiation gain due to in-scattering in radiation theory [34]. However, determination of the multiple scattering phenomena may require an extensive experimental analysis which is not in the scope of the thesis. Therefore, the effect of multiple internal scattering was neglected for the transmission measurements. Based on these assumptions, $T_\lambda^{i,r}$ measurements performed without integrating sphere (Figure 3.3(a)) gives Φ_λ^t in the optically heterogeneous medium of PE. Using identically thick samples, the key benefit of doing transmittance tests in two different configurations is to have a comparative analysis for estimating the effect of optical scattering in PE medium.

3.3.4.2. Multiple Angle Light Scattering (MALS) Tests

MALS tests were done using CASI Scatterometer (Schmitt Measurement Systems, Inc.) equipped with a helium-neon (He-Ne) laser at 632.8 nm. The tests were carried out at PROMES Laboratory. For the tests, both the PE-1 and PE-2 samples prepared in *QC* and *AN* conditions were used. Thanks to this step, the relation between the PE morphology and spatial distribution light scattering was analyzed.

The scatterometer sources a collimated laser beam where the laser hits the tested sample. The laser beam diameter was set as 1.5mm. The scattered light from the sample is detected by the in-plane rotation detector at the angles between 0° and 348° around the sample. The overview of the test setup is displayed

in Figure 3.4 (a). The angular resolution of the rotation detector was set to 0.522°, so that the angular scattered light intensity of PE was measured at around 700 spatial points around the sample. Since the scattered light was obtained at an angle range that covers almost all the periphery of the sample, the angular distribution of both the forward-scattered and back-scattered light intensity of the PE samples were measured. Theoretically, this enables to calculate *Bidirectional Reflectance Distribution Function (BRDF)* and *Bidirectional Transmittance Distribution Function (BTDF).* The angular integration of both the functions is called as *Bidirectional Scatter Distribution Function (BSDF)* [35,36]. Hence, the theoretical definition of all the three terms are identical, except denoting explicitly the directional behavior of the scattered light. The bidirectional distribution function for all the terms then can be defined as the ratio between differential radiance that scatters from a sample to the differential irradiance that arrives to the sample. This relation is given in Equation 3.2. In addition, this phenomenon is illustrated schematically in Figure 3.4 (b) with respect to BRDF measurements. As it is seen in the figure, the incident laser power (symbolized as P_i) at an angle of θ_i hits the sample surface and back-scattered (P_s) at a polar angle of θ_s and, at a finite solid angle of Ω (in steradians (sr)). The terms, P_i and P_s, are in watt, where also the unit of BRDF is in sr^{-1}. The θ_s appeared in Equation 3.2, represents a correction of radiance that is projected on the detector. Since the projected area of radiance changes regarding the angular position of the in-plane rotating detector, the difference between the scattered light from the sample surface and received by the detector at a specific angle has to be taken into account [35].

$$BDRF(sr^{-1}) = \frac{dP_s/d\Omega}{P_i Cos\theta} \approx \frac{P_s/\Omega}{P_i Cos\theta} \tag{3.2}$$

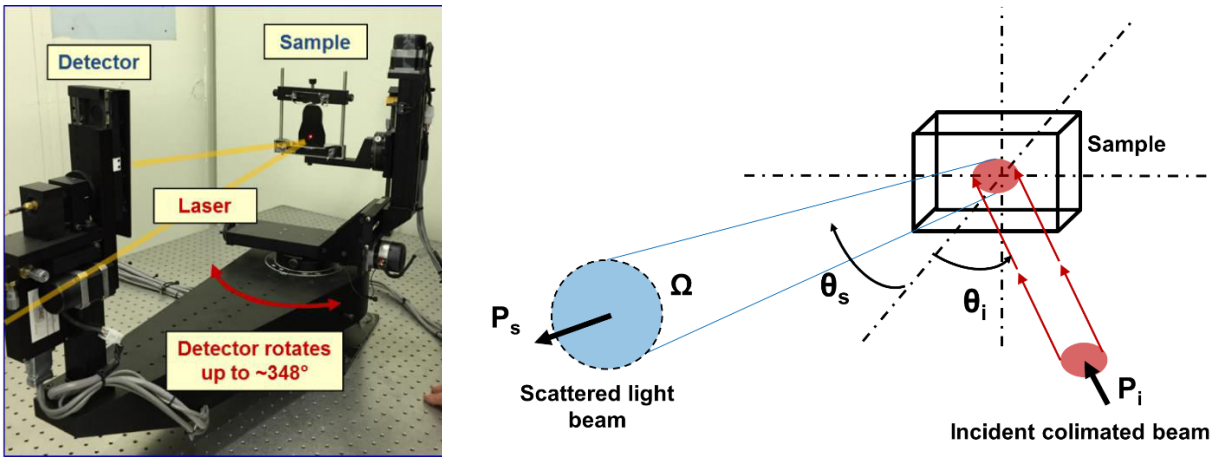

(a) (b)

FIGURE 3.4. The scatterometer used for the MALS tests (a) and schematical illustration of BRDF (b).

Before performing the MALS tests, a reference measurement was done with a sample -behaving like a diffuse reflector- to determine the incident reference power -P_i -. Thanks to this step, the scattered laser beam was normalized (BRDF or BDTF unit is in sr^{-1}) considering the ratio between the scattered light from the PE samples to the P_i measures at each corresponding angle. The scattered light power that arrives at the detector also passes through an aperture which has certain size. In the MALS of the PE samples, the aperture size was set to 13.675 mm. By knowing the distance between the sample and the detector, and also the aperture size, the finite size of solid angle Ω that appears in Equation 3.2 can be determined. The further discussions related to the measurements and test setup is given in Section 3.4.4.

3.4. Results and Discussions

3.4.1. The role of crystalline structure on the optical properties of polyethylene and wavelength dependency of optical scattering

In this section, the relation between the crystalline structure and optical properties of PE-1 were analyzed considering a two-step analysis. At very first step, the relation was analyzed considering samples with identical thicknesses and different morphologies, characterized here in terms of X_c. The optical characteristics of the PE-1 samples were analyzed at room temperature and in NIR and MIR spectral ranges, measuring its $T_\lambda^{i,r}$, $T_\lambda^{i,\cap}$ and $R_\lambda^{i,\cap}$. Thanks to the analyses, the role of crystalline structure of PE on its transmittance and reflectance characteristics was highlighted. The optical scattering in PE medium was discussed based on the $T_\lambda^{i,r}$ and $T_\lambda^{i,\cap}$ values of identical samples, and the wavelength dependency of the optical scattering was also addressed.

For the analyses, two groups of samples were prepared. The first group of PE-1 samples were prepared with the identical thickness but under QC and SC cooling conditions. The second group of samples were prepared in three thicknesses following the identical SC conditions. The overview of the tested PE-1 samples for the two-step analyses is presented in Table 3.2.

	1st group	**2nd group**
Cooling condition	*QC and SC*	*SC*
Sample thickness (mm)	0.5	0.42, 0.90 and 1.82
FTIR measurements	$T_\lambda^{i,r}$ and $R_\lambda^{i,\cap}$.	$T_\lambda^{i,r}$and $T_\lambda^{i,\cap}$

TABLE 3.2. The overview of the PE-1 samples prepared for the initial calorimetric and optical analyses.

The X_c of 0.5mm thick PE-1 QC and SC was determined via calorimetric analyses at a heating rate of 20 K/min. As mentioned in Section 3.3.3.2, small samples were cut from the compressed thin PE-1 films for the DSC measurements. For each QC and SC sample, two small samples were used for the DSC analyses. In order to avoid any potential morphological change in PE-1 due to secondary crystallization at room temperature, each sample was analyzed immediately after the compression-cooling steps of the prepared thin films. The analyses showed that the X_c of the PE-1 SC is around 73% whereas, the PE-1 QC samples have a X_c around 67%. It should be noted that the DSC measurements that were done for the identical samples in each group showed a X_c that varies +/- 1% which is a conventional uncertainty of crystallization measurement obtained via calorimetric analyses. Therefore, it is clear that the difference between the X_c of the PE-1 QC and SC samples is significant which attributes the difference in the level of crystallinity, and thus different morphologies.

Transmission characteristics of the 0.5mm thick PE-1 QC and SC samples were initially analyzed measuring their $T_\lambda^{i,r}$. Figure 3.5 (a) and (b) illustrate $T_\lambda^{i,r}$ of the samples over the spectral ranges of 1-2 µm and 2-20 µm, respectively. The $T_\lambda^{i,r}$ measurements clearly show that a slight variation in the X_c of PE-1 has a great effect on its $T_\lambda^{i,r}$, especially in NIR range. Conversely, the same trend is not seen in MIR range as the difference in crystallinity is somewhat effective on $T_\lambda^{i,r}$ until 3.5µm, where after the measurements of both the QC and SC samples are very similar (Figure 3.5 (b)). The difference in $T_\lambda^{i,r}$ of the identically thick PE-1 samples indicates lacking of measured Φ_λ^t due to optical scattering phenomenon that was induced by different X_c. However, this effect may not only be explained considering the difference in X_c, but also crystalline morphology of PE. In other words, based on the $T_\lambda^{i,r}$ measurements in NIR and MIR ranges, it is seen that the optical scattering behavior in PE medium changes under varying wavelength. And, this behavior may be explained considering both the theoretical relation between equivalent spherical scatterer size – directional dependency of scattered light (Figure 2.11 in Chapter 2) and X_c, which can represent the amount of crystals in the polymer medium. More rigorously speaking, the relation between wavelength of radiation and the scatterer in the medium -which can be represented by spherulites or lamellar crystals- is the key that governs this wavelength-dependent optical scattering. As reviewed in Chapter 2, this has been experimentally analyzed for various type of unfilled semi-crystalline thermoplastics, including PE, and similar crystallite formations were proposed as a scatterer, as presented in Table 2.2. In addition to this, similar wavelength-dependent trend was observed in [37] considering the transmission characteristics of semi-crystalline PP. It was also discussed in [37] that strong optical scattering seen in PP medium in VIS and NIR ranges becomes negligible in MIR range. This was attributed to the size of the scatterers in PP gets considerably smaller than the applied wavelength. Therefore, it was concluded that the size of scatterer in heterogeneous PP medium is

probably small thin lamellar structures which plays a key role in wavelength-dependent optical scattering phenomenon.

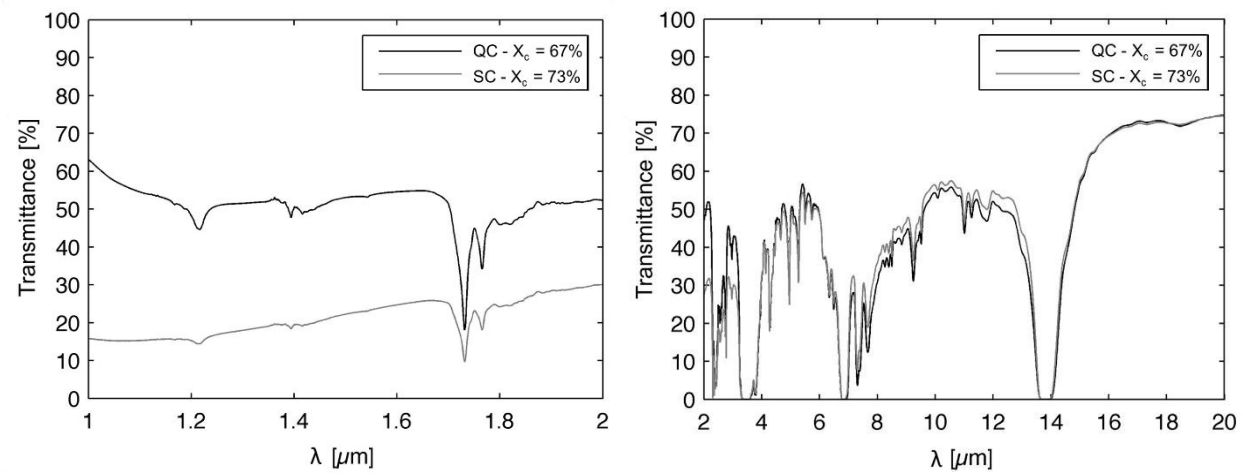

(a) (b)

FIGURE 3.5. $T_\lambda^{i,r}$ measurements in NIR (a) and MIR ranges (b) on the identically thick PE-1 QC and SC samples.

In contrast to the strong coupling between X_c and the transmittance characteristics of PE-1 in NIR range, the $R_\lambda^{i,\cap}$ measurements of the QC and SC samples showed that there is a relatively weak relation between crystallinity and $R_\lambda^{i,\cap}$ in the corresponding range. As displayed in Figure 3.6, a slightly higher $R_\lambda^{i,\cap}$ was obtained in NIR range (a) for the PE-1 SC samples which has the higher X_c whereas, no difference was observed in MIR range (b). It was also observed that $R_\lambda^{i,\cap}$ of both the samples show a decreasing trend with an increase in wavelength over NIR range. In this range, the difference between $R_\lambda^{i,\cap}$ of the PE-1 QC and SC samples is found around 3%.

Considering that the set temperature of a typical halogen IR lamp is around 2400 K (Table 2.1), λ_{max} of the lamp is around 1.2 µm regarding Wien`s Displacement Law (Equation 2.4). As discussed in Chapter 2, 95.6% of the emitted power from such an IR lamp occurs between 0.5 λ_{max} and 5 λ_{max}. As it is seen in the $T_\lambda^{i,r}$ measurements in NIR range (Figure 3.5 (a)), even an increase of 6% in the X_c of PE-1 samples causes a decrease of nearly 50% of the $T_\lambda^{i,r}$ in the spectral range around 1µm, where also this difference may still be considerable up to 3.5 µm. However, the strong effect of crystalline structure on the optical characteristics of PE-1 may be neglected in MIR range, as its effect on the $T_\lambda^{i,r}$ vanishes after 3.5 µm, where also it has no effect on the $R_\lambda^{i,\cap}$ in this range. Therefore, the effect of the crystalline structure on

the transmission characteristics around NIR range may not be neglected in case of building a radiation heat transfer model for IR heating assisted thermoforming processes of semi-crystalline PE.

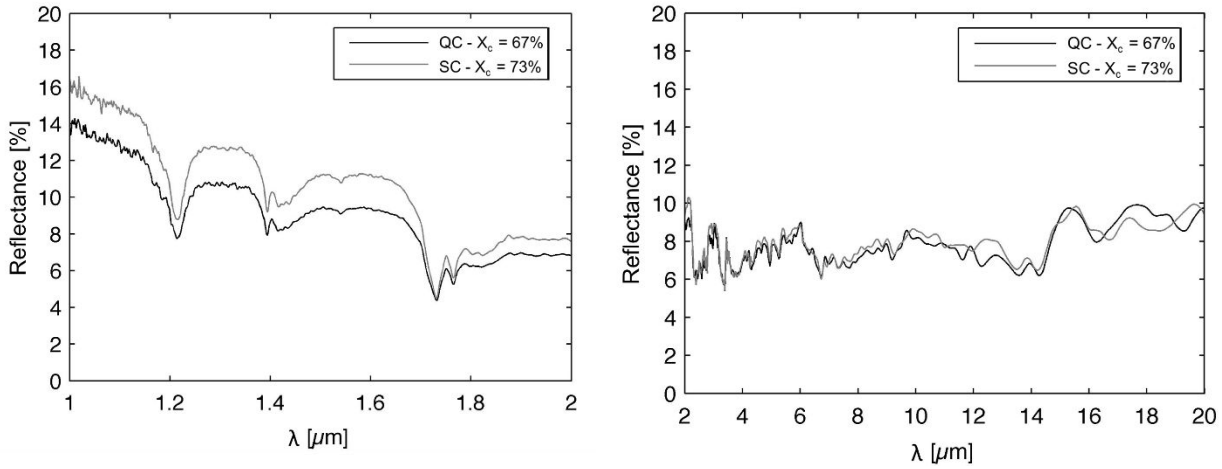

(a) (b)

FIGURE 3.6. $R_\lambda^{i,\cap}$ measurements in NIR (a) and MIR ranges (b) on the identically thick PE-1 QC and SC samples.

Based on the X_c and on the $T_\lambda^{i,r}$ of the first sample group, the analyses between the crystalline structure and the transmission characteristics of PE-1 were extended performing $T_\lambda^{i,r}$ and $T_\lambda^{i,\cap}$ measurements on the second group of samples (Table 3.2). Under the assumptions discussed in Section 3.3.4.1, it was estimated that the difference between both types of transmittance levels represents $\Phi_\lambda^{s\text{-}forward}$. For the sake of brevity in Figure 3.7, only the two samples -the thinnest and thickest ones- are displayed. As illustrated in Figure 3.7 (a), in the spectral range around 1-1.2 µm, the difference between the $T_\lambda^{i,r}$ and $T_\lambda^{i,\cap}$ values of 0.42 mm and 1.82 mm thick samples is around 60% and 40%, respectively. In addition, it can be realized that the estimated $\Phi_\lambda^{s\text{-}forward}$ values obtained from the two samples show difference around 20%. This may be explained by the prolonged optical path of the radiation passing through the medium due to scattering [38], that causes to increase absorption in an equivalent depth, as also stressed in [39]. Therefore, the reduction in the estimated $\Phi_\lambda^{s\text{-}forward}$ in the thicker sample may be attributed to the increase in the amount of the absorbed power in medium (but not to intrinsic absorption of the medium). It should also be noted that the repeated $T_\lambda^{i,r}$ measurements on the same sample may vary around 3% in NIR range whereas such a variation was not observed for the $T_\lambda^{i,\cap}$ measurements. This is not due to measurement accuracy of the FTIR spectrometer, but most likely due to optical scattering – crystalline structure relation which becomes significant at wavelengths shorter than 3.5 µm. Although all the measurements were taken near the center of the film samples, it was clearly observed that the

orientation of the tested samples causes such difference in the $T_\lambda^{i,r}$ levels. In other words, the $T_\lambda^{i,r}$ of the samples varied once they were simply rotated without changing their position in measurement zone. Such a behavior was reported in literature for semi-crystalline PP [23] and PE [40] which is difficult to control for obtaining repeatable measurements. In this study, although the film samples were fabricated under compression to introduce crystalline structure without orientation [40], anisotropy in crystalline phase can still be seen which is induced by radially growth lamellas sandwiched between amorphous phases in the spherulitic superstructures of PE [2]. Hence, once optical scattering becomes significant in PE medium, directional dependency in the scattered light (and thus $T_\lambda^{i,r}$) may vary regarding to either angle of incident light or the optical characteristics of the local crystalline zone where incident light passes through.

In MIR range (Figure 3.7 (b)), the differences between the $T_\lambda^{i,r}$ and $T_\lambda^{i,\cap}$ measurements of the identical samples are around 20% for the wavelengths lower than 3.5 μm where after the difference gradually decreases and becomes identical. This trend is identical to the first analyses revealed in Figure 3.5 (b). The same trend from the first and second step of the analyses are in good agreement with [23,37] where it was concluded that the size of a scatterer in PP semi-crystalline polymer is probably small. Based on the results obtained in the two-step analysis and in [23,37], it may thus be concluded that the identification of scatterer is of prime importance to understand the optical scattering phenomenon in semi-crystalline unfilled thermoplastics adequately.

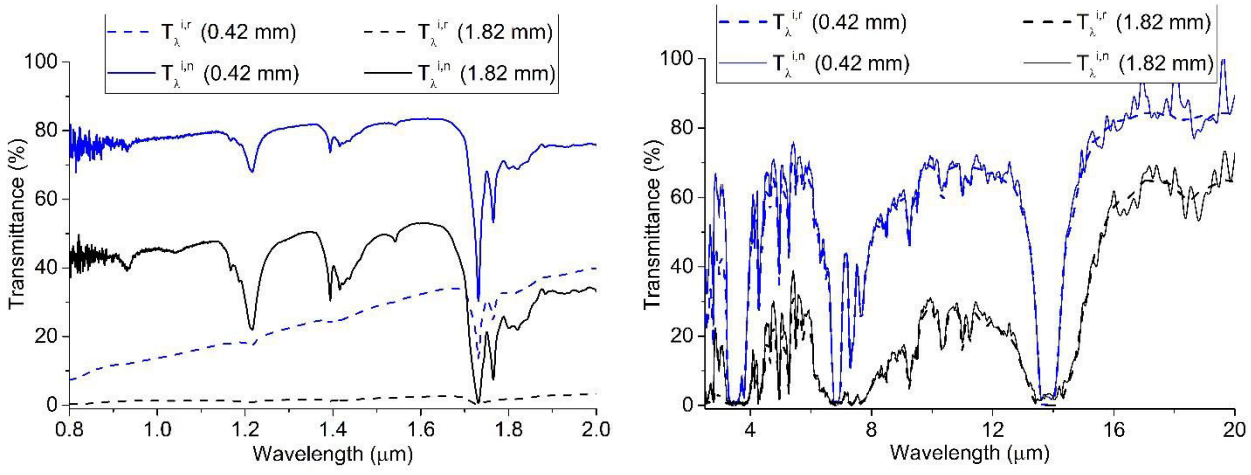

(a) (b)

FIGURE 3.7. Comparison between the $T_\lambda^{i,r}$ and $T_\lambda^{i,\cap}$ measurements of the PE-1 SC samples in NIR (a) and MIR ranges (b).

Both the X_c - $T_\lambda^{i,r}$ relations on the identically thick samples and, the $T_\lambda^{i,r}$ and $T_\lambda^{i,\cap}$ values of the same samples point out that optical scattering in PE medium changes under varying wavelength. The wavelength dependence of optical scattering thus opens a discussion about what type of crystalline formation is responsible for optical scattering in PE medium. Regarding to scattering theory, which was reviewed in Chapter 2, the direction of optical scattering is related to the size of scatterer and the wavelength of propagated radiation inside of the scattering medium (Equation 2.14). This point will be discussed further based on the analyses presented in Section 3.4.3 and 3.4.4.

On the other hand, it should be mentioned in this section that, there are three narrow spectral bands where all tested PE samples show zero transmittance. These three spectral bands are around 3.4, 7.6 and 13.6 µm, as shown in Figure 3.5 (b) and Figure 3.7 (b). It is avoided to call that PE is opaque in these bands because FTIR measurements of the thinner PE samples - down to 20 µm thick - [41–43] showed that PE medium still transmits some fraction of light in these bands. Nevertheless, these bands are known as absorption bands of PE polymer in which the material is close to be opaque. This is induced by its chemical compositions, namely carbon-hydrogen (C-H) bonds [41,44,45]. The absorption bands around 3.4, 7.6 and 13.6 µm are due to: CH_2 stretching [41,46], wagging deformation of CH_2 and twisting deformation CH_3 bonds [44], CH_2 rocking vibration / deformation [41,44,46], respectively. Molecular characteristics of PE and its relation to its absorption behavior will not be discussed further in this thesis. Nevertheless, fundamental understanding on the absorption bands - molecular relations in PE enables to tailor thermal radiation source where a polychromatic or monochromatic radiation source such as lasers, LED or IR emitters can be chosen regarding the process requirements and design demands in various type of thermoforming process. For instance, considering a radiative heating of PE for LTW or ISBM processes, the required temperate field for successful forming process may be different. More specifically, in LTW processes, the absorption of radiation at the interface of heated thermoplastic components could likely be the goal for successful fusion bonding. Whereas, a homogeneous temperature field may be more proper in ISBM processes, to achieve successful blowing process and uniform bottle thickness. Apart from this, in terms of non-invasive temperature measurements, the knowledge about the absorption behavior is of prime importance as the accuracy of IR-thermographic measurements is related to the opaqueness of materials to be monitored. This point will be discussed further in Chapter 5, considering numerical and experimental thermal measurements performed for IR heating of PE, and the related literature.

3.4.2. Time - dependent morphological - optical analyses in polyethylene and secondary crystallization at room temperature

In this analysis, potential evolutions in the PE morphology and its effect on its transmittance characteristics was analyzed. As discussed in Section 3.2, melt-crystallized PE morphology may still form thin or poor crystals at room temperature due to chain mobility above its T_g. The attention here is to be given on the point how such a change in PE morphology may induce a difference in its optical properties. As revealed in the previous section, the crystalline structure of PE may have a significant impact on its optical properties, particularly on its transmission behavior in NIR and VIS range. This point may be critical in terms of building IR radiation models for semi-crystalline PE. Firstly, thermo-optical properties of PE, which is the thermal radiation parameter used in radiation heat transfer model, is defined based on the optical characteristics. Secondly, the spectral range of considerable amount of radiation emitted from a halogen lamp lies in VIS and NIR range. In case there is a change in its optical properties due to evolution in the morphology, it may result in a lack of accuracy in the determined numerical input, and thus radiation absorption predictions.

The time - dependent morphological - optical analyses were performed using 0.25mm thick PE-1 and PE-2 QC samples. For each type of PE polymer, two film samples were fabricated. The fastest cooling adopted in this research, QC, was chosen for the PE-1 and PE-2 samples to hinder the formation of thick lamellae during film manufacturing, which in return may potentially stimulate crystal reorganization or potential lamellae thickening at lower temperatures, down to room temperature.

DSC measurements were done for estimating X_C and l_c distributions of the samples at each time step. For each PE-1 and PE-2 film sample, two DSC measurements were performed at each time step on small pieces cut from the sample film samples. Thus, 4 DSC measurements were done for each PE polymer at each step. The scans were carried out using a heating rate of 10K/min. Similarly, spectroscopic FTIR tests were done for each film sample. Since very small effect of crystalline structure was seen on the reflectance characteristics of PE, only $T_\lambda^{i,r}$ and $T_\lambda^{i,\cap}$ measurements were carried out on each sample at each adopted time step. The $T_\lambda^{i,r}$ measurements were performed separately over VIS, NIR and MIR ranges limited by the spectral resolution of different detectors used in spectrometer. However, due to reflectance characteristics of the infragold-coated integrating sphere [31], $T_\lambda^{i,\cap}$ measurements (Figure 3.3 (b)) could not be performed in VIS range and transmission were only recorded over NIR and MIR ranges. Calorimetric and spectroscopic measurements obtained at very first-time step was performed immediately after quenching the PE film samples. The subsequent measurements were also carried out following tightly the adopted time steps. Thus, the time interval between each DSC and FTIR measurement of each

sample was close to be identical with a time lag limited to +/- 30minutes. Overview of the analyses on the time-dependent morphological-optical characteristics of PE-1 and PE-2, are given in Table 3.3.

Polymer type		**PE-1**		**PE-2**		**Time steps (hrs)**
		No-1	**No-2**	**No-1**	**No-2**	
DSC		2 scans for each film samples at 10K/min				0, 22, 46, 94, 168, 387
FTIR (Spectral range)	$T_\lambda^{i,r}$	0.4 – 20 μm				
	$T_\lambda^{i,\cap}$	0.8 – 20 μm				

TABLE 3.3. Overview of the 0.25 mm thick PE-1 and PE-2 samples used for the time-dependent morphological-optical analyses.

In Figure 3.8, a typical behavior in MIR range obtained from the $T_\lambda^{i,r}$ and $T_\lambda^{i,\cap}$ measurements of the identically thick PE-1 (a) and PE-2 (b) samples is presented. The scattered data seen in the $T_\lambda^{i,\cap}$ measurements between 15 - 20 μm is due to low spectral resolution of the detector which was operated with the integrating sphere. All the four PE-1 and PE-2 samples tested at each time step showed that their $T_\lambda^{i,r}$ and $T_\lambda^{i,\cap}$ in MIR range does not change over time, especially for the wavelengths longer than 3.5 μm. As it can be seen in the figure, all $T_\lambda^{i,r}$ and $T_\lambda^{i,\cap}$ measurements of the samples follow almost identical level of transmittance after 3.5 μm, while somewhat considerable difference is seen below this wavelength. This behavior was found identical to the ones observed in the initial analyses of the crystalline structure – optical properties relation in PE, previously discussed in Section 3.4.1. In addition, $T_\lambda^{i,r}$ and $T_\lambda^{,\cap}$ of each PE-1 and PE-2 sample obtained in MIR range over time showed a difference up to 3%. This slight variation is potentially due to intrafilm thickness variations as scattering effect can be considered negligible. Whereas, in VIS and NIR ranges, the difference between the $T_\lambda^{i,r}$ values of the same samples obtained at different time steps was much more prominent. This greater difference can be attributed to both intrafilm thickness variations and scattering – crystalline structure relation induced by the orientation [23], or position of the sample, as discussed before. In order to minimize this effect seen in VIS and NIR ranges, several $T_\lambda^{i,r}$ measurements were obtained for each PE-1 and PE-2 sample at each time step and, the obtained measurements were averaged. However this effect could not be fully eliminated which resulted no consistent relation between time and the $T_\lambda^{i,r}$ of all the samples in NIR

range. The related $T_\lambda^{i,r}$ results and $T_\lambda^{i,\cap}$ of PE-1 and PE-2 in NIR range are presented in Annex A.2.3 (a) and (b), respectively.

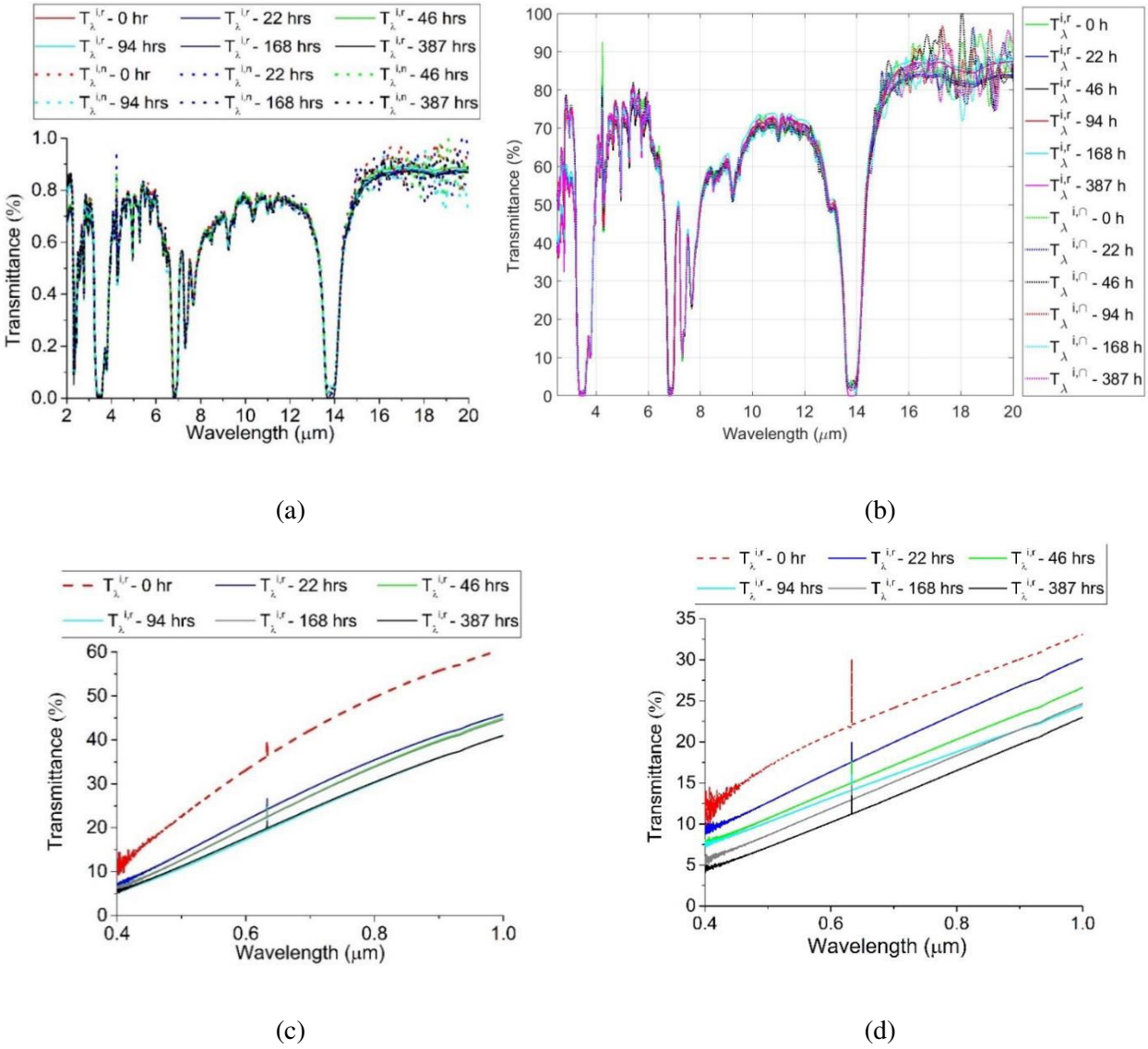

FIGURE 3.8. Time-dependent $T_\lambda^{i,r}$ and $T_\lambda^{i,\cap}$ of PE-1 QC (a) and PE-2 QC (b) in MIR range. And, the $T_\lambda^{i,r}$ of the same PE-1 QC (c) and PE-2 QC (d) samples over time in VIS range.

As shown in Figure 3.8 (c) and (d), time dependency was also analyzed in VIS range including the $T_\lambda^{i,r}$ of both PE-1 and PE-2. After very first measurements performed immediately after quenching (the dashed lines in Figure 3.8 (c) and (d)), the $T_\lambda^{i,r}$ of PE-1 distinctively drops by ~15% where very close $T_\lambda^{i,r}$ was obtained at the following time steps. This drop was also seen in PE-2 while it was less pronounced, which is around ~10%, regarding to more progressive drop up to 46 hrs. In addition to this, the similar trend was also observed in the $T_\lambda^{i,r}$ of the other identically prepared PE-1 and PE-2 samples. Their time-

dependent $T_\lambda^{i,r}$ measurements can be found in Annex A.2.4 (a) and (b). Considering all the tested PE-1 and PE-2 samples, the consistency was found about this decreasing trend up to 46 hrs. After this time limit, a stabilized level of $T_\lambda^{i,r}$ may be accepted where the measurements of each PE sample at the further time steps showed very similar level of transmittance. As stressed above, although several $T_\lambda^{i,r}$ measurements obtained at each time step and averaged, the effect of orientation on the optical scattering - and thus on the $T_\lambda^{i,r}$ values - may not be completely eliminated. Consequently, small uncertainties in the $T_\lambda^{i,r}$ obtained in VIS range may be responsible of such slight variations seen at longer times.

In Figure 3.9, typical melting endotherm of the PE-1 (a) and PE-2 (b) samples are seen. As it is seen in Figure 3.9 (b), after the very first DSC measurement, a small inflection point was appeared around 40°C in the melting endotherm of PE-2 which also became slightly more prominent over time. As reviewed in Section 3.2, this behavior can be attributed to secondary crystallization in PE that likely occurs at room temperature. Such evolution over time could be potentially seen in the PE-1 samples while it is probably less prominent than the one seen in the PE-2 samples. As the heat flow of the main peak by DSC (in milliwatt (mW) in the figure below) is much higher than the zone of inflection, potential time-dependent changes in the crystalline phase of PE over time are not clearly seen. Hence, the potential evolution in PE morphology was estimated based on the l_c distributions. Using the DSC measurements of each PE-1 and PE-2 sample at each time step, time-dependent behavior in their l_c distributions was determined.

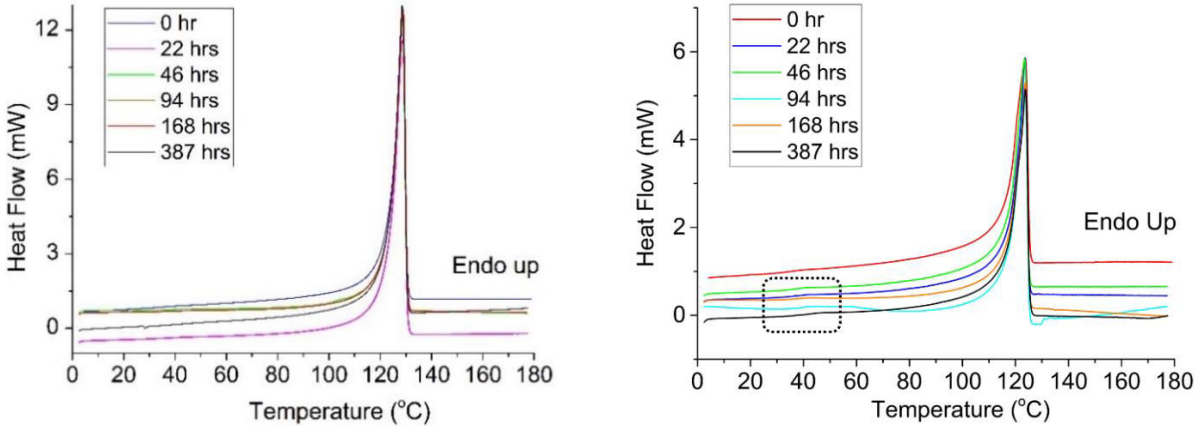

(a) (b)

FIGURE 3.9. Melting endotherm of the PE-1 QC (a) and PE-2 QC samples (b) obtained via DSC measurements at a heating rate of 10 K/min.

In Figure 3.10, the time-dependent evolution in the l_c distributions of PE-1 QC (a) and PE-2 QC (b) are displayed. As seen in the in figure, both the PE-1 and PE-2 polymer show bimodal distributions of lamellar morphology, where the two populations -or the peaks- of l_c are more pronounced in PE-2. The position of the 1st population is very similar for both type of PE, which is around 2 - 4 nm, while the 2nd population of PE-1 shows broader size distribution which is centered around 16 - 18 nm. The calorimetric analyses showed that the 1st population of the lamellar crystals of both the PE-1 and PE-2 become progressively more prominent over time indicating an increase in the normalized mass fraction of the thinner crystals. In other words, the mass fraction of the 2 - 4 nm thick lamellar crystals to the total crystalline phase increases over time in both type of PE. As it is seen in Figure 3.10 (b), the 1st peak of PE-2 showed a monotonically increasing trend with time while this was not fully clear in the 1st peak of PE-1. Nevertheless, increasing trend was prominent over time in the 1st population of thin lamellar crystals of both the PE-1 and PE-2 polymers. As discussed in Section 3.2, this may be plausible since the amorphous region that lies in the interlamellar zones may form into poorly ordered thin crystals due to limited chain mobility in PE at room temperature. Similar study was performed by Sella [47], where a branched PE was quenched -196°C from melt and analyzed over time. Time-dependent evolution in the long period of PE was analyzed up to 400 hrs at room temperature. Their analyses revealed that recrystallization occurs in PE at room temperature.

Apart from the time-dependent l_c distribution predictions, X_c of PE-1 and PE-2 was estimated for each time step using Equation 3.1. However, no consistent behavior over time was observed in the X_c values of all the tested samples. It was observed that X_c of PE-1 and PE-2 remained stable around 67% and 48% respectively, with difference around +/-1% over time. It is avoided here to name such fluctuation as margin of error as it is not known if this is only due to measurement error, or to a change in X_c over time. Regarding to theory, formation of thin lamellar crystals is supposed to not inducing a great increase in X_c. Similarly, it was stressed in [2] that X_c of PE is unlikely to increase by more than 2-3% at room temperature. Therefore, no conclusion can be given about any time dependence in the X_c of both type of PE tested here. Interestingly, although it was found that branched PE-2 has a much lower X_c -and also thinner l_c populations- than PE-1, its $T_\lambda^{i,r}$ was also lower. This may be explained with the directional dependency of optical scattered light in relation to scatterer size, at which forward scattered at very narrow-angles may be detected by the detector of the spectrometer, and potentially result higher level of $T_\lambda^{i,r}$. This point will be discussed further in the following sections of this chapter.

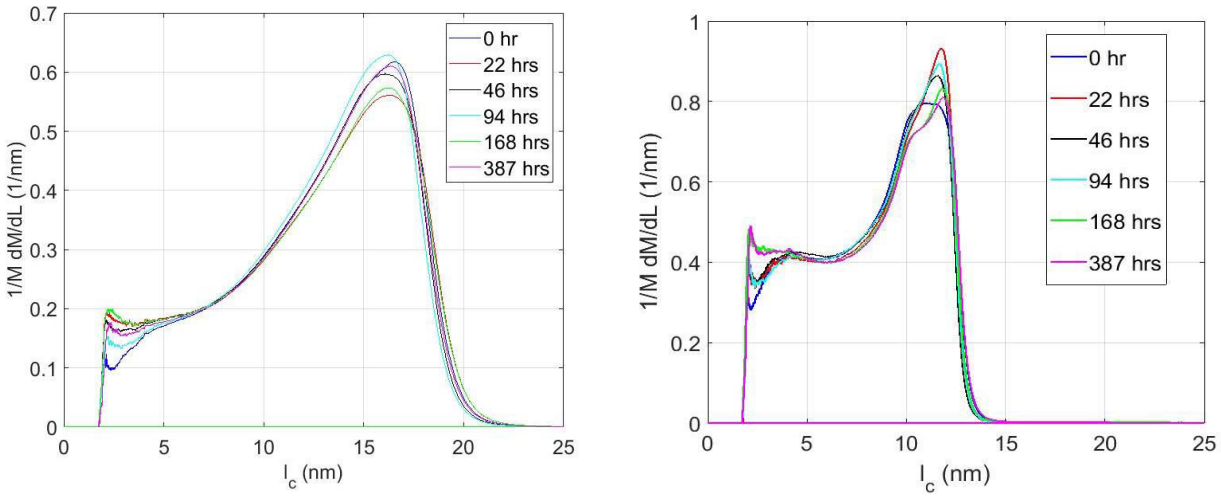

(a) (b)

FIGURE 3.10. Time-dependent l_c distributions of PE-1 QC (a) and PE-2 QC (b) samples.

Regarding to calorimetric analyses, significant difference was not observed in l_c distributions over time, except the evolution in thin lamellar crystals that lie in the 1st population of l_c distributions in both PE-1 and PE-2. The spectroscopic analyses over time showed that a consistent decreasing trend in the $T_\lambda^{i,r}$ of all the PE-1 and PE-2 samples in VIS range. The inconsistent behavior was seen in NIR range, which is probably induced by uncertainties in the $T_\lambda^{i,r}$ measurements affected by orientation – optical scattering relations, as explained before. Nevertheless, it can be concluded that time-dependent evolution in the lamellar morphology of PE becomes somewhat effective for reducing the $T_\lambda^{i,r}$ of PE up to 46 hrs. In relation to this fact, one critical point discussed here may be crucial for thermoforming process of PE: waiting up to 2 days may provide relatively stable condition in its lamellar morphology and optical properties. Therefore, the characterization of thermo-optical properties of PE may be relatively more accurate in case of building IR heating models for radiation absorption predictions. In addition, preforms (e.g injection molded preforms used for ISBM processes) may be waited up to this time limit before IR heating. In this thesis, the analyses from this point on, including all the optical analyses on the PE-1 and PE-2 were done after waiting 48 hours.

3.4.3. Morphology-dependent optical scattering in polyethylene medium

3.4.3.1. Spectroscopic analyses and estimation of morphology-dependent total scattered light

In this section, the effect of crystalline morphology on the optical scattering behavior in PE medium was analyzed considering calorimetric, microscopic and spectroscopic analyses. In order to introduce different morphological state in the PE media to be analyzed, both the PE-1 and PE-2 polymer were

prepared under two different cooling, QC and AN (Table 3.1). As reviewed in Chapter 2, there is an ambiguity in literature considering the size of scatterer inducing the optically heterogeneous behavior of PE medium. The analyses so far revealed in literature indicate that the scatterer size and the related crystallite formations are mainly spherulites, where also lamellar substructures are pronounced. Hence, in the analyses presented here, the crystalline phase of PE was investigated considering both lamellar crystals and spherulitic superstructures. Lamellar morphology of PE was estimated performing DSC measurements, where also its crystalline phase was examined under SEM microscope for the identification of spherulitic formations. Before the microscopic examinations, permanganic etching was applied to all the samples following the procedure explained in Section 3.3.3.1. The optical scattering in PE medium was analyzed here in an indirect way, by measuring $T_\lambda^{i,r}$ and $T_\lambda^{i,\cap}$ and $R_\lambda^{i,\cap}$ of the PE samples having different morphologies. Hence, the morphology dependence of the total forward and back scattered light ($\Phi_\lambda^{s\text{-}forward}$ and $\Phi_\lambda^{s\text{-}back}$, respectively) in PE medium was estimated without measuring its spatial distribution. All the spectroscopic measurements were done using Perkin Elmer 950 spectrometer which has an operating spectral range of 0.25 - 2.5 μm. Thanks to the integrating sphere made of spectralon, the $R_\lambda^{i,\cap}$ tests were performed also in VIS range [31], which was a limitation in the previous analyses that were performed using infragold-coated integrating sphere. The overview of all the analyzed PE-1 and PE-2 samples and further details related to the spectroscopic, microscopic and calorimetric analyses are given in Table 3.4.

Polymer type		**PE-1**		**PE-2**	
		QC	**AN**	**QC**	**AN**
Sample thicknesses (mm)		0.25 and 0.75		0.25	
DSC		2 scans for each film samples at 20K/min			
FTIR (Spectral range)	$T_\lambda^{i,r}$	0.4 – 0.9 μm			
	$T_\lambda^{i,\cap}$	0.25 – 2.5 μm			
	$R_\lambda^{i,\cap}$	0.25 – 2.5 μm			
Electron microscopy (SEM)		Examinations at 10keV			

TABLE 3.4. Overview of the PE-1 and PE-2 samples used for microscopic - calorimetric - spectroscopic analyses for bridging PE morphology to its optical scattering behavior.

In Figure 3.11, the $T_\lambda^{i,\cap}$ (a), $R_\lambda^{i,\cap}$ (b) and $T_\lambda^{i,r}$ (c) of all the tested PE-1 and PE-2 samples are displayed. As it is seen in Figure 3.11 (a), the $T_\lambda^{i,\cap}$ of all the 0.25 mm thick QC and AN samples are very close at the wavelengths longer than 1 μm while, their level of transmittance becomes somewhat different in VIS range. As shown in Figure 3.11 (b), in the same spectral range, the $R_\lambda^{i,\cap}$ of the same samples show an inverse trend to the one observed in their $T_\lambda^{i,\cap}$. All the measured $R_\lambda^{i,\cap}$ increase at shorter wavelengths and reach their maximum values around 0.4 μm. Interestingly, the $T_\lambda^{i,\cap}$ and $R_\lambda^{i,\cap}$ of each sample change with the same ratio (e.g: ~6 % change seen in the $T_\lambda^{i,\cap}$ and $R_\lambda^{i,\cap}$ of 0.75 thick PE-1, respectively) in the corresponding range. Considering that PE has semi-transparent medium in VIS and NIR ranges, the measured $R_\lambda^{i,\cap}$ is likely the combination of both $\Phi_\lambda^{s\text{-}back}$ that is reflected back from internal heterogeneous medium and, the reflection from surface. As discussed in Chapter 2, the latter one is strongly related to surface irregularities, or surface roughness which can also be induced by the crystalline structure of PE. However, regarding all the tested PE samples presented in Figure 3.11 (a) and (b), the change in their $T_\lambda^{i,\cap}$ and $R_\lambda^{i,\cap}$ may be explained by the increased amount of $\Phi_\lambda^{s\text{-}back}$ at shorter wavelengths, but not to the reflections from surface. A closer look in Figure 3.11 (b) points out that the $R_\lambda^{i,\cap}$ of all the PE-1 and PE-2 samples is almost identical for the wavelengths longer than 1.7 μm, indicating negligible effect of crystalline structure and sample thickness on the measurements. Therefore, the $R_\lambda^{i,\cap}$ values of all the samples obtained in this spectral range can be considered as the reflected light flux only from the surface of the samples, which is therefore morphology and thickness-independent. Consequently, it would be plausible that $\Phi_\lambda^{s\text{-}back}$ increases due to both morphological and thickness differences, for the wavelengths lower than 1.7 μm. This point was analyzed further measuring the $R_\lambda^{i,\cap}$ of 2.2 mm thick PE-1 and PE-2 samples (Annex A.2.5). Their $R_\lambda^{i,\cap}$ values support the point about increasing trend in $\Phi_\lambda^{s\text{-}back}$ with morphology and thickness. Apart from this, it was observed that the $T_\lambda^{i,\cap}$ of all the PE-1 AN samples slightly lower (and slightly higher for $R_\lambda^{i,\cap}$) than the PE-1 QC indicating stronger $\Phi_\lambda^{s\text{-}back}$. Whereas PE-2 QC and AN samples show inverse behavior until 0.6 μm which was followed by a dramatic increase in the $R_\lambda^{i,\cap}$ of PE-2 AN below 0.6 μm. This behavior was different from all the other tested samples.

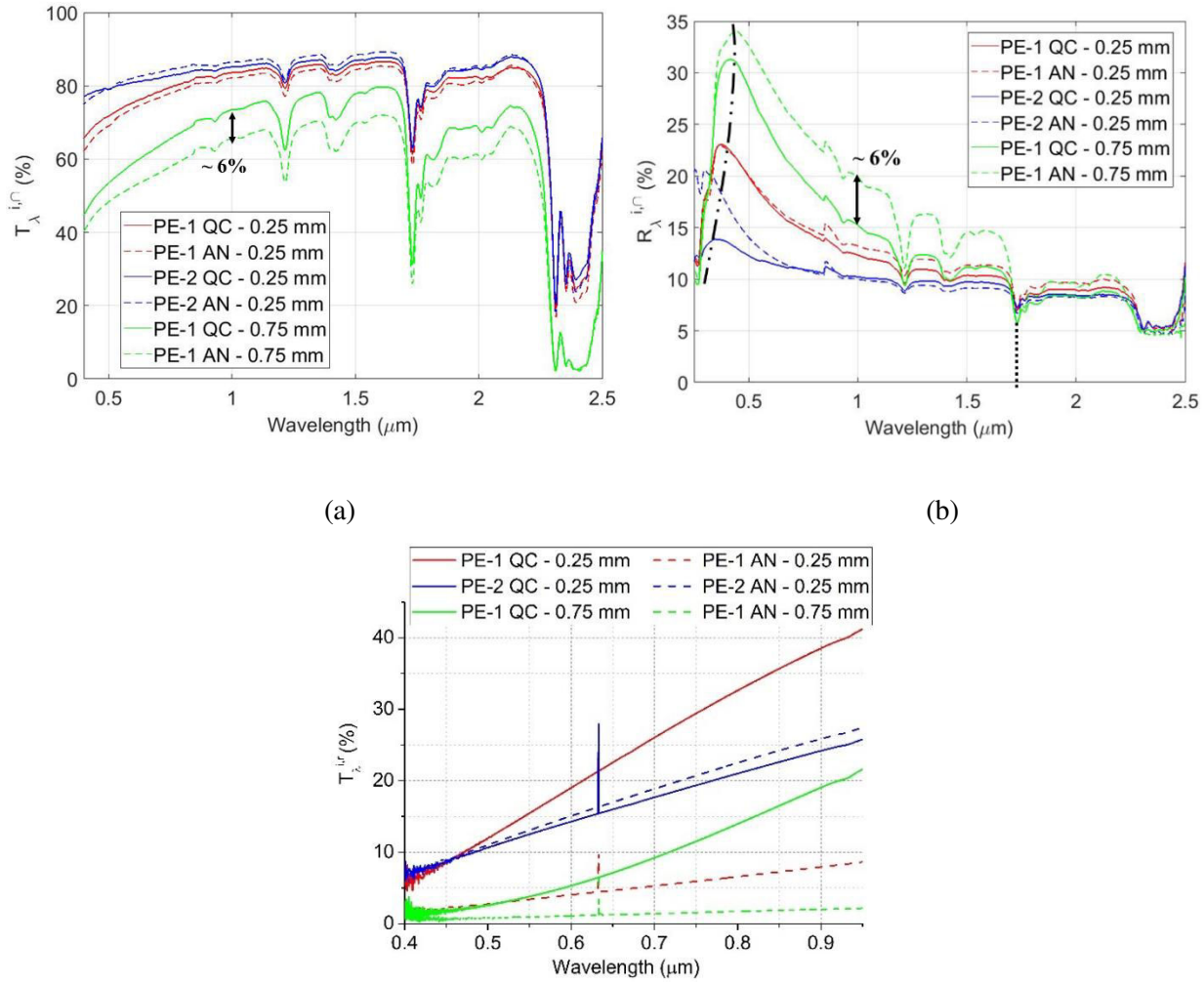

FIGURE 3.11. $T_\lambda^{i,\cap}$ (a), $R_\lambda^{i,\cap}$ (b) and $T_\lambda^{i,r}$ (c) of the analyzed PE-1 and PE-2 QC / AN samples.

In Figure 3.11 (c) above, $T_\lambda^{i,r}$ of the same PE-1 and PE-2 samples are presented. It should be noted here that several transmittance measurements were done simply rotating the samples in the measurement zone and the measured values were averaged to minimize the effect of orientation on the directly transmitted light. As it is seen in the figure above, $T_\lambda^{i,r}$ dramatically reduces when identically thick PE-1 samples are prepared under annealing (e.g: drop in the $T_\lambda^{i,r}$ by ~30 % at 1 μm). Again, conversely, such a drop was not observed between PE-2 QC and AN where they have the same transmittance. Beyond this fact, as discussed in detail in Section 3.3.4.1, the difference between the $T_\lambda^{i,\cap}$ and $T_\lambda^{i,r}$ of identical samples enable to estimate $\Phi_\lambda^{s\text{-forward}}$. As presented above in Figure 3.11 (a) and (c), the $T_\lambda^{i,r}$ and $T_\lambda^{i,\cap}$ measurements of obtained from the same samples are clearly evident for strong forward scattering in both the type of PE. Whereas, as observed in Figure 3.11(b), backscattering also becomes significant at

shorter wavelengths in VIS range. Before analyzing the ratio between the forward and backscattered light, and thus its spatial distributions, morphological characteristics of differently prepared PE-1 and PE-2 specimens are required to be understood. Thanks to this, the underlying reason for having wavelength-dependent trends in both their $T_\lambda^{i,\cap}$ and $R_\lambda^{i,\cap}$ can be highlighted as a first step.

As aforementioned, calorimetric analyses of each analyzed PE-1 and PE-2 sample were done to determine their X_c and l_c distributions. Two DSC experiments were done for each sample, which gave a basic insight about the repeatability of the calculated values. In Table 3.5, the mean calculated X_c of each sample are presented. The margin of error for all the calculated X_c was found again around +/-1%.

Polymer type	**Cooling condition and calculated X_c (%)**	
	QC	**AN**
PE-1 0.25 mm	67%	76%
PE-2 0.25 mm	51%	58%
PE-1 0.75 mm	69%	75%

TABLE 3.5. X_c of all the analyzed PE-1 and PE-2 QC / AN samples obtained via DSC.

Regarding to the optical properties analyzed in Figure 3.11 and the X_c given above, it can be clearly seen there is no direct relation between the optical scattering in PE and the amount of crystals, which is parametrized here as X_c. For instance, although 0.25 thick PE-1 QC sample has higher crystallinity than the identically thick PE-2 QC by 16%, its $T_\lambda^{i,r}$ is considerably higher than the one obtained in PE-2 QC medium indicating higher amount of light is directly transmitted in PE-1 QC medium (Figure 3.11 (c)). Similarly, no significant effect of X_c is seen on their $T_\lambda^{i,\cap}$, even though their X_c is distinctively different. It may therefore be concluded that the optical scattering behavior becomes stronger or weaker inside of PE medium not due to the amount of crystals -or crystallinity level- but, the amount or number of equivalent scatterer, which can eventually be identified as scatterer in semi-crystalline PE medium. In other words, as known from light scattering theories, the spatial distribution of optical scattering changes regarding the size of scatterer and the spectral characteristics of radiation propagated through a medium. The main question here is: what is the size and entity that causes optical scattering and changes its directional behavior in PE medium? As aforementioned, this point is analyzed here considering both the lamellar morphology and spherulitic superstructures of PE, and its relation to the optical scattering behavior estimated based on the spectroscopic analyses shown above.

In Figure 3.12, lamellar crystal size distribution of all the 0.25 mm thick PE-1 (a), PE-2 (b), and 0.75 mm thick PE-1 (c) samples are presented. For the sake of clarity in the illustration of cooling condition related lamellar morphology, the analyzed PE-1 and PE-2 samples are presented into three groups in the figure below. The crystal size distributions presented here refer to the mass fraction of lamellar crystals in certain thicknesses which was normalized to the total mass of crystalline phase -M-, appearing on y axis. In other words, weight distribution of the most probable l_c are represented in terms of crystalline mass. Therefore, the estimated crystal size distribution does not provide any insight about the number of lamellar crystals existed in whole the crystalline phase, which is rather ambiguous to determine due to dimensional uncertainties seen in different lamellar substructures, as schematically shown in Figure 3.1.

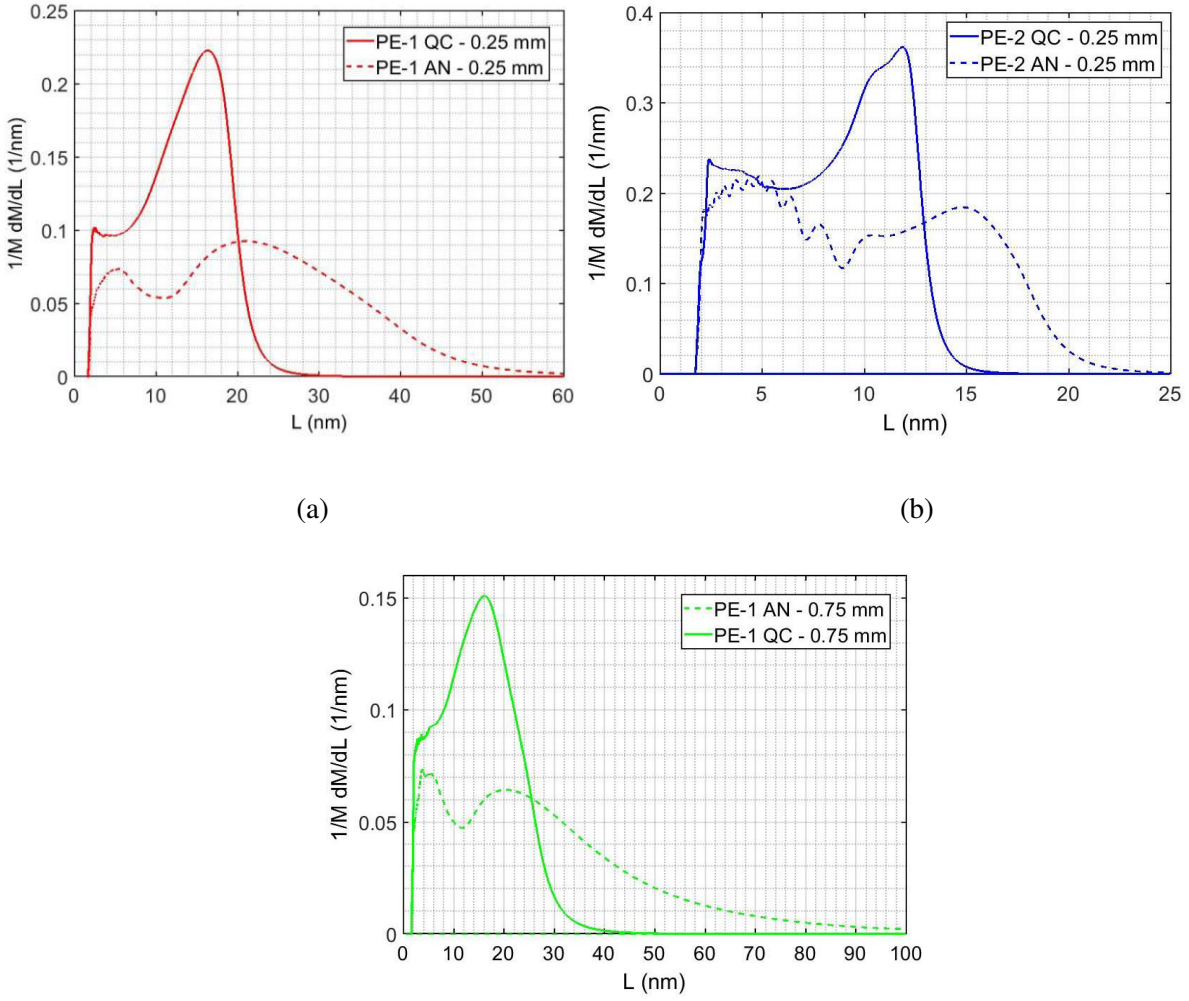

(a) (b)

(c)

FIGURE 3.12. l_c distributions of 0.25 mm thick PE-1 (a), PE-2 (b), and 0.75mm thick PE-1 (c) samples prepared under QC / AN conditions.

Different points may be raised regarding to the lamellar crystal size distributions and its relation with the cooling condition of the melt-crystallized samples presented above. First of all, the l_c distribution range of PE-1 QC and AN samples are around 3-30 nm and 3-100 nm, respectively, while the lamellar morphology of PE-2 QC and AN consists of much thinner lamellar crystals ranging between 5-15 nm and 5-25 nm, respectively. The l_c distribution ranges of both PE-1 and PE-2 presented here are in close agreement with the linear and branched PE, as reviewed in Chapter 2 (Table 2.3). In addition to this point, annealing of PE-1 and PE-2 introduces broader l_c distributions. Such a behavior was reported extensively for linear [4,15,19,48] and branched PE [21,49] in literature. The reason behind broadening in lamellar crystal size populations was discussed by Wlochowicz et al.[48]. This was related to the considerable number of polymer chains that pass through multiple number of lamellar stack and formation of extended-chain crystals. Similarly, Stack et al [19] reported that l_c distributions likely becomes broader at longer crystallization times at high temperatures, indicating more extended form of lamellar crystals and thus thicker crystal size. Secondly, the l_c distribution of all the PE-1 and PE-2 samples reveals that the 2nd population of their thicker lamellar crystals shift to greater ranges indicating the thickening of lamellar crystals. Conversely, except the PE-2 AN samples, the 1st population -which represent the thinner crystals- is almost not affected by annealing process under stepwise cooling. These trend were also found in close agreement with QC and AN samples of linear HDPE analyzed in [15] at which the 1st population of HDPE was unchanged with annealing process and were centered around 5-7nm. Whereas the 2nd population of HDPE shifted from around 14nm to 22nm.

As also seen in the figure above, the 1st populations of all PE-1 and PE-2 samples are centered around 4-6nm. In addition to this, only the 1st population of PE-2 AN exhibits several small peaks due to the stepwise cooling applied to this sample down to 40°C (Table 3.1). Similarly, small distinctive peaks were observed in [50] during the thermal fractionation of PE applied down to 62°C. As discussed in Section 3.2, the capacity of chain folding length in semi-crystalline polymers is related to branching degree, also the time and temperature of crystallization. Hence, it is plausible to see more pronounced effect of annealing on the lamellar morphology of branched PE-2. Because, it facilitates to reorganize linear polymer chains in certain lengths existed in the branched polymer chain structure of PE-2. Consequently, each fluctuation in the 1st population of PE-2 corresponds to particular length of each linear portion which is limited by the branched chains. Apart from this, it should also be mentioned here that bimodal population distributions are seen whether linear or branched PE is prepared under QC or AN condition. This point was analyzed in [15] where it was pointed out that two typical lamellar populations are the results of crystallization at relatively high and low temperatures so that thermal gradient occurs on cooling from melt to the room temperature. Therefore, it likely happens that the 1st population of thin crystals are due to secondary crystallization which potentially continues for PE down to room

temperature. Similar point was stressed in [51] and [21] for branched and linear PE, pointing out that small peak of the 1st populations probably arises from secondary crystallizations when thin lamellae structures are created.

(a)

(b)

(c)

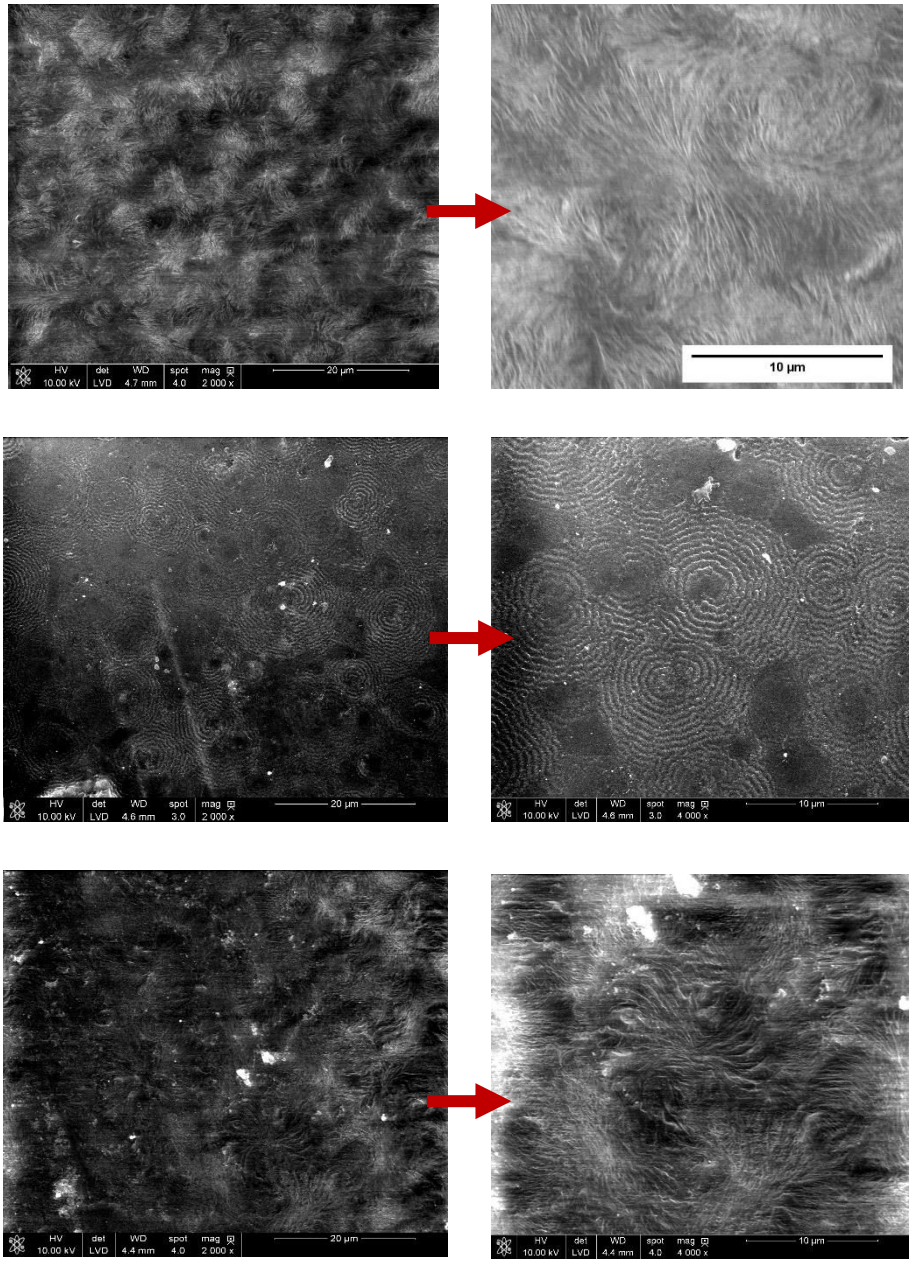

FIGURE 3.13. Spherulitic crystalline structures of 0.25 mm thick PE-1 QC (a), PE-2 QC (b) and PE-2 AN samples obtained via SEM examinations.

In Figure 3.13, the SEM micrographs of identically thick PE-1 QC (a), PE-2 QC (b) and AN (c) are displayed. As seen in Figure 3.13 (a) and (c), the crystalline phase of PE-1 QC and PE-2 AN shows

densely packed lamellar morphology, where also dark zones represent the amorphous interlamellar regions [6]. Due to the densely packed crystallite formations seen in PE-1 QC and PE-2 AN, spherulites were likely impinged to each other which eventually resulted some ambiguity about their sizes. Consequently, clear spherulitic morphology was not distinctive in the whole part of the examined region in these samples. This hypothesis was confirmed examining multiple regions on their surface of interest. It was observed that the center of nucleation and radius of spherulites were sometimes quite clear even though for the case that the radial border of their spherulitic superstructures was not clearly distinguished. The micrographs shown with rightward-directed arrows in Figure 3.13 (a), (b) and (c), illustrate typical spherulites that were clearly observed in several zones analyzed in 0.25 mm thick PE-1 QC, PE-2 QC and AN samples. In these micrographs, the radial arrangement of spherulites and their lamellae growth in b-axis towards to the radius of the spherulites are distinctively seen. In Figure 3.13 (a) and (c), the curved lamellae -so called S-shaped lamellae in literature [5,27,28]- arrangements from the nucleus towards to edge of spherulites are seen. In contrast to this, PE-2 QC (Figure 3.13 (b)) shows spherulites which typically form as concentric rings, known as banded spherulites [52]. As widely reported in literature [2,5,52], this is likely due to twisting in the c-axis of lamellar stacks which laterally grown in b-axis (along the radius of spherulites), and thus show an optical texture consisting of periodic concentric rings under microscopic examinations [6,53]. Similar spherulitic structure observed here was also reported in literature for permanganic-etched both linear and branched PE [28,29]. In Figure 3.14 below, typical spherulitic structure of linear (a) and branched PE (b) obtained in other studies [28,29] are presented. The high similarity between the crystalline phase texture of the samples studied here and the ones reported in literature is seen. Although, spherulitic structures 0.25 mm thick PE-1 QC, PE-2 QC and AN samples were clearly visualized and compared to literature, it was not sufficient for performing quantitative analysis to determine an averaged size of spherulites due to the impinging effect, especially seen for the annealed samples. In addition, no clear vision of spherulitic texture could be obtained for the 0.25 mm thick PE-1 AN and 0.75mm thick PE-1 QC and AN samples, where also densely packed lamellar morphology was usually observed in their micrographs. Nevertheless, based on the clearly visualized spherulitic superstructures of differently prepared PE-1 and PE-2 samples, one point can be clearly concluded: annealing or quenching of PE-1 and PE-2 samples may not cause significant change in their spherulites sizes, whereas lamellar morphology may be quite different. In addition to this, as shown in Figure 3.13, the identically thick PE-1 QC, PE-2 QC and AN samples also shows spherulites in very similar, whose diameters was found around 10 μm.

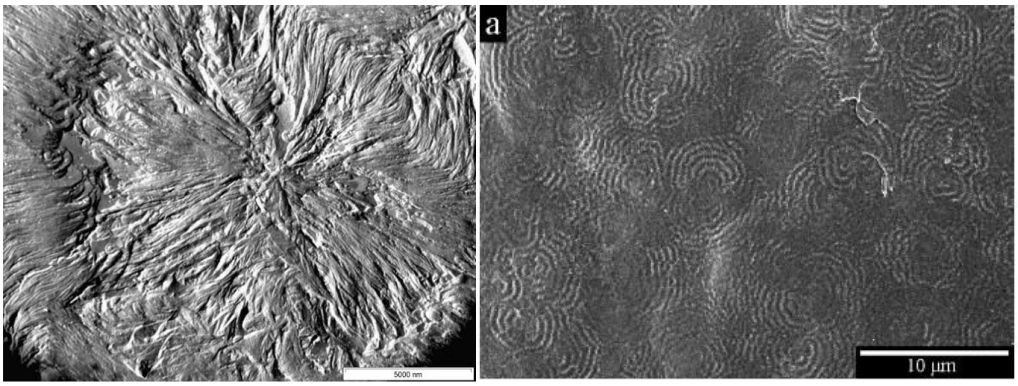

(a) (b)

FIGURE 3.14. Electron micrograph of similar spherulitic crystalline structure of permanganic-etched linear PE (a) [28] and branched (b) [29] LDPE.

Based on the characteristics of lamellar crystals and spherulite superstructures of PE-1 and PE-2 polymers analyzed here, several points can be concluded on the morphology-dependent optical scattering in PE medium. First of all, it can be stated that the change in l_c distribution evolutions in PE causes a significant effect on the optical scattering behavior in VIS and NIR ranges, while the effect of spherulites is rather ambiguous. As shown in Figure 3.11, the difference in the $T_\lambda^{i,\cap}$, $R_\lambda^{i,\cap}$ and $T_\lambda^{i,r}$ of the identically thick PE-1 and PE-2 samples becomes distinctive at shorter wavelengths. The microscopic examinations clearly revealed that the diameter of spherulites in 0.25 mm thick PE-1 AN, PE-2 QC and AN samples were very close to each other, which are around 10 μm. However, their lamellar morphology was found significantly different, which was analyzed through their l_c distributions (Figure 3.12) and qualitatively observed in the SEM micrographs, as suggested in [6,13]. Spherulite structures - l_c distributions - optical scattering relations in PE were also analyzed in [40] and, a similar remark was pointed out on the significant role of lamellar morphology on the optical scattering behavior in PE medium. Nevertheless, it should be mentioned that further analyses performed with significantly different spherulitic structures may be required to provide further evidence about the negligible or significant role of spherulites on optical scattering in PE.

At a closer look, further explanations can be given on the directional dependence of optical scattering and, its potential relation to lamellar morphology of PE: Focusing again on the l_c distributions - spectroscopic analyses of 0.25 mm thick PE-1 and PE-2, it can be seen that thickening of lamellar crystals due to annealing (Figure 3.12 (a) and (c)) was significant in PE-1 samples, where also a significant drop was seen in their $T_\lambda^{i,r}$ (Figure 3.11 (c)). Conversely, the shift in the l_c distributions due to annealing was much lower for PE-2, while their $T_\lambda^{i,r}$ surprisingly showed a slight increase. The $T_\lambda^{i,\cap}$ of these identically thick PE-1 and PE-2 samples also showed similar downward and upward trends, respectively. However it

was in much less pronounced manner in comparison to the change in their $T_\lambda^{i,r}$. In addition to this, in comparison to 0.25 mm thick PE-1, annealing caused very similar evolutions in the lamellar morphology and transmittance characteristics of 0.75mm thick PE-1. Summary of these observations indicate that thickening of lamellar crystals of PE potentially causes broadening in the forward scattered light and thus reduces Φ_λ^t. Whereas, the effect of annealing is likely much smaller on backscattering, which can be correlated to the very small difference seen between the $T_\lambda^{i,\cap}$ of all the 0.25 mm thick AN and QC samples. Beyond this fact, it was interestingly found there is an inverse relation between the range of the l_c distributions and the wavelength at which maximum value of $R_\lambda^{i,\cap}$ was observed (dashed line in Figure 3.11 (b)). As discussed before, the difference seen in the $T_\lambda^{i,\cap}$ and $R_\lambda^{i,\cap}$ values of PE-1 and PE-2 samples at shorter wavelengths can be attributed to the change in $\Phi_\lambda^{s\text{-}back}$. Considering the general decreasing trend in the l_c distribution range of all the tested samples (e.g: the greatest and smallest crystal thickness ranges are seen in 0.75 mm thick PE-1 AN and 0.25 thick PE-2 QC, respectively), the increase in the $R_\lambda^{i,\cap}$, and thus potential amount of $\Phi_\lambda^{s\text{-}back}$, at lower wavelengths may be indicative for media with relatively smaller scatterer size. This point will be discussed further in the following section, focusing on the spatial distribution of scattering in PE medium and its relation to the scattering theory of spherical particles.

3.4.3.2. Morphology-dependent spatial distribution of light scattering and MALS Tests

The PE-1 and PE-2 QC / AN samples analyzed in the spectroscopic- microscopic - calorimetric analyses (Table 3.4) were also characterized with MALS technique. Thus, the analysis of morphology-dependence in the total amount of both forward and back scattered light is thus extended further considering its spatial distributions. As presented in Section 3.3.4.2, the MALS tests were carried out using a scatterometer equipped with a collimated laser beam at 632.8 nm. Since a morphology-dependent dramatic change in the optical properties of PE was seen in VIS range, the MALS tests provide further understanding about identifying the equivalent size of scatterer in PE medium and its effect on the optical scattering behavior.

In Figure 3.15, the spatial distribution of light scattering through the medium of 0.25 mm thick PE-1 (a), PE-2 (b), and 0.75 mm thick PE-2 (c) are displayed in polar angles. The scattering profiles are given in the figure below in terms of normalized BSDF. As seen in the figure, all the PE-1 and PE-2 samples show broader backscattering where also a forward scattering is seen at very narrow angles, which was appeared as a line in the figure below. However, due to the high scattering at narrow angles, it is difficult to visualize in this figure the morphology dependence of angular scattered light intensity in PE.

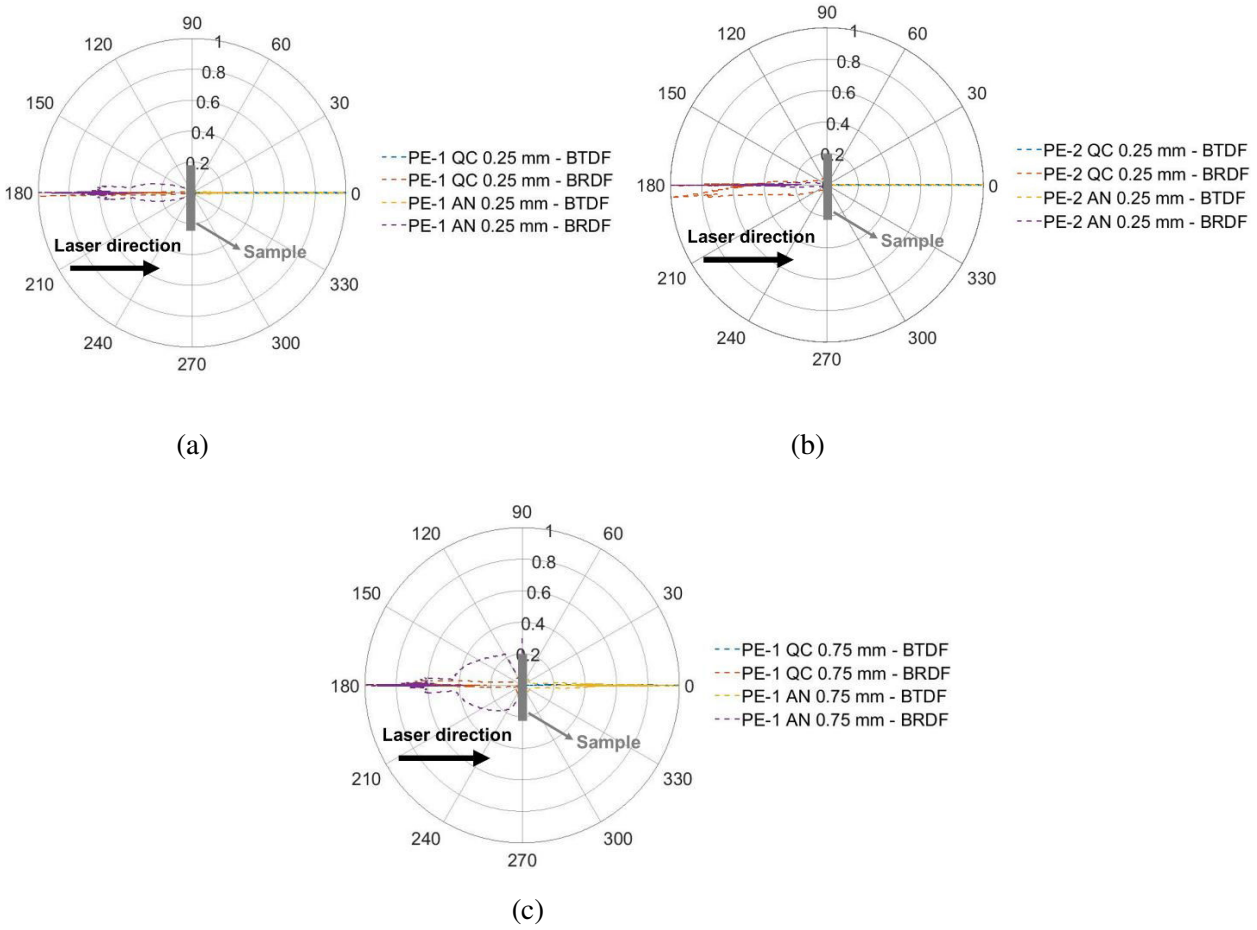

FIGURE 3.15. Polar angular distribution of forward and back scattered light in 0.25 mm thick PE-1 (a), PE-2 (b), and 0.75 mm thick PE-1 (c) media at 632.8 nm.

The representation of scattering distribution at polar angles may be useful in terms of adopting an inverse analysis to identify the size of equivalent scatterer. In other words, following an inverse methodology, a theoretically calculated ϕ_λ can be fitted to the experimentally obtained angular distribution of scattered light. Thus, an equivalent spherical scatterer size can be identified. This point opens further discussions in terms of modeling optical scattering in PE medium including scatterer size and shape, whereas this is out of the scope of this thesis.

In order to analyze the morphology dependence on both the scattered light intensity and its angular distributions, the BSDF measurements presented Figure 3.15 was reproduced, and displayed in Figure 3.16. It should be noted here that almost symmetric angular distributions were observed at zero angle including each BRDF and BTDF measurements of each sample. The zero angle corresponds here to the surface normal of the samples (which is 90º in each RDF and BTDF measurement). Therefore, the BRDF and BTDF results shown in Figure 3.16 represents one-half of each BRDF and BTDF, that were chosen

between 0° - 90° (it is schematically shown at the top right of the figure). The full angular distribution of the measured BSDF of each tested PE-1 and PE-2 sample, can be found in Annex A.2.6 (a), (b) and (c). The BRDF and BTDF values shown in the figure below are not normalized for doing comparison between the intensity of the scattered light and its relation to the morphology, especially for the case of identically thick PE-1 and PE-2.

Considering the overall trend in both BRDF and BTDF of each sample, their total forward and back scattered light can be analyzed at 632.8 nm and compared to ones estimated via the spectroscopic analyses shown in previous section. Different points in terms of morphology-dependency spatial distribution of light intensity can be discussed. Firstly, as illustrated in Figure 3.16 (a) and (c), higher BTDF values of PE-1 QC samples show more dominant forward scattering over backscattering. Similarly, both the PE-2 QC and AN samples show stronger scattering at forward directions, as shown in Figure 3.16 (b). The BTDF of both the PE-1 and PE-2 samples are in accordance with their high level of $T_\lambda^{i,\cap}$ which were measured around 75% and 82% at 632.8 nm, respectively (in Figure 3.11 (a)). The BDTF values of the PE-1 QC samples changes over angles at higher slopes, indicating a highly narrow-angle forward scattering. While, this slope is much lower for the BTDF of the PE-1 AN samples which also show lower values than PE-1 QC samples. This behavior means that annealing in PE-1 causes decreasing in $\Phi_\lambda^{s\text{-forward}}$ where also its spatial distribution becomes broader. Conversely, no significant effect of annealing seen on the backscattered light in PE-1 media, except a slight increase seen at angles greater than 2°, leading to have light intensities at broader angles. Looking back again Figure 3.11 (a) and (c), it can be seen that this trend perfectly matches with the drop in the $T_\lambda^{i,r}$, $T_\lambda^{i,\cap}$ and the increase in the $R_\lambda^{i,\cap}$ of 0.25 and 0.75 mm thick PE-1 samples with annealing. The broadened forward scattered light distributions can also explain the more pronounced decrease in the Φ_λ^t and thus in the measured $T_\lambda^{i,r}$ values of annealed PE-1. As shown in Figure 3.16 (b), both the BTDF and BRDF of PE-2 QC and AN samples show almost no change with annealing, in contrast to the effect of annealing seen in PE-1. Annealing-induced morphological changes in PE-2 indeed confirmed there was no change in the diameter of spherulites where only a slight increase in the l_c distributions range in PE-2 was observed. At a closer look, it is seen that annealing in PE-2 causes slightly more balanced ratio between forward and back scattered light regarding to the slightly decreased BTDF and, the increased BRDF values.

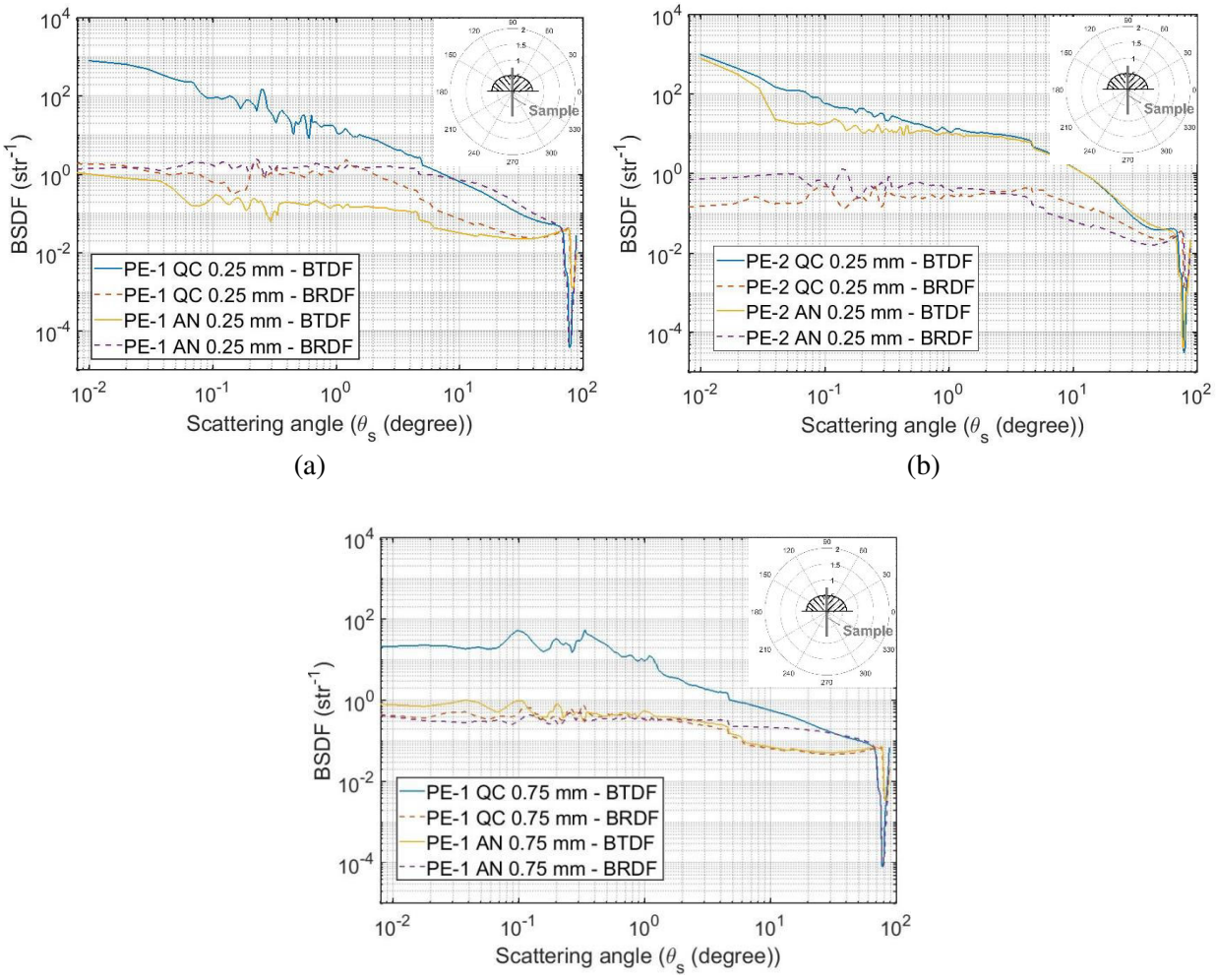

FIGURE 3.16. The effect of crystalline morphology on the angular scattering distribution of 0.25mm thick PE-1 (a), PE-2 (b) and 0.75mm thick PE-1 (c) media, shown for the angles between 0º and 90º in both forward and back directions of samples.

As reviewed in Chapter 2, the size and shape of scatterer in semi-crystalline PE medium is unknown, which can be defined either in arbitrary or spherical shapes. As also discussed before, the well-known optical scattering theories - such as Mie, Rayleigh or RDG - were mainly developed for the perfectly spherical scatterers. This point opens further discussions in terms of modeling optical scattering in PE medium including scatterer size and shape. However, this is out of the scope of this thesis. Nevertheless, assuming spherical scatterers in the crystalline phase of PE, initial estimation about the equivalent spherical scatterer size range (Equation 2.14) can be done based on the morphology-dependent spatial distribution of light scattering. Regarding to the theoretically calculated scattering phase function - ϕ - of spherical scatterers, an increase in ξ values - for instance starting from ξ =0.1 up to ξ =10 - leads to have

stronger forward scattering at narrower angles, as shown in Figure 2.11. At a constant wavelength, an increase in the scatterer size likely causes to have such an evolution in forward scattering. It was interestingly found that the trend between the morphological characteristics and the equivalent scatterer size range in PE-1 medium shows an inverse behavior. More specifically, annealing resulted lamellae thickening in PE-1 medium where its l_c distributions range becomes broader up to 100 nm. However, thickening of lamellar morphology in PE-1 medium probably reduces the equivalent scatterer size, and thus broadens the spatial distribution of forward scattered light. This consistent behavior seen in 0.25 and 0.75 mm thick PE-1 media may be the key in terms of identifying the equivalent scatterer size. Because, although thickening in lamellar morphology was seen, the lowered theoretical scatterer size which was estimated based on the change in their BTDF profiles after annealing clearly indicates that equivalent scatterer size in PE may not be identified based on only lamellar morphology, but probably some entities greater than lamellar crystals. In addition, the equivalent scatterer size in PE medium may not be represented by a mono-sized scatterer, but scatterers which has a size range or histogram. In that sense, it would be plausible to have a lowered equivalent scatterer size range induced by thickening in lamellar morphology, since lamellar crystals probably represents the relatively smaller scatterers in PE medium. It should also be mentioned again that l_c population distributions estimated here based on their normalized mass fraction existed in the crystalline phase. Therefore, it does not provide any number or quantity about the lamellar crystals which have different thicknesses. Consequently, further analyses to estimate the number of lamellar crystals may be required to identify equivalent scatterer size in PE medium, obviously only under the assumption of spherical scatterers.

Apart from this, the BTDF of both PE-2 QC and AN showed very similar level of scattered light intensity in comparison to the BTDF of PE-1 QC where also it was found that the diameter of spherulites observed in those media were very close (Figure 3.13). Therefore, negligible or significant effect of spherulite is ambiguous as it could not be detected on the all the samples. Therefore, no clear correlation can be proposed to identify the equivalent scatterer size based on spherulite size and lamellae thicknesses, which probably corresponds to different morphological entities in PE medium. This point needs to be analyzed further to confirm the equivalent scatterer size in PE medium. Nevertheless, the morphological – optical analyses here demonstrates the role of lamellar morphology on optical scattering in PE medium.

3.5. Summary

In this chapter, the morphology dependent optical properties of PE are analyzed bridging the crystalline structure to its transmittance, reflectance characteristics and the spatial distribution of optical scattering at 632.8 nm. At very first step, the role of crystalline structure on the optical properties of PE was analyzed performing spectroscopic and calorimetric analyses using PE-1 prepared under different

cooling conditions. The analyses showed the strong coupling between crystalline structure and optical scattering in VIS and NIR ranges, especially for transmittance characteristics. Even an increase of 5% of the X_c in PE-1 caused a decrease of nearly 50% of the $T_\lambda^{i,r}$ in the spectral range around 1µm. However, slight effect of crystalline structure was found in the reflectance characteristics in NIR range. In addition, the initial analyses between the crystalline morphology-optical scattering relation in PE revealed that wavelength dependence of optical scattering becomes negligible in MIR range. Time-dependent morphological-optical analyses were performed using PE-1 and PE-2 over the time up to 387 h. The analyses showed that the slight decrease in the $T_\lambda^{i,r}$ in VIS range was probably due to thin lamellar formations organized at room temperature, which is known as secondary crystallization. It was also observed that the potential effect of secondary crystallization may be considered negligible after 46 h, as the $T_\lambda^{i,r}$ values did not evolve further.

The relation between the morphological characteristics of PE and optical scattering were analyzed following calorimetric, microscopic and spectroscopic analyses using PE-1 and PE-2 polymers prepared under two different cooling conditions, QC and AN. The optical scattering in PE medium was initially analyzed in an indirect way, by measuring $T_\lambda^{i,r}$ and $T_\lambda^{i,\cap}$ and $R_\lambda^{i,\cap}$ of the PE samples having different morphologies. Hence, the morphology dependence of the total forward and back scattered light in PE medium was estimated without measuring its spatial distribution. The morphology-dependent optical scattering in PE was extended further performing MALS tests at 632.8 nm. Lamellar morphology of PE was estimated via DSC analyses, where also its spherulitic superstructures was examined under SEM. The analyses showed there is no direct relation between the optical scattering in PE and the amount of crystals, which is parametrized here as X_c. The comparison between the X_c, $T_\lambda^{i,r}$ and $T_\lambda^{i,\cap}$ identically thick PE-1 and PE-2 samples was a clear evidence for the fact that optical scattering behavior becomes stronger or weaker inside of PE medium not due the amount of crystals - or X_c - but, the amount or number of equivalent scatterer which cause optical scattering.

It was observed that annealing introduces significant lamellae thickening in PE-1, while this was much less prominent in PE-2. In addition, the SEM examinations revealed that the diameter of spherulites of the most of the PE-1 and PE-2 samples prepared under QC and AN conditions were very close to each other. The diameter of spherulites was mostly found around 10 µm. Due to impingement of spherulitic superstructures, no clear radial formation of spherulitic texture could be obtained in some of the analyzed samples. In terms of difference in the optical scattering in the PE-1 and PE-2, it was observed that annealing in PE-1 causes decreasing in $\Phi_\lambda^{s\text{-forward}}$ where also its spatial distribution becomes broader. Conversely, no remarkable effect of annealing seen on the backscattered light in PE-1 media, except a slight increase seen at angles greater than 2^o leading to have light intensity at broader angles at back

directions. It was found that this inverse trend perfectly matches with the morphology-dependent total scattered light estimated from the spectroscopic $T_\lambda^{i,r}$, $T_\lambda^{i,\cap}$ and $R_\lambda^{i,\cap}$ measurements. Conversely, the BTDF and BRDF of PE-2 samples showed almost no change with annealing process. Interestingly, their $T_\lambda^{i,r}$, $T_\lambda^{i,\cap}$ and $R_\lambda^{i,\cap}$ also did not show a significant change by annealing. The morphological information obtained via SEM and l_c distributions confirmed there was no change in the diameter of spherulites of PE-2 with annealing while, a slight increase in the l_c distributions was observed. Assuming spherical scatterers in the crystalline phase of PE, initial estimation about the equivalent spherical scatterer size range was done. It was interestingly found that the trend between the morphological characteristics and the equivalent scatterer size range in PE-1 medium shows an inverse behavior. More specifically, annealing resulted lamellae thickening in PE-1 medium where its l_c distributions range becomes broader up to 100 nm. However, thickening of lamellar morphology in PE-1 medium probably reduces the equivalent scatterer size, and thus broadens the spatial distribution of forward scattered light. Because, although thickening in lamellar morphology was seen, the theoretical equivalent scatterer size could be reduced since the BTDF of PE-1 showed a lower value in a lower slope after annealing, indicating broader scattering. This may indicate that equivalent scatterer size in PE may not be identified based on only lamellar morphology, but probably some entities greater than lamellar crystals, whereas this is quite ambiguous to conclude at this step. It should be mentioned again that l_c population distributions estimated here based on their normalized mass fraction existed in the crystalline phase. Therefore, it does not provide any number or quantity about lamellar crystals which have different thicknesses. In addition, the size and shape of scatterer in PE medium is unknown, which can be defined either in arbitrary or spherical shape. Although, no clear correlation can be proposed to identify the equivalent scatterer size based on spherulite or lamellar crystal size in PE, the morphological – optical analyses presented here demonstrate the role of lamellar morphology on optical scattering in PE medium.

The measured spatial distribution of scattered light measured as BTDF and BRDF was not only used for estimation of the morphology dependent scattering, but also confirmation for the accuracy of the spectroscopic analyses. The transmittance and reflectance measurements in different configurations enabled to estimate the total scattered light closely, which can be helpful to identify the scatterer size range following quick and accurate spectroscopic measurements. Nevertheless, it may be required to adopt further methodologies to estimate the equivalent scatterer size in PE. The most accurate way to identify the scatter size in PE medium may be adopting an inverse methodology to fit the experimentally the obtained spatial distribution of scattered light with theoretically calculated scattering phase functions. However, refractive index of both crystalline phase and interlamellar amorphous region in PE medium are other parameters to be known. The analyses and further perspectives proposed here can also be adopted for obtaining equivalent scatterer size in any type of unfilled semi-crystalline polymer.

References

[1] Reiter G, Strobl GR, editors. Progress in understanding of polymer crystallization. Berlin ; New York: Springer; 2007.

[2] Peacock AJ. Handbook of polyethylene: structures, properties, and applications. New York: Marcel Dekker; 2000.

[3] Wunderlich B. Thermal analysis of polymeric materials. Berlin: Springer; 2005.

[4] Alamo R, Mandelkern L. Origins of endothermic peaks in differential scanning calorimetry. J Polym Sci Part B Polym Phys 1986;24:2087–105.

[5] Gedde UW, Mattozzi A. Polyethylene Morphology. In: Albertsson A-C, editor. Long Term Prop. Polyolefins, vol. 169, Berlin, Heidelberg: Springer Berlin Heidelberg; 2004, p. 29–74.

[6] Electron Microscopy of Polymers. Berlin, Heidelberg: Springer Berlin Heidelberg; 2008.

[7] Rastogi S, Lippits DR, Terry AE, Lemstra PJ. The Role of the Interphase on the Chain Mobility and Melting of Semi-crystalline Polymers; A Study on Polyethylenes. In: Reiter G, Strobl GR, editors. Prog. Underst. Polym. Cryst., Berlin, Heidelberg: Springer Berlin Heidelberg; 2007, p. 285–327.

[8] Keller A. A note on single crystals in polymers: Evidence for a folded chain configuration. Philos Mag J Theor Exp Appl Phys 1957;2:1171–5.

[9] Till PH. The growth of single crystals of linear polyethylene. J Polym Sci 1957;24:301–6.

[10] Kobayashi K, Nishijima Y, Goto S, Kurokawa M. Super micellar structures of high polymers. In: Möllenstedt G, Niehrs H, Ruska E, editors. Phys.-Tech. Teil, Springer Berlin Heidelberg; 1960, p. 728–728.

[11] Bassett DC, Keller A, Mitsuhashi S. New features in polymer crystal growth from concentrated solutions. J Polym Sci A 1963;1:763–88.

[12] Bassett DC, Hodge AM. On the morphology of melt-crystallized polyethylene - I. Lamellar profiles. Proc R Soc Lond A 1981;377:25–37.

[13] Bassett DC, editor. Developments in Crystalline Polymers—1. Springer Netherlands; 1982.

[14] Wlochowicz A, Eder M. Distribution of lamella thicknesses in isothermally crystallized polypropylene and polyethylene by differential scanning calorimetry. Polymer 1984;25:1268–1270.

[15] Alberola N, Cavaille JY, Perez J. Mechanical spectrometry of alpha relaxations of high-density polyethylene. J Polym Sci Part B Polym Phys 1990;28:569–586.

[16] Song S, Feng J, Wu P. Annealing of melt-crystallized polyethylene and its influence on microstructure and mechanical properties: A comparative study on branched and linear polyethylenes. J Polym Sci Part B Polym Phys 2011;49:1347–59.

[17] Barham PJ, Chivers RA, Keller A, Martinez-Salazar J, Organ SJ. The supercooling dependence of the initial fold length of polyethylene crystallized from the melt: unification of melt and solution crystallization. J Mater Sci 1985;20:1625–30.

[18] Hu W. Intramolecular Crystal Nucleation. In: Reiter G, Strobl GR, editors. Prog. Underst. Polym. Cryst., Berlin, Heidelberg: Springer Berlin Heidelberg; 2007, p. 47–63.

[19] Stack GM, Mandelkern L, Voigt-Martin IG. Changes in crystallite size distribution during the isothermal crystallization of linear polyethylene. Polym Bull 1982;8:421–8.

[20] Sumpter BG, Noid DW, Wunderlich B. Theoretical studies of the effects of anharmonicity on polymer dynamics: temperature dependence of heat capacity. Polymer 1990;31:1254–9.

[21] Sun Y, Fischer S, Jiang Z, Tang T, Funari SS, Gehrke R, et al. Morphological Changes of Linear, Branched Polyethylenes and their Blends during Crystallization and Subsequent Melting by Synchrotron SAXS and DSC. Macromol Symp 2012;312:51–62.

[22] Zachmann HG, Wutz C. Studies of the Mechanism of Crystallization by Means of WAXS and SAXS Employing Synchrotron Radiation. In: Dosière M, editor. Cryst. Polym., Dordrecht: Springer Netherlands; 1993, p. 403–14.

[23] Hakoume D, Dombrovsky LA, Delaunay D, Rousseau B. Spectroscopic diagnostics of morphological changes arising in thermal processing of polypropylene. Appl Opt 2014; 53:2702.

[24] Wunderlich B. Analysis by calorimetry. Thermochim Acta 1973; 5:369–76.

[25] Bassett DC, Hodge AM. On lamellar organization in certain polyethylene spherulites. Proc R Soc Lond A 1978;359:121–32. doi:10.1098/rspa.1978.0035.
[26] Trifonova D, Drouillon P, Ghanem A, Vancso GJ. Morphology of extruded high-density polyethylene pipes studied by atomic force microscopy. J Appl Polym Sci 1997;66:515–23.
[27] Lee SY, Bassett DC, Olley RH. Direct observations of differential lamellar deformation on drawing isolated polyethylene spherulites n.d.:10.
[28] Mattozzi A. SMALL MOLECULE DIFFUSION IN SPHERULITIC POLYETHYLENE n.d.:72.
[29] Karlsson M, Xu X, Gaska K, Hillborg H, Gubanski SM, Gedde UW. DC Conductivity Measurements of LDPE: Influence of Specimen Preparation Method and Polymer Morphology n.d.:6.
[30] Sasic S, Ozaki Y. Raman, Infrared, and Near-Infrared Chemical Imaging. John Wiley & Sons; 2011.
[31] Balling B. A Comparative Study of the Bidirectional Reflectance Distribution Function of Several Surfaces as a Mid-wave Infrared Diffuse Reflectance Standard. Master Thesis. Air Force Institute of Technology, 2009.
[32] Manara J, Arduini-Schuster M, Hanssen L. Integrating sphere reflectance and transmittance intercomparison measurements for evaluating the accuracies of the achieved results. High Temp–High Press 2009;38:259–276.
[33] Apetz R, van Bruggen MPB. Transparent Alumina: A Light-Scattering Model. J Am Ceram Soc 2003;86:480–6.
[34] Howell JR, Menguc MP, Siegel R. Thermal Radiation Heat Transfer, 5th Edition. 5 edition. Boca Raton: CRC Press; 2010.
[35] Bass M, Optical Society of America, editors. Handbook of optics. 2nd ed. New York: McGraw-Hill; 1995.
[36] Padilla C, Fritschel P, Magaña-Sandoval F, Muniz E, Smith JR, Zhang L. Low scatter and ultra-low reflectivity measured in a fused silica window. Appl Opt 2014;53:1315.
[37] Hakoume D., Dombrovsky LA, Delaunay D, Rousseau B. Effect of Processing Temperature on Radiative Properties of Polypropylene and Heat Transfer in the Pure and Glassfibre Reinforced Polymer, Begellhouse; 2014..
[38] Poprawe R, editor. Tailored Light 2. Berlin, Heidelberg: Springer Berlin Heidelberg; 2011.
[39] Geiger M, Frick T, Schmidt M. Optical properties of plastics and their role for the modelling of the laser transmission welding process. Prod Eng 2009; 3:49–55.
[40] Fratini CM. Study of the Morphology and Optical Properties of Propylene/Ethylene Copolymer Films 2006.
[41] Gulmine J., Janissek P., Heise H., Akcelrud L. Polyethylene characterization by FTIR. Polym Test 2002; 21:557–63.
[42] Tsilingiris PT. Comparative evaluation of the infrared transmission of polymer films. Energy Convers Manag 2003; 44:2839–56.
[43] Milton J. University of Arizona, Ph.D., 1968 Botany- n.d.:122.
[44] Kossack W, Papadopoulos P, Parkinson M, Prades F, Kremer F. IR transition moment orientational analysis on semi-crystalline polyethylene films. Polymer 2011; 52:6061–5.
[45] Bendada A, Cole K, Lamontagne M, Simard Y. A hollow waveguide infrared thermometer for polymer temperature measurement during injection moulding. J Opt Pure Appl Opt 2003;5:464.
[46] Ennis CP, Kaiser RI. Mechanistical studies on the electron-induced degradation of polymers: polyethylene, polytetrafluoroethylene, and polystyrene. Phys Chem Chem Phys 2010;12:14884.
[47] Sella C. Etude des polyethylenes par diffraction des rayons X aux petits angles. Comptes Rendus Chim 1959;248:1819.
[48] Wlochowicz A, Eder M. Distribution of lamella thicknesses in isothermally crystallized polypropylene and polyethylene by differential scanning calorimetry. Polymer 1984;25:1268–70.
[49] Hallman Jr RL. The Effect of Processing Parameters on Barrier Properties of Polymers 2013.

[50] Lorenzo AT, Arnal ML, Müller AJ, Lin M-C, Chen H-L. SAXS/DSC Analysis of the Lamellar Thickness Distribution on a SSA Thermally Fractionated Model Polyethylene. Macromol Chem Phys 2011; 212:2009–16.
[51] Feng L, Kamal MR. Distributions of Crystal Size from DSC Melting Traces for Polyethylenes. Can J Chem Eng 2008;82:1239–51.
[52] Shahin MM, Olley RH, Blissett MJ. Refinement of etching techniques to reveal lamellar profiles in polyethylene banded spherulites. J Polym Sci Part B Polym Phys 1999; 37:2279–86.

This page intentionally left blank.

Chapter 4

TEMPERATURE-DEPENDENCY IN THE OPTICAL PROPERTIES AND CRYSTALLINE MORPHOLOGY OF SEMI-CRYSTALLINE THERMOPLASTICS

4.1. Introduction

This chapter discusses the temperature dependence in the optical properties of semi crystalline thermoplastics. The temperature dependency in their optical properties is likely due to the evolutions in the optical behavior inside of heterogeneous polymer medium induced by crystalline phase evolutions, which is reported in literature for various types of semi-crystalline polymers at monochromatic wavelengths. Here, the temperature dependency in the optical properties of semi-crystalline PE was investigated in VIS and NIR ranges using quasi-linear and branched PE polymers. Considering different types of PE polymer, cooling condition, sample thickness and type of measurements, three main points were aimed to address in this chapter:

- The effect of transmittance testing setup configurations on the accurate characterization of temperature-dependent thermo-optical properties of an optically heterogeneous medium.

- *Characterization of temperature-dependent thermo-optical properties of PE* based on its temperature-dependent transmittance and reflectance measurements. The characterized temperature-dependent thermo-optical properties can be adopted as: *radiation absorption parameter for radiation heat transfer modeling of PE.*

- Bridging the crystalline structure evolutions under heating and temperature dependent optical properties, in particular transmittance characteristics, to address the effect of crystal melting on the optical scattering behavior in PE medium. More specifically, it is aimed to understand the crystalline structure evolution, based on lamellae melting under heating, and correlate the temperature dependent transmittance characteristics to the lamellae melting of PE. Thanks to this step, it may possible to address the question about: *what is the most probable crystal size that melts and induces significant change in the optical scattering behavior in PE medium under heating?*

4.2. Characterization of temperature-dependent optical properties

4.2.1. Materials and experimental methodology

Similar to the experimental methodology adopted in Chapter 3, the temperature-dependent optical properties of PE were analyzed considering two different PE polymers, namely HDPE and LLDPE, which have different polymer chain structures. As aforementioned, in this thesis, HDPE and LLDPE are named as PE-1 and PE-2, respectively. In this research project, the PE-1 represents the type of polymer which is used for the IR-heating assisted thermoforming processes. The branched polymer, PE-2, was also adopted in this study to perform comparative analyses to bridge the crystalline structure evolutions under heating

to temperature dependent optical properties. Thanks to the comparative analyses, the effect of crystal melting on the optical scattering behavior in PE medium is addressed. PE-1 polymer samples were prepared in three different thicknesses (0.25, 0.50 and 0.75mm). However, only 0.25mm thick samples of PE-2 polymer was prepared. The intrafilm thickness variation was found around +/- 20 μm whereas interfilm thickness variation was slightly higher, around +/- 30 μm. With the aim of introducing different morphological states, both the PE-1 and PE-2 samples were either quenched in LN_2, or annealed applying stepwise cooling, as explained in detail in Chapter 3. As followed in Chapter 3, the samples quenched in LN_2 or annealed under stepwise cooling are called here again as *QC* and *AN*, respectively. Further details related to the samples tested for the temperature-dependent spectroscopic measurements are presented in the Section 4.2.1.1 and 4.2.1.2.

4.2.1.1. Temperature-dependent transmittance tests

The temperature dependency in the transmittance properties of PE was analyzed performing $T_\lambda^{i,r}(T)$ and $T_\lambda^{i,\cap}(T)$ tests. The overview of the test setups used for $T_\lambda^{i,r}(T)$, and $T_\lambda^{i,\cap}(T)$ measurements are schematically displayed in Figure 4.1 (a) and (b), respectively. The $T_\lambda^{i,r}(T)$ tests were done using a Fourier Transform Infrared (FT-IR) spectrometer (Bruker Vertex 70) and, the $T_\lambda^{i,\cap}(T)$ tests were performed employing another FTIR spectrometer (Perkin Elmer 950) combined with an integrating sphere. The measurements done via Bruker Vertex 70 were carried out in our laboratory, whereas the remaining tests done with Perkin Elmer 950 were realized in Procédés, Matériaux et Energie Solaire (PROMES) – CNRS laboratory. For both the $T_\lambda^{i,\cap}(T)$ and $T_\lambda^{i,r}(T)$ tests , a heating stage (Bruker A599) was used so that the PE samples, which has a diameter (D) of 13mm, were mounted into the heating stage and, heated by conduction during the measurements. The heating stage was positioned at the entrance port of the integrating sphere for the $T_\lambda^{i,\cap}(T)$ tests whereas no integrating sphere was used in the $T_\lambda^{i,r}(T)$ tests. Considering an optically heterogeneous medium, Φ_λ^i may be either directly transmitted or scattered. Hence, as shown in Figure 4.1 (b), transmittance tests performed with integrating sphere enable to detect both the $\Phi_\lambda^{s\text{-}forward}$ and Φ_λ^t which travel through such an heterogeneous medium. The identical temperature steps were adopted for both types of the transmittance test. Between the two consecutive measurement steps of both the $T_\lambda^{i,\cap}(T)$ and $T_\lambda^{i,r}(T)$ tests, the samples were heated up in a monotonically increasing manner and waited for 2 minutes to reach a steady-state temperature.

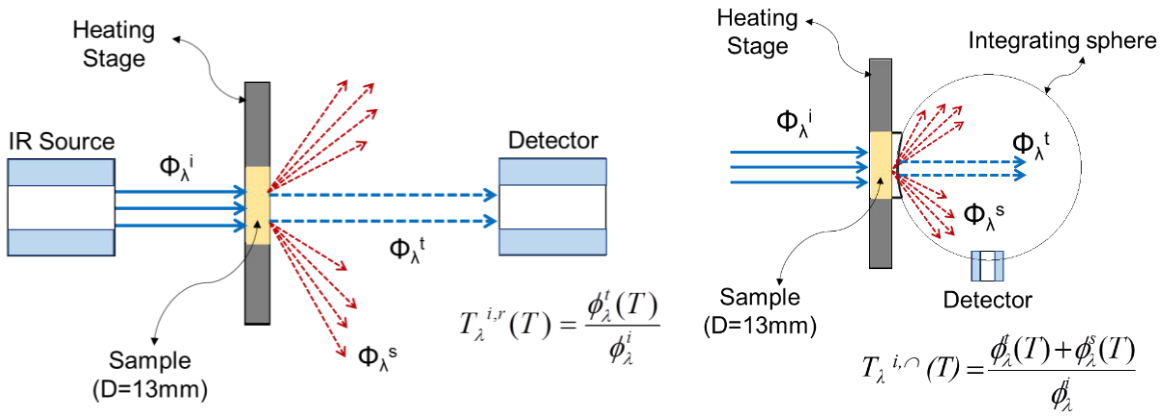

(a) (b)

FIGURE 4.1. The test setups for $T_\lambda^{i,r}$ (a) and $T_\lambda^{i,\cap}$ (b) measurements.

It should be mentioned here that the crystalline morphology of PE may be altered under varying temperature, in particular the crystalline substructures, namely the lamellae [1,2]. Hence, several numbers of samples were prepared in identical condition and each sample was used for each individual $T_\lambda^{i,r}(T)$ and $T_\lambda^{i,\cap}(T)$ tests. The reason behind this is to eliminate potential change in the optical characteristics of PE that may be induced by the difference in the crystalline phase of an already-tested sample. However, the waiting time at each temperature step of all the $T_\lambda^{i,r}(T)$, $T_\lambda^{i,\cap}(T)$ and $R_\lambda^{i,\cap}(T)$ tests may allow melting-reorganization in the crystalline phase of quasi-linear PE [3], especially at the temperatures close to its melting range. Nevertheless, it was assumed that the potential effect of the reorganization in the crystalline phase of PE to the optical characteristics is negligible. This point is discussed further based on the experimental results presented in Section 4.3.2.

Overview of all the temperature-dependent transmittance tests, including the type and spectral range of the transmittance measurements, the adopted temperature steps, and the details of the prepared PE-1 and PE-2 samples are presented in Table 4.1. As each sample was used only once concerning each test, eight PE-1 and two PE-2 samples were prepared in different thicknesses and cooling conditions for these tests. In each $T_\lambda^{i,r}(T)$ and $T_\lambda^{i,\cap}(T)$ test, the transmittance measurements were performed at 15 different temperature steps. In the table, the temperature steps represent the actual temperature (T_{actual}) on the sample surface where the measurements were done. It was observed that the set temperature (T_{set}) on the heating device and, the T_{actual} on the measurement zone were different. Thus, preliminary tests were done for determining the T_{actual} of each adopted measurement step prior to the temperature-dependent transmittance tests.

Cooling condition		**QC**		**AN**	
Type of measurement		$T_\lambda^{i,r}(T)$	$T_\lambda^{i,\cap}(T)$	$T_\lambda^{i,r}(T)$	$T_\lambda^{i,\cap}(T)$
Sample type and thickness (mm)	**PE-1**	0.75	0.25, 0.50 and 0.75	0.25 and 0.75	
	PE-2	-	0.25	0.25	-
Temperature steps (T_{actual} (°C)) of the measurements		25, 48, 71, 84, 97, 110, 114, 116, 118, 120, 121, 122, 123, 126, 128			
Spectral range of the measurements		0.4 - 2.5 μm	0.25 - 2.5 μm	0.4 - 2.5 μm	0.25 - 2.5 μm

TABLE 4.1. The PE-1 and PE-2 samples used for the temperature-dependent transmittance measurements and, overview of the test characteristics.

Apart from determining the T_{actual} for all the tests, the temperature variations alongside the polymer surface was investigated for the heating case applied in both the $T_\lambda^{i,r}(T)$ and $T_\lambda^{i,\cap}(T)$ tests. The temperature-controlled heating stage used in these tests is equipped with a PID controller. It heats the material from its edge, and therefore the middle of the sample -where transmittance measurements are performed- has a lower temperature which may be critical in terms of accuracy in the measurements. The preliminary tests dedicated for analyzing these points were carried out using 0.75mm thick PET samples. For each temperature step, the temperature profile on the PET surface was recorded using an IR camera (FLIR SC325). PET was chosen as a reference material for these analyses as it is opaque in the operating range of a typical IR camera, in contrast to PE [4]. Hence, a reliable surface temperature on PET could be obtained non-invasively via IR-thermographic measurements [5]. In terms of thermal conductivity (k), it is known that PET has k which is around 0.25 W/mK [6], whereas it is between 0.25 - 0.4 W/mK for PE [7] which may enable to adopt the obtained T_{actual} for the identically thick PE samples. However, considering the combined effect of all the thermophysical properties of PET and PE which are slightly different, the question arises about the difference in their temperature profile. This was analyzed performing two-step numerical-experimental comparisons. At very first step, the experimental measurements were obtained on the PET surface. In Figure 4.2, the heating stage used for the temperature-dependent transmittance tests (a), a thermal image acquired via the IR-camera and the arbitrarily defined vertical and horizontal profiles on the PET surface are displayed (b). Obtaining the temperature edge-to-edge profile through the middle of the sample enables to adjust the size of the incident light that is transmitted through the sample, which represents transmittance measurement zone.

Because the temperature variations are desired to be negligibly small in the transmittance measurement zone so that a reliable correlation between the actual measured temperature and the transmittance can be obtained at each measurement step, the actual temperature was identified over the whole temperature range of interest. IR thermographic measurements were thus achieved on the PET surface at eight different steady-state temperature steps, at which T_{set} of the heating stage were adjusted between 25°C and 105°C. In Figure 4.2 (c), the surface temperature of PET sample read throughout the vertical and horizontal profiles are presented. These profiles were obtained when the T_{set} of the heating was 95°C. The symmetric vertical and horizontal temperature profiles obtained at all the steady-state temperature steps can be found in Annex A.3.1. Based on all the obtained temperature profiles at each temperature step, the beam width of the incident light that is sourced from the spectrometer was set to 1.5 mm since the maximum temperature variation inside this zone was lower than 0.3°C.

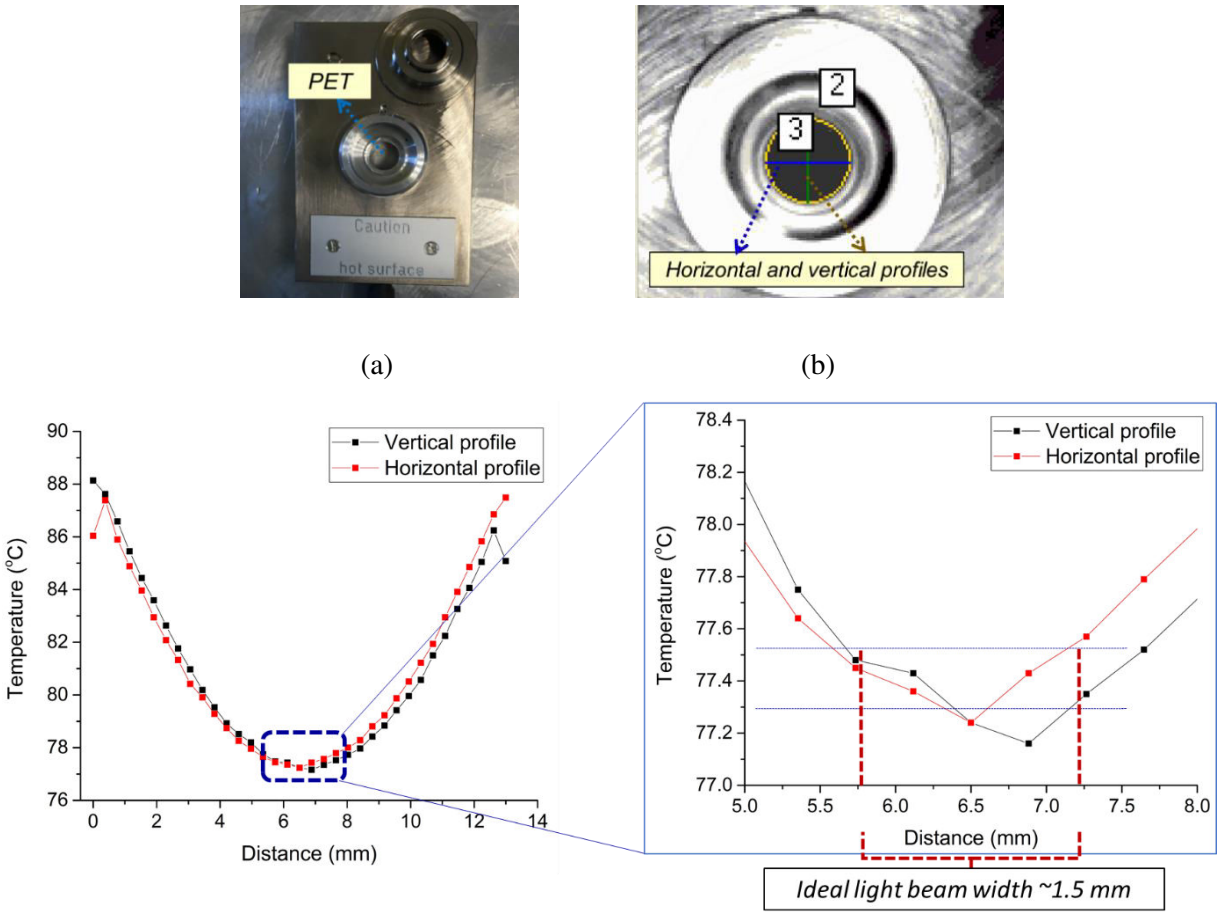

FIGURE 4.2. The heating stage (a), thermal image of the PET acquired by the IR camera (b) and the temperatures read on the vertical and horizontal profiles at T_{set} = 95°C (c).

For the preliminary tests, the maximum T_{set} was chosen as 105°C since PET is known to undergo cold crystallization for temperatures above it [8], which may change accuracy of the surface temperature measurements obtained via IR thermography by inducing a potential change in the emissivity of PET (ε_{PET}). Hence, for the T_{set} values greater than 105°C, the experimentally obtained temperature difference (ΔT (°C)) between T_{set} and T_{actual} was extrapolated and, T_{actual} for the T_{set} values greater than 105°C was obtained. Both the experimentally obtained and extrapolated values of T_{actual} and T_{set} of the heating stage are presented in Figure 4.3.

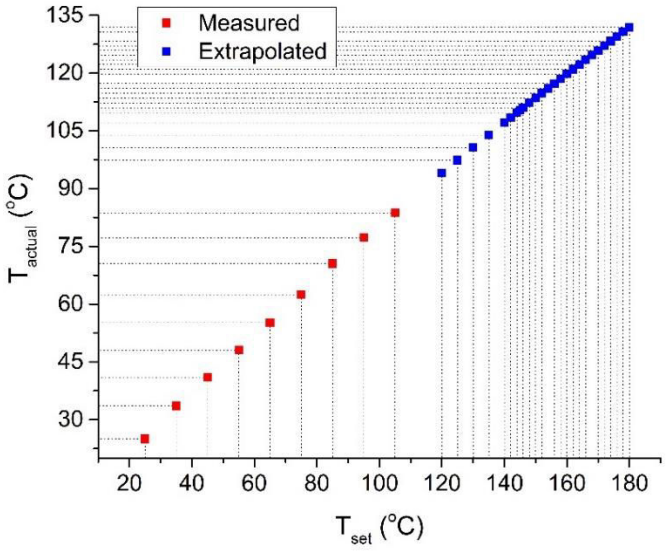

FIGURE 4.3. The experimentally obtained and extrapolated T_{actual} values on the measurement zone of the PET sample.

After the experimental analyses, identically thick PET sample was modeled in COMSOL considering the identical heating conditions and geometrical features that were applied in the measurements. The predicted temperature profiles as each T_{set} were fitted to the experimental data. In other words, the experimentally measured and extrapolated temperatures of PET were used as reference to compute the exact temperature profiles on the identically thick sample under identical heating condition. By adopting the known thermophysical properties of PET [9], these numerical - experimental fitting was done to predict the convection cooling through the sample surface during step-wise heating, which is parametrized as convective heat transfer coefficient (h (W/m^2K)). As applied in the IR thermographic measurements, continuous step-wise heating was defined in the model following the identical duration of heating (2 minutes) for each temperature step. Thus, at the end of each heating step, the predicted temperature profile over the surface of circular sample was taken for the comparisons. In the model, self-emission of the heating stage and the polymer was ignored. It was found that the predicted temperature

profiles were very close to the experimentally measured / extrapolated values for the case that h is 3.7 W/m^2K.

At the second step of the numerical simulations, the predicted h value was adopted for the case of simulating geometrically identical 0.75 mm thick PE. By also knowing the thermophysical properties of PE, the predicted temperature profiles at each T_{set} were compared to the numerical and experimental results of PET. The temperature-dependent apparent heat capacity ($C_{p,}^{apparent}$ (T)) of PE was measured using the power compensated DSC, presented in Chapter 3. The temperature-dependence in the k of PE was also considered, which was adopted from literature [7]. In Figure 4.4 (a), the comparisons between the experimental measurements and, the predicted temperature profiles of PET and PE at each corresponding T_{set} are illustrated. In addition to this, the predicted temperature profiles of PET and PE were compared to the extrapolated experimental values (Figure 4.4 (b)). For the sake of clarity, only several measurement steps are displayed here. The overview of the modeled geometry and the comparisons at the remaining T_{set} points can be found in Annex A.3.2 and A.3.3. As can be seen in Figure 4.4 (a), the predicted temperature distributions of PET matches closely (less than 1°C) with the experimental values in the middle zone of the sample, where the transmittance measurements are done. For the case of heating an identically thick PE sample, slightly different temperature profiles were obtained. For the T_{set} values up to 160°C, the predicted temperatures in the middle zone of PE slightly underestimated (by ~1.5°C) the measured and extrapolated experimental values. Beyond this temperature, for each T_{set} values greater than 160°C, the temperature difference between the predicted and extrapolated values in the middle zone of the PE sample became more pronounced. It should be emphasized here that T_{actual} in the middle zone of the identically thick samples is higher than 120°C, for the T_{set} values above 160°C (Figure 4.3). Considering that $C_{p,}^{apparent}$ (T) of PE is higher than PET especially between 120° - 130°C due to melting of its crystalline phase, it would be plausible that the temperature on PE surface is lower. Nevertheless, the averaged maximum ΔT between the experimental and predicted T_{actual} values in the middle zone was found not greater than ~2°C regarding all the temperature steps starting from 25°C. Based on the experimental-numerical analyses, it can be assumed that the experimentally measured / extrapolated T_{actual} values obtained on the PET surface is close to be identical for the identically thick PE samples.

The adoption of these values for samples with different thicknesses was another point to be investigated. As shown in Table 4.1, the thinnest PE sample used for the temperature dependent transmittance tests was 0.25 mm. Considering this thickness, another simulation was performed however slightly more underestimated values were observed for T_{actual} above 120°C. Since the surface area of any polymer sample mounted in the heating stage is identical, it likely introduces convection heat transfer at

the sample-air interface in similar manner. Whereas the difference in temperature profiles is potentially due to melting behavior / phase transitions in different polymer samples, which was not the case for PE regarding most of the measurement steps adopted for the temperature-dependent optical properties tests. Thus, the temperature profile measured on the 0.75 mm thick sample was assumed identical for the 0.25 and 0.50 mm thick samples and, the experimentally measured / extrapolated T_{actual} values were also adopted for these PE samples.

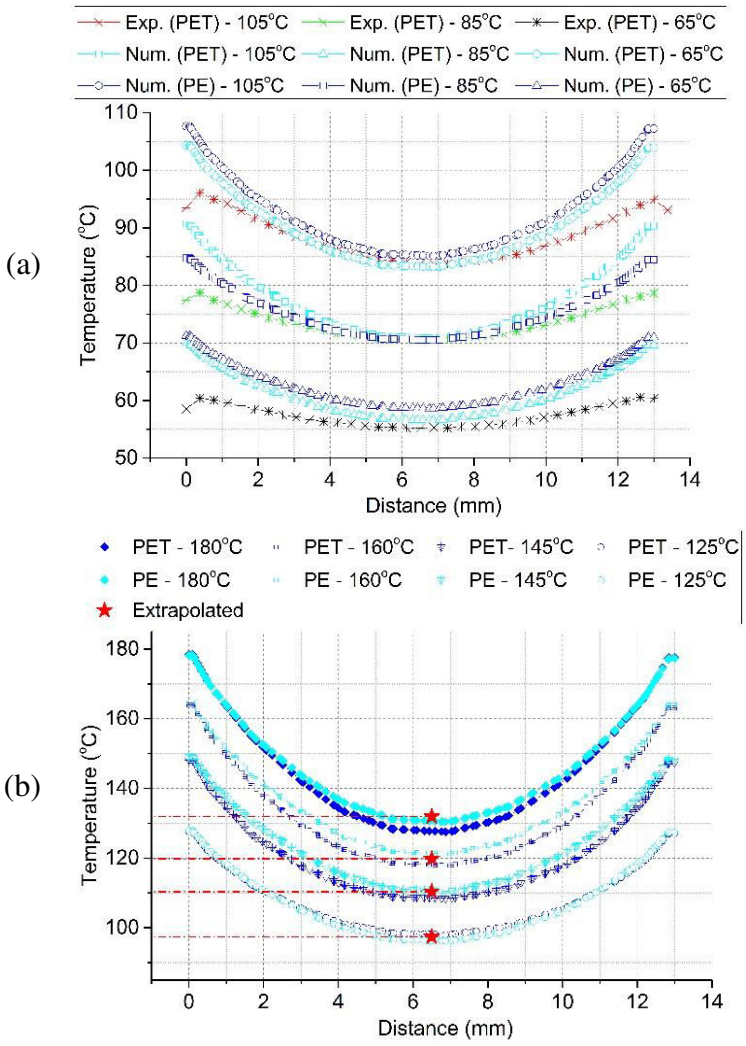

FIGURE 4.4. Comparisons between the predicted (Num.) and the experimentally measured (Exp.) temperature profiles (a), and the extrapolated T_{actual} values (b) on the transmittance measurement zone of identically thick PET and PE samples.

4.2.1.2. Temperature-dependent reflectance tests

The $R_{\lambda}^{i,\cap}(T)$ tests were done employing SOC-100 model Hemispherical Directional Reflectometer (HDR) built by Surface Optics Corporation. These tests were also carried out in PROMES – CNRS

laboratory. The overview of the test setup is illustrated schematically Figure 4.5. The testing device has a blackbody source which emits total hemispherical radiation (incident light). The hemispherical incident light strikes the sample surface and, is received by the detector at each specific angle. Theoretically, this represents the hemispherical-directional reflectance ($R_\lambda^{\cap, i}$), where reciprocity exists between both types of reflectance ($R_\lambda^{i,\cap} = R_\lambda^{\cap, i}$) [10], as designed in SOC-100 HDR. Similar to the temperature-dependent transmittance tests, the PE samples were also heated by conduction using the heating unit of the SOC-100 HDR where the average waiting time for the $R_\lambda^{i,\cap}(T)$ tests was around 5 minutes. Since two different heating units were used for heating the samples in the temperature-dependent transmittance and reflectance tests, the waiting time for reaching steady-state temperature at each consecutive temperature step was different.

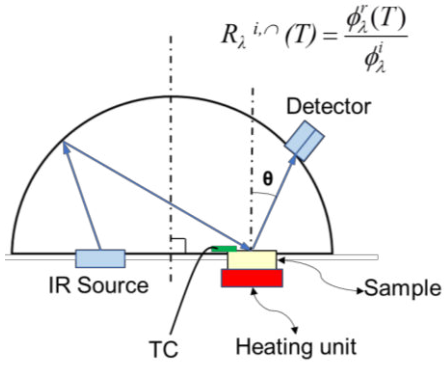

FIGURE 4.5. The test setup for the $R_\lambda^{i,\cap}(T)$ measurements.

The $R_\lambda^{i,\cap}(T)$ tests were carried out using only 0.25, 0.50 and 0.75mm thick PE-1 QC samples. As discussed in previous chapter, the reflectance characteristics of PE does not show a significant difference in relation to different thicknesses and morphologies. Therefore, the reflectance characteristics analyzed here only aimed to be used for the determination of temperature-dependent thermo-optical properties of PE, but not for further analyses to bridge the crystalline structure - optical properties evolutions under heating. As applied in the temperature-dependent transmittance tests, several numbers of samples were prepared in identical condition and each sample was used for each individual $R_\lambda^{i,\cap}(T)$ test to eliminate potential change in the reflectance characteristics of PE that may be induced by the difference in the crystalline phase of an already-tested sample. Although 5 minutes waiting time is longer than the one applied in the transmittance tests, it was again assumed that the potential effect of the reorganization in the crystalline phase of PE to the optical characteristics is negligible. Overview of the $R_\lambda^{i,\cap}(T)$ tests are presented in Table 4.2.

Type of measurement	Sample thickness (mm)	Temperature steps (T_{actual} (°C)) of the measurements	Spectral range of the measurements
$R_\lambda^{i,\cap}$ (T)	0.25, 0.50 and 0.75	25, 71, 97, 103, 107,110, 114, 118, 120, 124, 128	2 - 20 µm

TABLE 4.2. Overview of the temperature-dependent reflectance tests and the tested PE-1 QC samples.

In the table above, the temperature steps represent again T_{actual} on the sample surface where it was determined performing another series of preliminary measurements prior to the $R_\lambda^{i,\cap}$ (T) tests. The measurements were done using 0.5 mm thick PE samples and the T_{actual} of each measurement step was determined using the thermocouple (TC) of the heating unit in SOC-100 HDR. As shown in Figure 4.5, the TC is attached on the top surface of the sample where also the reflectance measurements are performed. Since the sample is heated from below in these tests, the temperature variation through its thickness is likely to happen. However, it may be relatively small considering the thicknesses of the tested samples, which are between 0.25 and 0.75mm. Hence, it was assumed that the effect of thickness on the top surface temperature of all the tested samples is negligibly small. Therefore, T_{actual} of each measurement step obtained using 0.5mm thick samples was also adopted for 0.25 mm and 0.75 mm thick samples. In addition, thermal coupling agent was used between the heating unit and the sample to secure good thermal contact in each $R_\lambda^{i,\cap}$ (T) test. In addition, a thin piece of black metal plate was mounted between the heating unit and the PE sample at each $R_\lambda^{i,\cap}$ (T) test, since the experimental analyses presented in Chapter 3 showed that PE is highly semi-transparent in the spectral range of the tests. Thanks to this step, the amount of radiation flux that is transmitted through the sample medium was not reflected back and, which avoided having erroneous reflectance measurements. The low reflectance of the mounted metal plate was previously verified considering the measurements in the spectral range of the $R_\lambda^{i,\cap}$ (T) tests, between 2.5 and 20 µm. Its reflectance characteristics in the corresponding range are given in Annex A.3.4.

4.3. Results and Discussions

4.3.1. Temperature dependent optical properties - optical scattering relations and extinction coefficient calculations

As introduced in Section 4.1, the objectives of the studies presented in this chapter are categorized into three main discussion points. In this section the first two points are discussed. At first, the difference between the $T_\lambda^{i,r}$ (T) and $T_\lambda^{i,\cap}$ (T) measurements was criticized using identically prepared 0.75 mm thick PE-1 QC samples. Based on the comparisons, the question on which test configuration is the best for the

accurate determination of the absorption characteristics of PE was addressed. The analyses were extended characterizing $T_\lambda^{i,\cap}$ (T) and $R_\lambda^{i,\cap}$ (T) of PE-1 QC samples in three different thicknesses. Assuming an optically homogeneous medium, the measured $T_\lambda^{i,\cap}$ (T) and $R_\lambda^{i,\cap}$ (T) values of the PE-1 QC samples were used to calculate an equivalent temperature-dependent extinction coefficient (β_λ (T)), which represents radiation absorption parameter of PE for radiation heat transfer modeling. It should be mentioned here again that PE-1 QC was chosen for the β_λ (T) characterizations since, PE-1 represents the type of polymer which is used for the IR-heating assisted thermoforming processes. In addition, regarding to the type of preform used for the thermoforming processes, the material state of the prepared preforms are close to the condition of the PE film samples cooled in the fastest manner, which is QC in this study. This point was discussed in Chapter 3 through the cooling conditions / crystalline structure relations of PE-1, including the variations in its X_c and l_c distributions. For the sake of clarity, the samples used in these analyses are derived from Table 4.1 and 4.2 and, presented in Table 4.3.

Type of measurement	**Sample thickness (mm)**	**Temperature steps (T_{actual} (°C)) of the measurements**	**Spectral range of the measurements**
$T_\lambda^{i,r}$ (T)	0.75	25, 48, 71, 84, 97, 110, 114, 116, 118, 120, 121, 122, 123, 126, 128	0.4 - 2.5 μm
$T_\lambda^{i,\cap}$ (T)	0.25, 0.50 and 0.75		0.25 - 2.5 μm
$R_\lambda^{i,\cap}$ (T)	0.25, 0.50 and 0.75	25, 71, 97, 103, 107,110, 114, 118, 120, 124, 128	2 - 25 μm

TABLE 4.3. The PE-1 QC samples and the testing characteristics of the $T_\lambda^{i,r}$ (T), $T_\lambda^{i,\cap}$ (T) and $R_\lambda^{i,\cap}$ (T) measurements.

In Figure 4.6, the $T_\lambda^{i,r}$ (T) of a PE-1 QC sample was compared to its $T_\lambda^{i,\cap}$ values that were measured at 25°C. In the figure, the $T_\lambda^{i,r}$ (T) measurements are labeled regarding the temperature at which they were obtained. As displayed in the figure, there is a significant difference between the measured $T_\lambda^{i,r}$ and $T_\lambda^{i,\cap}$ of the identical PE sample. The dashed line displayed in the figure show that the $T_\lambda^{i,\cap}$ of the sample is around 72% at 1 μm, whereas its $T_\lambda^{i,r}$ measured at 25°C is around 4%. It is a clear evidence that significant part of the transmitted light flux is actually forward-scattered as the $T_\lambda^{i,r}$ measurements lack in detecting all the transmitted light flux through the optically heterogeneous medium. It should also be noted that some amount of the light flux may also be back-scattered inside of the polymer medium and may not enter the integrating sphere [11]. This point is discussed further in the previous chapter, based on the comparison between the $T_\lambda^{i,r}$ and $T_\lambda^{i,\cap}$ of PE samples prepared in different thicknesses and analyzed

at room temperature. It was observed that the amount of back-scattered light, $\Phi_\lambda^{s\text{-}back}$, may be negligible in comparison to $\Phi_\lambda^{s\text{-}forward}$ considering the same spectral range presented in Figure 4.6.

At higher temperatures, the $T_\lambda^{i,r}(T)$ values increases and surpasses the $T_\lambda^{i,\cap}$ that was obtained at 25°C, which can be attributed to the weaker optical scattering under heating condition. Once the temperature is above 114°C a dramatic increase in the $T_\lambda^{i,r}(T)$ is seen. It reaches its maximum values above 120°C which is around 90% transmittance at 1 μm. The changes in the color of the polymer under heating can also be seen clearly in the successively taken photos during the test (Figure 4.6). The PE polymer has a milky color at lower temperatures and becomes totally transparent at temperatures above 120 °C. The reason behind these changes is obviously related to crystalline structure evolutions since the optical scattering becomes weaker at higher temperatures, especially closer to the melting range of PE [12]. In addition, the comparisons between the $T_\lambda^{i,r}(T)$ and $T_\lambda^{i,\cap}$ of an identical PE sample indicates that the amount of scattered and transmitted light may not be negligible for optically heterogeneous semi-crystalline PE medium, otherwise its temperature-dependent absorption characteristics may be overestimated, due to underestimation of transmittance levels. Consequently, in this study, the temperature-dependent absorption characteristics in semi-crystalline PE was determined characterizing its $T_\lambda^{i,\cap}(T)$ and $R_\lambda^{i,\cap}(T)$.

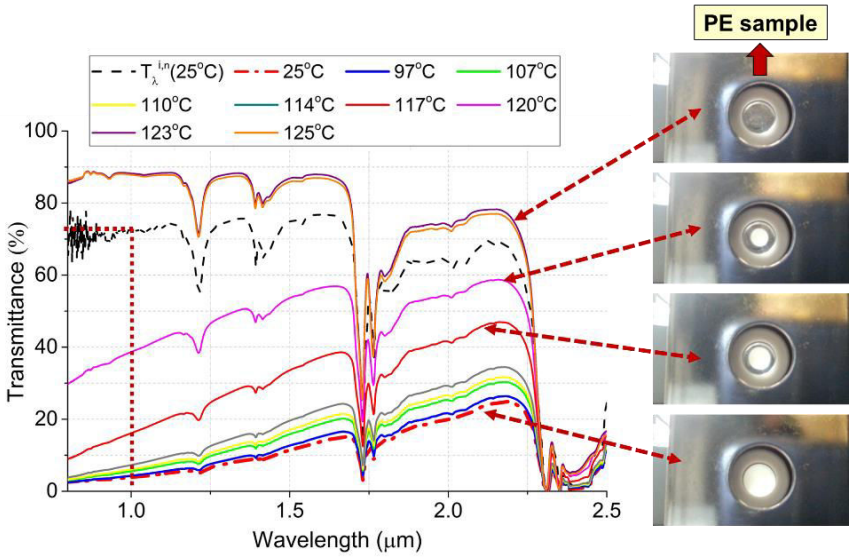

FIGURE 4.6. Comparison between the $T_\lambda^{i,r}(25°C)$ and $T_\lambda^{i,\cap}(25°C)$ of the 0.75mm thick PE-1 QC sample and, the evolution of its $T_\lambda^{i,r}(T)$ under heating condition.

In Figure 4.7, the $T_\lambda^{i,\cap}(T)$ measurements of another 0.75mm thick PE-1 QC sample are presented. It is seen in the figure that the $T_\lambda^{i,\cap}$ of the sample increases under heating where the increase is more

pronounced after 116 ºC, especially in the spectral range of 0.4-1.7µm. This corresponds to temperatures close to the melting range of PE [12]. In addition, no significant change was observed in $T_\lambda^{i,\cap}$ of all the tested 0.25, 0.5 and 0.75mm thick PE-1 QC samples, for the wavelengths greater than 1.7 µm. Concerning the β_λ (T) calculations, it was thus assumed that $T_\lambda^{i,\cap}$ remains unchanged under heating considering the spectrum between 1.7 and 2.5 µm. Furthermore, similar to the trend seen in the $T_\lambda^{i,r}$ (T) measurements, the $T_\lambda^{i,\cap}$ at 1 µm of the 0.75mm thick sample that is around 72% at 25°C increases up to 90% at 128°C. Hence, one can analyze that the $T_\lambda^{i,r}$ (T) and $T_\lambda^{i,\cap}$ of the identically prepared PE-1 QC samples show the same level of transmittance once the polymer becomes transparent above 120°C. It is a clear evidence that PE medium becomes completely optically homogeneous above these temperature, since the $T_\lambda^{i,r}$ (T) and $T_\lambda^{i,\cap}$ measurements obtained from two different FTIRspectrometer are very close. The variation between all the identically prepared and tested samples was found around 0.3 - 0.5 % which can be attributed to small variations in the sample thicknesses. For the sake of brevity in Figure 4.7, the temperature dependent trend in the $T_\lambda^{i,\cap}$ values are presented considering only certain number of measurement steps.

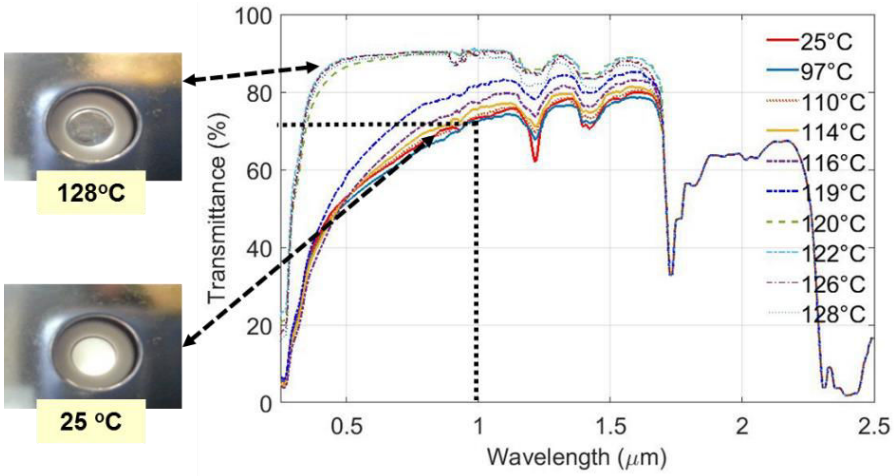

FIGURE 4.7. The $T_\lambda^{i,\cap}$ measurements of 0.75mm thick PE-1 QC samples under varying temperature.

In Figure 4.8 (a) and (b), the $T_\lambda^{i,\cap}$ (T) measures of 0.25 mm and 0.50 mm thick PE-1 QC samples are illustrated, respectively. As it is seen in these figures, the temperature dependent trend in the $T_\lambda^{i,\cap}$ values of 0.25 and 0.5mm thick PE-1 QC samples showed similar behavior to the one presented in Figure 4.7 although, small variations were observed about the temperature at which their $T_\lambda^{i,\cap}$ greatly increases. This might be due to the difference in their optical scattering characteristics that may result from some differences in their crystalline morphology. Indeed, although all the PE samples were quenched into LN_2,

the difference in sample thicknesses can cause some variations in their cooling history and thus in morphology of the quasi-linear PE [13].

In addition, small fluctuations are seen in the range of spectrum greater than 0.85 μm, especially for the transmittance values obtained at high temperatures, as shown in the figures below. This is due to the increased level of background noise in the FTIRmeasurements induced by the heating stage. The heating stage which was positioned at the entrance port of the integrating sphere perturbs the data acquisition of the Lead Sulfide (PbS) detector of the spectrometer, which operates in NIR range [14]. These perturbations were however not seen for the measurement lower than 0.85 μm since the spectrometer switches over to another detector in ultraviolet (UV) - VIS ranges. This limitation was carried out applying noise filtering to the raw data based on median filtering in MATLAB.

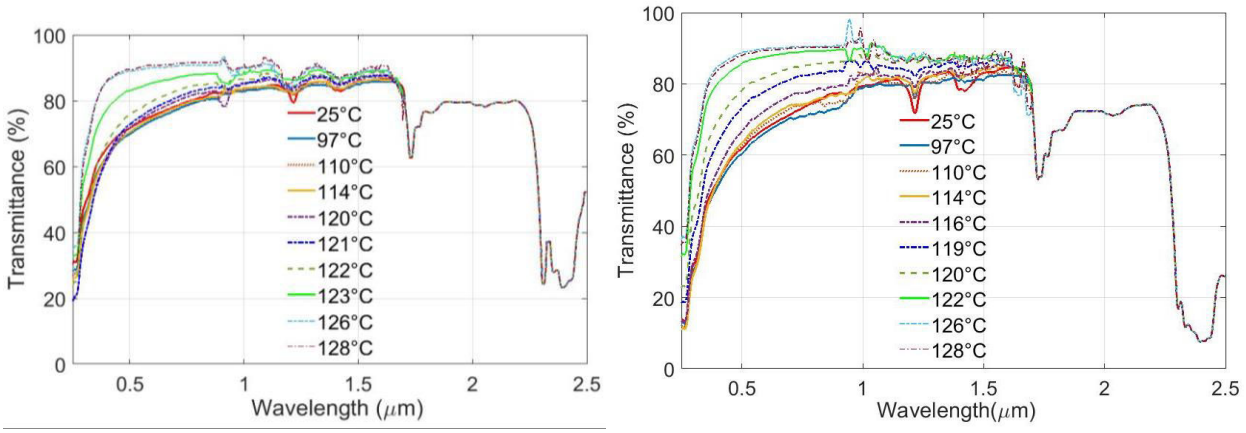

(a) (b)

FIGURE 4.8. The $T_\lambda^{i,\cap}$ (T) measurements of 0.25 mm (a) and 0.50 mm thick (b) PE-1 QC samples.

Apart from noise filtering of the raw data in a specific spectral range, small underestimation in the $T_\lambda^{i,\cap}$ values were observed due to the testing configurations. More specifically, it was found out that the $T_\lambda^{i,\cap}$ values of PE mounted in the heating stage (Setup-1) is slightly lower than the one tested when the same sample is positioned at the entrance port of the integrating sphere (Setup-2). This point was similarly pointed out in the testing standard of ASTM for *Haze and Luminous Transmittance of Transparent Plastics -D1003* [15], where it was suggested that no distance between integrating sphere and an optically heterogeneous medium -also called *hazy* medium -should exist in case of $T_\lambda^{i,\cap}$ measurements. Prior to the $T_\lambda^{i,\cap}$ (T) tests, the $T_\lambda^{i,\cap}$ of each PE-1 QC sample was obtained using the two test setups at 25ºC. For all the tested samples, a clear shift between the measurements of both the test setups was confirmed, as shown for 0.50 mm thick one in Figure 4.9 (a). This is likely due to lack of

detecting part of the forward scattered light from the sample medium. At large angles, the scattered light does not reach to the detector due to the distance between the heating stage and integrating sphere. In Figure 4.9 (b), the schematical illustration of this phenomenon is presented comparing the two testing configurations. In case of neglecting this effect on the $T_\lambda^{i,\cap}$ (T) measurements, it is obvious that the theoretically calculated β_λ (T) would be overestimated due to underestimation of all the light flux transmitted through PE medium.

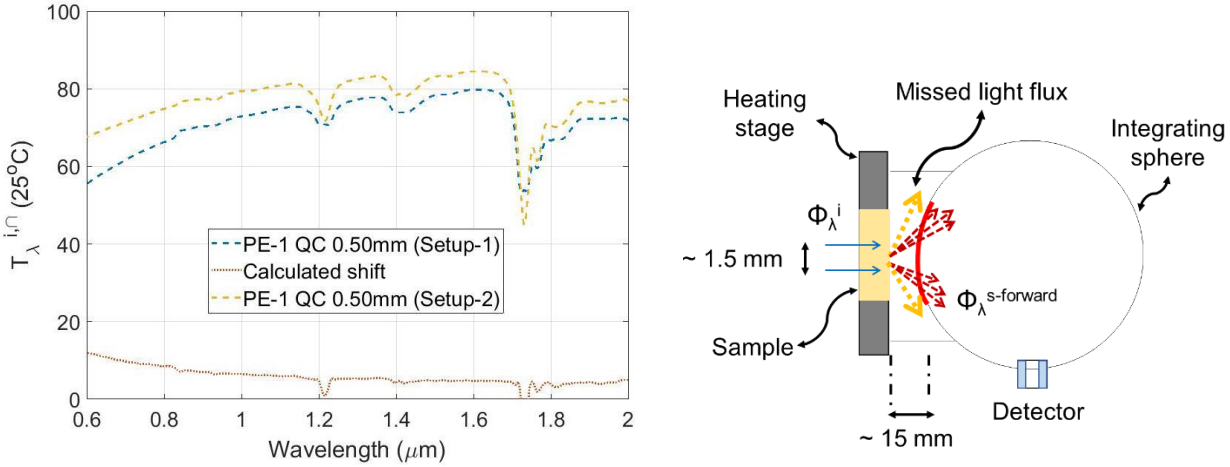

(a) (b)

FIGURE 4.9. The shift between the $T_\lambda^{i,\cap}$ curves of 0.50 mm sample measured at 25°C with and without heating stage (a) and, the schematical illustration of missing light flux when heating stage is in-use (b).

To limit the effects of such technical issue, temperature dependent $T_\lambda^{i,\cap}$ (T) curves were corrected so as to consider the missed light flux for each sample - which is the measured shift between the $T_\lambda^{i,\cap}$ (25°C) curves obtained from each testing configuration-. As this shift varies reciprocally with temperature, a ratio of this missing flux was added to $T_\lambda^{i,\cap}$ (T) of each corresponding sample at each temperature. The ratio of the total flux to be added to the $T_\lambda^{i,\cap}$ (T) of each sample was determined normalizing the $T_\lambda^{i,\cap}$ (T) values adopting min-max normalization. Thus, a normalizing ratio (α) was determined at each single wavelength of each sample, which varies from 0 at 25 °C to 1 around 128°C. In other words, the total amount of missed flux was added to the $T_\lambda^{i,\cap}$ measurements where they show no or negligible increasing trend with temperature. Once the $T_\lambda^{i,\cap}$ values show notable change at higher temperatures, the temperature dependency in the missed flux was considered where the amount of flux to be added to $T_\lambda^{i,\cap}$ (T) was decreased by increase in temperature. For the $T_\lambda^{i,\cap}$ measurements which reach the maximum $T_\lambda^{i,\cap}$ around 128°C, no flux was added. The assumption adopted here may not be wrong in terms of physical phenomenon of light scattering in PE. Because the optical scattering in PE medium becomes weaker

under heating, especially at temperatures close to melting range where after it becomes negligible once the PE medium is completely transparent. The experimental analyses obtained from the $T_{\lambda}^{i,r}(T)$ and $T_{\lambda}^{i,\cap}(T)$ measurements of the identically prepared samples confirm such decreasing trend in the optical scattering behavior of PE. The further details related to the measured shift in the $T_{\lambda}^{i,\cap}$ values of 0.25mm and 0.75mm thick samples, the exponential increasing trend in $T_{\lambda}^{i,\cap}(T)$ at selected wavelengths and min-max normalizations are presented in Annex A.3.5, A.3.6 and A.3.7, respectively.

In contrast to the trend in $T_{\lambda}^{i,\cap}(T)$, an inverse relation between the $R_{\lambda}^{i,\cap}$ of PE and temperature was observed. The $R_{\lambda}^{i,\cap}(T)$ measurements of the 0.25mm, 0.50mm and 0.75mm thick PE-1 QC samples are displayed in Figure 4.10 (a), (b) and (c), respectively. As shown in these plots, the temperature change is less effective on the reflectance of PE in comparison to its temperature-dependent transmittance. Similar to the findings in the $T_{\lambda}^{i,\cap}(T)$ tests, consistency was observed in the decreasing trend in the $R_{\lambda}^{i,\cap}(T)$ of all the tested PE samples tests around 110°C. Regarding to the spectral range between 13 – 20 µm, the reflectance values and the behavior of all the samples are almost identical. Whereas, small variations between the samples are seen in term of reflectance levels at shorter wavelengths. The general trend observed in the spectral range between 2 - 13µm is that the reflectance levels are inversely proportional to the sample thickness, where the 0.75mm thick sample has lower reflectance than the thinner ones in the corresponding range. Although a question may be raised considering the reflectance characteristics of metal plate positioned at the back surface of the PE samples, this may not be the reason for having such an effect. Indeed, once the material becomes fully transparent at high temperatures, the $R_{\lambda}^{i,\cap}$ reduces to 4% which is almost identical for all the tested samples. Considering that the PE medium is semitransparent and, optically heterogeneous due to its crystalline phase, this behavior may be explained by the amount of $\Phi_{\lambda}^{s\text{-}back}$ which is transmitted through the PE medium and reflected back by its bulk medium, but not from the metal surface. Furthermore, identical drops are seen in the $R_{\lambda}^{i,\cap}$ of all the samples in different spectral bands around 3.4, 7.6 and 13.6µm. As reported in detail in Chapter 3, these are absorption bands of PE medium which is induced by its chemical compositions, namely C-H bands [16–18]. Such a reduced level of reflectance in those spectral bands also points out that the crystalline structure may be responsible for the change in the level of reflectance of PE-1 QC samples in different thicknesses. However, further analyses may be required to understand the reflectance and backscattering of heterogeneous PE medium relations, which is out of the scope of this thesis. Nevertheless, in the spectral range between 2 - 13µm, it is seen that the maximum variation between the $R_{\lambda}^{i,\cap}$ of all the samples is around 4%, which is much lower than the variation in the temperature dependent transmittance values of the identical PE-1 QC samples. For the sake of brevity in the figure below, the temperature dependent trend in the $R_{\lambda}^{i,\cap}$ values are presented considering only certain number of measurement steps.

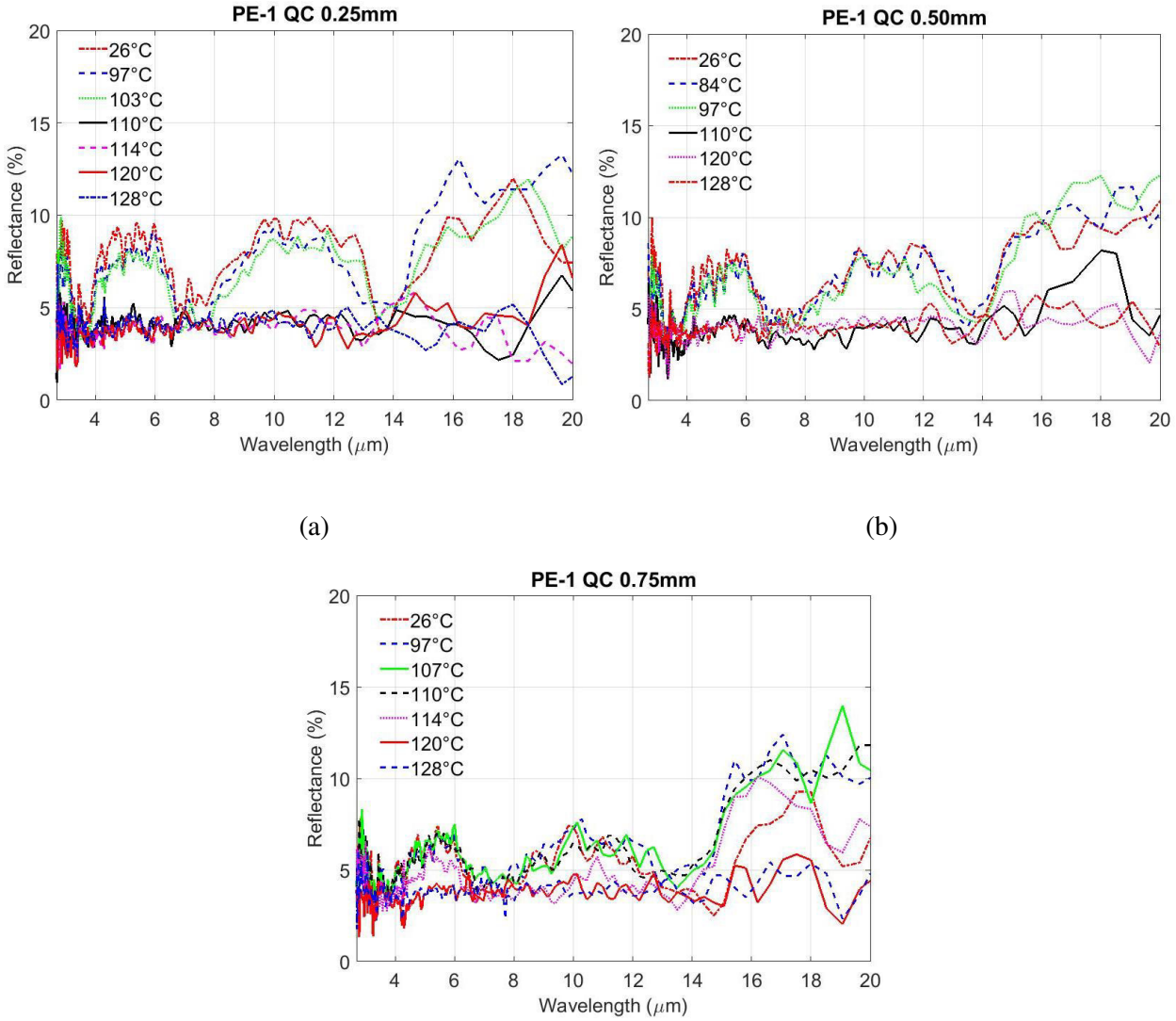

(a) (b)

(c)

FIGURE 4.10. $R_\lambda^{i,\cap}$ measurements of 0.25mm (a), 0.50mm (b) and 0.75mm thick (c) PE-1 QC samples under varying temperature.

In previous studies [12,19], it was found that the strong coupling between crystalline morphology and the transmittance characteristics of PE becomes negligible in MIR range (2-25 μm). It was therefore assumed in this study that the transmittance characteristics of PE in MIR range are independent of temperature. Hence, $T_\lambda^{i,\cap}$ of the PE samples measured at room temperature was adopted for this range. Conversely, no temperature-dependent $R_\lambda^{i,\cap}$ (T) measurements were able to be obtained for the wavelengths smaller than 2 μm, due to the limitations in the spectral response of the employed FTIR devices. Therefore, temperature dependency in the reflectance characteristics of PE was assumed negligible for the wavelengths smaller than 2 μm. Although this is not a rigorous assumption, as discussed

in Chapter 3, the $R_\lambda^{i,\cap}$ tests were done at 25°C in the corresponding spectral range using PE-1 and PE-2 samples prepared with different crystalline structures, but with identical thicknesses. It was observed that the crystalline structure of PE has a slight effect on its $R_\lambda^{i,\cap}$ values, only at shorter wavelengths in VIS range. It was thus assumed the $R_\lambda^{i,\cap}$ of PE is independent of morphological changes under varying temperature.

Hence, based on the measured $T_\lambda^{i,\cap}(T)$, $R_\lambda^{i,\cap}(T)$ and the adopted assumptions, $\beta_\lambda(T)$ of PE was calculated for each temperature considering an optically homogeneous medium. Regarding the conversation of radiative energy (Equation 4.1) and the transmittance and the reflectance characteristics of a semi-transparent optically homogeneous medium (Equation 4.2), β_λ can be calculated [20].

$$A_\lambda^{i,\cap}(T) + T_\lambda^{i,\cap}(T) + R_\lambda^{i,\cap}(T) = 1 \tag{4.1}$$

$$R_\lambda^{i,\cap}(T) = \rho_\lambda\left[1 + \tau_\lambda^{\,2}\frac{(1-\rho_\lambda)^2\tau_\lambda^{\,2}}{1-(\rho_\lambda\tau_\lambda)^2}\right] \text{ and, } T_\lambda^{i,\cap}(T) = \frac{(1-\rho_\lambda)^2\tau_\lambda}{1-(\rho_\lambda\tau_\lambda)^2} \text{ where; } \tau_\lambda = e^{-\beta_\lambda . x} \tag{4.2}$$

In Equation 2, τ_λ and ρ_λ represent intrinsic transmittivity and reflectivity of the PE, respectively [20]. The computation of β_λ at each temperature step was carried out in MATLAB adopting an inverse method based on SQP (Sequential Quadratic Programming) estimation algorithm. In the method, double objective function (J) was created considering the experimental and numerically computed reflectance ($R_{numerical}(T)$) and transmittance ($T_{numerical}(T)$) (Equation 4.3) with multiple iterations. $T_{numerical}$ and $R_{numerical}$ was computed using Equation 4.2 where iteration begins with initial guessed values for ρ_λ and τ_λ. The iterative-based computation was performed until the error condition for J was satisfied and, the ρ_λ, τ_λ values, and eventually β_λ was computed. This computation was done for the each measured $T_\lambda^{i,\cap}(T)$ $R_\lambda^{i,\cap}(T)$ values at each corresponding temperature step. The in-house developed estimation algorithm is explained further in [21].

$$J = \left|\frac{T_\lambda^{i,\cap}(T) - T_{numerical}(T)}{T_\lambda^{i,\cap}(T)}\right| + \left|\frac{R_\lambda^{i,\cap}(T) - R_{numerical}(T)}{R_\lambda^{i,\cap}(T)}\right| \tag{4.3}$$

In Figure 4.11 (b), the computed $\beta_\lambda(T)$ values are presented considering the spectrum between 0.6 - 7 μm and, the temperature dependence in β_λ between 0.6 - 1.6 μm is illustrated in Figure 4.11 (a). Again, for the sake of clarity, some of the computed $\beta_\lambda(T)$ values are not presented in the figure. It is clearly seen that the trend in $\beta_\lambda(T)$ between 0.6 - 1.6 μm is monotonically decreasing under heating while it remains stable for higher wavelength. This is plausible, as the increase in the $T_\lambda^{i,\cap}(T)$ values is significant in this spectrum, as presented in Figure 4.7 and 4.8. In terms of IR heating with an IR lamp, such an evolution in

the thermo-optical properties of semi-crystalline polymers may be crucial as considerable amount of radiation energy may be emitted in the corresponding spectrum. To illustrate this point, the spectral ranges of $E_{\lambda b}$ at 2000 and 2600 K were displayed together with the β_λ (T) of PE in Figure 4.11 (b). Considering the fact that a halogen IR lamp used for ISBM processes has a temperature around 2000 - 2600 K, maximum emission wavelength, λ_{max} (μm), of the lamp should be theoretically around 1.1 - 1.4 μm, regarding to Wien's displacement law [10,20]. In addition, nearly 95% of total energy emitted by such an IR lamp lies between λ_{max} / 2 and $5\lambda_{max}$ which reflects a spectral range roughly between 0.6 - 7 μm [4,10,20]. It can therefore be concluded that the temperature dependence in the thermo-optical properties of semi-crystalline PE seen in NIR range has a significant effect on the amount of absorbed energy, due to both high level of emitted radiation by IR lamp and the variation in its absorption characteristics.

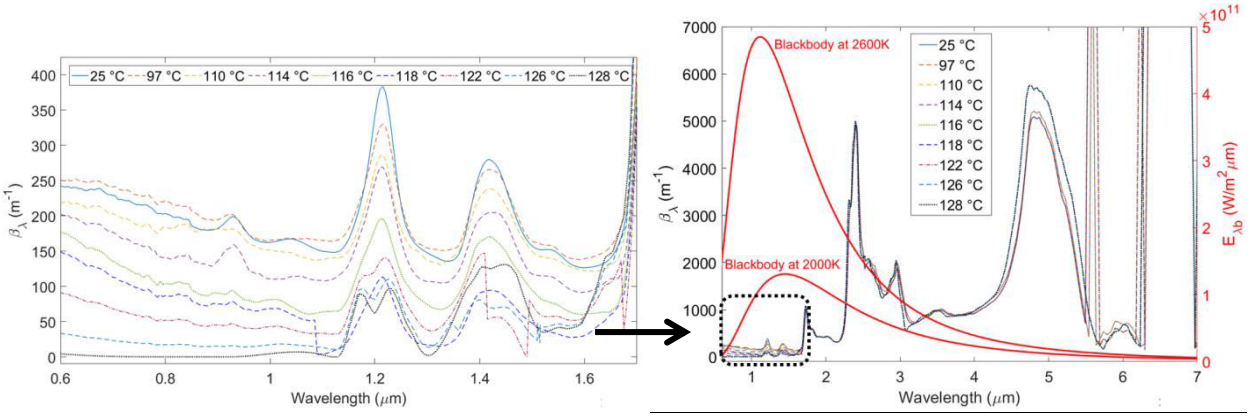

(a) (b)

FIGURE 4.11. The significant variation in β_λ (T) of PE between room temperature and 128 °C (a) and the β_λ (T) values in the spectral ranges of a black body at 2000 and 2600 K (b).

4.3.2. The crystalline structure - optical scattering evolutions of PE under heating and scatterer size predictions

Based on the temperature-dependent transmittance and reflectance characteristics of PE, it was shown in the previous section that the optical scattering behavior of PE becomes weaker under heating. In this section, a comparative analysis was carried out to bridge the crystalline structure evolutions under heating and temperature dependent transmittance characteristics of PE, to highlight the effect of crystal size and melting on the optical scattering behavior in the polymer medium**.** Thanks to this step, it may possible to address the question about: *what is the most probable crystal size that melts and induces significant change in the optical scattering behavior in PE medium under heating?*

In Figure 4.12 (a), the typical trend obtained from the temperature dependent transmittance of identically thick PE-1 QC and AN samples are displayed. Here, in the figure, the $T_{\lambda}^{i,r}$ (T) of the 0.75 mm thick PE-1 AN and QC are compared. As it is seen in the figure, the different crystalline structures introduce different increasing trends in the transmittance values. Under heating condition starting from room temperature, it is likely to happen that phase transitions in PE medium starts to occur as its melting range can extend down as far as room temperature, in return it may include very thin lamellae structures [3]. As reviewed in Chapter 2, regarding the Gibbs Free energy, it is known that thinner crystallites - which are thermodynamically less stable than thicker crystals - melt at lower temperatures than the thicker ones because they have a higher surface-to-volume ratio and hence a relatively greater contribution from the interfacial free energy term [3,22]. To highlight this effect, calorimetric DSC analyses of all the samples used in this study were done at 20 K/min. Based on the DSC measurements of all the samples their X_c was calculated. For the calorimetric analysis of each sample, two small samples were prepared and tested. The determined X_c of each sample used in this study is presented in Table 4.4. The values displayed here are the averaged value of the two DSC scans performed for each sample.

Sample type	PE-1 AN (0.25 & 0.75mm)	PE -1 QC	PE -2 QC	PE-2 AN
X_c (%)	76	67	51	58

TABLE 4.4. The averaged X_c values of the samples calculated from DSC scans at the heating rate of 20 K/min.

In Figure 4.12 (b), the typical melting endotherm obtained from DSC analyses and, the temperature-dependent $T_{\lambda}^{i,r}$ curve of the same PE sample at 1.2 µm are illustrated. The melting endotherm itself may not be indicative in terms of comparisons to the temperature dependent transmittance behavior of PE.

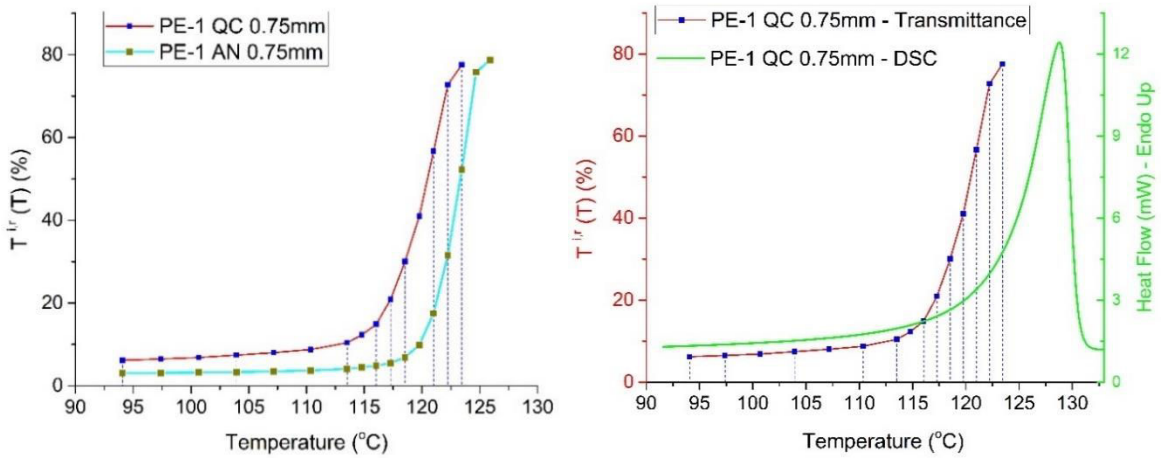

FIGURE 4.12. Typical difference between the increasing trend in the transmittance of PE at the wavelength of 1.2 µm due to different morphology(a), and its similarity to melting endotherm (b).

Following the methodology reviewed in Chapter 2, for each sample studied here, the normalized mass fraction of l_c population distributions and, most probable single l_c that melts at specific temperature was thus analyzed (Equation 2.15 and 2.16). The estimated lamellar morphology was correlated to their temperature dependent transmittance characteristics. Using that methodology, the results can be analyzed through the comparison of four pairs of sample that differ in their morphology and thickness. The Table 4.5 displays the sample pairs used for the comparative analyses. The Table 4.5 is reproduced from Table 4.1, for the sake of clarity in this section. Besides the two types of transmittance measurements, both the transmittance characteristics of PE under room and varying temperature showed that the optical scattering in PE is wavelength dependent, which varies strongly in VIS and NIR ranges. Therefore, in this study, we chose only two different monochromatic wavelengths, 632.7 nm and 800 nm, for the comparisons. The former wavelength was chosen to enable bridging the analyses presented here to the MALS tests performed at this wavelength using PE-1 and PE-2 polymers prepared with different morphology, as discussed in Chapter 3.

The discussions were started with the comparisons based on the $T_\lambda^{i,r}(T)$ measurements of annealed PE-1 and PE-2. Although $T_\lambda^{i,\cap}(T)$ data may enable to calculate the most accurate radiation absorption parameter of PE, it was illustrated in Figure 4.6 that the change in $T_\lambda^{i,r}$ of the polymer under varying temperature is much more significant, because of the strong forward scattering. The temperature dependent $T_\lambda^{i,\cap}$ of PE may also help to understand the change in the light backscattering behavior as both $\Phi_\lambda^{s\text{-forward}}$ and Φ_λ^{t} could be detected. This is analyzed through the comparison of data recorded for the samples of the second and third pairs. The analyses were extended using the fourth pair of sample to highlight the relation between lamellar crystal melting and evolution in the backward - forward scattering

in PE-1 medium under heating. These analyses helped to do a first estimation on the equivalent scatterer size in PE-1 under the assumption of perfectly spherical scatterer.

Sample pairs	Sample thicknesses	Transmittance measurement	Monochromatic wavelength for the comparisons
PE-1 AN & PE -2 AN	0.25	$T_\lambda^{i,r}$ (T)	632.7 and 800nm
PE-1 QC & PE-2 QC	0.25	$T_\lambda^{i,\cap}$ (T)	
PE-1 QC & PE-1 AN	0.25	$T_\lambda^{i,\cap}$ (T)	
PE-1 AN & PE-1 AN	0.25 and 0.75	$T_\lambda^{i,r}$ (T) and $T_\lambda^{i,\cap}$ (T)	

TABLE 4.5. Overview of the comparative analysis on the crystalline structure - optical scattering evolutions of PE.

Before correlating the temperature-dependent transmittance measurements to the l_c distributions of PE, a conversion between the different scales of l_c distributions is shown in Figure 4.13 (a) and (b). In the figure, as presented before in Chapter 3, Figure 4.13 (a) represents classical the relation between the most probable single l_c (x axis) and its normalized mass fraction (y axis) [22], which has a thickness in the range of L and L+dL and melts between the temperature T and T+dT (Equation 2.16). In order to correlate the melting temperature of most probable l_c to the temperature steps of the transmittance measurements, the reciprocal of most probable l_c ($1/l_c$ (nm^{-1})) and its corresponding melting temperature was plotted, as shown in Figure 4.13 (b).

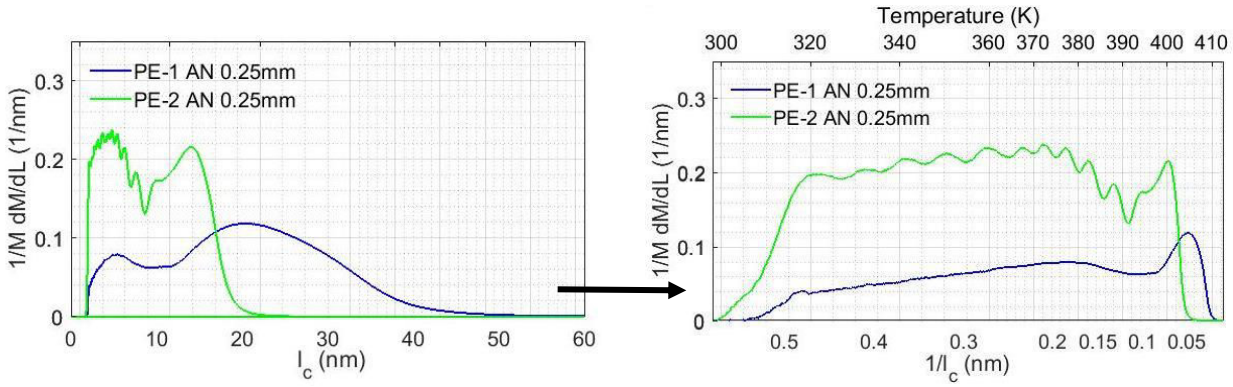

FIGURE 4.13. The normalized mass fraction of the most probable l_c (a), and its representation in terms of melting temperature of most probable $1/l_c$ (nm^{-1}) (b).

Therefore, in this section, the reciprocal l_c distributions ($1/l_c$ (nm^{-1})) and its temperature-dependency is presented for the comparative analyses. In Figure 4.14, the increasing trend in the $T_\lambda^{i,r}$ of the 0.25mm thick PE-1 AN and PE-2 AN samples were compared at monochromatic wavelengths at 632.7 nm (a) and 800 nm (b). In the figure below, the dashed lines show the correlation between the $T_\lambda^{i,r}$ of both type of PE samples and the reciprocal l_c distributions (c). The colors of the dashed lines were chosen appropriately with the color of the transmittance values and the reciprocal l_c distributions of each PE sample.

Considering the $T_\lambda^{i,r}$ of both type of 0.25 mm thick PE samples and their lamellar morphology, three different points can be discussed here. First of all, clear difference between the $T_\lambda^{i,r}$ behavior and the bimodal l_c population distributions of 0.25 mm thick PE-1 and PE-2 samples is seen. In comparison to the initial $T_\lambda^{i,r}$ value of PE-1 at room temperature, its value does not increase up to 380 K where after a small increase is seen between 380 - 392 K which reflects most probable l_c around 6 - 8 nm. In addition, it was observed that this behavior is identical at 632.7 (a) and 800 nm (b). Similar increase in the $T_\lambda^{i,r}$ of PE-2 is seen between 370 - 380 K which reflects slightly thinner lamellae around 4 - 6nm. Therefore, it may be stated that the melting of crystals that lie in the 1st peak of their bimodal population distributions may be the responsible for a small increase in the $T_\lambda^{i,r}$ levels of both type of PE. Secondly, the significant increase in the $T_\lambda^{i,r}$ of PE-1 is between 394 - 403 K whereas this increase is distinctively lower for PE-2, which is between 381 - 391 K. As shown with the vertical dashed lines in the figure below, the correlation from this temperature range to the reciprocal l_c distributions reveals that the most probable l_c which have thicknesses greater than 10 nm (or 0.1 nm^{-1} in the figure) may be responsible for such a change in the $T_\lambda^{i,r}$ of PE-1. Whereas, melting of crystals which is thicker than 6 nm (around 0.16 nm^{-1} in the figure) results in a dramatic change in the $T_\lambda^{i,r}$ of PE-2. Regarding the bimodal population distributions of l_c in PE-1 and PE-2, it is seen that the l_c values greater than 10 nm and 6 nm reflect the 2nd peak of the reciprocal population distributions (Figure 4.14 (c)). Although the minimum l_c sizes of both PE polymers are close to each other, the 2nd peak of their bimodal distributions are quite different where PE-1 has probability to have much thicker lamellae, up to 50 nm. Therefore, PE-1 may have significant jump at least 13 K higher than the PE-2, as thicker crystals potentially melts at higher temperatures in comparison to thinner crystals.

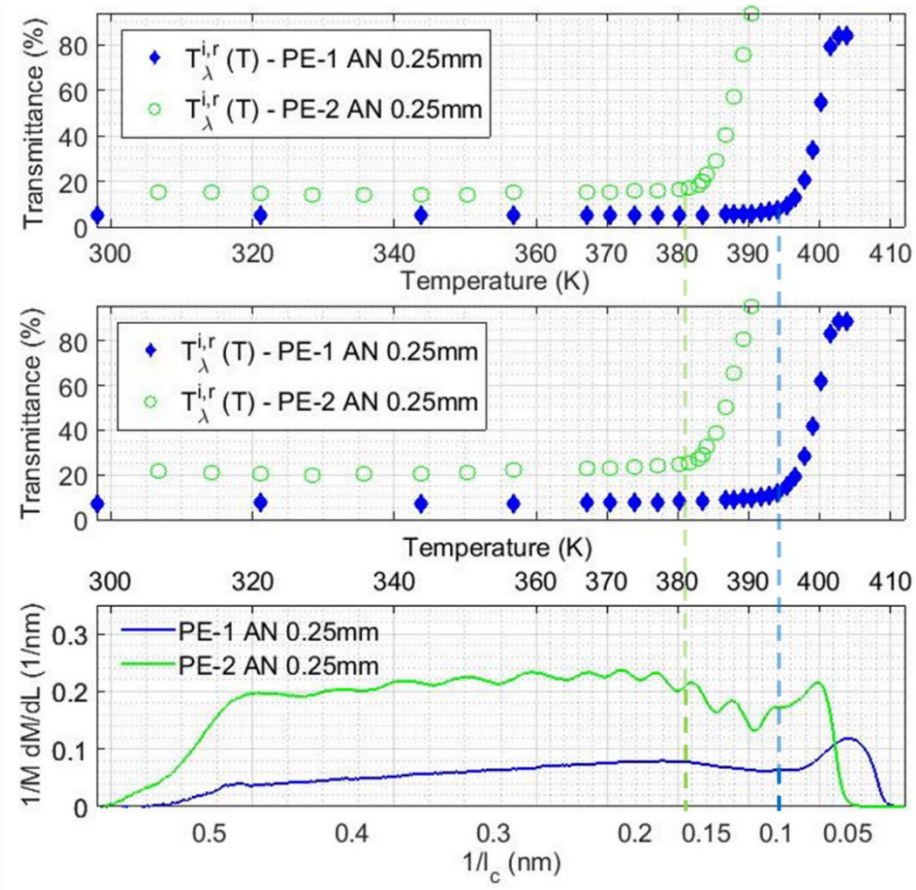

FIGURE 4.14. The temperature dependent increase in the $T_\lambda^{i,r}$ of PE-1 AN and PE-2 AN at λ=632.7nm (a) and 800nm (b) and, their correlations to the melting of most probable crystals (c).

In Figure 4.15 (a), (b) and (c), similar correlations between the $T_\lambda^{i,\cap}(T)$ - l_c distributions of 0.25 mm thick PE-1 QC and PE-2 QC samples are shown. In the similar manner observed in Figure 4.14, the $T_\lambda^{i,\cap}(T)$ of PE-1 increased significantly around 390 K - 401 K, which is slightly lower than the previous comparison. Correlation of this temperature range to the l_c distribution of PE-1 QC shows that melting of 7 - 15 nm thick crystals, which are thinner than the previous case, results to have such a dramatic increase in its $T_\lambda^{i,\cap}(T)$. The $T_\lambda^{i,\cap}(T)$ of PE-2 shows a dramatic increase after 370 K, which is around 20 K lower than the trend observed in the $T_\lambda^{i,\cap}(T)$ of PE-1. In addition, the $T_\lambda^{i,\cap}(T)$ of PE-2 reaches its maximum value again around 395 K. Regarding to l_c distributions of PE-2 QC (Figure 4.15 (c)), 4 - 9 nm thick lamellar crystals may be responsible for the increasing trend. For both PE-1 and PE-2, the increasing trend seen at reduced temperature levels may refer to directional dependency of scattering behavior which is involved differently in the two different transmittance measurements. Because, $T_\lambda^{i,\cap}(T)$ measurements done with integrating sphere may only be indicative for the change in backscattered light, whereas $T_\lambda^{i,r}$ (T) may reflect the variation in the optical scattering in both forward and back directions. It should be

emphasized here again that, stepwise heating was applied for the temperature dependent transmittance tests, where also the samples were heated for 2 minutes between each consecutive temperature step. However, l_c distributions of the same PE QC samples were obtained at a heating rate of 20K/min. Thus, the lamellar morphology of the stepwise heated PE QC samples potentially reorganizes under heating which may result a small shift in their reciprocal l_c distributions presented here. Therefore, the correlations shown here can only be qualitative for all the QC samples. Such reorganization under stepwise heating may still be assumed negligible for the AN samples on more rigorous basis. Because, the AN samples presented here were prepared applying thermal fractionation by isothermal stepwise cooling. Thus, it is theoretically supposed to have thermodynamically more stable crystals under annealing [23,24].

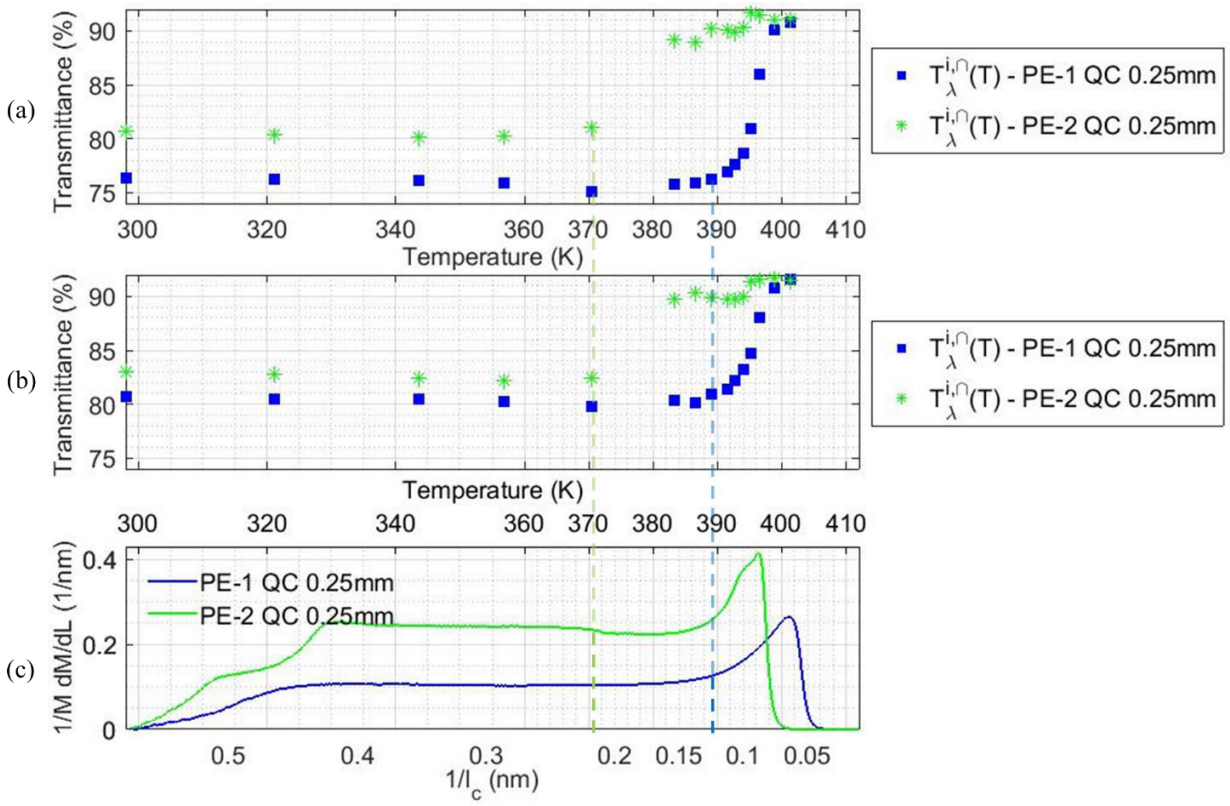

FIGURE 4.15. The temperature dependent increase in the $T_\lambda^{i,\cap}$ of PE-1 QC and PE-2 QC at λ=632.7 nm (a) and 800nm (b) and, their correlations to the melting of most probable crystals (c).

The difference in the temperature dependent transmittance - crystalline phase evolutions is presented so far considering two different types of PE, where a significant difference in their both the $T_\lambda^{i,r}$(T), $T_\lambda^{i,\cap}$(T) values, as well as l_c distributions was observed. In Figure 4.16 (a), (b) and (c), same type of polymer, PE-1, was analyzed considering QC and AN conditions. Interestingly, it is seen in Figure 4.16 (a) and (b) that the $T_\lambda^{i,\cap}$(T) of PE-1 QC and AN show a significant increase around the same temperature - 390 K - whereas, PE-1 AN reaches its maximum $T_\lambda^{i,\cap}$ value at a temperature somewhat lower than the one

observed for the PE-1 QC sample. Considering their reciprocal l_c distributions, the 2nd peak of the bimodal distribution is different. In addition, based on the initial values of $T_\lambda^{i,\cap}$ obtained at 298 K, it is clearly seen that the backscattering in PE-1 AN medium is slightly stronger than the PE-1 QC. We can extend this comparison including the initial $T_\lambda^{i,\cap}$ of identically thick PE-2 QC -which is shown in the previous figure- and, the l_c distributions of these PE-1 QC / AN and PE-2 QC samples. The thicker the lamellar population distributions, the slightly lower the initial $T_\lambda^{i,\cap}$, and thus stronger backscattering, in the identically thick PE medium can be observed. This trend is in accordance with the angular scattered light distributions of the identical samples measured via MALS tests (Chapter 3). The thickening in lamellar morphology, particularly seen as a shift in 2nd peak of the bimodal distributions, causes to have slightly stronger backscattering, indicating that reduced size of equivalent scatterer with an increase in the l_c distributions. Again, this point strengthens the fact that equivalent scatterer size in PE may not identified based on only lamellar morphology, but probably some entities greater than lamellar crystals, which is ambiguous to identify at this stage. Nevertheless, the role of lamellar morphology in the temperature-optical scattering behavior in PE medium is demonstrated here.

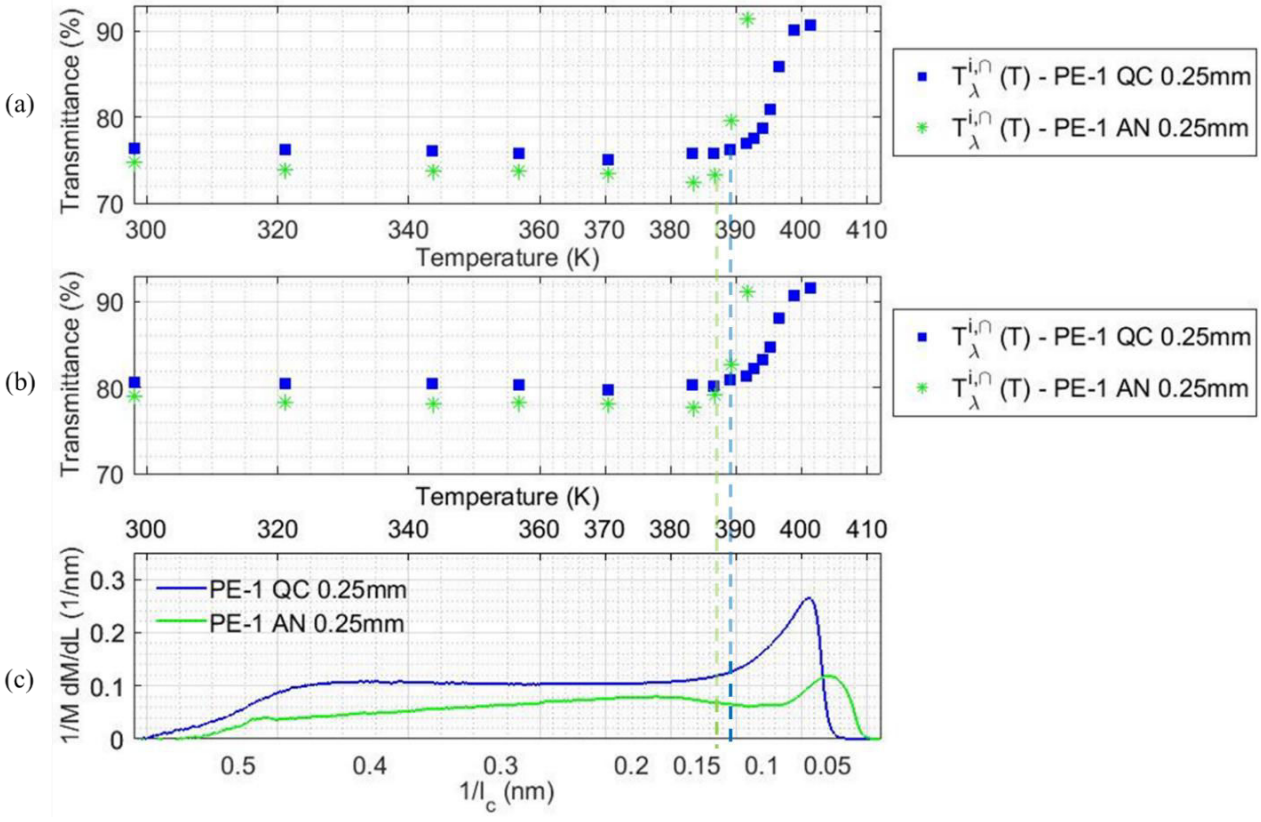

FIGURE 4.16. The temperature dependent increase in the $T_\lambda^{i,\cap}$ of PE-1 QC and PE-1 AN at λ=632.7nm (a) and 800nm (b) and, their correlations to the melting of most probable crystals (c).

As displayed in Figure 4.17 (a), (b) and (c), the increasing trend in the $T_\lambda^{i,\cap}(T)$ of 0.75mm thick PE-1 AN is identical to the trend observed in the $T_\lambda^{i,\cap}(T)$ of tested other PE-1 samples. Considering the analyses on the $T_\lambda^{i,\cap}(T)$ of different PE-1 samples prepared in different thicknesses and morphologies, it can be stated that melting of lamellar crystals, which has sizes likely between 1st and 2nd peak of the population distributions, governs the path of increasing trend in the transmittance. In addition, the size of crystal playing a role in back and forward scattering may be different. In comparison to the $T_\lambda^{i,r}(T)$ of 0.25 mm thick PE-1 AN presented in Figure 4.14, one can be seen that the increase in the $T_\lambda^{i,\cap}(T)$ of the identical PE-1 AN sample is slightly lower, which is below 390 K.

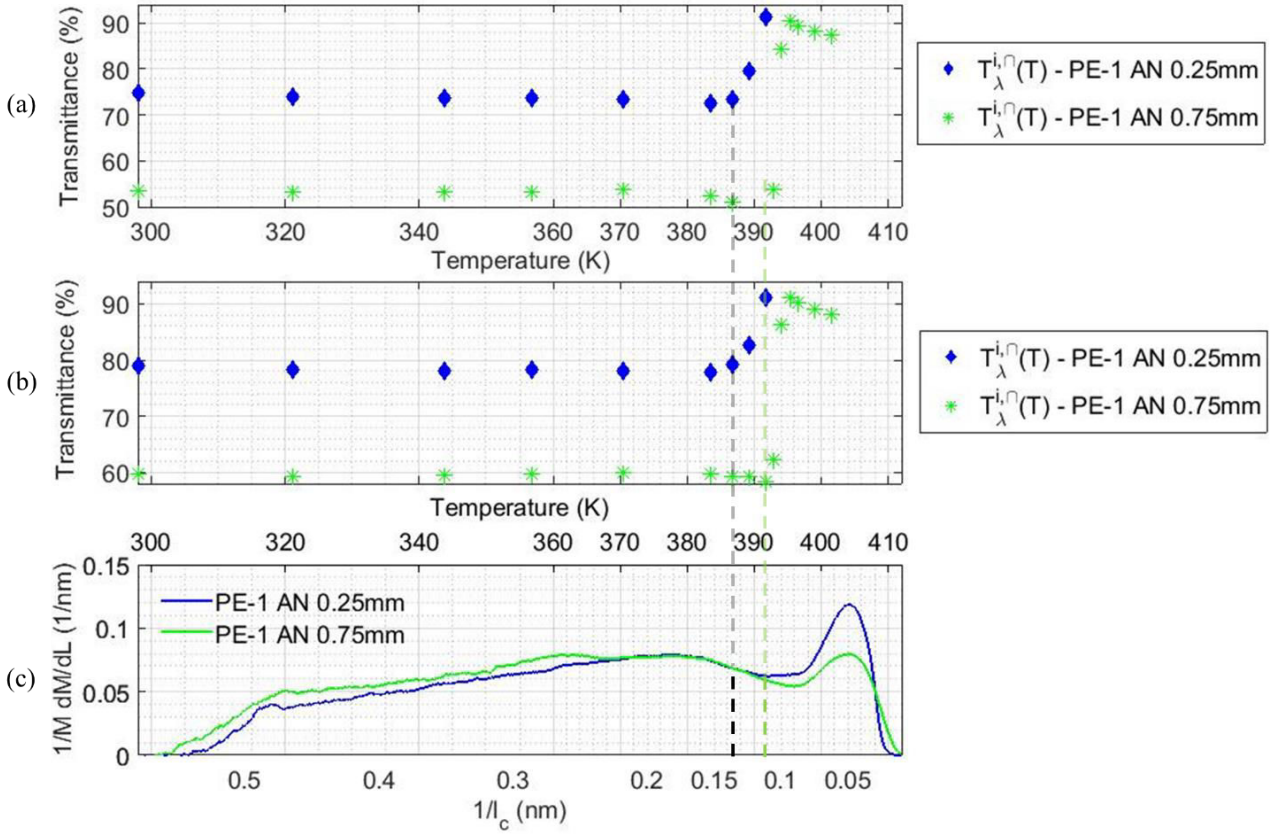

FIGURE 4.17. The temperature dependent increase in the $T_\lambda^{i,\cap}$ of 0.25mm and 0.75mm thick PE-1 AN at λ=632.7nm (a) and 800nm (b) and, their correlations to the melting of most probable crystals (c).

In order to analyze this point further, the $T_\lambda^{i,r}(T)$ and $T_\lambda^{i,\cap}(T)$ of identically prepared 0.25mm thick PE-1 samples were compared. The increasing trend in the $T_\lambda^{i,r}(T)$ and $T_\lambda^{i,\cap}(T)$ of 0.25mm thick PE-1 AN and its correlation to its l_c distributions is presented in Figure 4.18 (a), (b) and (c). First of all, regardless of the type of PE polymer, morphological characteristics, or type of transmittance measurements, the identically thick PE medium gives the same level of transmittance once it is in melting

range. This is a clear evidence that PE medium becomes fully optically homogeneous, which similarly observed in the other comparisons shown here. Whereas, as shown in Figure 4.14 and 4.16, small variations in the $T_\lambda^{i,r}(T)$ or $T_\lambda^{i,\cap}(T)$ levels may be seen at these temperatures which is probably due to the interfilm thickness variations. In addition, at both 632.7 nm and 800 nm, it is clearly seen that the increasing trend is somewhat different for the two types of transmittance measurements. $T_\lambda^{i,\cap}(T)$ shows a great jump around 387 K while this trend is seen in the $T_\lambda^{i,r}(T)$ values around 394 K. Furthermore, the difference is more significant between the temperatures at which both the $T_\lambda^{i,\cap}(T)$ and $T_\lambda^{i,r}(T)$ becomes maximum, even though both the transmittance values are almost identical. Interestingly, regarding the maximum transmittance reached in the $T_\lambda^{i,\cap}(T)$ and $T_\lambda^{i,r}(T)$ values, the temperature is around 392 K and 403 K, respectively. Correlating these temperatures to the l_c distributions of the sample shows that the crystals that melt between 387 - 392 K lie in the 1st peak of the population distributions. This temperature range refers to lamellae thicknesses between 7 - 9nm (or 0.11 and 0.14 1/nm, as seen in the figure). Whereas, regarding the significant increase in the $T_\lambda^{i,r}(T)$ measurements, the most probable crystal that melts and causes to weaken optical scattering behavior should be around 10 to 20 nm.

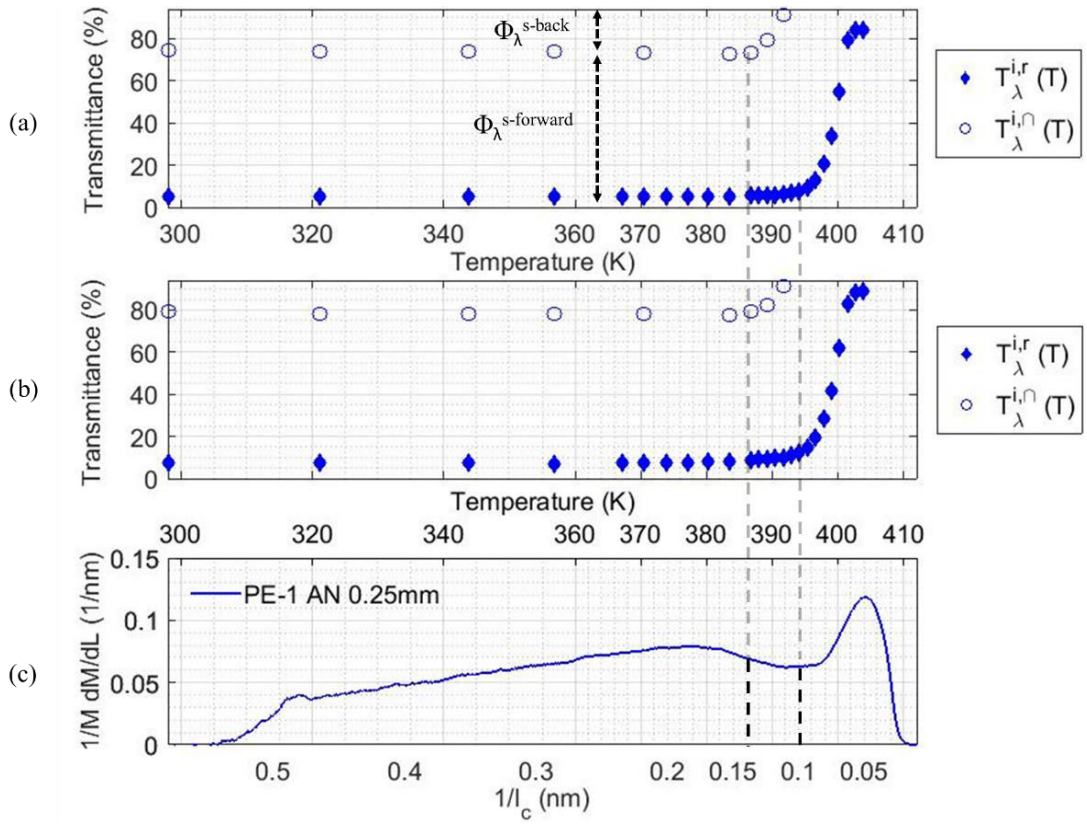

FIGURE 4.18. The temperature dependent increase in the $T_\lambda^{i,r}(T)$ and $T_\lambda^{i,\cap}(T)$ of 0.25mm thick PE-1 AN at λ=632.7nm (a) and 800nm (b) and, their correlations to the melting of most probable crystals (c).

Similar trend was also observed in the $T_\lambda^{i,r}(T)$ and $T_\lambda^{i,\cap}(T)$ of 0.75mm PE-1 AN, whereas it was found that the difference between both the type of transmittance measurements is less pronounced (Annex A 3.8). Regarding the theory [20,25], this may be plausible based on the spatial distribution of scattered light - ξ relations, as explained in Chapter 2. Considering optical scattering at a constant wavelength from two different spherical scatterers in different radii, the smaller scatterer should have smaller ξ value (Equation 2.14) indicating greater fraction of backscattering, as shown in Figure 2.11 (a). Hence, for the case analyzed in Figure 4.18, it may be stated that the smaller crystals which are likely responsible for greater amount of backscattering, which melts earlier than the thicker crystals. Consequently, the increase in the $T_\lambda^{i,\cap}(T)$ values is seen at lower temperatures than the $T_\lambda^{i,r}(T)$.

This point can be analyzed further considering the obtained light fluxes from the two different transmittance measurements, and also their wavelength dependency. As explained before, $T_\lambda^{i,\cap}(T)$ may help to understand the change in the behavior of backscattered light as, both $\Phi_\lambda^{s\text{-}forward}$ and Φ_λ^{t} could be detected using an integrating sphere in this measurement. Based on the assumption that the reflected light flux from the PE surface is independent of temperature, the increasing trend observed in the $T_\lambda^{i,\cap}$ values may point out the reduced amount of $\Phi_\lambda^{s\text{-}back}$ under heating. In contrast, it is likely to happen that the variation in both $\Phi_\lambda^{s\text{-}back}$ and $\Phi_\lambda^{s\text{-}forward}$ causes a change in the $T_\lambda^{i,r}(T)$ values. Using the difference between the $T_\lambda^{i,r}$ (25°C) and $T_\lambda^{i,\cap}$ (25°C), $\Phi_\lambda^{s\text{-}forward}$ can be estimated. Similarly, the difference between the maximum transmittance value seen in the melting range and $T_\lambda^{i,\cap}$ (25°C) enables to estimate $\Phi_\lambda^{s\text{-}back}$. Based on this assumption, at 800nm, the $\Phi_\lambda^{s\text{-}back}$ of 0.25 mm thick PE-1 AN is around 10% while the $\Phi_\lambda^{s\text{-}forward}$ is a lot higher, which is around 70%, as displayed in Figure 4.18 (b). Furthermore, at 632.7nm, the $\Phi_\lambda^{s\text{-}forward}$ and $\Phi_\lambda^{s\text{-}back}$ were found around 66% and 16%, respectively (Figure 4.18 (a)). Further comparisons at different monochromatic wavelengths showed that the ratio of $\Phi_\lambda^{s\text{-}forward}$ / $\Phi_\lambda^{s\text{-}back}$ reduces for shorter wavelengths in VIS range. In other words, the amount of backscattered light flux increases at shorter wavelengths. At 330 nm, this ratio becomes equal so that, both the fraction of $\Phi_\lambda^{s\text{-}forward}$ and $\Phi_\lambda^{s\text{-}back}$ is close to be identical. In Annex A 3.9 and 3.10, the comparisons between the $T_\lambda^{i,r}(T)$ and $T_\lambda^{i,\cap}(T)$ measurements of 0.25 mm and 0.75 mm thick PE-1 AN at 330 nm and 450 nm are presented, respectively. As also stressed in Chapter 2, Rayleigh theory can be convenient to predict ϕ_λ only when spherical scatterer size is much smaller than monochromatic wavelength. More specifically, the theory can be dedicated for the scatterer sizes that are much smaller than the wavelength, or simply with $\xi < 0.1$ [20]. As a quick guess at 330 nm, if we assume that scattering in PE medium follows Rayleigh scattering theory, the $\phi_{\lambda\text{-}Rayleigh}$ shows balanced fraction for $\Phi_\lambda^{s\text{-}forward}$ and $\Phi_\lambda^{s\text{-}back}$ for unpolarized light flux when ξ = 0.1 [20,25]. Then the size of spherical scatterer inside of PE medium may be estimated at this

monochromatic wavelength using Equation 2.14. That equation is restated here (Equation 4.4) to show the relation between the and radius of scatterer (r), and the calculated radius of the spherical scatterer:

$$\xi = \frac{2\pi r}{\lambda_m} \quad \text{assuming that } \xi = 0.1 \text{ at } \lambda_m = 330 \text{ nm};\ r \approx 5.5 \text{ nm} \tag{4.4}$$

Based on the assumptions and the measured $T_\lambda^{i,r}$ (T) and $T_\lambda^{i,\cap}$ (T) at room temperature, the calculated value for the scatterer size interestingly lies in the l_c distributions, which was found around 5.5nm. The synthesized analyses of this chapter and Chapter 3 indicate that the optical scattering behavior in PE medium may not be only related to lamellar morphology, but also the amount or number of equivalent scatterer in PE medium. This may point may be strengthened considering the $\Phi_\lambda^{s\text{-forward}}$ and $\Phi_\lambda^{s\text{-back}}$ of 0.75mm thick PE-1 AN, where the fraction of $\Phi_\lambda^{s\text{-back}}$ is much greater than the one seen in 0.25mm thick PE-1 AN (Annex A.3.9). In addition to this, the analyses on the $\Phi_\lambda^{s\text{-forward}}$ and $\Phi_\lambda^{s\text{-back}}$ at room temperature indicated that the optical scattering behavior in PE medium may not be only related to lamellar morphology, but also some entities greater than lamellar crystals. Apart from that, as also discussed in Chapter 2, the size and shape of scatterer in semi-crystalline PE medium is unknown, which can be defined either in arbitrary or spherical shapes. Whereas, a simple estimation done here is based on perfectly spherical scatterers. Therefore, there is no clear evidence at this stage to propose a unique equivalent scatterer size and quantity for any type of PE polymer prepared at various morphological state. Nevertheless, the approach shown above can be extended further considering wavelength, temperature and morphology dependency of optical scattering in any type of semi-crystalline polymer medium, to identify equivalent scatterer size and its evolution under heating. However, this is beyond of the scope of this thesis. Therefore, here only the existence of the relation between scatterer and crystalline phase evolutions in PE medium was highlighted based on the experimental analyses and theoretical approach.

4.4. Summary

The temperature dependence in the optical properties of PE, namely transmittance and reflectance characteristics, were experimentally analyzed under heating condition. The experimental analyses showed that the change in the optical properties, in particular transmittance characteristics, under heating is related to change in the optical scattering behavior in PE medium since it is strongly affected by its crystalline structure, whereas a slight effect of temperature dependency was observed on the reflectance characteristics of PE. Using the temperature dependent transmittance and reflectance levels of PE, temperature-dependent thermo-optical properties of PE - β_λ (T) - was determined. The calculated β_λ (T) values showed a decreasing trend under heating which indicates that potentially absorbed radiation inside of PE medium may be weakened, especially at temperatures close to its melting range. This temperature

dependent parameter of PE may be adopted as a radiation absorption parameter for radiation heat transfer modeling of PE so that a potential change in the radiation absorption inside of PE medium may be taken into account. This is not likely due to stronger absorption behavior inside of PE medium, but due to weakening in the optical scattering behavior of PE under heating. Considering the samples prepared with identical thickness, all the $T_\lambda^{i,r}(T)$ and $T_\lambda^{i,\cap}(T)$ tests up to melting range confirmed that no matter what type of PE, morphology or transmittance measurements is used, the PE medium reaches almost identical level of transmittance. It is a clear evident indicating that polymer medium becomes fully optically homogeneous once it is in melting range and thus, optical scattering becomes negligible.

The relation between crystalline structure – optical scattering behavior evolutions were analyzed further performing comparative analysis including $T_\lambda^{i,r}(T)$ and $T_\lambda^{i,\cap}(T)$ measurements of PE-1 and PE-2 polymers prepared in different thicknesses and morphologies. The comparisons were done at two monochromatic wavelengths, at 632.7 nm and 800 nm. It was generally observed that the crystals which lie between the end of the 1st peak up to the 2nd peak of the bimodal l_c distributions mainly govern the path of dramatic increase in the transmittance. However, the level of transmittance may not be only due to l_c distributions, but also the amount or number of equivalent scatterer in PE medium, which is ambiguous to identify based on the analyses carried out here. For both PE-1 and PE-2, it was found that the increasing trend in the $T_\lambda^{i,\cap}(T)$ occurs at temperature levels lower than the ones observed in the $T_\lambda^{i,r}(T)$ measurements. Considering the optically heterogeneous medium of PE, the $T_\lambda^{i,\cap}(T)$ measurements may only be indicative for the change in backscattering of its medium, where also $T_\lambda^{i,r}(T)$ may reflect the variation in the optical scattering in both forward and back directions. Such a behavior can be explained by the size of melting lamellar crystals and directional dependency of optical scattering as a function of scatterer size. Thus, we believe that the thinner crystals in the 1st peak of the bimodal distributions, which are likely responsible for greater amount of backscattering, melts earlier than the thicker crystals and hence, increase in the $T_\lambda^{i,\cap}(T)$ values is seen at lower temperatures than the $T_\lambda^{i,r}(T)$. Although it may seem that this point contradicts the observed relations between lamellae thickening and backscattering in PE at room temperature (which is discussed in detail in Chapter 3), this may be explained by the size distributions of equivalent scatterers in PE medium. In other words, as aforementioned, the equivalent scatterer size in PE medium may not be identified with a mono-sized entity, but with scatterers which has a size range or histogram. In that sense, it would be plausible to have a reduced size of equivalent scatterer induced by thickening in lamellar morphology, since lamellar crystals probably represents the relatively smaller scatterers in PE medium. In the similar manner, melting of thinner crystals may increase the population of greater scatterers -and thus equivalent scatterer size - which potentially reduces backscattering, regarding to light scattering theory.

The directional dependency in optical scattering and the size of molten crystals relations were analyzed further considering the comparisons between the $T_{\lambda}^{i,r}(T)$ and $T_{\lambda}^{i,\cap}(T)$ of identically prepared PE-1 samples at various wavelengths in VIS range. It was observed that the ratio of $\Phi_{\lambda}^{s\text{-forward}}$ / $\Phi_{\lambda}^{s\text{-back}}$ reduces for smaller wavelengths in this spectral range. In other words, the amount of backscattered light flux increases at shorter wavelengths. For instance, for the 0.25mm thick PE-1 AN samples this ratio became equal at 330 nm so that, both the fraction of $\Phi_{\lambda}^{s\text{-forward}}$ and $\Phi_{\lambda}^{s\text{-back}}$ is close to be identical. As a simple estimation, it was assumed that scattering in PE medium follows Rayleigh scattering theory. Considering that $\phi_{\lambda\text{-Rayleigh}}$ shows a balanced $\Phi_{\lambda}^{s\text{-forward}}$ and $\Phi_{\lambda}^{s\text{-back}}$ for unpolarized light flux when $\xi = 0.1$, the size of scatterer was calculated at the wavelength of 330 nm. The radius of spherical scatterer was found around 5.5 nm which interestingly lies in the l_c distributions of the tested sample. Nevertheless, there is no clear evidence to propose a unique scatterer size and quantity for any type of PE polymer prepared at various morphological states. Because, again, the directional scattering light - equivalent scatterer size estimations was done here using the relation developed for perfectly spherical scatterers, which is a remarkable uncertainty for the crystalline morphology of PE. The synthesized analyses of this chapter and Chapter 3 indicate that the optical scattering behavior in PE medium may not be only related to lamellar morphology, but also to some entities greater than lamellar crystals. In this chapter, only the relation between temperature-dependent optical scattering behavior and the crystalline phase evolutions, particularly lamellar melting, in PE medium was highlighted based on the experimental analyses and theoretical approach. This approach can be extended further considering wavelength, temperature and morphology dependency of optical scattering in any type of semi-crystalline polymer medium, to identify equivalent scatterer size and its evolution under heating, which is beyond of the scope of the thesis.

References

[1] Wunderlich B. Thermal analysis of polymeric materials. Berlin: Springer; 2005.
[2] Michler GH. Electron microscopic investigations of morphology and structure formation of polymers. J Macromol Sci Part B 1996;35:329–55.
[3] Peacock AJ. Handbook of polyethylene: structures, properties, and applications. New York: Marcel Dekker; 2000.
[4] Le Maoult Y, Schmidt F. Infrared Radiation Applied to Polymer Processes. John Wiley & Sons, Inc; 2016.
[5] Monteix S, Maoult YL, Schmidt F, Arcens JP. Quantitative infrared thermography applied to blow moulding process: measurement of a heat transfer coefficient. Quant InfraRed Thermogr J 2004;1:133–50.
[6] Schmidt FM, Agassant JF, Bellet M. Experimental study and numerical simulation of the injection stretch/blow molding process. Polym Eng Sci 1998;38:1399–412.
[7] Klein R. Laser Welding of Plastics. John Wiley & Sons; 2012.
[8] Wellen RMR, Rabello MS. The kinetics of isothermal cold crystallization and tensile properties of poly(ethylene terephthalate). J Mater Sci 2005;40:6099–104.
[9] Cosson B, Schmidt F, Le Maoult Y, Bordival M. Infrared heating stage simulation of semi-transparent media (PET) using ray tracing method. Int J Mater Form 2011;4:1–10. doi:10.1007/s12289-010-0985-8.
[10] Modest MF. Ch. 9 - The Equation of Radiative Transfer in Participating Media, Radiat. Heat Transf. Second Ed., Burlington: Academic Press; 2003, p. 263–87.
[11] Manara J, Arduini-Schuster M, Hanssen L. Integrating sphere reflectance and transmittance intercomparison measurements for evaluating the accuracies of the achieved results. High Temp–High Press 2009;38:259–76.
[12] Boztepe S, Gilblas R, de Almeida O, Gerlach C, Le Maoult Y, Schmidt F. The role of microcrystalline structure on optical scattering characteristics of semi-crystalline thermoplastics and the accuracy of numerical input for IR-heating modeling. Int J Mater Form 2017.
[13] Billon N, Henaff V, Pelous E, Haudin JM. Transcrystallinity effects in high-density polyethylene. I. Experimental observations in differential scanning calorimetry analysis. J Appl Polym Sci 2002;86:725–33.
[14] Perkin Elmer 950UV/VIS Manual,. www.perkinelmer.com; n.d.
[15] ASTM International. ASTM D1003-13, Standard Test Method for Haze and Luminous Transmittance of Transparent Plastics. West Conshohocken PA 2013.
[16] Gulmine J., Janissek P., Heise H., Akcelrud L. Polyethylene characterization by FTIR. Polym Test 2002;21:557–63.
[17] Kossack W, Papadopoulos P, Parkinson M, Prades F, Kremer F. IR transition moment orientational analysis on semi-crystalline polyethylene films. Polymer 2011;52:6061–5. doi:10.1016/j.polymer.2011.10.051.
[18] Bendada A, Cole K, Lamontagne M, Simard Y. A hollow waveguide infrared thermometer for polymer temperature measurement during injection moulding. J Opt Pure Appl Opt 2003;5:464.
[19] Boztepe S, Thiam A, de Almeida O, Le Maoult Y, Schmidt F. Experimental analysis on the coupled effect between thermo--optical properties and microstructure of semi--crystalline thermoplastics.
[20] Howell JR, Menguc MP, Siegel R. Thermal Radiation Heat Transfer, 6th Edition. CRC Press; 2015.
[21] Asséko ACA, Cosson B, Schmidt F, Maoult YL, Lafranche E. Laser transmission welding of composites-Part A: Thermo-physical and optical characterization of materials. Infrared Phys Technol 2015;72:293–9.
[22] Wlochowicz A, Eder M. Distribution of lamella thicknesses in isothermally crystallized polypropylene and polyethylene by differential scanning calorimetry. Polymer 1984;25:1268–70.

[23] Hosoda S, Nozue Y, Kawashima Y, Utsumi S, Nagamatsu T, Wagener K, et al. Perfectly Controlled Lamella Thickness and Thickness Distribution: A Morphological Study on ADMET Polyolefins. Macromol Symp 2009;282:50–64.
[24] Wrasidlo W. Thermal Analysis of Polymers. Berlin Heidelberg: Springer-Verlag; 1974.
[25] Bohren CF, Huffman DR. Absorption and Scattering of Light by Small Particles. John Wiley & Sons; 2008.

This page intentionally left blank.

Chapter 5

PROCESS SIMULATIONS FOR IR HEATING OF SEMI-CRYSTALLINE THERMOPLASTICS

5.1. Introduction

As aforementioned, semi-crystalline thermoplastics have relatively narrow thermoforming window, which is induced by its crystalline phase. The more the amount of crystals the narrower the thermoforming window is seen as semi-crystalline phase still stands that keeps the material in tough-elastic state until crystals melt down in melting range [1,2]. Consequently, the final temperature state at the end of the heating stage plays significant role for achieving a successful forming process with respect to the quality of a thermoformed part. Therefore, predictive model for accurate temperature distributions is crucially important.

In this chapter, a novel combined numerical-experimental approach is proposed for IR heating of semi-crystalline thermoplastics. The proposed experimental and numerical approaches were analyzed here for the case of IR heating of HDPE. As already mentioned in the previous chapters, HDPE and LLDPE are named in this thesis as PE-1 and PE-2, respectively. The challenges for radiation transport in semi-crystalline polymers may be categorized into the two main aspects: optical heterogeneity in polymer medium due to semi-crystalline nature and, semi-transparency in certain type of such polymers, like PE, as discussed in detail in Chapter 3. In the frame of the successive analyses presented in this chapter, an experimental method and a radiation heat transfer model were developed for both temperature field predictions and surface temperature measurements on PE. The experimental approach proposed here focuses on non-invasive surface temperature measurements on the semi-transparent PE medium via IR thermography. Considering radiatively heated polymer media, IR thermography may be one of the most suitable methods to monitor temperature field without perturbing the heating process whereas, accurate temperature measurements may not be simply obtained on a semi-transparent medium.

At the first part of the chapter, the background of the radiation heat transfer model and the adopted assumptions are presented. Adopting the temperature-dependent β_λ (T) of PE as radiation absorption parameter - or numerical input -, temperature-dependent numerical model was developed which considers the change in the thermal radiation absorption capacity of PE under heating. In the second part, the experimental method for IR thermography on semi-transparent PE was discussed and, the accuracy of the method was analyzed performing preliminary IR heating experiments. The accuracy of the numerical model was assessed performing numerical-experimental IR heating studies. For the analyses, PE-1 polymer in two different geometries were used: injection molded square plates and, test tube-shaped preforms which are typically used for ISBM processes. At the last part of the chapter, experimental IR heating experiments of geometrically identical PE-1 and PE-2 plates are presented. Under an equivalent heating time and identical test conditions, the heating behavior and final temperature field in both type of

PE polymer was analyzed. The morphology-dependent thermal radiation absorption capacity in PE-1 and PE-2 medium and temperature field relations were highlighted.

Considering any type of monochromatic or polychromatic radiation source, the combined experimental-numerical approach proposed here may be adopted for temperature field predictions and non-invasive temperature measurements on the radiatively heated semi-crystalline thermoplastics.

5.2. Cost-effective modeling for IR heating of semi-crystalline thermoplastics

As discussed in Chapter 2, in terms of modeling the radiation heat transfer in optically heterogeneous media, numerous examples of modelling approaches exist in literature that adopt well-known optical scattering theories, such as RDG [3] or LMT [4,5], which allows to predict the spatial distribution of the scattered light intensity accurately. However, radiation heat transfer models that handle complex radiation physics in optically heterogeneous media can be computationally costly especially if spectral complexity of radiation source or geometrical complexity in a heated component is involved [6]. Thus, it is likely difficult to implement such predictive models in practical purposes unless the heated product is at small scales or in simple geometry, unlike the thermoforming processes of polymer-based components at macroscale. In addition, in contrast to laser heating applications, the radiation emitted by an IR source and transferred through a polymer medium is not monochromatic, but in a range. This introduces spectral complexity in terms of modeling of optical scattering, since scattering behavior may change under varying wavelength in the spectral range of emitted radiation. Such a wavelength-dependent scattering behavior in unfilled semi-crystalline polymers was discussed in [7–9]. The point that was commonly observed in those studies is that the scattering behavior becomes weaker considering an increase in the wavelengths roughly between 0.5 μm and 2 μm, which lies in VIS and NIR ranges. This is in close agreement with the spectroscopic analyses of PE, which was discussed in Chapter 3.

Apart from the computational cost due to spectral complexity of IR radiation, the strong coupling between the crystalline structure of unfilled semi-crystalline thermoplastics and their optical scattering behavior may also increase the complexity of a numerical approach, and thus computational cost. As discussed in Chapter 4 for semi-crystalline PE, optical scattering behavior may evolve under heating due to a potential change in crystalline phase, especially at the temperatures close to melting range. Modeling optical scattering in such an evolving medium may introduce a remarkable uncertainty in terms of modeling radiation transport and scattering path which could theoretically be a function of the equivalent scatterer size that evolves under heating. Hence, it may be useful to adopt a numerical approach that considers these temperature-dependent optical characteristics in semi-crystalline thermoplastics to simplify this phenomenon. Thanks to this, the change in the thermal radiation absorption capacity of the

heterogeneous polymer medium under heating could be taken into account at macroscale without computing the scattering path and absorbed energy at microscale. Generally speaking, the literature review on the radiation heat transfer simulations (Chapter 2) reveals that most of the temperature-dependent models are dedicated for laser assisted heating which were performed at monochromatic wavelength. Thus, the temperature dependence in the thermo-optical properties of semi-crystalline thermoplastics was generally characterized at monochromatic wavelengths. In contrast, the radiation emitted from an IR lamp is not at a monochromatic wavelength but in a spectral range. Hence, in case of IR heating of semi-crystalline polymers, the temperature dependence in their optical properties is required to be characterized in the spectral range of emitted radiation.

The numerical model presented in this study was built based on optically homogeneous medium. In the previous chapter, the temperature dependence in the thermo-optical properties of PE was addressed and the equivalent β_λ (T) of its medium was determined between 0.25 and 2.5 μm. Concerning the spectral range of emitted IR radiation, the calculated β_λ (T) values were adopted as radiation absorption parameter in the model. Thus, the developed temperature-dependent numerical model considers the change in the optical scattering behavior and thermal radiation absorption capacity of PE-1 medium under heating without modeling how the light scatters inside of the medium. Consequently, the model proposes a macroscopic numerical approach without modeling the spatial distribution of the scattered light intensity at microscale, which offers computationally cost-effective numerical solutions.

5.2.1. Background of the numerical model

5.2.1.1. Temperature-dependent thermophysical properties

The temperature dependence in the thermophysical properties of PE, namely thermal conductivity k and specific heat capacity (C_p (J/kgK)), were taken into account in the model. It is known that temperature-dependence in thermal conductivity of semi-crystalline polymers is strongly affected by their crystalline structure [1,10] . The temperature-dependent conductivity k (T) of PE used in the model was adopted from literature [1]. The variation over temperature in the adopted data [1] was reproduced and illustrated in Figure 5.1 (a). Although, variations in the crystalline ratio X_c may result in an increase of the conductivity of semi-crystalline polymers [1,11,12], it was assumed here that k was independent of X_c. In addition, highly ordered crystalline structures that form in certain directions may introduce anisotropy in the thermal conductivity of semi-crystalline polymers as stressed in [11,13]. Such a potential effect was neglected in the numerical model and isotropic conductivity was assumed for PE.

The apparent heat capacity $C_{p,}^{apparent}$ of the PE, that represents the total energy required for increasing the temperature of unit mass of polymer, was measured employing a power compensated DSC. As shown

in Figure 5.1 (b), the $C_{p,}^{apparent}$ of PE under heating conditions is not strictly monotonic but exhibits a phase transition related to the melting of the crystalline phase of PE. The temperature-dependent apparent heat capacity $C_{p,}^{apparent}(T)$ can thus be described with Equation 5.1 considering the temperature-dependent specific heat capacity $C_p(T)$ and the phase transition enthalpy $\Delta H_{melting}$ [10,14]. For the sake of simplicity, the melting kinetic was however not modeled and the $C_{p,}^{apparent}(T)$ was directly used as an input in the numerical model. It should be noted that $C_{p,}^{apparent}(T)$ may cause overestimation or underestimation in the phase transition enthalpy of PE regarding to heating rate during IR heating whereas, this point was not analyzed at this stage.

$$C_p^{\ apparent}(T) = C_p(T) + \frac{\Delta H_{melting}}{dT} \tag{5.1}$$

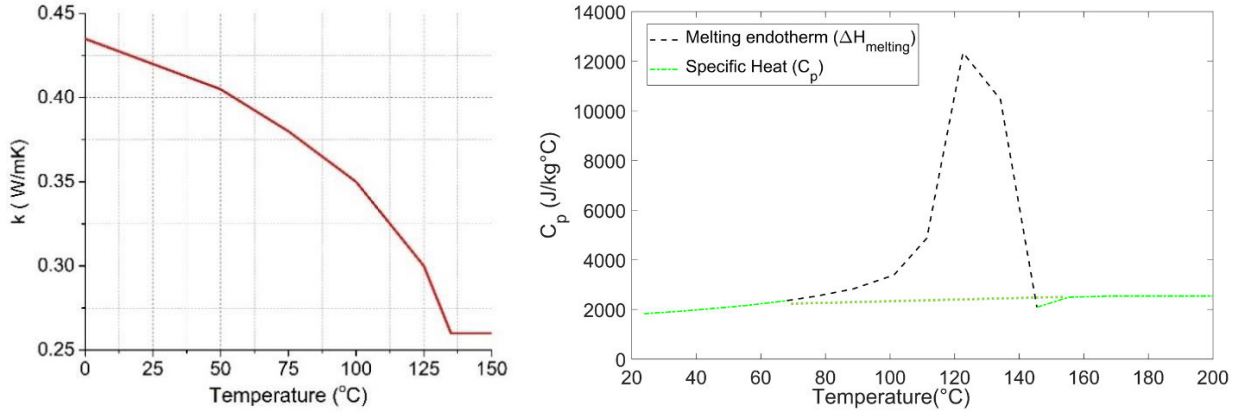

(a) (b)

FIGURE 5.1. k (T) of PE adopted from [1] (a) and, superposition of $C_p(T)$ and $\Delta H_{melting}$ of PE obtained from the DSC measurements (b).

Under heating condition, the potential reduction in X_c due to partial melting of crystalline phase may also cause to change the density (ρ) of PE [10,12,15]. As a consequence, the specific volume ($\bar{V}$ (m^3/kg)) of the material -which is reciprocal of ρ- may change significantly under varying temperature [1,16] which physically addresses the thermal expansion of polymer medium. Considering isochoric simulations, such expansion in polymer geometry was not taken into account hence; the spatial expansion in the node coordinates of the modeled mesh elements is ignored under varying temperature. On the contrary, in terms of computational cost for radiation transport and the absorbed radiation energy in the model, the consideration of this effect would introduce complexity as the ray tracing computations should be restarted at each computational step. Therefore, temperature-dependent ρ of PE was considered as negligible in the model. Although some remarkable change may be seen in the ρ of PE, the increase in

$\bar{V}$ [1,17] or decrease in ρ of PE occurs at very high temperatures in the melting range. Considering IR heating of PE until semi-molten state, this negligence may not cause a significance in the numerical predictions. Nevertheless, the initial value of the ρ was defined as a function of the X_c of PE samples in the model. The two-phase model was adopted for defining the global density (ρ_{global}) of PE regarding the fraction of crystalline and amorphous phases (Equation 5.2) [15,18]. The ρ_{global} in Equation 5.2 represents the macroscopic density of simulated polymer geometry.

$$\rho_{global} = \frac{1}{(\frac{X_{crystalline}}{\rho_{crystalline}}) + (\frac{1 - X_{crystalline}}{\rho_{amorphous}})} \tag{5.2}$$

The X_c of PE was obtained from calorimetric analyses using Equation 3.1. The obtained X_c values are then used as input in the model where it assigns ρ_{global} based on Equation 5.2. For the injected PE plates and preforms, X_c was taken as 67 % and 64 %, respectively. These values correspond to the average value measured from several PE plates and preforms. The ρ of crystalline and amorphous phases of PE that are appeared in Equation 5.2 were adopted from literature [12,19], as 1000 and 855 kg/m^3, respectively. Hence, ρ_{global} was defined for the PE plate and preform as 952 and 942 kg/m^3, respectively.

5.2.1.2. Radiation Heat Transfer modeling approach based on temperature-dependent thermo-optical properties

As aforementioned, absorbed radiation inside of PE medium was computed using an in-house developed radiation heat transfer algorithm -RAYHEAT-. In the algorithm, thermal radiation computations are done based on ray tracing method, so that the emitted radiation from an IR lamp is modeled as traveling in straight lines, called rays. In RAYHEAT, only the tungsten filament of an IR lamp is taken into account. Each single filament with diameter of 2 mm is modeled by equivalent cylinders where its spiral form is neglected. The emitted energy from the filament of a halogen IR lamp is assumed Lambertian and the source is considered as a grey body. The directional dependency of emitted power from halogen IR lamps, which is reviewed in Chapter 2 (Figure 2.5), is in close agreement with Lambertian assumption. In addition, discretization of the ray from the surface of IR lamp was performed adopting a stochastic approach [20,21]. Thanks to this, a numerous number of rays are released randomly from the modeled IR lamp. The total amount of energy emitted by the IR lamp is uniformly shared among all the rays. Once a ray intersects the polymer geometry, some of the carried energy is reflected and the remaining part of the energy is transmitted through the polymer medium, where the absorbed energy is computed. The current version of RAYHEAT is based on optically homogeneous medium assumption. Therefore, the attenuation of radiative energy is computed following the Beer-Lambert Law, according to

Equation 2.11. The further details about RAYHEAT including ray tracing method, discretization of emitted rays and radiation transport between an IR lamp and polymer medium is shown in Annex A 2.3.

Considering absorbing-scattering medium of PE, the radiative power absorbed by the polymer medium - $\nabla.q_r$ - at the depth "z" is defined with Equation 5.3, which is derived from Equation 2.12. Here, theoretically, the intensity of radiation is attenuated exponentially based on absorbing and scattering characteristics of PE medium, where the attenuation capacity of the medium is represented by β_λ, which is the sum of both κ_λ and D_λ:

$$\nabla \cdot q_r(z) = \int_0^\infty -\beta_\lambda I_\lambda(0) e^{-\beta_\lambda z} d\lambda = \int_0^\infty -(\kappa_\lambda + D_\lambda) I_\lambda(0) e^{-(\kappa_\lambda + D_\lambda) z} d\lambda \tag{5.3}$$

In the model, prior to the $\nabla.q_r$ computations, the β_λ (T) is integrated concerning the spectral range of 95.6 % of the overall emitted power of each modeled IR lamp (Equation 5.4). This spectral range is between $\lambda_{max}/2$ and $5\lambda_{max}$ which can be determined by knowing the temperature of each lamp and adopting Wien's displacement law, presented in Chapter 2 (Equation 2.4).

$$\overline{\beta}(T) = \frac{\int_{\lambda_1=\lambda_{max}/2}^{\lambda_2=5\lambda_{max}} \beta_\lambda(T) I_\lambda^o d\lambda}{\int_{\lambda_1=\lambda_{max}/2}^{\lambda_2=5\lambda_{max}} I_\lambda^o d\lambda} \tag{5.4}$$

Each calculated $\overline{\beta}(T)$ is then used as radiation absorption parameter -or numerical input - in the model for computing $\nabla.q_r$ at each corresponding temperature step. As mentioned in Chapter 4, no variation in both $T_\lambda^{\,i,\cap}$ (T) and $R_\lambda^{\,i,\cap}$ (T) of PE was observed at some of the temperature steps. For instance, the $T_\lambda^{\,i,\cap}$ (T) measurements obtained between 25°C and 97°C showed almost no variation. Thus, the transmittance values measured in this temperature range were ignored for the $\overline{\beta}(T)$ computations. By the same token, the $R_\lambda^{\,i,\cap}$ (T) measurements between 25°C and 107°C were ignored. Consequently, regarding the $\overline{\beta}(T)$ values calculated at 12 different temperature steps between 25°C - 128°C, 12 different scenarios of $\nabla.q_r$ were created for each corresponding step. The main reason to neglect the optical measurements that show no temperature dependency is to reduce computational cost. Thanks to this, the number of potential scenarios for the computed $\nabla.q_r$ was reduced. By reducing the number of computed $\nabla.q_r$, the number of iteration steps of the closed-loop computations can eventually be reduced. The computation times in relation to various numerical inputs are discussed in Section 5.4, where different simulation cases built for different PE geometries are presented. The working algorithm of the model is displayed schematically in Figure 5.2. The existing version of RAYHEAT was developed in this

study and converted into an iterative closed-loop computation algorithm. As RAYHEAT is a MATLAB-based code, the iterative closed-loop between RAYHEAT and COMSOL Multiphysics® was established using MATLAB LiveLink feature which allows to transfer the computed $\nabla.q_r$ into COMSOL Multiphysics® as a numerical input at each time interval.

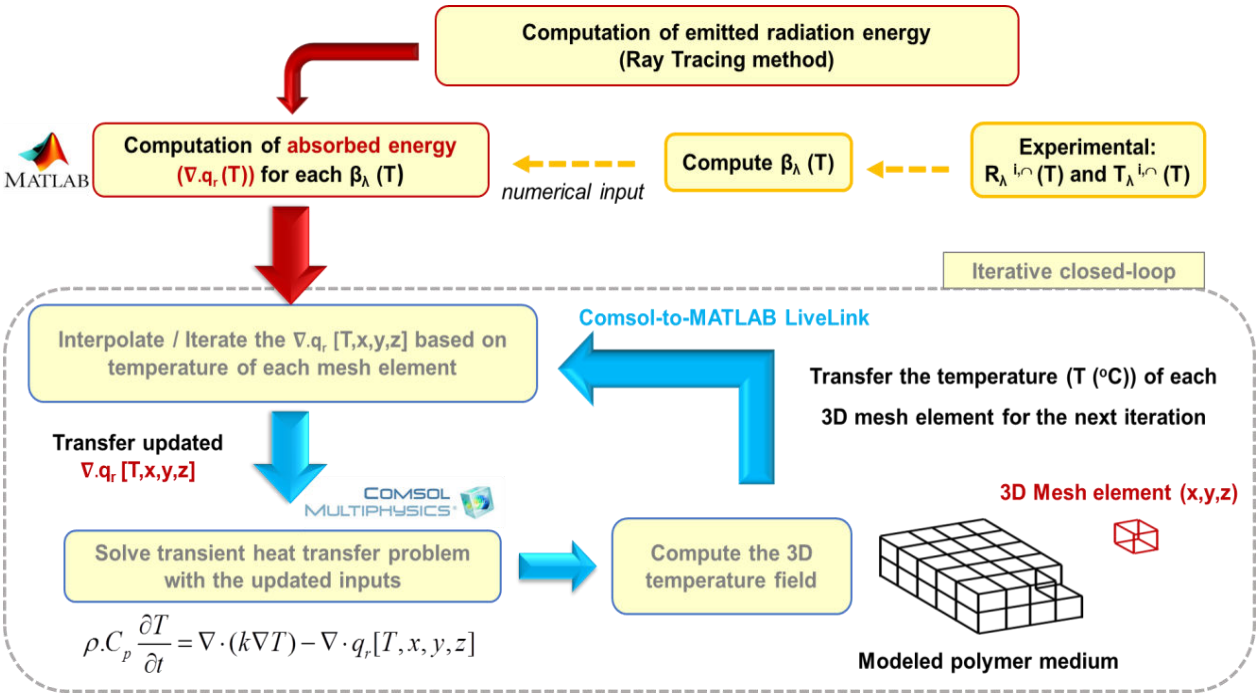

FIGURE 5.2. Working algorithm of the developed numerical model.

The algorithm then assigns COMSOL Multiphysics® for solving the transient heat transfer equation (Equation 5.5) to predict the temperature field and calls back RAYHEAT for updating the $\nabla.q_r$ of polymer medium regarding the computed temperature at the end of each iteration step. Therefore, the change in the amount of radiative power absorbed by the PE medium during each iteration step is introduced in the model. This change was modeled at mesh scale so that the change in absorption capacity in PE medium was considered regarding the temperature and spatial coordinates of mesh elements. The model interpolates the $\nabla.q_r$ of each mesh element regarding the $\nabla.q_r$ of the two most close temperature steps in case that computed temperature of mesh element is somewhere between the adopted temperature steps. Otherwise, in a case that the temperature of a mesh element is lower than 25°C or higher 128°C, the model assigns the $\nabla.q_r$ computed at 25°C or 128°C, respectively. Temperature dependency of k (T) and $C_{p,}^{apparent}$ (T) were assigned as a global parameter for PE medium. Hence, the model computes the average temperature of the medium and updates the thermophysical parameters at each computational time step.

$$\rho.C_p \frac{\partial T}{\partial t} = \nabla \cdot (k\nabla T) - \nabla \cdot q_r[T,x,y,z] \tag{5.5}$$

For thermal radiation computations based on ray tracing method, one of the important parameters is the number of modeled rays. In RAYHEAT, the effect of the number of ray on computational time and accuracy in the $\nabla.q_r$ was analyzed in [35] considering a square PET plate heated by a single IR lamp. Their convergence studies suggested that the modeled rays greater than $1.5*10^6$ allows computing the absorbed radiation with an error less than 5% in RAYHEAT. Nevertheless, this suggestion may only be a reference for heating a simple geometry since an increase in the complexity of the geometry may also affect the accuracy of ray tracing computations. The accuracy may not be related to the ray tracing method as it is independent of geometric complexity but to the finite element meshing of the complex geometries and, its interaction to the intersected modeled rays [21]. Increasing the number of modeled mesh element, in return, will increase the computational cost. The boundary conditions and adopted input parameters for radiation heat transfer modeling of PE are presented in Table 5.1. Considering all the numerical variables and inputs, the main strategy was to reduce the computational cost by decoupling the computational steps of the coupled radiation-conduction-convection heat transfer problem. More specifically, computations for radiation transport and heat transfer equation was separated. Firstly, the radiation transport of modeled rays and the thermal radiation absorption of each modeled 3D mesh element was computed. Therefore, all the potential scenarios of the $\nabla.q_r$ values absorbed by each mesh element were computed adopting all the $\overline{\beta}\,(T)$ values and, saved before starting the iterative closed-loop computations for energy-balance equation.

	Input parameter	**Source of the parameter**
Thermophysical properties of PE	k (W/mK)	Adopted from [1] (Figure 5.1(a))
	$C_p^{apparent}$ (J/kgK)	DSC measurements (Figure 5.1(b))
	ρ_{global} (kg/m^3)	Equation 5.2 and DSC measurements
Thermo-optical properties & temperature-dependent absorption characteristics of PE	$\overline{\beta}\,(T)$	Calculated from the measured $T_\lambda^{\,i,\cap}$ (T) and $R_\lambda^{\,i,\cap}$ (T) at 12 temperature steps: 25, 97, 110, 114, 116, 118, 120, 121, 122, 123, 126, 128°C
	$\nabla.q_r$ (T)	**For T < 25C:** $\nabla.q_r$ (25°C) for all mesh elements **For 25 <T < 128°C:** $\nabla.q_r$ (T) between the two closest temperature steps **For T > 128°C:** $\nabla.q_r$ (128°C) for all mesh elements

TABLE 5.1. The assumptions and the input parameters adopted for the IR heating modeling of PE.

It should be mentioned that the adopted computational strategy does not mean decoupling the multiple heat transfer modes modeled here. Decoupling the computational steps of radiation transport and energy-balance equations approximates implicitly that radiation intensity is quasi-steady, so that no time dependency is considered in radiation transport. Regarding most of the coupled radiation-conduction and / or convection heat transfer problems at macroscale, radiation intensity and thus RTE is considered time independent [4,9,20,22,23]. However, time dependency may needed to be taken into account in RTE, especially for radiation-material interactions in very short time or length scale, as studied in [5,24,25]. The underlying reason here is related to the characteristic time of heat transfer modes, at which it is known that the characteristic time of radiation transfer is several orders of smaller than conduction and convection mode of heat transfer [26]. Therefore, the radiation propagation is much more faster than any change of physical parameters which eventually allows to approximate that the radiation intensity field is quasi-steady [27] for radiation heat transfer modeling at macroscale.

Coming back to our case study for IR heating of PE, considering radiation transport and heat transfer phenomena in time domain, it is obvious that the radiation emitted from IR lamp can be modeled as steady state unless emitted radiation from an IR heating is perturbed or varied over time. Therefore, the attenuation of each modeled ray over the distance travelled through in PE medium is related only to the absorption characteristics of each mesh element of modeled geometry. At a closer look, the negligence of effect of temperature change over time on radiation attenuation in the modeled medium can be seen. But this negligence is limited to the time step intervals which are adopted in the model for the iterative closed-loop computations. As illustrated in Figure 5.2, the transient change in 3D temperature field of PE medium is computed at the end of each iteration step and, the absorption characteristics of each mesh element is updated. Consequently, the effect of time-dependent temperature change on the radiation attenuation, and thus on the intensity of each ray, is considered only at the corresponding time of each iteration step, but not for the time assigned for solving transient heat transfer problem in each iteration. Howell et al [23] reviewed the coupled radiation-conduction-convection studies for participating media having temperature-dependent properties and volumetric energy generation, which is indeed absorbed radiative power - $\nabla.q_r$ (T) -. It was pronounced that iterative-type computations using transient solution can be one of efficient method in terms of computational cost and the convergence of the numerical solution techniques. Furthermore, they reviewed the work of Hogan et al [28], where they analyzed solution strategies for coupled radiation-conduction problems. In this work [28], they adopted iterative strategy, which is very similar to our method, so that decoupled radiation transport and energy-balance equation was solved subsequently and compared to the fully coupled transient method. Regarding the concluding remarks in [28], Howell et al. [23] suggested that iterative-type numerical method for decoupling computational steps of radiation transport and energy-balance equation can be one of the best

approaches for complex radiation-conduction problems. Similar point was analyzed in detail in [29] where they proposed similar modeling strategy to the one adopted here. They decoupled the computations of radiative transfer and heat transfer problem so that $\nabla.q_r$ was computed only once using Monte Carlo – ray tracing algorithm and transient heat transfer problem solved. Beyond this fact, it was concluded that radiation-condition coupling in time domain becomes less significant for participating media with higher D_p (m) - or lower optical thickness -. The radiation attenuation in PE medium follows low level of optical thickness which was analyzed considering the D_p of PE calculated regarding each $\overline{\beta}\,(T)$.

5.3. IR heating of PE and model predictions

The accuracy of the numerical model was assessed performing numerical-experimental comparisons for the case of IR heating of PE prepared in the form of square plates and preforms. Therefore, two different study cases were created for IR heating of PE plates and preforms, namely *Study Case - 1* and *Study Case - 2*, respectively. Numerical - experimental comparisons presented here does not only aim to assess the prediction accuracy of the model including $\overline{\beta}$ (T) as numerical input, but also reveals the lack of prediction if a constant, $\overline{\beta}$ (25 °C), is taken into account in the model, especially for the cases where PE is heated up to temperatures close to its melting range. To analyze both the points, two parametric simulation cases were built in each study case where only thermal radiation absorption capacity of PE medium is modified. In the simulation case-1 (C-1) thermal radiation absorption capacity of the PE medium was modeled as independent of temperature adopting only $\nabla.q_r$ (25 °C) which was computed using $\overline{\beta}$ (25 °C). In the simulation case-2 (C-2), the computation was done considering the temperature dependent absorption characteristics ($\nabla.q_r$ (T)) which were computed using the $\overline{\beta}\,(T)$ values. For both the cases, all the other boundary conditions were built in exact manner adopting the identical conditions applied in the IR heating experiments. The overview of the study cases and their parametric sub-cases (C-1 and C-2) are presented in Table 5.2. The further details of each IR heating experiments of PE plate and preform are presented in Section 5.4.1 and 5.4.2, respectively.

		Radiation absorption in PE medium
Study Case - 1 & Study Case - 2	**Simulation Case - 1 (C-1)**	Constant radiation absorption with ∇.qr (25 °C)
	Simulation Case - 2 (C-2)	Temperature-dependent radiation absorption with $\nabla.q_r$ (T) between 25 and 128°C

TABLE 5.2. The identical case studies adopted for the IR heating simulations of PE plate and preform.

For all the IR heating experiments, single or multiple number of identical IR lamps with a power of 1kW (Toshiba JHS 235V) were used. The cylindrical tungsten filament of the used IR lamp is 300mm long, with a diameter of 2.15 mm. During IR heating experiment of each PE plate, IR thermography and conventional TCs were employed for the surface temperature measurements while, TC could not be attached for the case of preform heating since it was rotated under heating, which is typically applied in ISBM processes. Therefore, IR thermography becomes one of the proper methods not only for providing surface temperature measurements non-invasively, but also due to difficulties for obtaining measurements on radiatively heating of polymer component under motion. Due to the semi-transparent nature of PE, an experimental methodology was developed to obtain the most accurate surface temperature on PE via IR thermography. The accuracy of the method was analyzed performing preliminary IR heating experiments. Before discussing the numerical-experimental analyses of IR heating of PE, the developed experimental method for IR thermography on semi-transparent PE is presented in the following section.

At the last section, a comparative experimental analysis is presented concerning IR heating of geometrically identical PE-1 and PE-2 plates. Under an equivalent heating time and identical testing conditions, the heating behavior and final temperature field in both type of PE polymer was analyzed in relation to their morphological difference.

5.3.1. IR thermography in semi-transparent PE medium and preliminary experiments

In order to state the problem clearly about obtaining accurate IR thermographic measurements on semi-transparent PE surface, a comparison between the absorption bands of PET and PE is presented. As it is seen in Figure 5.3 (b), PE has three narrow bands in MIR range where it shows very low transmittance and therefore it is close to be opaque [30,31]. Whereas, PET shows a similar behavior in relatively larger spectral range, that is roughly between 6 - 14 μm. A typical long-wave (LW) IR camera has an operating spectral range between 7-14 μm [32], consequently, a reliable surface temperature can be obtained on PET surface simply using any type of LW-IR Camera. In contrast to this, the situation is much more complex for PE, as it has two narrow absorption bands - around 7.6 and 13.6 μm, respectively- which lie in the operating spectral range of typical LW-IR Camera. However, as they are relatively narrow in comparison to the operating range of such a IR camera, narrow bandpass (NBP) optical filters are necessary for quantitative IR thermographic measurements at these spectrums. Therefore, it can be stated that accurate IR thermographic measurements on PE surface may be only performed in these spectral bands. It should be noted here that middle-wave (MW) IR camera can also be thought as an option for the measurements while the IR detectors and the application range is generally for measurements relatively at high temperatures [33]. This is related to the emitted power of a real body [24,25], as shown in Figure 2.3, whereas it will not be discussed further as it is out of the scope of the

thesis. In the frame of this study, it is known that PE can be monitored up to complete molten state, which is theoretically lower than 150°C. Therefore, such a MW-IR camera is not considered in this study.

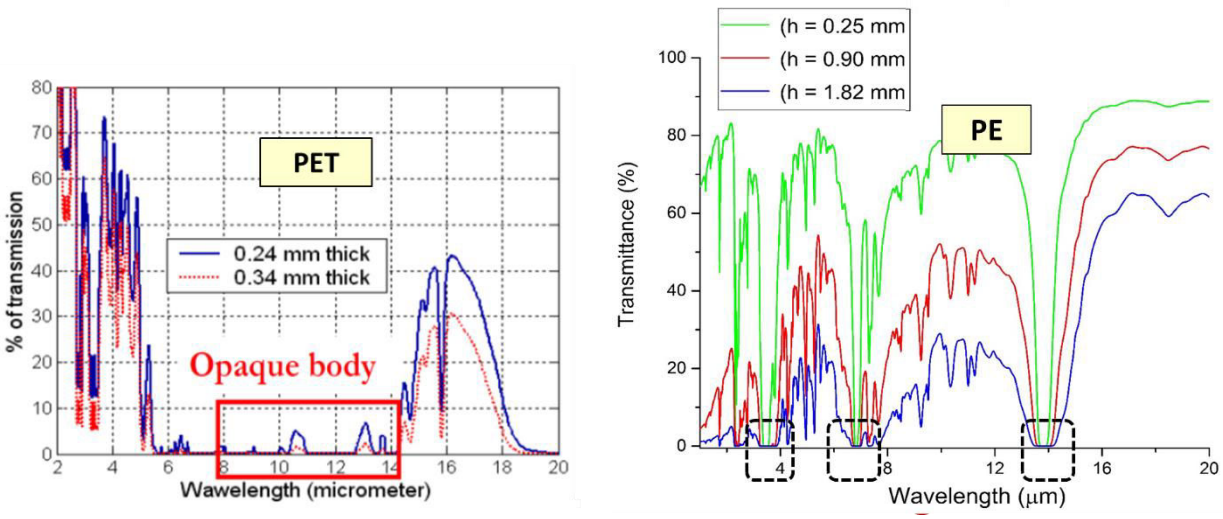

(a) (b)

FIGURE 5.3. Comparison between the absorption bands of PET(a) [35] and PE (b).

At very first step, two different NBP optical filters (Northumbria Optical Coatings) close to 7.6 and 13.6μm with bandwidths of ±0.10 μm and ±0.21 μm respectively were employed for the IR thermography of PE polymer. Both the filters were externally mounted and tested on two different IR cameras, namely a LN_2 cooled LW IR camera (AGEMA Thermovision 880) and an uncooled microbolometric IR camera (FLIR SC325). Thanks to this step, the sensitivity of both the employed IR cameras was analyzed at these preferably selected wavelengths. Initial analyses showed that the sensitivity of FLIR SC325 was too low for both the narrow bands, whereas enough sensitivity was recorded by the cooled LW IR camera only for the NBP filter which has a spectrum between 7.5 - 7.7 μm. These results obtained the two IR camera may not be surprising since they have two different type of IR detector having different response times. The employed LW IR camera has a mercury cadmium telluride (HgCdTe) detector. It is known that the response time of quantum detectors, like HgCdTe, has much shorter response time than microbolometric detectors [34]. In addition, it should be mentioned here that HgCdTe detector operates in the spectral range between 8 and 12 μm [36] indicating that spectral sensitivity of the IR detector is nominal in the corresponding range. Whereas the HgCdTe detector is still sensitive at the wavelengths beyond, but close to, this range. This behavior was shown in [34], at which the spectral sensitivity of various type of infrared detectors, including microbolometric and HgCdTe detectors, were reviewed. The spectral responses of microbolometric and HgCdTe detectors at the two absorption bands of PE are presented in Annex A 4.1. The figure in the annex was taken from [34]. Similarly, our sensitivity analyses showed that

the NBP filter mounted LW IR camera is still sensitive enough in the spectral band around 7.6µm. Nevertheless, an extra step was required to be applied to adjust the sensitivity of the IR camera in terms of obtaining a correct temperature related to the energy captured by the IR detector. Therefore, the NBP filter mounted IR camera was calibrated using a black body calibration source (Landcal P550P) so that correlation between the IR radiation captured by the camera and a measured temperature was established. The calibration was done choosing reference temperatures on the black body source between 50 and 140°C. The isothermal unit (UI_{bb}) detected by the IR camera was registered at each reference temperature. Thus, a calibration function was developed which enables to convert the detected energy emitted from the surface of PE to a temperature value, as shown in Figure 5.4. The adopted calibration function, which is the semi-empirical representation of Planck's Law, is shown in Equation 5.6:

$$UI = \frac{R}{(e^{\frac{B}{(T+273)}} - F)} \tag{5.6}$$

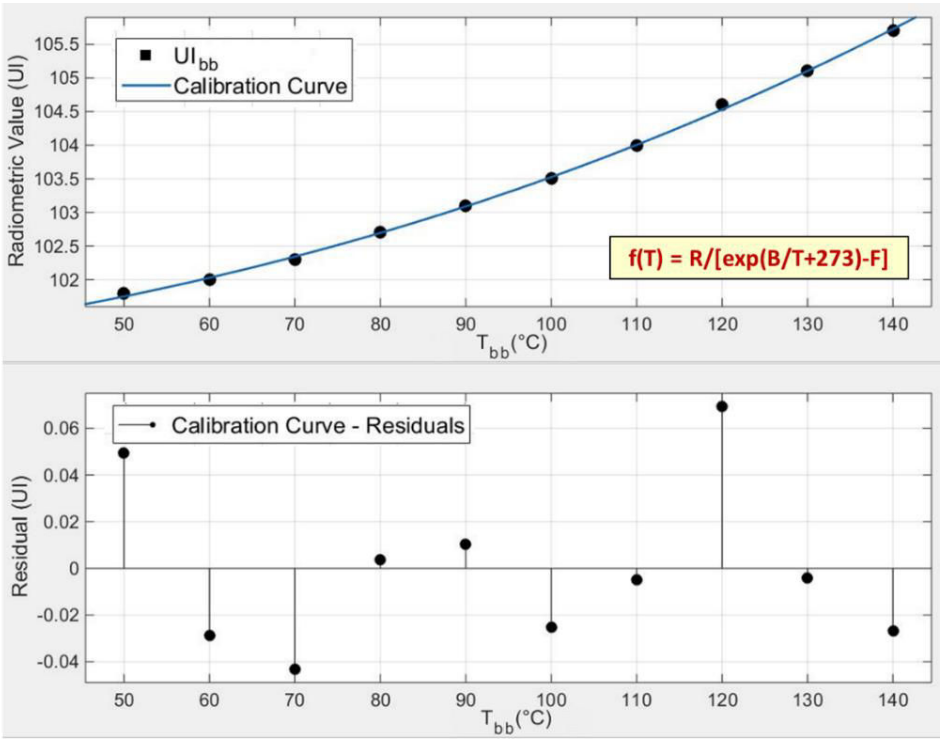

FIGURE 5.4. Calibration curve (a) obtained using the UI values at the chosen reference temperatures, and the computed residual indicating the goodness of the fitting (b).

The question arises here about the sensitivity of the NBP filter mounted IR camera in case of receiving the emitted energy from a real body, unlike a black body. This point was analyzed performing IR

thermography tests using PET. As aforementioned, PET behaves opaque in the operating spectral range of a typical IR camera. More specifically, it was reported in [36] that the D_p of PET is around 30 µm in the spectral range between 5-20 µm. Hence, PET was used as a reference material for obtaining a reliable surface temperature via IR thermography and, analyzing the accuracy of the filter mounted LW IR camera. For the tests, a PET plate with dimensions of 78x78x2.2 mm was heated using a single IR lamp and its back surface was monitored by the filter mounted LW IR camera. The back surface temperature was also measured employing the second IR camera, FLIR SC 325. Since the default spectral range of this camera is between 7.5-13.5µm [32], no filter was used. Thus, the measurements obtained from FLIR SC325 were considered as a reference for analyzing the accuracy of the NBP filter mounted AGEMA Thermovision 880. In addition, one TC was attached in the middle zone of the back surface for the comparisons. During the experiments, power of the IR lamp P_{lamp} was changed between 15% and 35% of its nominal power and the temperature measurements were done once back surface temperature reached steady state. At the end, 5 different measurements were obtained between 50 to 70°C. The surface temperature was read by the two IR cameras on the arbitrarily chosen zone which was next to the attached TC. All the recordings obtained by the IR cameras and the TC were compared at each steady-state temperature step, as displayed in Figure 5.5 (a). It was found that ΔT between the values recorded by the two IR camera was around 1°C (Figure 5.5 (b)) verifying that the filtered energy captured by the NBP filter mounted IR camera is sufficient to obtain accurate temperatures on a real body.

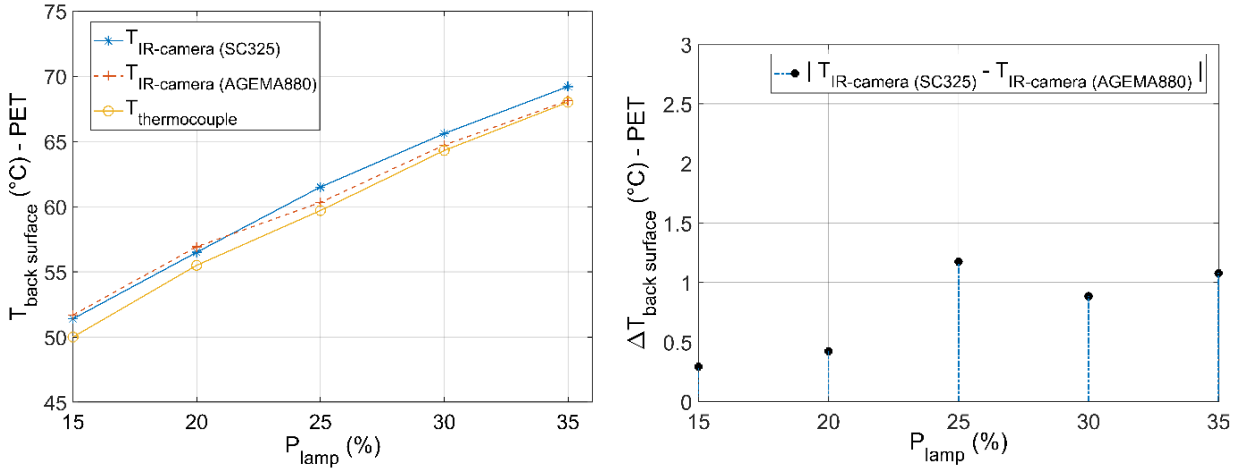

(a) (b)

FIGURE 5.5. Preliminary IR thermography tests using PET plate for the sensitivity analyses of the NBP filter mounted IR camera (a) and, ΔT between the measured values of the two IR cameras (b).

Apart from the sensitivity of the IR camera, the accuracy of the surface temperature measurements on PE was analyzed in terms of the D_p of PE in the spectral range where IR thermography was achieved. As

presented in Equation 5.7, the D_p of PE was calculated considering the spectral band of the employed NBP optical filter ($7.5 \leq \lambda \leq 7.7$ µm) and at temperature (T = 373 K) close to the thermoforming temperature of the polymer. The equation below is reproduced from using Equation 2.13 considering the conditions adopted for PE.

$$\bar{\kappa}(T = 373K) = \frac{\int_{\lambda_1=7.5\,\mu m}^{\lambda_2=7.7\,\mu m} \kappa_\lambda . I_\lambda^o(T_{373K}) d\lambda}{\int_{\lambda_1=7.5\,\mu m}^{\lambda_2=7.7\,\mu m} I_\lambda^o(T_{373K}) d\lambda} \quad \text{with;} \quad D_p = \frac{1}{\bar{\kappa}(T = 373\ K)} \tag{5.7}$$

Unlike to PET, it was found that its D_p of PE is around 350µm indicating that the absorbed and therefore emitted radiation may not be considered on the surface of polymer but, in a range close to surface. The relatively high D_p of PE raises another question related to the accuracy of the surface temperature of PE obtained by IR thermography. In other words, the temperature read by the IR camera may correspond to the temperature of the 350 µm thick layer beyond the surface. The problem here can be illustrated schematically, like in Figure 5.6. As displayed below, in the spectral band of the used NBP filter, the emitted radiation from the 350 µm thick range likely causes to have temperature readings by the IR camera that is slightly different than the actual surface temperature.

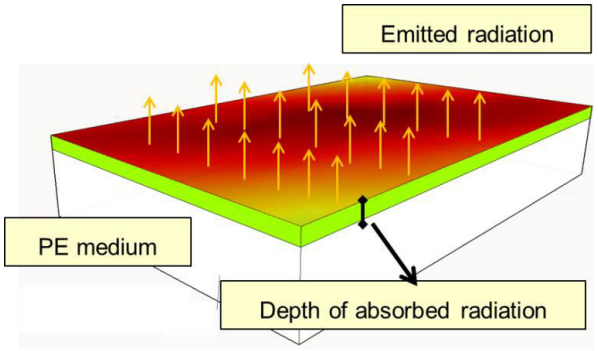

FIGURE 5.6. Schematical illustration of the relatively high D_p of PE and the emitted radiation range.

Due to the relatively high D_p of PE, it is required to understand how much difference may occur between the actual surface temperature and the recorded temperature by the IR camera. This point was investigated performing another preliminary IR thermography test using a PE plate. The used PE plate was geometrically identical to the PET plate. Similar to the former preliminary tests done with PET, the plate was heated using a single IR lamp and the back surface temperature of the PE plate was recorded by the NBP filter mounted IR camera and two TCs, namely TC-1 and TC-2. P_{lamp} was changed between 60 % and 90 % and four different measurements were obtained at four steady state temperatures. In Figure

5.7 (a) and (b), the test setup for IR heating of PE plate is presented. As it is shown Figure 5.7 (b), the TC-1 and TC-2 were attached in the midpoint and 4 mm away from the lower edge, respectively. A wood-based panel made of medium-density fiberboard (MDF) was used as a barrier and positioned in front the IR lamp. A small frame (70x70mm) was designed for positioning the PE plate. The reason for using a barrier was to perform an IR-thermographic measurement on the back surface of the PE plate, without any disturbance of a direct emission from IR lamp to the IR camera. In addition, the front surface of the barrier was covered with metallic adhesive tape in order to limit heating on the barrier, as potential heat transfer from the barrier to the PE plate would cause an erroneous temperature measurement. Furthermore, a transparent adhesive tape was used to fix the position of the attached TCs, as also presented in Figure 5.7 (b). The optical characteristics of the used adhesive tape were analyzed via FTIR spectroscopy prior to the IR heating experiments. The optical measurements showed that the tape has very low absorption capacity verifying that negligible amount of radiation can potentially be absorbed its medium, and thus it does not perturb the measured temperature. The measured $T_{\lambda}^{i,r}$ and $R_{\lambda}^{i,\cap}$of the transparent tape can be found in Annex A 4.2.

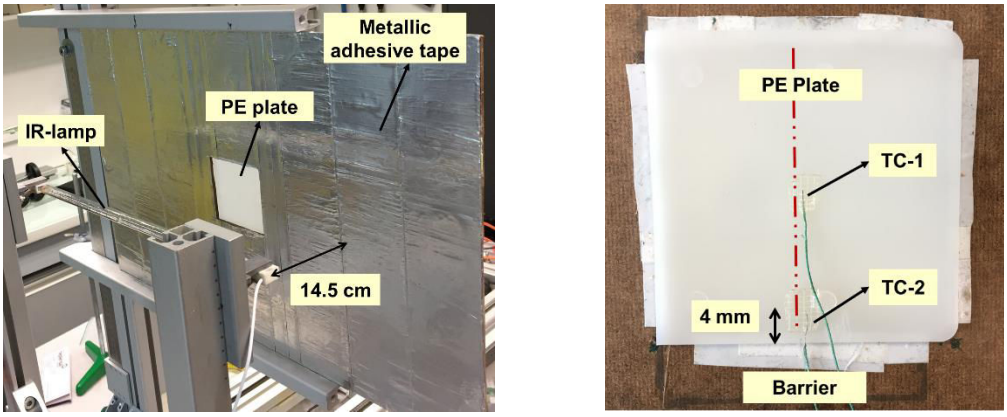

(a) (b)

FIGURE 5.7. Test setup for IR heating of PE plate (a) and the positions of the mounted TCs on the back surface (b).

The comparison between the IR thermography and the TC measurements are displayed in Figure 5.8 (a) and (b). The temperature read by the IR camera alongside the height of the PE plate and, the TC recordings obtained at steady state condition are presented in Figure 5.8 (a). The term -position- in Figure 5.8 (a) represents the distance between the endpoints of the axis defined in the vertical direction, which is shown with dashed line in Figure 5.7 (b). The temperature values were read alongside the axis which was positioned halfway between the right and left edges of the plate, like the TC-1 and TC-2. As it is seen in Figure 5.8 (b) the general trend in the ΔT between the TC and the IR thermography was around 1-2 °C,

except the two measurements which show difference around 3 °C. Apart from the relatively high D_p of PE, the potential uncertainties on the contact quality between the TCs and the plate during the IR heating may increase the margin of error of measurement, and thus ΔT. Nevertheless, it was assumed that the NBP filter mounted IR camera provided surface temperature on PE with a small error, which is mostly less than 2°C. Considering that the average measured temperature is around 70°C, it can be stated that the error in the temperature read by the IR camera is less than 3%.

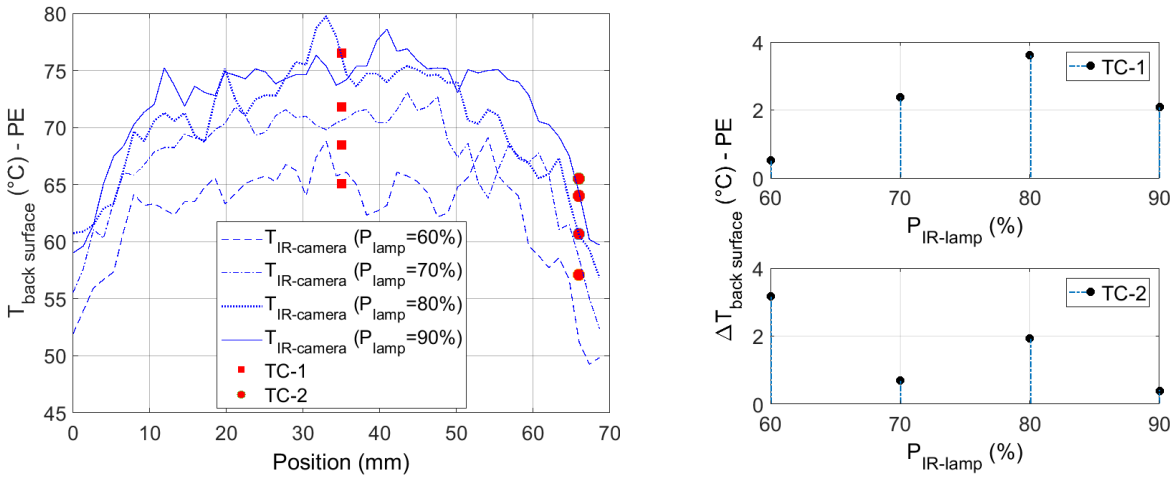

(a) (b)

FIGURE 5.8. The temperature fields obtained via IR thermography and the TC recordings on the PE plate surface (a) and, ΔT between IR thermography and TC recordings at each IR heating step (b).

In addition to this metrological analysis, another IR thermography test was performed on 2.2 mm thick PE sheet where the polymer is heated by conduction from its front surface. The back surface temperature of PE was monitored again by the NBP filter mounted IR camera where also two small reference zones were created on the PE surface using a thin layer of black coating. The thickness of the coating was measured via eddy current probe (Section 3.3.2.1) and found as 40 µm. The optical properties of the coating showed that its integrated ε between 7.5-13.5 µm is around 0.92. Therefore, the black zones are monitored by FLIR SC325 IR camera equipped with no filter. The measurements were performed at 10 steady-state temperatures between 50 and 95°C. Similar to the measurements shown in Figure 5.8, the difference between the temperature values read on reference zones and PE surface were less than 2°C. Hence, in terms of error in the read surface temperature, a consistency was observed between the values obtained by the two employed IR camera in two different test setups. The overview of the test setup for heating PE sample by conduction is given in Annex A 4.3. Furthermore, the reflectance characteristics of black coating, IR thermography of PE and the comparisons between the temperature readings of two different IR cameras can be found are in Annex A 4.4, 4.5 and 4.6, respectively.

Apart from the relatively high D_p and semi-transparency issue in PE medium, the second limitation of the developed experimental methodology at this moment is that the surface temperature measurements can only be done at steady-state conditions. It was observed in all the preliminary IR thermography tests that the externally mounted optical filter causes a potential drift in the UI values registered by the IR-detector where the UI values increased over time. Unlike the factory built-in filters that are mounted inside IR cameras, the externally mounted filter is not cooled which eventually may cause a potential self-heating on the filter over time and thus, may cause an additional radiation detected by the IR detector [37]. Hence, the accurate IR thermography could only be obtained in this study applying two-step measurements at each steady-state temperature. The two-step measurements include the strategy of obtaining IR thermography of PE surface which is immediately followed by a reference measurement, done with IR thermography of a non-reflective black board at each steady state temperature (Annex A 4.7). Thanks to the two measurements, image treatment can be applied in the software of IR camera and the noisy measurements seen in the IR thermography of PE can thus be eliminated.

The two points related to the error in the surface temperature of PE and, the IR-thermographic measurements obtained only at steady state temperatures are therefore needed to be analyzed further. Nevertheless, the developed experimental methodology enables to obtain a surface temperature on semi-transparent PE medium that is close enough to the real surface temperature, which may not be obtained using a typical IR camera due to the relatively narrow low-transmittance bands of PE. IR heating experiments performed here under different test setup conditions showed the reproducibility of surface temperature readings on semi-transparent PE medium by NBP filter mounted IR camera.

5.3.2. Experimental - Numerical Comparisons for IR heating of PE

5.3.2.1. Study case - 1: IR heating of PE plate

The comparisons between the predicted and experimentally measured temperatures were done adopting the identical conditions for the case of IR heating of a PE plate. IR heating experiments were carried out using an identical PE plate tested in the preliminary IR thermography experiments (78*78*2.2 mm). Similar to the preliminary experiments shown in Figure 5.7 (a), the PE plate was heated with a single IR lamp. Whereas, P_{lamp} was set to 100% of its nominal power, at which the temperature of the IR lamp filament was 2400K. In order to cross verify the temperature fields obtained from IR thermography, three TCs were attached on the back surface of the PE plate, namely TC-1, TC-2 and TC-3. The TC-1 and TC-2 were positioned 9mm and 4mm away from the left and the lower edges of the plate, respectively. TC-3 was attached in the midpoint of the back surface. The IR heating and the TC recordings were started simultaneously so that the real-time temperature evolution of the plate was recorded in three different

points for comparing it with the predicted heating behavior obtained from the numerical studies. In addition, it was observed that the back surface temperature reached steady-state after 600 seconds of heating and the IR-thermographic measurements were thus obtained at this time.

In this study case, the front surface of the PE plate was positioned 8 cm away from the IR lamp. This distance was chosen based on the β_λ (T) behavior of PE and the temperature profile observations obtained from the preliminary IR heating experiments of the PE plate. More specifically, it was aimed to reach a steady-state temperature on the PE plate which is below, but close to its melting range Since the β_λ (T) of PE changes significantly at temperatures close to its melting range (Figure 4.11), heating the PE plate up to this range may help to highlight how the temperature dependency in β_λ affects temperature field predictions. As aforementioned, the simulation case-1, (C-1), considers absorption characteristics of PE computed at 25 ^oC, while C-2 takes into account temperature dependent thermal radiation absorption capacity of the polymer medium. In the model, PE plate geometry was meshed with 2800 linear hexagonal elements, and the temperature of each mesh element was computed as the average temperature of its nodes' temperatures. Based on the experimental time required for reaching the steady-state, heating of the plate was simulated up to 600 seconds. The emitted radiation from the IR lamp was modeled using $1.5*10^6$ rays. This number of ray was chosen regarding the convergence analyses reported by Cosson et al. [20], which run ray tracing computations using RAYHEAT. In terms of computational cost, the ray tracing and $\nabla.q_r$ computations took 10 minutes for C-1 and 65 minutes for C-2 using an Intel Core i5 processor (with 2.40 GHz, 8.0 Gb of RAM).

As mentioned in Section 5.2.1.2, the transient heat transfer problem combined with conduction and convection, beside of radiation phenomenon, was solved using COMSOL Multiphysics where the iterative closed-loop computations were performed establishing a connection between RAYHEAT and COMSOL Multiphysics® via MATLAB LiveLink. Conduction between the barrier and the PE plate was taken into account including thermal contact resistance (TCR) at the barrier/plate interface. The value of the TCR between the MDF barrier and the PE plate contact surfaces was chosen as 600 W/m2K. In addition, the thermophysical properties of the barrier were adopted from literature. The thermophysical properties of different types of MDF were experimentally analyzed in [38,39]. Since the MDF type of the barrier used in this study is not known, the thermophysical properties of MDF found in [38,39] were averaged and adopted for the barrier. In the model, the C_p, k and ρ of the barrier were defined as 1000 J/kg/K, 0.10W/m/K and 690 kg/m^3, respectively. It was also assumed that all these adopted parameters are independent of temperature. In addition, potential heat losses due to convection and self-emission of the PE plate were taken into account in the model. The natural convection cooling on the PE plate was modeled using the relation proposed by Churchill and Chu [40] for vertical wall surfaces. In case of IR

heating up to 600 seconds, the momentum of buoyancy-driven air flow over the vertical surfaces of the plate was also considered. At very first step, the regime of the buoyancy-driven heated air flow was estimated calculating the Grashof Number [41]. It was found that the laminar flow can be assumed, regarding the geometrical dimensions of the PE plate and, the maximum and minimum temperatures of the plate surface. Considering the identical case used in the IR heating experiments and assuming a laminar flow for air, the heat transfer coefficient h was computed in COMSOL Multiphysics considering the front and back surfaces of the plate and, used as input in the iterative closed-loop computations. The further details about the h computations are given in Annex A 4.8 and 4.9.

The self-emission was also modeled on both front and back vertical surfaces of the PE plate. Using the $T_{\lambda}^{\,i,\cap}$ (97°C) and $R_{\lambda}^{\,i,\cap}$ (97°C) measurements of the thinnest PE film used in this study (250µm thick samples), the emissivity of PE was calculated around 0.77. The measurements at this temperature step were chosen considering that the polymer was heated up to 130 °C for forming processes. It should be pointed out here that, in the finite element modeling (FEM) software, emissivity is modeled on the surface considering a case of opaque materials which is parametrized as surface emissivity ($\varepsilon_{surface}$). Therefore, it is assumed that all incident radiation is either absorbed or reflected on the surface of opaque medium, whereas no transmission of radiation through its medium is considered. However, this is not the case for PE polymer as it is semi-transparent [30,31,42], which is also shown in this study considering its spectroscopic measurements. Simply, the emissivity of semi-transparent materials is a global physical quantity which theoretically represent emission from medium but not from surface [32,43], due to volumetric absorption. In other words, the emitted energy, and thus the value of emissivity, of an opaque material does not change by a change in their thickness, conversely it is strongly affected by a change in the thickness of semi-transparent materials [44] which makes $\varepsilon_{surface}$ fundamentally unsound. Nevertheless, it may be assumed that the emissivity measurements in very thin PE samples may represent $\varepsilon_{surface}$. For instance, the optical properties of 100 µm thick HDPE and LDPE films was experimentally characterized by Okada et al. [30] and, the emissivity values for both type of PE polymer was found around 0.28. The absorption bands of both the studied PE polymers in [30] show close agreement with the spectroscopic analyses of PE samples studied here. In addition, the reflectance and transmittance characteristics of 100 µm thick HDPE film was reported by Mastai et al. [42] which also show close agreements with [30]. Therefore, the emissivity value of 100 µm thick PE proposed in [30] was assumed as $\varepsilon_{surface}$ in the model, instead of adopting emissivity value of the 250µm thick PE sample that was used in this study.

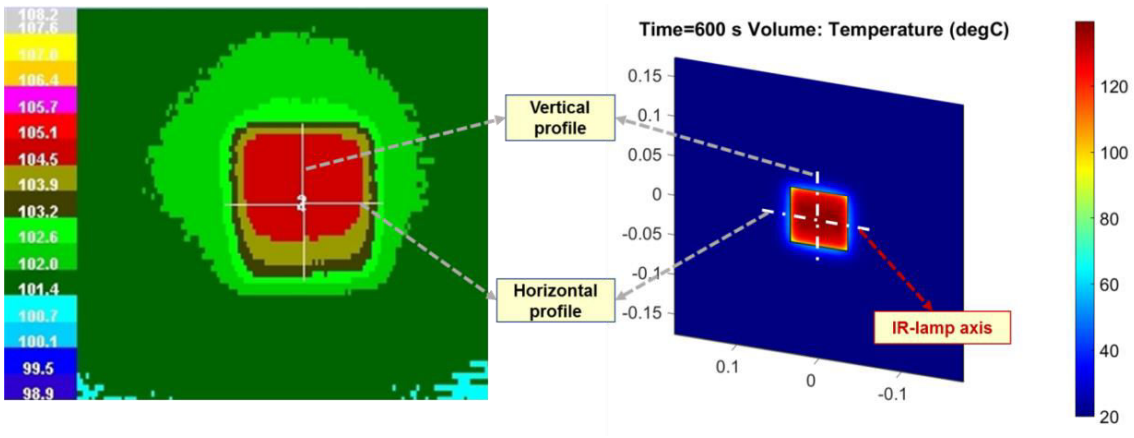

(a) (b)

FIGURE 5.9. Temperature field comparisons on identically-created vertical and horizontal profiles on both the IR thermography (a) and the numerical simulation (b) of the PE plate.

For the numerical - experimental comparisons; two profiles were defined in vertical and horizontal directions on the PE plate. The horizontal profile was defined alongside the IR lamp axis whereas the vertical profile was perpendicular to the IR lamps axis. In Figure 5.9 above, identically-created profiles on both IR thermography of the plate (a) and, the numerical simulation (b) are presented. The scale bar on the IR thermography of the plate (in Figure 5.9 (a)) represents the radiometric values (UI).

In Figure 5.10, the comparisons between the temperature profiles obtained from the experimental and the numerical studies are presented on the vertical (a) and horizontal (b) profiles. As it is seen, C-2 predicts the back-surface temperature of the PE plate closely, whereas C-1 overestimates the experimental results by around 10°C. Considering that the measured temperature in the middle zone of the plate is around 123°C, the averaged global error in the predicted temperature is around 8% for C-1. In terms of accuracy of the model built as C-2, two different points may be raised further. First of all, ΔT between the predicted and experimentally measured temperature is less than 3°C throughout the vertical profile, where the error in the predicted temperature through the vertical profile is less than 2.4% for C-2. In terms of comparisons on the horizontal profile, this small difference was only seen on the middle zone of the plate (the position between 10 - 60mm, defined in x axis). In the related zone, ΔT is less than 2.5°C (or the error in the predicted temperature is less than 2%). Conversely, ΔT on the horizontal profile becomes somewhat significant considering the zones close to the edge of the plate at which may be attributed to the underestimation of the potential conduction heat losses between the barrier and PE plate. As aforementioned, the thermophysical properties of the wood-based barrier were adopted from literature, but not experimentally characterized. Secondly, such difference does not exist on the vertical profile where also a non-balanced temperature distribution alongside the vertical direction of the plate is seen, as

illustrated in Figure 5.10 (a). The non-balanced profile is induced by the heated air that moves upward along the heated vertical surface. The close prediction then shows that the computed h which considers the buoyancy-driven air flow in the vertical direction was well defined. This may also be the dominating mode of heat transfer on the vertical direction, rather than conduction between the barrier and the plate, and thus results in better convergence between the predicted and experimental results on the vertical profile. Considering that the thermoforming window of semi-crystalline PE is around 4-5°C, the ΔT between the experimental results and both the predicted values of C-1 and C-2 clearly indicates that characterization of the temperature-dependent thermo-optical properties of semi-crystalline polymers may be one of the key factors for the accuracy in temperature field predictions.

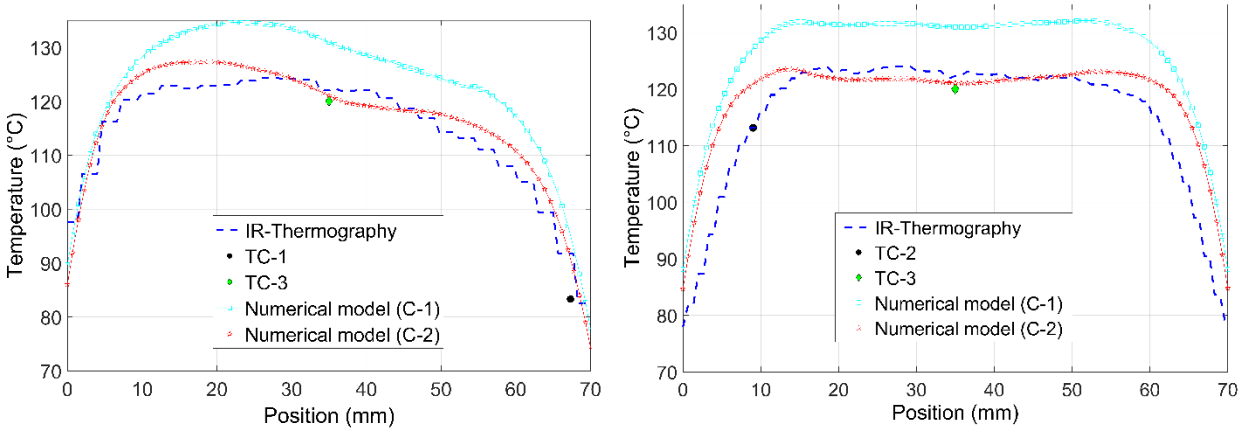

(a) (b)

FIGURE 5.10. The predicted and measured steady state temperature profiles on the vertical (a) and horizontal profiles (b), defined on the PE plate's back surface.

The real-time temperature evolution on the PE plate was also analyzed comparing the TC recordings to the numerical results obtained from C-2. The numerical results were taken at the same location of the TC-3, which was attached at the midpoint of the back surface. In both the TC-1 and TC-2 measurements, the fluctuations were seen which was probably due to contact quality between the TC and the PE plate, in contrast to the TC-3 measurements. In this drawback, the contact quality is deteriorated not only due to securing a fixed position for the TC but also the softening behavior of the PE polymer, especially seen when it is close the melting range. Therefore, it may be stated that the non-invasive IR thermography may provide more reliable temperature measurements that can also be a reference for the numerical-experimental comparisons. Nonetheless, since no such fluctuations were observed in the TC-3 measurements, the comparison between the predicted real-time temperature evolutions to the TC-3 recordings was presented in Figure 5.11. Furthermore, in terms of comparisons between the TCs and the

predicted temperature, the position of the TC-3 may be the most reliable to analyze the accuracy of the temperature-dependent numerical model with respect to the absorbed radiation. As illustrated in Figure 5.11, the temperature evolution was closely predicted, especially at the steady state temperature zone. Regarding the entire time range up to 600 seconds, ΔT between the experimental and numerical values may not be fully negligible in the temperature ramp-up period, where after the ΔT reduces to 1°C at the steady state zone. Using the current IR heating test setup configurations, C-2 may still need to be optimized in terms of accuracy in the numerical inputs, other than radiation absorption parameters of the heated polymer. However, it should be mentioned here that, the IR heating experiments carried out in this section are the pilot analyses prior to the studies on the actual IR heating stage of PE dedicated for ISBM processes. In the IR heating stage of ISBM processes, thermal radiation is typically the dominant mode of heat transfer where no barrier is used around a polymer which is heated in shorter time duration than the one adopted here. Such type of IR heating condition -which is closer to the reality- is presented in the next section, considering the case for IR heating of PE preforms.

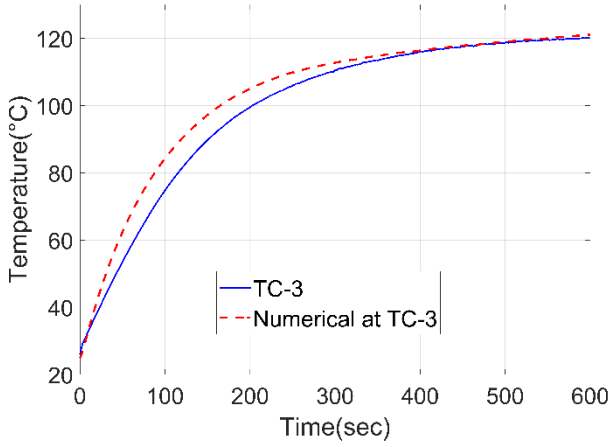

FIGURE 5.11. Experimental and numerical (simulation case-2) comparisons on the midpoint of the PE plate's back surface, considering the real-time temperature evolutions until reaching steady state.

5.3.2.2. Study case - 2: IR heating of PE preform and an overview of heating stage for ISBM processes

This study case is dedicated for simulating the IR heating of PE used ISBM processes, at which multiple number of lamp is typically used for heating the injection molded test tube-shaped preforms before blowing the final product. As discussed in Chapter 2, higher fraction of crystalline phase in semi-crystalline thermoplastics introduces narrower thermoforming, as schematically shown in Figure 2.1. Hence, such type of highly crystalline polymers, like PE-1 studied here, are thermoformed when they are in semi-molten state. Consequently, accurate temperature field predictions and monitoring of temperature

state become more critical for successful forming processes. In this study, the analyses do not only provide an insight into the modeling predictions of the components used for industrial applications, but also helps to assess the accuracy of the model predicting surface temperature field on a more complex geometry in comparison to the PE plate used in the previous study case.

In Figure 5.12, the geometrical details IR heating experiments including both the PE-1 preform and IR heating lamps are schematically displayed (a) and, overview of the heating experiments are presented (b). As aforementioned, identical 1kW halogen IR lamp was used for all the IR heating experiments presented in this chapter. In this study, 5 identical IR lamps were employed. Since non-reflector IR lamp (no ceramic reflector coating on its backside) was used, a metallic reflector was positioned at the backside of the lamps so that the potential losses in the emitted radiation which does not reach to the preform medium could be minimized (Figure 2.4 (d)). The height of the vertically aligned part of the metallic reflector is 150 mm where also it has an inclined part with a length of 50 mm, as shown in Figure 5.12 (b). The heating of the PE-1 preform was done for 60 seconds where also the preform was rotated with a constant rotational speed. The rotational speed imposed by the IR heating – blowing units was previously determined in our lab as revolution per second (rps), which is 1.2 rps here.

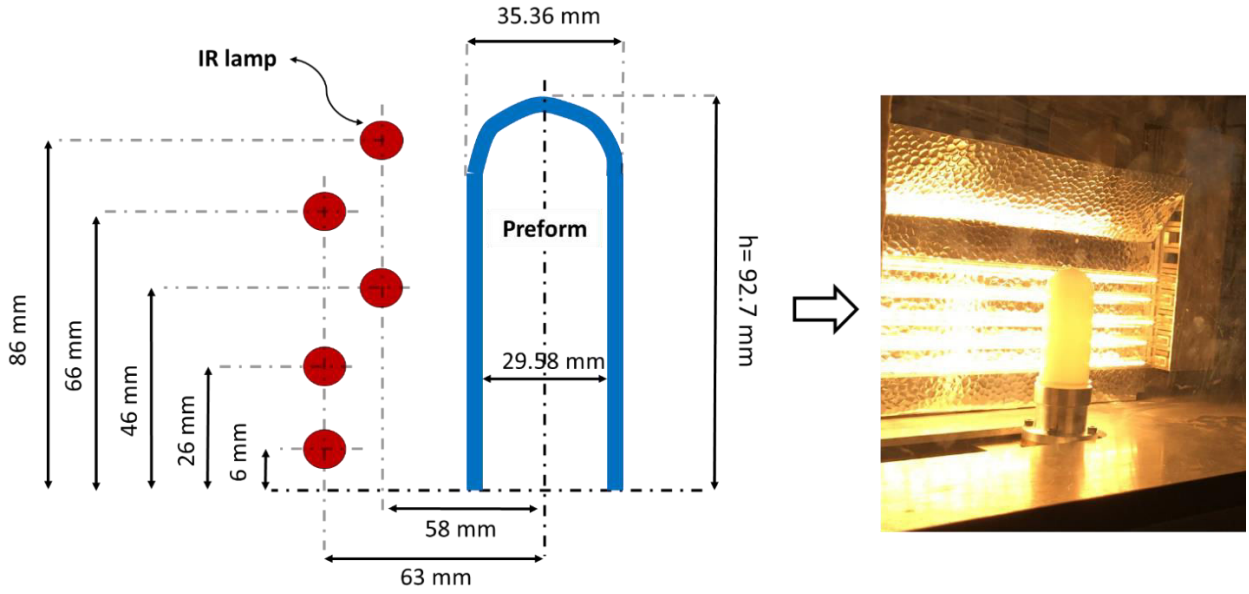

(a) (b)

FIGURE 5.12. The schematical illustration of testing configurations, the geometrical details of IR heating of the preform (a) and, the overview of the heating experiments (b).

IR thermographic measurements were done on the preform surface monitoring the geometry from a sideview for minimizing potential disturbance of a direct emission from IR lamp to the IR camera. It was observed that this type of monitoring from side reduced the disturbance greatly in IR thermography. However, it could not be eliminated completely which resulted erroneous measurements, especially on the zones of preform closer to the IR lamp. The similar disturbance effect in a reduced manner was still observed even the IR heating unit was switched off. This is due to the tungsten of IR lamps at very high temperatures continues to emit some radiation for some short amount of time, which can be seen in MIR range but not in VIS range. This was verified by two different IR cameras where only IR lamps were monitored just after switching off the heating unit. In order to overcome this issue, an opaque barrier was manually positioned between IR lamps and the preform just immediately after switching off the heating unit, which was followed by IR thermographic measurements on PE preform surface. It was observed that the time passed between stopping heating and obtaining IR thermography of the preform was no longer than 10 seconds.

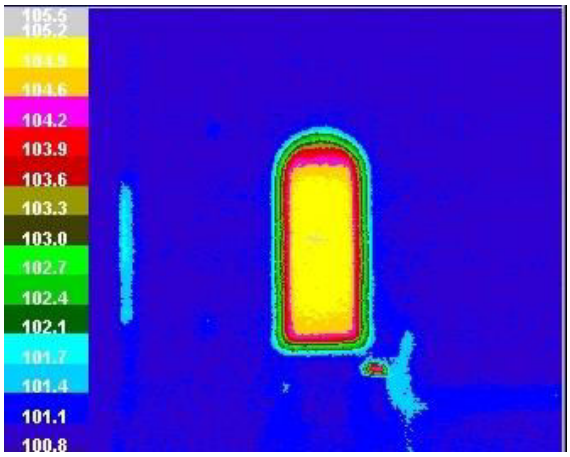

FIGURE 5.13. IR thermography of the PE-1 preform obtained immediately after switching off the IR heating unit.

In the model, the identical time for heating the preform and obtaining IR thermography was considered. Therefore, $\nabla.q_r$ was applied to the preform geometry up to 60 seconds where after no heat source was considered for additional 10 seconds, for simulating the time passed for getting IR thermography after switching off the IR heating unit. The boundary conditions were set regarding the experimental set up shown in Figure 5.12 (a). The exact positions of the 5 IR lamps and their length (300 mm) were defined in the model. In addition, the flat metallic reflector was modeled. Its integrated reflectivity ($\bar{\rho}$) was defined as 0.80 in the model, which was adopted from [20]. As mentioned in Table 5.1, two simulation cases, C-1 and C-2, were developed based on temperature-independent ($\nabla.q_r$ (25 ^oC))

and temperature-dependent thermal radiation absorption capacity ($\nabla.q_r(T)$), respectively. In the model, PE preform geometry was meshed with 5075 linear hexagonal elements, and the temperature of each mesh element was computed as the average temperature of its nodes' temperatures. The emitted radiation from the IR lamp was modeled using again $1.5*10^6$ rays. It was observed that computational cost increased dramatically due to increase in the number of employed IR lamp, especially for the case of $\nabla.q_r(T)$ at 12 temperature steps. Using the identical CPU of the previous study case, the ray tracing computations took around 60 minutes for 5 lamps. The computation of the single source term, $\nabla.q_r(25\ ^oC)$, took 20 minutes for C-1. Considering 12 different scenarios of $\nabla.q_r(T)$, the computations was done for each lamp at each temperature step, so that 60 combinations of the $\nabla.q_r(T)$ computations took around 230 minutes. Similarly, the closed loop iterative computations for solving energy-balance equation took 10 minutes for C-1 and 35 minutes for C-2, respectively. As test tube-shaped preform is rotated under heating at constant rotational speed, it is required to compute the $\nabla.q_r$ under dynamic conditions whereas it would increase the computational time dramatically. An easy way to tackle this problem was proposed in RAYHEAT by Cosson et al [20], modeling a rotating IR source instead of rotating the preform which reduces the computational cost significantly. Since the important physical phenomenon here is about the relative rotational speed between the IR heating unit and the preform, introduction of rotational movement IR source, and thus spatially rotating $\nabla.q_r$ on the preform geometry simulates the physical phenomenon properly as long as constant rotation speed and steady-state radiation is emitted.

Similar methodology could be thought for the rotating preform in still air. More specifically, rotational speed can be converted into linear (or tangential) speed represented on the preform surface and it can be considered as the speed of air flow applied through a preform under static condition. In literature, there are redundant sources specifically dedicated for rotating cylindrical-shaped solids in still air which propose calculations of Nusselt Number (Nu), and thus h. For instance, Dropkin et al [45] studied experimentally the problem of natural convection of rotating cylinders in still air. Considering both rotation and natural convection, they proposed an equation between Reynolds (Re), Grashof (Gr) and Nu numbers (Annex 4.10). In our case, considering the linear speed as 0.133m/s for the rotating PE preform; Re, Gr and Nu numbers were calculated and, h was determined around 16 W/m^2K regarding to the adopted equation. More recently, Liga et al [46] studied the convection cooling on rotating PET bottles, and they suggested h = 17 W/m^2K for the exterior surface of cylindrical PET. However, their rotational speed was somewhat higher than our case which was around 3.3 rps. Based on the h calculations using the adopted equations and comparisons to literature, h was chosen as 16 W/m^2K on the exterior surface of the PE-1 preform. The convection cooling was also considered in the interior side. The h value was chosen as 7 W/m^2K on the interior surface, as adopted by Cosson et [20] for PET preforms in analogous shape.

Similar to the previous study case, numerical - experimental comparisons were done on two profiles that were defined in the vertical and horizontal directions on the preform. In Figure 5.14, the comparisons on the horizontal axis are presented. The horizontal profile was defined at the mid-height of the preform. In the model, the predicted temperature field on the identical coordinates was chosen. In the figure, the 3D temperature field seen at left represents the temperature field computed from C-2. As it is seen in the figure, C-2 closely predict temperature whereas there is a slight overestimation in the predicted temperature by 4 °C whereas the overestimated temperature field is greater in C-1 which was around 7 °C. The variation in the predicted temperature values alongside the mid-height of preform is very small, whereas somewhat reduced values are seen at the edge of IR thermography. This is probably due to directional dependence of emitted radiation from the curved preform surface so that IR thermographic measurement accuracy is potentially deteriorated on these curved zones.

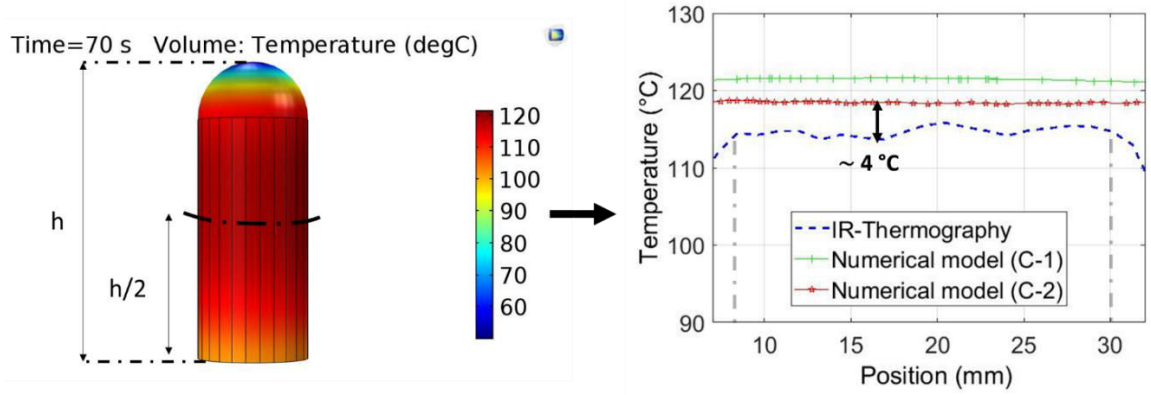

FIGURE 5.14. Predicted temperature field via two simulation cases and, its comparisons to the IR thermography on the horizontal axis (dashed line at left) of the PE preform determined at its half-height.

In Figure 5.15, the numerical -experimental temperature field comparisons on the vertical axis of the preform are displayed. The vertical profile was defined starting from the neck of the preform up to its apex, as shown in the figure at bottom. Similar to the comparisons on the horizontal profile, C-2 closely predicts the temperature field, especially on the cylindrical middle zones of the preform where radiation absorption is potentially more prominent. In addition to this, slight overestimation in the predicted temperature field of C-2 is seen (around 4 °C). Whereas this overestimation is more pronounced for C-1, which was found around 7 °C. Considering again the measured temperatures in the middle zones of the preform (around 115 °C), the averaged global error in the predicted temperature is around 6% and 3.5% for C-1 and C-2, respectively. This is not surprising as, C-1 ignores the potential weakening in the thermal radiation absorption capacity of PE under heating. However, for both C-1 and C-2 cases, the overestimated temperature field in the middle zones of the preform may be related to the underestimation

of convection heat transfer under dynamic motion. As discussed before, based on the equations proposed in literature, h values were chosen for the exterior and interior surfaces of test tube-shaped preform, but not experimentally determined. Beyond the comparisons in the middle zone of the preform, two points are needed to be discussed further concerning the relatively less accurate temperature field predictions close to the neck of preform and on its apex. The failed predicted temperature on the apex of the preform may be explained by the modeling all the geometrical details of the IR heating unit. As shown in Figure 5.12 (b), the metallic reflector is flat where its upper part is inclined which potentially sends more radiation towards apex. However, this inclined part was not modeled, and the metallic reflector was considered as completely flat on vertical axis. In addition, the neck of preform is typically designed for assembling into the rotating spindle which facilitates rotation and translation of the preform into the mold during ISBM processes. In the model the geometrical details of the preform neck was not modeled, and no rotating spindle was also designed. The lower temperature read by IR camera is likely the result of conduction heat transfer between the metallic rotating spindle and the heated preform

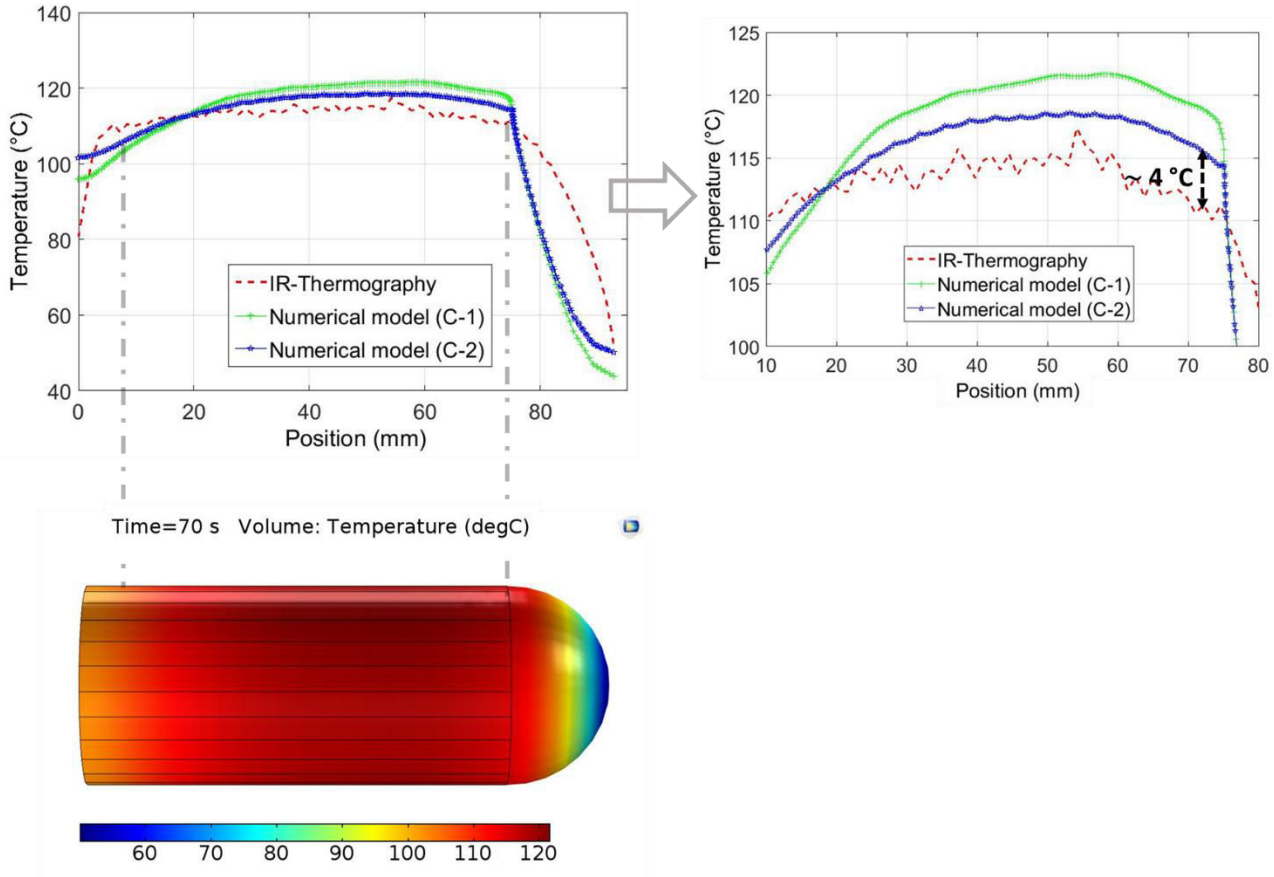

FIGURE 5.15. Predicted temperature field via two simulation cases and, their comparisons to the IR thermography alongside the vertical axis (at bottom) of the PE preform, up to its apex.

The comparisons between the ΔT of C-1 and C-2 studied in the cases of IR heating of PE plate and preform, may raise another interesting point. Considering the ΔT between C-1 and C-2 of both the study cases, it can be seen that is almost doubled in the PE plate case, as shown in Figure 5.10, 5.14 and 5.15. This is inherently due to more pronounced weakening in the absorption characteristics of PE once it is closer to its melting range. Considering that PE is thermoformed at semi-molten state, it is a clear evidence that temperature dependency could be one of the key factors for modeling purposes of IR heating, and thus successful forming processes. In case that the polymer is required to be heated at lower temperatures, this temperature dependency may be ignored as the prediction accuracy of both the cases would likely converge at lower temperatures.

5.4. An experimental analysis on the crystalline structure dependent temperature field in semi – crystalline polyethylene

In this study, the heating behavior and temperature field of two types of PE polymer was experimentally analyzed performing IR heating experiments under identical conditions. Following the same strategy presented before in the several analyses in Chapter 3 and 4, the experimental comparisons were done between PE-1 and PE-2. For the analyses, the geometrically identical 78*78*2.2 mm thick PE-1 and PE-2 plates were heated. The characteristics of the IR heating experiments were identical to the one presented in Figure 5.7. For the thermal measurements, the two contact TCs were positioned on the exact location in both the PE-1 and PE-2 plates, as illustrated in Figure 5.7 (b). The IR heating and the TC recordings were started simultaneously so that the real-time temperature evolution of the plate was recorded.

As shown in Figure 5.16 (a), the heating behavior in both the PE-1 and PE-2 plates were considerably different on the midpoint of the plates (TC-1), while no such difference was observed on the zone close to the edge of the plates (TC-2). As discussed before, radiation is likely the dominating mode of heat transfer in the middle zones of the plate whereas its effect reduces towards to edges due to the test setup. This may explain why the heating behaviors of both the polymers are very similar in this zone, especially up to 300 seconds, where after the contact quality of the TC-2 on PE-1 was probably deteriorated. Considering the TC measurements at the midpoint point of both the PE-1 and PE-2, no such fluctuation is seen in the recorded temperature values over 600 seconds. Interestingly, it is seen that the temperature on the midpoint of PE-1 increases much faster than PE-2 up to 300 seconds, whereafter ΔT is almost leveled off so that a constant shift is seen between the recorded temperatures. This heating rate difference in the both types of PE may be attributed to the increased thermal radiation absorption capacity by the fraction of crystalline phase. As discussed in Chapter 3, the absorption bands of PE is related to chemical compositions, more specifically, it is related to C-H bands. These bands are very similar for PE-1 and PE-

2, whereas the amount of absorbed radiation may slightly differ regarding to slightly different chemical compositions [47,48]. Hence, the significant in the heating rate behavior may not be fully related to the absorbed radiation by a unit amount of material, but probably to the incresased amount of absorbed radiation by a unit volume. More speficially, regarding the calorimetric analyes shown in previous chapters, PE-2 has somewhat lower X_c around 50 -55% whereas this is around 65-75% for PE-1. Higher X_c results greater density in an equivalent medium is likely the reason for absorbing more radiation since it potentially contains more C-H bands and stronger absorption in the equivalent medium. In addition to this, as reviewed in Chapter 2, the radiation travels through an optically heterogeneous medium may be prolonged due to potential changes in its direction caused by stronger optical scattering. The spectroscopic measurements and MALS tests shown in Chapter 3 demonstrated that optical scattering is stronger in PE-1 medium, which supports this hypotesis.

Secondly, the energy required to melt crystalline phase of PE-1 and PE-2, and their corresponding melting temperature range is somewhat different. Considering that Xc of PE-1 is higher, the energy required the melt PE-1 phase is higher which indeed can be considered as inversely driven mechanism that may reduce heating rate. Regarding to the almost leveled-off ΔT between PE-1 and PE-2 at higher temperatures, both the factors may be effective: stronger absorption-crystalline structure relation and the energy required for phase transitions. However, in this analysis, it is difficult to separate both the potential factors that causes such ΔT in two different PE.

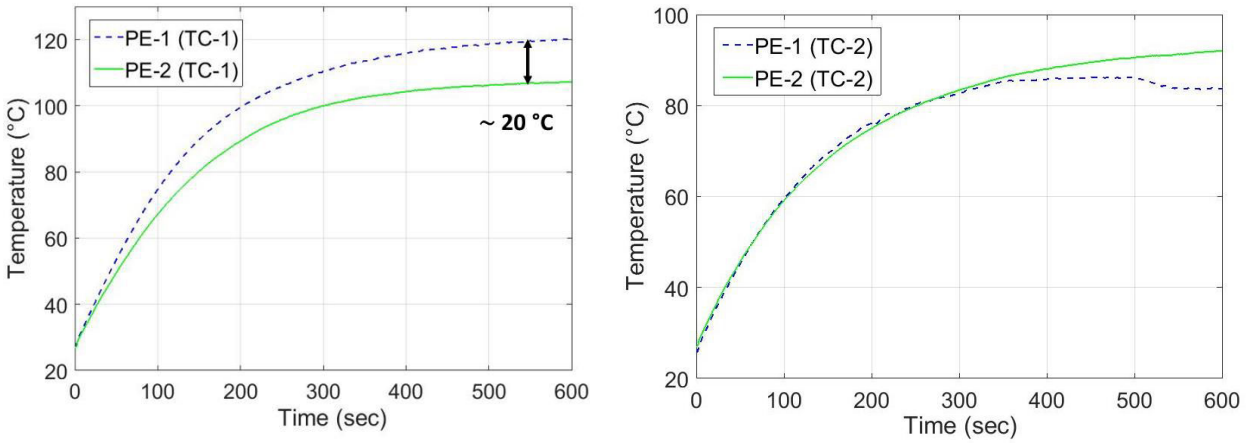

(a) (b)

FIGURE 5.16. Comparisons between the real-time temperature evolutions of the geometrically identical PE-1 and PE-2 plates measured via TC-1 (a) and TC-2 (b) attached on the identical positions.

Similar to the study case in Section 5.3.2.1, the IR-thermographic measurements were obtained just after 600 seconds, at which the back-surface temperature both the plates reached steady-state. In Figure

5.17, the comparisons on the horizontal (a) and vertical profiles (b) of the PE-1 and PE-2 plates are presented. Balanced and non-balanced temperature distributions are seen on the horizontal and vertical axes of both PE-1 and PE-2. The non-balanced temperature profiles on vertical axes of both plates are somewhat similar. As explained before, such non-balanced temperature field alongside the vertical direction is potentially due to the buoyancy-driven air flow. Interestingly, the temperature distributions on their horizontal axes show realtively more different behavior. As it is seen in Figure 5.17 (a), the temperature over the horizontal axis is distributed more uniformly on PE-1 plate. This may be explained again by the stronger optical scattering behavior. This hypotesis may be questioned focusing on the analogous analyses seen in LTW processes. As reported in [4,49–51], the greater intensity distribution of laser beam at stronger optical scattering which potentially results more evenly distributed temperature profiles. Nevertheless, the potential explanations given here are not fully on rigorous basis, which thus may only provide qualitative comparisons between PE-1 and PE-2. In addition to this, as discussed in both Chapter 3 and 4, the analyses showed the remarkable effect of lamellar morphology whereas a unique size of scatterer can not be proposed at this stage. By not having a knowledge on what exactly causes scattering, it is also ambigious to define the distribution of scatterers in PE volume. Therefore, further analyses may be required to define the equivalent scatterer size, and to analyze the distribution of crystalline phase in such geometry. Based on such type of analyses, the role of crystalline phase for the heating behavior and temperature field of semi-crystalline polymers can be explained on stronger basis. Notwithstanding, the experimental analyses shown here demonstrate the difference in the temperature field on the two types of PE, which is likely induced by the difference in their crysttalline structure.

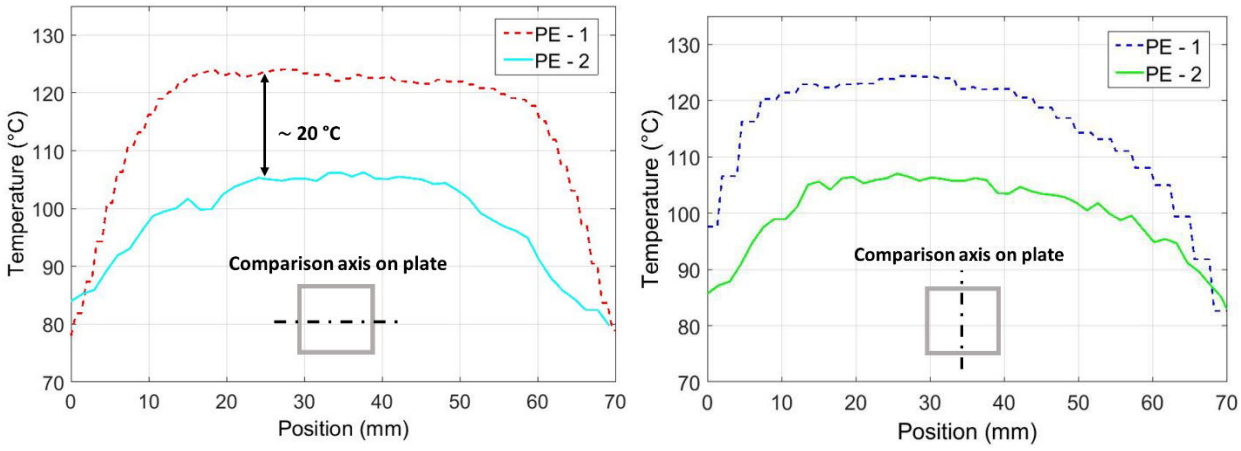

(a) (b)

FIGURE 5.17. The temperature field distributions on the horizontal (a) and vertical (b) axes of PE-1 and PE-2 plates obtained via IR thermography.

5.5. Summary

In this chapter, combined experimental-numerical approaches were proposed for radiation heat transfer in semi-crystalline thermoplastics. The proposed experimental and numerical approaches were analyzed here for the case of IR heating of PE-1. The challenges for radiation transport in semi-crystalline polymers may be categorized into the two main aspects: optical heterogeneity in polymer medium due to semi-crystalline nature and, semi-transparency in certain type of semi-crystalline polymers, such as PE analyzed here. Considering any type of monochromatic or polychromatic radiation source - such as laser and LED - the combined experimental-numerical approach proposed in this study may be adopted for temperature field predictions and non-invasive temperature measurements for the radiatively heated semi-crystalline thermoplastics.

Optical scattering is inherent for any type of semi-crystalline polymer due to their semi-crystalline nature, at which it especially becomes a key in a case that the polymer is also semi-transparent regarding the spectral range of IR radiation. Temperature-dependent numerical model was developed which considers the change in thermal radiation absorption capacity of semi-crystalline PE under heating without modeling how the light scatters inside of polymer medium. Therefore, the developed model proposes a macroscopic numerical approach without modeling the spatial distribution of the scattered light intensity at microscale, which offers computationally cost-effective numerical solutions. The computational studies were carried out adopting iterative closed-loop computations where radiation transport was computed via RAYHEAT and the energy-balance equation was solved using commercial FEM software -COMSOL Multiphysics®-. For the iterative closed-loop computations, the connection was established between RAYHEAT and COMSOL using MATLAB LiveLink feature. Thanks to the closed-loop iterative computation algorithm built in the model, the temperature dependence in the absorption characteristics was modeled at mesh scale. Due to the semi-transparency of PE, an experimental methodology was developed prior to the numerical-experimental comparisons. The accuracy of the method was analyzed performing preliminary IR heating experiments. The preliminary analyses performed under different test setup conditions showed the reproducibility of surface temperature readings on the semi-transparent PE medium obtained by NBP filter mounted IR camera, even though small error was still observed due its relatively high D_p Nevertheless, the developed experimental methodology enables to obtain the most accurate surface temperature possible on semi-transparent PE medium that is close enough to the real surface temperature.

The accuracy of the model was assessed performing numerical-experimental comparisons for the case of IR heating of PE analyzed in two different geometries: injection molded square plates and, test tube-shaped preforms which are typically used for ISBM processes. The experimental-numerical comparisons

showed that the temperature field on PE can be closely predicted using its temperature-dependent thermal radiation absorption capacity. Thanks to the adopted comparative case study, it was demonstrated how the temperature field predictions may deviate from the experimental thermal measurements due to the ignorance of this temperature dependence. Such deviations were more significant at relatively higher temperatures which was inherently caused by more pronounced weakening in the absorption characteristics of PE once it is closer to its melting range. Considering that the thermoforming window of semi-crystalline PE is around 4-5°C which lie in polymer's melting range, it is a clear evidence that temperature dependency could be one of the key factors for modeling purposes of IR heating, and thus successful forming processes. In case that the polymer is required to be heated at lower temperatures, this temperature dependency may be ignored as the prediction accuracy of both the cases would likely converge at lower temperatures. The experimental-numerical IR heating studies under different conditions showed that all the modes of the heat transfer may be critical in the combined radiation-conduction-convection problems in terms of improving further the modeling accuracy. Even though the dominating mode of heat transfer is radiation, it was observed that the predicted temperature field may show somewhat deviation due to the conduction and convection effects.

At last, the heating behavior and temperature field of PE-1 and PE-2 polymers were experimentally analyzed performing IR heating experiments under identical conditions. It was observed that heating rate is higher for PE-1 especially at lower temperatures, where after the temperature difference between PE-1 and PE-2 was almost leveled off. In addition, somewhat different temperature distributions were observed on the PE-1 and PE-2 plates. The different heating behaviors and temperature fields at steady-state conditions may be attributed two main factors: Firstly, higher X_c resulting greater density in an equivalent medium is likely the reason for absorbing more radiation where it potentially contains more C-H bands. In addition to this, radiation that travels through an optically heterogeneous medium may be prolonged due to potential changes in its direction caused by stronger optical scattering. Secondly, the energy required to melt crystalline phase of PE-1 and PE-2, and their corresponding melting temperature range is somewhat different. Considering that X_c of PE-1 is higher, the energy required the melt PE-1 phase is higher which indeed can be considered as inversely driven mechanism that may reduce heating rate. Regarding to almost leveled-off ΔT between PE-1 and PE-2 at higher temperatures, both the factors may be effective: stronger absorption-crystalline structure relation and the energy required for phase transitions. However, in this analysis, it is difficult to separate both the potential factors that causes such ΔT in two different PE. Nevertheless, the potential explanations given here are not fully on rigorous basis, which thus may only provide qualitative comparisons. As discussed in both Chapter 3 and 4, the analyses showed the remarkable effect of lamellar morphology whereas a unique size of scatterer can not be proposed at this stage. By not having a knowledge on what exactly causes scattering, it is also ambigious

to define the distribution of scatterers in PE volume. Therefore, further analyses may be required to define the equivalent scatterer size, and to analyze the distribution of crystalline phase in such geometry. Notwithstanding, the experimental analyses shown here demonstrate the difference in the temperature field on the two types of PE, which is likely induced by the difference in their crysttalline structure.

As a future work, a numerical model at microscale can be developed which may address two different problems discussed here: The spatial distribution of the scattered light in relation to the crystalline morphology of semi-crystalline polymers may be determined and, a complete solution for the absorbed radiation in 3D polymer medium may be obtained. In addition, microscale models may provide further understanding about how morphology-dependent optical scattering causes a change in the heating behavior and final temperature field.

References

[1] Klein R. Laser Welding of Plastics: Materials, Processes and Industrial Applications. Weinheim, Germany: Wiley-VCH Verlag GmbH & Co. KGaA; 2011.

[2] Burkhardt Gert, Hüsgen Ulrich, Kalwa Matthias, Pötsch Gerhard, Schwenzer Claus. Plastics Processing, 1. Processing of Thermoplastics. Ullmanns Encycl Ind Chem 2011.

[3] Apetz R, Bruggen MPB. Transparent Alumina: A Light-Scattering Model. J Am Ceram Soc 2003;86:480–6.

[4] Ilie M, Kneip J-C, Matteï S, Nichici A, Roze C, Girasole T. Laser beam scattering effects in non-absorbent inhomogenous polymers. Opt Lasers Eng 2007;45:405–12.

[5] Berrocal E, Sedarsky DL, Paciaroni ME, Meglinski IV, Linne MA. Laser light scattering in turbid media Part I: Experimental and simulated results for the spatial intensity distribution. Opt Express 2007;15:10649–65.

[6] Humphrey A, Harman T, Berzins M, Smith P. A scalable algorithm for radiative heat transfer using reverse monte carlo ray tracing. Int. Conf. High Perform. Comput., Springer; 2015, p. 212–230.

[7] Boztepe S, Gilblas R, de Almeida O, Gerlach C, Le Maoult Y, Schmidt F. The role of microcrystalline structure on optical scattering characteristics of semi-crystalline thermoplastics and the accuracy of numerical input for IR-heating modeling. Int J Mater Form 2017.

[8] Tsu DV, Muehle M, Becker M, Schuelke T, Slagter J. Quantification of diffuse scattering in glass and polymers by parametric power law analysis of UV to NIR light. Surf Coat Technol 2017. doi:10.1016/j.surfcoat.2017.08.054.

[9] Denis A, Dargent E, Lebaudy PH, Grenet J, Vautier C. Dependence on the spectral scattering coefficient on crystallinity into semicrystalline polyester. J Appl Polym Sci 1996;62:1211–8.

[10] Wunderlich B. Thermal analysis of polymeric materials. Berlin: Springer; 2005.

[11] Choy CL. Thermal conductivity of polymers. Polymer 1977;18:984–1004.

[12] Peacock AJ. Handbook of polyethylene: structures, properties, and applications. New York: Marcel Dekker; 2000.

[13] Kurabayashi K. Anisotropic thermal properties of solid polymers. Int J Thermophys 2001;22:277–288.

[14] Höhne G, Hemminger W, Flammersheim H-J. Differential scanning calorimetry: an introduction for practitioners. Berlin; New York: Springer-Verlag; 1996.

[15] Glenz W, Morosoff N, Peterlin A. Density of Drawn polyethylene. J Polym Sci Part C Polym Lett 1971;9:211–217.

[16] Perepechko I. Low-Temperature Properties of Polymers. Elsevier; 2013.

[17] Leute U, Dollhopf W, Liska E. Dilatometric measurements on some polymers: The pressure dependence of thermal properties. Colloid Polym Sci 1976;254:237–46.

[18] Yenikolopyan NS, Raspopov LN, Pomogailo AD, Khrisostomov FA, Bochkin AM, Filippov VV, et al. Structure and density of the amorphous and crystalline phases in low-density linear polyethylenes. Polym Sci USSR 1989;31:2882–91.

[19] Gedde UW, Mattozzi A. Polyethylene Morphology. In: Albertsson A-C, editor. Long Term Prop. Polyolefins, vol. 169, Berlin, Heidelberg: Springer Berlin Heidelberg; 2004, p. 29–74.

[20] Cosson B, Schmidt F, Le Maoult Y, Bordival M. Infrared heating stage simulation of semi-transparent media (PET) using ray tracing method. Int J Mater Form 2011;4:1–10.

[21] Vueghs P, de Koning HP, Pin O, Beckers P. Use of geometry in finite element thermal radiation combined with ray tracing. J Comput Appl Math 2010;234:2319–26.

[22] Devrient M, Da X, Frick T, Schmidt M. Experimental and Simulative Investigation of Laser Transmission Welding under Consideration of Scattering. Phys Procedia 2012;39:117–27.

[23] Howell JR, Menguc MP, Siegel R. Thermal Radiation Heat Transfer, 6th Edition. CRC Press; 2015.

[24] Kim K, Guo Z. Multi-time-scale heat transfer modeling of turbid tissues exposed to short-pulsed irradiations. Comput Methods Programs Biomed 2007;86:112–23.

[25] Wang C-H, Feng Y-Y, Zhang Y, Yi H-L, Tan H-P. Transient/time-dependent radiative transfer in a two-dimensional scattering medium considering the polarization effect. Opt Express 2017;25:14621.
[26] Amaya J. Unsteady coupled convection, conduction and radiation simulations on parallel architectures for combustion applications n.d.:312.
[27] Dombrovsky LA. Radiation transfer theory and the computational methods n.d. doi:10.1615/thermopedia.000072.
[28] Hogan RE, Gartling DK. Solution strategies for coupled conduction/radiation problems. Commun Numer Methods Eng 2008;24:523–42.
[29] Perraudin DYS, Haussener S. Numerical quantification of coupling effects for radiation-conduction heat transfer in participating macroporous media: Investigation of a model geometry. Int J Heat Mass Transf 2017;112:387–400.
[30] Okada T, Ishige R, Ando S. Analysis of thermal radiation properties of polyimide and polymeric materials based on atr-ir spectroscopy. J Photopolym Sci Technol 2016;29:251–254.
[31] Tsilingiris PT. Comparative evaluation of the infrared transmission of polymer films. Energy Convers Manag 2003;44:2839–56.
[32] Le Maoult Y, Schmidt F. Infrared Radiation Applied to Polymer Processes. In: Boyard N, editor. Heat Transf. Polym. Compos. Mater., John Wiley & Sons, Inc.; 2016, p. 385–423.
[33] Usamentiaga R, Venegas P, Guerediaga J, Vega L, Molleda J, Bulnes F. Infrared Thermography for Temperature Measurement and Non-Destructive Testing. Sensors 2014;14:12305–48. doi:10.3390/s140712305.
[34] Carlomagno GM, Cardone G. Infrared thermography for convective heat transfer measurements. Exp Fluids 2010;49:1187–218.
[35] Le Maoult Y, Schmidt F. Infrared Radiation Applied to Polymer Processes. John Wiley & Sons, Inc; 2016.
[36] Monteix S, Maoult YL, Schmidt F, Arcens JP. Quantitative infrared thermography applied to blow moulding process: measurement of a heat transfer coefficient. Quant InfraRed Thermogr J 2004;1:133–50.
[37] Vollmer M, Mallmann K-P. Infrared Thermal Imaging: Fundamentals, Research and Applications. John Wiley & Sons; 2017.
[38] Kawasaki T, Kawai S. Thermal insulation properties of wood-based sandwich panel for use as structural insulated walls and floors. J Wood Sci 2006;52:75–83.
[39] Li KY, Fleischmann CM, Spearpoint MJ. Determining thermal physical properties of pyrolyzing New Zealand medium density fibreboard (MDF). Chem Eng Sci 2013;95:211–20.
[40] Churchill SW, Chu HHS. Correlating equations for laminar and turbulent free convection from a vertical plate. Int J Heat Mass Transf 1975;18:1323–9.
[41] Incropera FP, Incropera FP, editors. Fundamentals of heat and mass transfer. 6th ed. Hoboken, NJ: John Wiley; 2007.
[42] Mastai Y, Diamant Y, Aruna ST, Zaban A. TiO2 nanocrystalline pigmented polyethylene foils for radiative cooling applications: synthesis and characterization. Langmuir 2001;17:7118–7123.
[43] Lai G-Y, Rietveld JX. Role of polymer transparency and temperature gradients in the quantitative measurement of process stream temperatures during injection molding via IR pyrometry. Polym Eng Sci 1996;36:1755–1768.
[44] Gardon R. The emissivity of transparent materials. J Am Ceram Soc 1956;39:278–285.
[45] Dropkin, D, Carmi, A. Natural convection heat transfer from a horizontal cylinder rotating in air. Trans ASME 1957;79:741–9.
[46] Liga A, Montesanto S, Mannella GA, La Carrubba V, Brucato V, Cammalleri M. Study on heat transfer coefficients during cooling of PET bottles for food beverages. Heat Mass Transf 2016;52:1479–88.
[47] Kossack W, Papadopoulos P, Parkinson M, Prades F, Kremer F. IR transition moment orientational analysis on semi-crystalline polyethylene films. Polymer 2011;52:6061–5.

[48] Jung MR, Horgen FD, Orski SV, Rodriguez C. V, Beers KL, Balazs GH, et al. Validation of ATR FTIRto identify polymers of plastic marine debris, including those ingested by marine organisms. Mar Pollut Bull 2018;127:704–16.
[49] Chen M. Gap bridging in laser transmission welding of thermoplastics 2009.
[50] Mamuschkin V, Roesner A, Aden M. Laser Transmission Welding of White Thermoplastics with Adapted Wavelengths. Phys Procedia 2013;41:172–9.
[51] Zak G, Mayboudi L, Chen M, Bates PJ, Birk M. Weld line transverse energy density distribution measurement in laser transmission welding of thermoplastics. J Mater Process Technol 2010;210:24–31.

This page intentionally left blank.

Chapter 6

CONCLUSIONS AND FUTURE WORK

6.1. Conclusions

Around the main focus on *understanding of IR heating of semi-crystalline thermoplastics* several issues were addressed. The key aspects for IR heating of semi-crystalline thermoplastics can be categorized as: *crystalline morphology-optical scattering relations, radiation transport in optically heterogeneous polymer medium* and *IR thermography of semi-transparent PE*. The key conclusions of this thesis are therefore summarized under three main issues listed below:

Crystalline morphology – optical scattering relations in unfilled semi-crystalline PE:

- The spectroscopic - calorimetric analyses showed the strong coupling between crystalline structure and optical scattering in VIS and NIR ranges, especially for the transmittance characteristics. Whereas, slight effect of crystalline structure was found in the reflectance characteristics, in NIR range. It was also observed that the optical scattering becomes negligible in MIR range, especially for the wavelengths shorter than 3.5 μm.

- The relation between the PE morphology and optical scattering characteristics was studied based on the comparative spectroscopic – calorimetric – microscopic analyses between PE-1 and PE-2. It was found that the shift in the l_c distributions of PE-1 induced by lamellae thickening causes a significant change on its optical scattering behavior in VIS and NIR ranges. The spherulitic texture in the PE-1 and PE-2 samples was not fully clear in the microscopic analyses. Nevertheless, it was qualitatively observed that the spherulite diameter in most of the PE-1 and PE-2 (quenched or annealed) is around 10 μm. The role of spherulites on optical scattering was therefore ambiguous.

- It was observed that both the populations of the bimodal l_c distributions influence optical scattering in PE-1. On one hand, thin lamellar structures forming at room temperature likely cause a slight decrease in the $T_\lambda^{i,r}$ in VIS range which was analyzed through the time-dependent morphological-optical analyses up to 387 h. On the other hand, thickening of lamellar morphology in PE-1 causes decreasing in $\Phi_\lambda^{s\text{-}forward}$ where also its spatial distribution becomes broader, whereas no remarkable effect on the $\Phi_\lambda^{s\text{-}back}$ was seen. It was observed that this trend obtained from the MALS tests perfectly matches with the morphology-dependent total scattered light estimated from the spectroscopic test, which confirms the role of thickening of lamellar morphology on the forward-scattered light. The comparison between PE-1 and PE-2 was a clear evidence for the fact that optical scattering behavior becomes stronger or weaker in PE medium not due to the amount of crystals - or X_c -, but to the amount or number of equivalent scatterer.

- Assuming spherical scatterers in PE-1 medium, initial estimation was done for the equivalent spherical scatterer size. It was interestingly found that the thickening of lamellar morphology in PE-1 up to 100 nm, broadens the spatial distribution of forward scattered light, which theoretically refers to a reduced size of equivalent spherical scatterer. This may be indicative that the equivalent scatterer size in PE may not be identified based only on lamellar morphology, but probably some entities greater than lamellar crystals.

- Thanks to the $T_\lambda^{i,\cap}(T)$ and $T_\lambda^{i,r}(T)$, temperature-dependent total backward and forward-scattered light were estimated and, correlated to the melting of most probable lamellar morphology under heating. Therefore, the separate role of each population in the bimodal l_c distributions of PE-1 and PE-2 was highlighted. The dramatic increase in the $T_\lambda^{i,\cap}(T)$ values was consistently seen at lower temperatures than the one in the $T_\lambda^{i,r}(T)$. Hence, the thinner crystals in the 1st peak of the bimodal distributions are likely responsible for greater amount of backscattering, which melt earlier than the thicker crystals. At temperatures higher than 115^{o}C, the dramatic increase was seen in the transmittance values of PE-1 indicating that the crystals between the end of the 1st peak up to the 2nd peak of the l_c distributions mainly govern the path of dramatic increase in the transmittance.

- All the temperature-dependent transmittance tests up to the temperatures in the melting range confirmed that PE-1 and PE-2 media becomes fully optically homogeneous once their crystalline phases melt and thus, optical scattering becomes negligible. In contrast to the strong temperature-dependency in the transmittance characteristics of both the type of PE, a temperature-dependent effect was somewhat small on their reflectance characteristics.

IR thermographic measurements on radiatively heated semi-transparent polymers:

- Due to the semi-transparency of PE, an experimental methodology was developed for IR thermographic measurements. The absorption bands of PE were analyzed through the spectroscopic measurements and the proper absorption bands were chosen for the application of NBP filters mounted on IR camera. The accuracy of the method was analyzed performing preliminary IR heating experiments which showed the reproducibility of surface temperature readings on the semi-transparent PE medium, even though small error was still observed due its high D_p.

Radiation heat transfer modeling in unfilled semi-crystalline thermoplastics:

- Thanks to the spectroscopic measurements under heating, temperature-dependent thermo-optical properties of PE-1 was determined and used as radiation absorption parameter in the radiation heat transfer model. Temperature-dependent numerical model was developed considering the change in thermal radiation absorption capacity of semi-crystalline PE under heating without modeling how the light scatters inside of polymer medium. Therefore, the developed model proposes a macroscopic numerical approach without modeling the spatial distribution of the scattered light intensity at microscale which offers computationally cost-effective numerical solutions. The temperature dependence in the absorption characteristics of PE-1 was modeled at mesh scale.

- The accuracy of the model was assessed performing numerical-experimental comparisons for the case of IR heating of PE using two different geometries. The experimental-numerical comparisons showed that the temperature field on PE can be closely predicted using its temperature-dependent thermal radiation absorption capacity. Thanks to the comparative case study, it was demonstrated how the temperature field predictions may deviate from the experimental thermal measurements due to the ignorance of this temperature dependence. Such deviations were more significant at relatively higher temperatures, close to the melting range of PE, because of the more pronounced weakening in its absorption characteristics.

- Thermoforming window of semi-crystalline PE is around 4-5°C. Considering this temperature tolerance, the simplification of radiation transport in the optically heterogeneous medium of PE by means of temperature-dependent extension coefficient may be sufficient for optimizations of the IR heating stage of its thermoforming processes.

- The morphology-dependent thermal radiation absorption capacity in PE-1 and PE-2 media were qualitatively analyzed performing IR heating experiments under identical conditions. It was observed that heating rate is higher for PE-1 especially at lower temperatures. The different heating behavior may be attributed to two factors: optical scattering and stronger absorption in denser crystalline medium and, the difference in the temperature range of phase transitions, whereas the qualitative analysis performed in this thesis may not be enough to conclude. Notwithstanding, the IR heating experiments demonstrate the difference in the temperature field on the two types of PE, which is likely induced by the difference in their crysttalline structure.

- Considering any type of monochromatic or polychromatic radiation source, the combined experimental-numerical approach proposed here may be adapted for temperature field predictions

and non-invasive temperature measurements on the radiatively heated semi-crystalline and semi-transparent thermoplastics.

6.2. Recommendations and future work

In this section, the key points to be focused for further research are listed under two main points:

Determination of scatterer size in unfilled semi-crystalline thermoplastics and scatterer – optical scattering evolutions under varying temperature:

- Further chemical etching / staining methods may be adopted for better visualization of spherulitic structures and employing other microscopic techniques, including AFM and POM.

- The heating rate of temperature-dependent optical measurements are required to be synchronized to the heating rate of calorimetric analyses performed for predicting lamellar morphology. In this thesis, temperature-dependent backward and forward optical scattering was estimated under step wise heating which potentially cause reorganization in the lamellar morphology. Whereas, the predicted lamellar morphology was obtained at a constant heating rate. Although it provides the range of the size of lamellar crystals causing optical scattering, the exact size may only be obtained adopting the identical heating rate for both the temperature-dependent optical measurements and calorimetric analyses.

- The morphology-dependent spatial distribution of light scattering in semi-crystalline polymer media may be required to analyze at further wavelengths. Based on the obtained behavior at different wavelengths, the inverse method for theoretical-experimental analyses discussed in the thesis may be adopted for defining the equivalent scatter size. Uncertainty about the shape of scatterer, (e.g: spherical or arbitrary shape) in unfilled semi-crystalline polymers may then be discussed based on the fitting to the adopted light scattering theory.

Radiation heat transfer modeling in unfilled semi-crystalline thermoplastics and accuracy in the temperature control techniques:

- The developed model in this thesis does not consider melting kinetics of semi-crystalline thermoplastics. Considering various type of radiative heating applications and industrial forming processes, the heating rate may be different. Hence, the model may require to be improved considering the heating rate dependence of phase transitions of polymers.

- Radiation transport may be modeled at microscale considering optical scattering phenomenon. As a starting point of such modeling may require characterizing the size of scatterer in semi-crystalline media, following the inverse methodology discussed in this thesis.

- Under radiative heating, non-invasive methods such as IR thermography may be one of the most suitable methods, as proposed in this thesis. However, concerning semi-transparent nature of an analyzed medium, such as PE, further solutions may be required for the assessments on the numerical solutions proposing higher accuracy.

This page intentionally left blank.

Synthèse de la thèse

1. Problématique et motivation

Aujourd'hui, les thermoplastiques et les composites thermoplastiques sont des candidats prometteurs pour la fabrication de composants hautement rentables et écologiques en termes de formage rapide et de recyclabilité. La production en grande série de produits à base thermoplastique intérresse un large éventail de secteurs, notamment : l'aérospatiale, l'automobile, l'emballage, le bâtiment et la construction, etc. L'industrie de l'emballage détient la plus grande part du marché des produits à base thermoplastique, suivie de la construction et du secteur automobile et aérospatial [1]. Pour les productions à volume élevé, le bon traitement est crucial pour fabriquer le produit souhaité.

Les procédés de thermoformage, tels que le thermo-estampage [2,3], le formage sous vide [4], l'injection-soufflage en cycle froid (ISBM) [3], le soudage laser pas transmission [5] sont largement utilisés pour la production en grande série de produits à base thermoplastique. Le thermoformage des thermoplastiques et de leurs composites est réalisé en adoptant une combinaison d'étapes de chauffage et de formage au cours desquelles la préforme est chauffée avant le formage afin d'améliorer la formabilité en ramollissant le polymère, comme illustré à la figure 1. Les thermoplastiques semi-cristallins peuvent être suffisamment ramollis autour de leur température de fusion car leur phase cristalline maintient le matériau à l'état élastique caoutchouteux jusqu'à ce qu'il fonde [6]. Par conséquent, contrairement aux polymères amorphes, la structure cristalline du matériau réduit la fenêtre de mise en œuvre. La température doit rester suffisamment proche de la température de fusion du matériau, tout en restant au-dessous.

Le chauffage radiatif est couramment utilisé pour le procédé de thermoformage des thermoplastiques, car les polymères ont généralement une faible conductivité thermique et des milieux peuvent être semi-transparents. Le principal avantage du chauffage par rayonnement réside dans le fait qu'une partie de l'énergie radiative pénètre au cœur du polymère, où des densités de flux thermiques élevées peuvent être utilisées pour réduire le temps de chauffage sans causer de dommage thermique à la surface du polymère [6]. Différentes sources de rayonnement sont utilisées pour les procédés de thermoformage ou de soudage de thermoplastiques dans lesquels des sources de rayonnement polychromatiques ou monochromatiques telles que les infrarouges (IR), les diodes électroluminescentes (DEL) ou les lasers sont couramment utilisées. Contrairement aux applications de chauffage par laser, le rayonnement infrarouge est émis dans une gamme spectrale qui varie en fonction de la puissance et de la température d'un émetteur infrarouge. L'absorption du rayonnement dans les milieux polymères se produit dans la gamme des infrarouges par

excitation des vibrations dans les molécules [5], afin que la génération de chaleur se produise. Quel que soit le type de chauffage radiatif, l'objectif principal de la phase de chauffage est d'obtenir un champ de température approprié dans le milieu polymère avec un chauffage rapide. Les propriétés viscoélastiques dépendantes de la température des polymères thermoplastiques ont un effet important sur le comportement de la matière et sur la mise en forme [7]. Par conséquent, l'état final de la température à la fin de la phase de chauffage joue un rôle prépondérant dans la réussite du formage en ce qui concerne la qualité d'une pièce thermoformée. Compte tenu de la fenêtre de thermoformage relativement étroite des thermoplastiques semi-cristallins, le contrôle précis de la température et la surveillance étroite du champ de température gagnent en importance. Cette thèse porte donc sur la compréhension du chauffage infrarouge de thermoplastiques semi-cristallins qui vise à identifier, analyser et comprendre les modes de transport du rayonnement infrarouge dans ce type de support polymère. En outre, la thèse propose un modèle prédictif pour le transfert de chaleur par rayonnement dans les polymères semi-cristallins. L'objectif est d'être capable de développer un code de calcul suffisamment robuste pour permettre une bonne prédiction du champ de température tout en conservant des temps de calcul raisonnables.

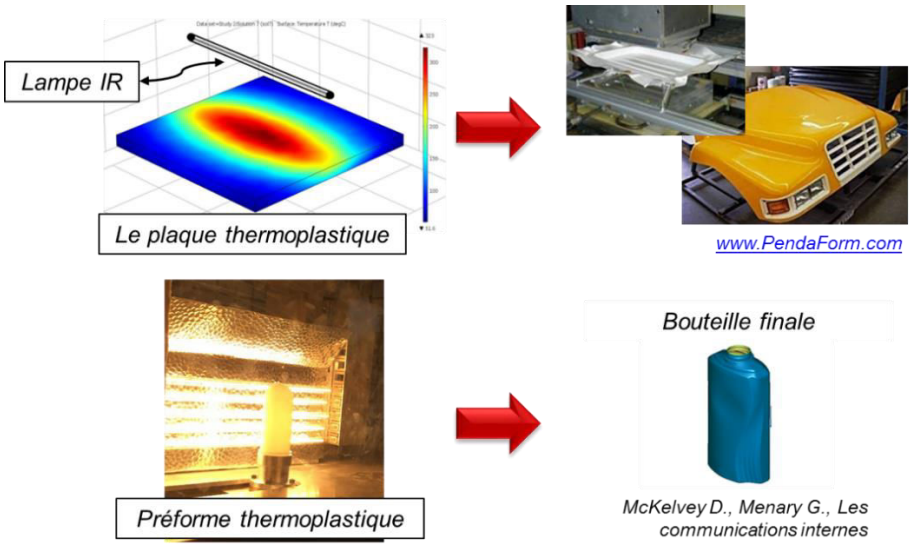

FIGURE 1. Vue d'ensemble des différents types de procédés de thermoformage des thermoplastiques.

Ces travaux se concentrent sur un matériau particulier : le polyéthylène haute densité (PEHD), qui est un polymère hautement cristallin. Le couplage entre les propriétés optiques et la structure cristalline du PEHD a été analysé grâce à des techniques de mesures avancées. Ce projet de recherche est soutenu par Procter & Gamble, une entreprise de biens de consommation, dont l'un des domaines de prédilection est l'industrie de l'emballage. En se concentrant à nouveau sur l'industrie de l'emballage, il est connu que la part de marché de la famille du polyéthylène -comprenant le PEHD, le polyéthylène basse densité (PEBD) et le polyéthylène linéaire basse densité (PEBDL)- est d'environ

deux tiers du total de la production thermoplastiques en Europe, comme indiqué dans 2001 [1]. Ce travail de recherche présenté ici vise à aborder le rôle de la structure cristalline sur le transfert de chaleur par rayonnement dans les thermoplastiques semi-cristallins non chargés. Dans le cadre de cette recherche, les approches numériques expérimentales développées peuvent ainsi être adoptées pour le chauffage radiatif de tout type de thermoplastique semi-cristallin non chargé.

2. Chauffage infrarouge de thermoplastiques semi-cristallins

La relation couplée entre la structure cristalline et les propriétés optiques des thermoplastiques semi-cristallins

Comme indiqué dans la section précédente, l'absorption des radiations dans le domaine des infrarouges est principalement régie par l'excitation de molécules dans un matériau chauffé par rayonnement. Ce phénomène a une relation directe avec les propriétés optiques des matériaux chauffés par rayonnement suivant leurs bandes d'absorption, ce qui a été étudié de manière approfondie pour le PE [8,9]. Considérant que l'emplacement de l'absorption du rayonnement est lié à la façon dont le rayonnement se propage à l'intérieur du milieu polymère. Le facteur primordial est la structure cristalline des thermoplastiques semi-cristallins, car elle introduit un milieu optiquement hétérogène. Le terme -milieu optiquement hétérogène- représente les discontinuités optiques dues aux phases amorphes et cristallines de ce type de polymères, ce qui provoque éventuellement une diffusion optique dans leur milieu. Compte tenu du transport du rayonnement et de leur absorption dans des milieux polymères semi-cristallins, il est nécessaire que le couplage entre leur structure cristalline et leurs propriétés optiques soit bien comprise. La relation entre la structure cristalline et les propriétés optiques des thermoplastiques semi-cristallins a suscité une attention particulière dans le passé, y compris le large éventail de thermoplastiques [10–15], où cette relation a été principalement analysée à la température ambiante. L'accent a été mis principalement sur la compréhension des formations de cristallites ou des unités responsables de la diffusion optique, alors que des incertitudes subsistent quant aux caractéristiques de diffusion des polymères semi-cristallins non chargés, y compris leur taille et leur forme.

Compte tenu du chauffage IR de polymères semi-cristallins, la structure cristalline a probablement un double effet : premièrement, comme mentionné ci-dessus, il existe une ambiguïté concernant les caractéristiques de diffusion de la phase cristalline provoquant une diffusion optique. Par conséquent, la détermination de la distribution spatiale du rayonnement diffusé et la localisation de l'absorption à l'intérieur d'un milieu semi-cristallin sont encore complexes. Deuxièmement, la phase cristalline, en particulier la morphologie lamellaire, évolue sous les contraintes thermiques, ce qui peut potentiellement entraîner une modification des caractéristiques du diffuseur, et donc des propriétés de diffusion optique du milieu.

Ce problème ne doit pas être confondu avec le transfert de chaleur par rayonnement dans les thermoplastiques dopés [16,17] ou à fibres courtes [18] car les caractéristiques du diffuseur -qui est lié à la taille des particules dopées ou remplies- ne changent pas potentiellement sous chauffage. Pour le chauffage de PE non-chargé à partir de la température ambiante, des transitions de phase entre les phases amorphes et cristallines commencent potentiellement à se produire car son intervalle de fusion peut s'étendre jusqu'à la température ambiante. En contrepartie, des cristallites plus minces -qui sont thermodynamiquement moins stables que des cristaux plus épais- fondent à des températures plus basses, plus tôt que les plus épais [19,20]. L'évolution potentielle de la diffusion optique dans des polymères semi-cristallins non chargés due au chauffage a été analysée expérimentalement dans la littérature, où les propriétés optiques dépendantes de la température de polymères semi-cristallins ont été étudiées [21–24]. Un changement remarquable des propriétés optiques des thermoplastiques semi-cristallins sous chauffage, en particulier proches de la température de fusion, a été mis en évidence. Ces études étaient généralement axées sur les procédés de formage assistés par laser [21–23], ainsi, l'effet de la diffusion optique et des propriétés optiques dépendant de la température ont été principalement étudiés à des longueurs d'onde monochromatiques.

Étant donné qu'une source infrarouge émet un rayonnement polychromatique, il faut également tenir compte de la dépendance spectrale de la diffusion optique. Autrement dit, dans le domaine spectral du rayonnement émis, le comportement de diffusion optique dans un milieu semi-cristallin peut changer en fonction de chaque longueur d'onde. Par conséquent, dans le cas du chauffage IR, il est nécessaire d'analyser les propriétés optiques de diffusion et les propriétés optiques des thermoplastiques semi-cristallins non chargés dans le domaine spectral du rayonnement émis.

Transport de rayonnement dans les thermoplastiques semi-cristallins et modélisation du transfert de chaleur par rayonnement

Les modèles prédictifs sont essentiels pour un contrôle précis de la température et pour obtenir un champ de température approprié à la fin de la phase de chauffage IR des thermoplastiques semi-cristallins. En ce qui concerne les relations opto-morphologiques discutées ci-dessus, la relation entre leur structure cristalline et leurs propriétés optiques est la clé pour développer un modèle de transfert de chaleur par rayonnement incluant à la fois la modification potentielle du transport de radiation dans un milieu polymère semi-cristallin et les évolutions de la diffusion optique sous chauffage.

La plupart des modèles de transfert de chaleur par rayonnement développés pour le chauffage IR ou les procédés de formage assistés par laser de thermoplastiques reposent sur l'hypothèse d'un milieu optiquement homogène. Comme le montre schématiquement la figure 2, le rayonnement émis par une source (ou une lampe) infrarouge frappe la surface du polymère est réfléchie ou pénètre dans

le milieu polymère. En supposant un milieu optiquement homogène, l'atténuation du rayonnement diminue de manière exponentielle dans le milieu suivant la loi de Beer-Lambert, qui a été largement adoptée pour le chauffage par rayonnement de thermoplastiques amorphes ou faiblement cristallins [21–23,25]. Sur la base de cette hypothèse, le transfert de chaleur par rayonnement dans les polymères amorphes et faiblement cristallins a été bien expliqué et modélisé avec précision. Cependant, cette hypothèse peut être mal définie pour les polymères qui sont hautement cristallins car elle n'explique pas correctement la propagation et absorption du rayonnement dans leur milieu. Dans ce sens, la question se pose de savoir comment le transport de rayonnement dans le milieu optiquement hétérogène de polymères semi-cristallins non chargés peut être modélisé correctement dans des conditions de chauffage.

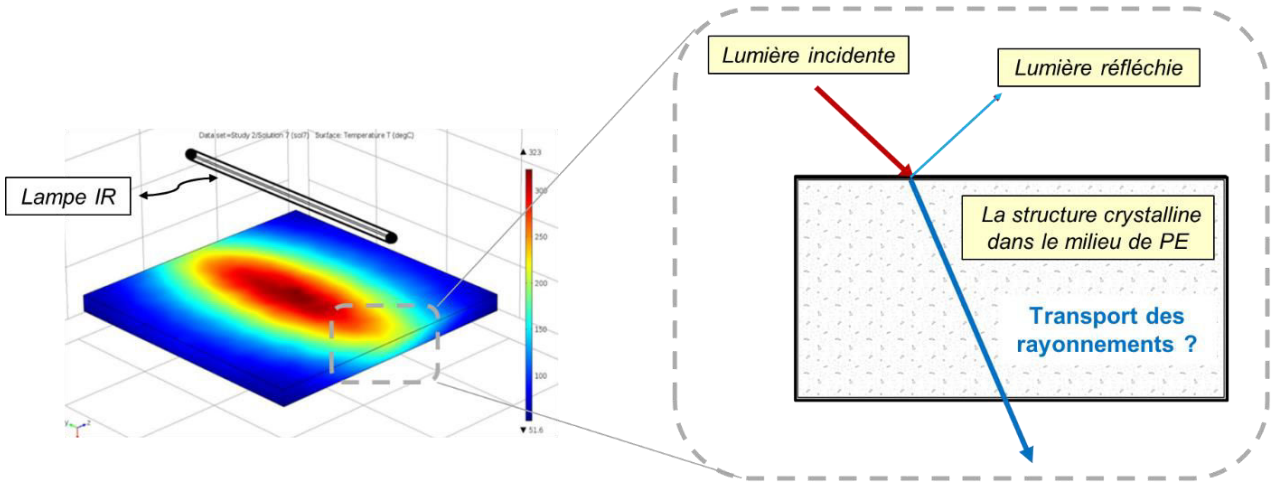

FIGURE 2. Illustration schématique du problème du transport de rayonnement en milieu polymère semi-cristallin.

En termes de modélisation du rayonnement thermique dans des milieux optiquement hétérogènes, il existe de nombreux exemples dans la littérature [16,26,27], ce qui permet de prédire fidèlement la distribution spatiale de l'intensité de la lumière diffusée. Cependant, les modèles de transfert de chaleur par rayonnement qui prédisent la physique du rayonnement dans des milieux optiquement hétérogènes peuvent être coûteux en calcul, en particulier si la complexité spectrale de la source de rayonnement ou la complexité géométrique d'un composant chauffé est impliquée [28]. Ainsi, il est potentiellement aisé de mettre en œuvre de tels modèles prédictifs dans la pratique si le produit chauffé est à petite échelle ou à géométrie simple, contrairement aux procédés de thermoformage de composants à base de thermoplastique à une échelle macroscopique.

De plus, les caractéristiques de diffusion dans les polymères semi-cristallins non chargés restent incertaines. On peut résoudre ce problème en adoptant des analyses inverses où la caractérisation expérimentale de la distribution spatiale de la lumière diffusée dans un milieu polymère peut être adaptée

aux théories de la diffusion de la lumière [29]. En utilisant cette stratégie, et en supposant une forme de diffuseur arbitraire ou sphérique, la taille équivalente du diffuseur en milieu polymère semi-cristallin peut être proposée. La dépendance spectrale du comportement de diffusion optique peut ensuite être estimée en considérant la plage spectrale du rayonnement infrarouge émis et utilisée comme entrée pour la modélisation du chauffage infrarouge.

Au-delà de ce fait, la complexité du problème du transport de rayonnement dans les polymères semi-cristallins non chargés augmente principalement en raison de l'évolution potentielle des caractéristiques du diffuseur sous sollicitation thermique, induite par les transitions de phase amorphes-cristallins. Dans ce cas, il peut être nécessaire d'analyser les propriétés optiques dépendantes de la température et la diffusion optique angulaire des supports polymères. De telles analyses, y compris la diffusion optique angulaire dans le PE, ont été analysées expérimentalement à une longueur d'onde monochromatique et l'évolution de la distribution spatiale de la lumière diffusée a été montrée dans[11]. Sachant que le rayonnement infrarouge est émis dans une gamme spectrale, la modélisation de la diffusion optique dans un milieu aussi évolutif introduit une incertitude importante sur la prévision du transport du rayonnement et du trajet de diffusion. Celui-ci pourrait théoriquement être fonction du diffuseur équivalent qui évolue sous l'effet du chauffage et de la gamme spectrale du rayonnement IR.

Par conséquent, un des verrous majeurs de ce travail de recherche a donc consisté à établir un coefficient permettant une description des transferts radiatifs dans un milieu homogène équivalent qui intègre le caractère optiquement hétérogène du milieu dû à la présence de structures cristallines. En adoptant cette approche, la modification de la capacité d'absorption des radiations du support polymère hétérogène en cours de chauffage pourrait être prise en compte à l'échelle macroscopique, sans calculer le trajet de diffusion ni l'emplacement de l'énergie absorbée à l'échelle microscopique. Par conséquent, la physique sous-jacente du transport et de l'absorption des radiations dans des milieux polymères semi-cristallins peut être correctement estimée sans calculer le transport des radiations à l'échelle microscopique, ce qui peut offrir des solutions numériques rentables. Considérant qu'il est primordial de comprendre comment obtenir une prévision précise du champ de température en adoptant cette simplification. Cette approche doit être analysée en termes de tolérance à la température de la fenêtre de thermoformage relativement étroite des thermoplastiques semi-cristallins.

Contexte de la thèse

L'objectif de ce travail de recherche est la compréhension de l'interaction du rayonnement IR avec les

cristaux de PE qui diffusent le rayonnement et font de ce matériau un « milieux semi transparent diffusant». Pour atteindre cet objectif les mécanismes fondamentaux induits par le transport du rayonnement infrarouge en milieu polymère ont été analysés. In fine, un modèle prédictif du transfert de chaleur par rayonnement dans des polymères semi-cristallins a été proposé. En ce qui concerne l'évaluation de la précision de la modélisation, une méthodologie expérimentale a été proposée pour les mesures non invasives de la température de surface de la PEHD semi-transparent par thermographie IR.

Les analyses morphologiques-optiques ont été réalisées à la température ambiante et dans des conditions de chauffage pour répondre à ce problème : *quelles formations de cristallites provoquent une diffusion optique dans des milieux polymères semi-cristallins et comment leur relation couplée évolue-t-elle dans des conditions de chauffage*. Afin de corréler la morphologie cristalline - propriétés optiques et comportement de diffusion optique, une différence significative dans la morphologie analysée devait être introduite en adoptant un autre type de polyéthylène : PEBDL. Pour toutes les méthodes d'analyses morphologiques-optiques présentées dans cette thèse, les deux types des polyéthylènes ont été utilisés pour effectuer des analyses comparatives. Sauf indication ou citation de la littérature, dans tous les chapitres suivants, PEHD et PEBDL sont nommés respectivement *PE-1* et *PE-2*. Cette thèse consiste en quatre chapitres principaux :

Le *chapitre 2* présente une revue de la littérature sur les relations morphologie cristalline-diffusion optique dans les polymères semi-cristallins et la modélisation du rayonnement thermique dans des milieux polymères optiquement hétérogènes. Le chapitre présente d'abord les bases théoriques de la physique de rayonnement infrarouge. Les études proposant des formations cristallites entraînant une diffusion optique dans divers types de thermoplastiques semi-cristallins non chargés ont été passées en revue. Les approches théoriques expérimentales pour estimer la relation morphologie cristalline-diffusion optique dans les polymères semi-cristallins ont été discutées. À la fin, des approches de modélisation du rayonnement thermique développées pour des milieux thermoplastiques semi-cristallins ou dopés ont été présentées.

Le *chapitre 3* vise à faire un pont entre les caractéristiques optiques et morphologiques du polyéthylène (PE) à température ambiante, sur la base de mesures expérimentales comparatives sur le PEHD et le PEBDL. Dans ce but, la diffusion optique dépendant de la morphologie dans le milieu PE a été étudiée en effectuant des analyses spectroscopiques - calorimétriques - microscopiques successives. Grâce aux analyses, le rôle de la structure cristalline sur les propriétés optiques du PE et la dépendance spectrale de la diffusion optique a été mis en évidence. La dépendance morphologique de la lumière diffusée totale a été estimée dans les directions avant et arrière. La relation entre la distribution spatiale de la lumière diffusée et la morphologie de PE a été étudiée à 632,8 nm.

Les formations cristallines ou la taille des unités morphologiques dans le milieu PE entraînant une diffusion optique ont été étudiées.

Le *chapitre 4* est consacré aux évolutions de la morphologie cristalline et des caractéristiques optiques du PEHD et du PEBDL sous sollicitation thermique. Les mesures spectroscopiques à différentes températures ont permis de déterminer les propriétés thermo-optiques dépendantes de la température du PEHD sur la plage de température comprise entre la température ambiante et la plage de fusion du PEHD. Les études calorimétriques - optiques expérimentales présentées dans ce chapitre ont pour objectif de corréler les caractéristiques de transmittance sous chauffage à la fusion des lamelles dans le milieu PEHD et PEBDL. La taille de cristal lamellaire la plus probable fondant et induisant un changement remarquable du comportement de diffusion optique dans le milieu PE sous chauffage a été déterminée.

Au *chapitre 5*, une nouvelle approche combinant expérimental et numérique est proposée pour le chauffage IR de thermoplastiques semi-cristallins. Le modèle de transfert de chaleur par rayonnement a été développé en considérant la simplification du transport de rayonnement dans le milieu optiquement hétérogène du PE sous chauffage. Les propriétés thermo-optiques dépendantes de la température et caractérisées au *chapitre 4* ont été adoptées dans ce chapitre en tant que paramètres d'absorption du rayonnement pour la modélisation du rayonnement thermique du PEHD. En parallèle, une méthode expérimentale a été proposée concernant les mesures non invasives de la température de surface sur du PE semi-transparent par thermographie IR. La précision du modèle numérique a été évaluée en effectuant des études comparatives expérimentales-numériques sur le chauffage IR utilisant différentes configurations de chauffage IR. La capacité d'absorption du rayonnement thermique dépendant de la morphologie dans les milieux de PEHD et PEBDL a été analysée qualitativement. Le cœur de la thèse et l'axe des chapitres sont décrits schématiquement sur la Figure 3.

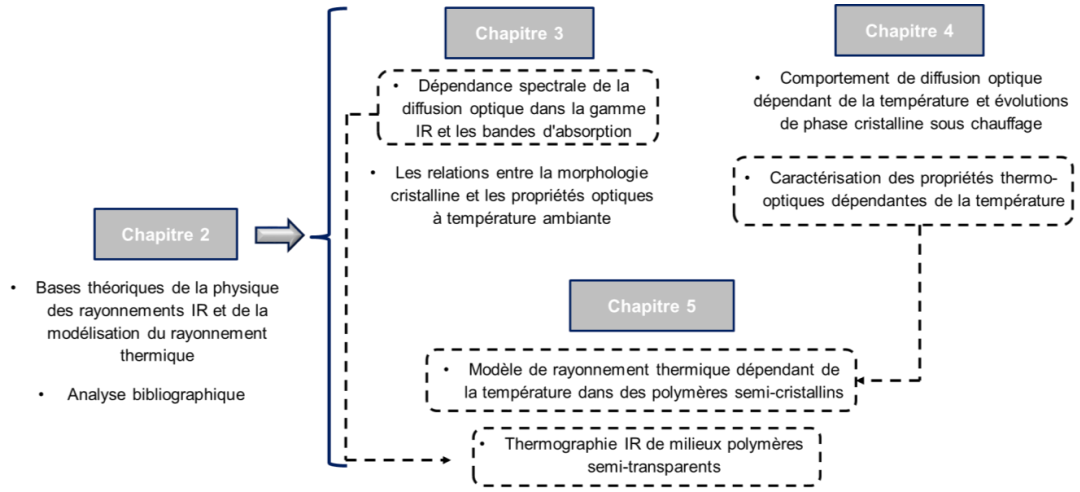

FIGURE 3. Résumé de la thèse et de l'organisation des chapitres.

Le dernier chapitre de la thèse (*chapitre 6)*, résume les principales conclusions de l'ensemble de l'étude et fournit des recommandations pour les travaux futurs. De plus, considérant la physique sous-jacente du problème complet mis en évidence ici, une discussion est présentée pour élargir l'applicabilité des approches expérimentales-numériques proposées dans cette thèse pour le chauffage radiatif de tout type de thermoplastiques semi-cristallins non chargés.

Les principales conclusions de la thèse

Sur la base de l'objectif principal pour la compréhension du chauffage IR de thermoplastiques semi-cristallins, plusieurs aspects ont été abordés. Les aspects essentiels du chauffage IR des thermoplastiques semi-cristallins sont les suivants : relations entre la morphologie cristalline et diffusion optique, transport du rayonnement en milieu optiquement hétérogène et thermographie IR de PE semi-transparent. Les principales conclusions de cette thèse sont donc résumées en trois points principaux :

La relation entre la morphologie cristalline et la diffusion optique dans le milieu semi-cristallin de PE :

- Les analyses spectroscopiques - calorimétriques ont montré le fort couplage entre structure cristalline et diffusion optique dans les gammes VIS et NIR, en particulier sur les caractéristiques de transmittance. Par contre, les caractéristiques de réflectance ont été légèrement influencées par la structure cristalline dans NIR. Il a également été observé que la diffusion optique devient négligeable dans MIR, notamment pour les longueurs d'onde inférieures à 3,5 µm.

- La relation entre la morphologie de PE et les caractéristiques de diffusion optique a été étudiée sur la base d'analyses spectroscopiques - calorimétriques - microscopiques entre PE-1 et PE-2. Il a été constaté que l'épaississement des lamelles dans PE-1 provoque un changement significatif de son comportement de diffusion optique dans les domaines VIS et NIR. Les textures sphérolitiques dans les échantillons de PE-1 et PE-2 n'étaient pas clairement visibles par les analyses microscopiques. Néanmoins, il a été observé qualitativement que le diamètre de la sphérolite dans la plupart des PE-1 et PE-2 est d'environ 10 µm. Le rôle des sphérolites sur la diffusion optique était donc ambigu.

- Il a été observé que les deux populations de la distribution bimodale de l_c influent sur la diffusion optique dans le PE-1. D'une part, les structures lamellaires minces qui se forment à la température ambiante entraînent une légère diminution en $T_\lambda^{i,r}$ dans le gamme VIS qui a été analysée par les analyses morphologiques et optiques en fonction du temps jusqu'à 387 h. D'autre part, l'épaississement de la morphologie lamellaire dans PE-1 provoque une diminution de $\Phi_\lambda^{s\text{-forward}}$, où sa distribution spatiale devient également plus large. Par contre aucun effet remarquable sur le $\Phi_\lambda^{s\text{-}}$

^{back} n'a été observé. Il a été observé que cette tendance obtenue par les tests MALS correspond parfaitement à la lumière diffusée totale dépendante de la morphologie estimée grâce aux tests spectroscopiques, ce qui confirme le rôle de l'épaississement de la morphologie lamellaire sur la lumière diffusée vers l'avant. La comparaison entre PE-1 et PE-2 était une preuve évidente du fait que le comportement de diffusion optique devient plus fort ou plus faible dans le milieu PE pas en raison de la quantité de cristaux - ou X_c -, mais de la quantité ou du nombre de diffuseur équivalent.

- En supposant des diffuseurs sphériques dans le milieu PE-1, une estimation initiale a été réalisée pour la taille équivalente du diffuseur sphérique. Il est intéressant de noter que l'épaississement de la morphologie lamellaire dans le PE-1 jusqu'à 100 nm élargit la distribution spatiale de la lumière diffusée vers l'avant, ce qui correspond théoriquement à une taille réduite du diffuseur sphérique équivalent. Cela peut indiquer que la taille équivalente du diffuseur dans le PE peut ne pas être identifiée uniquement sur la base de la morphologie lamellaire, mais probablement de certaines entités supérieures aux cristaux lamellaires.

- Grâce à $T_\lambda^{i,\cap}(T)$ et $T_\lambda^{i,r}(T)$, la lumière totale diffusée en arrière et en avant dépendante de la température a été estimée et corrélée à la fusion de la morphologie lamellaire la plus probable sous chauffage. Par conséquent, concernant les échantillons des PE-1 et PE-2, le rôle distinct de chaque population dans les distributions bimodales des l_c a été mis en évidence. L'augmentation spectaculaire dans les valeurs de $T_\lambda^{i,\cap}(T)$ a constamment été observée à des températures inférieures à celle de $T_\lambda^{i,r}(T)$. Par conséquent, les cristaux plus minces dans le premier pic des distributions bimodales sont probablement responsables d'une plus grande quantité de rétrodiffusion, qui fond plus tôt que les cristaux plus épais. À des températures supérieures à 115 ° C, les valeurs de transmittance de la PE-1 ont considérablement augmenté, ce qui indique que les cristaux entre la fin du 1er et le 2^{e} pic de la distribution l_c déterminent principalement la trajectoire d'augmentation considérable dans la transmittance.

- Tous les tests de transmittance dépendant de la température jusqu'aux températures dans l'intervalle de fusion ont confirmé que les milieux PE-1 et PE-2 deviennent totalement optiquement homogènes sur le plan optique lorsque leurs phases cristallines ont fondu et que, par conséquent, la diffusion optique devient négligeable. Au contraire, un effet dépendant de la température sur leurs caractéristiques de réflectance était quelque peu limité.

La thermographique IR sur polymères semi-transparents chauffés par rayonnement :

- A cause du milieu semi-transparent PE, une méthodologie expérimentale a été développée pour les mesures thermographiques IR. Les bandes d'absorption de PE ont été analysées par des mesures spectroscopiques et les bandes d'absorption appropriées ont été choisies pour l'application de filtres NBP montés sur une caméra IR. La précision de la méthode a été analysée en effectuant des expériences préliminaires de chauffage IR qui ont montré la reproductibilité des lectures de température de surface sur le milieu semi-transparent, même si une petite erreur était toujours observée en raison de son D_p élevé.

Modélisation du rayonnement thermique dans les thermoplastiques semi-cristallins non chargés :

- Grâce aux mesures spectroscopiques en température, les propriétés thermo-optiques dépendant de la température du PE-1 ont été déterminées et utilisées comme paramètre d'absorption du rayonnement dans le modèle de transfert de chaleur par rayonnement. Un modèle numérique dépendant de la température a été développé en tenant compte de la modification de la capacité d'absorption du rayonnement du PE semi-cristallin sous chauffage, sans modéliser la dispersion du rayonnement à l'intérieur du milieu polymère. Par conséquent, le modèle développé propose une approche numérique macroscopique sans modéliser la distribution spatiale de l'intensité du rayonnement diffusé à l'échelle microscopique, ce qui offre des solutions numériques rentables en termes de temps de calcul.

- La précision du modèle a été évaluée en effectuant des comparaisons entre les résultats expérimentaux et numériques pour le cas du chauffage IR de PE en utilisant deux géométries différentes. Les comparaisons montrent que le champ de température peut être prédit de près en utilisant sa capacité d'absorption de rayonnement dépendante de la température. Grâce à l'étude de cas comparative, il a été démontré que les prévisions de champ de température pouvaient différer des mesures thermiques expérimentales en raison de la négligence de cette dépendance à la température.

- La fenêtre de thermoformage du PE semi-cristallin est d'environ 4 à 5 ° C. Compte tenu de cette tolérance de température, la simplification du transport des rayonnements dans le milieu optiquement hétérogène du PE au moyen d'un coefficient d'extension dépendant de la température peut être suffisante pour l'optimisation de son étage de chauffage IR.

- La capacité d'absorption du rayonnement dépendant de la morphologie dans les milieux PE-1 et PE-2 a été analysée qualitativement en réalisant des expériences de chauffage IR dans des

conditions identiques. Il a été observé que la vitesse de chauffage est plus élevée pour le PE-1, en particulier à des températures plus basses. Le comportement différent du chauffage peut être attribué à deux facteurs: l'absorption plus forte dans un milieu cristallin plus dense et la différence dans la plage de température des transitions de phase, alors que l'analyse qualitative réalisée dans cette thèse peut ne pas être suffisante pour conclure. Néanmoins, les expériences de chauffage infrarouge démontrent la différence de champ de température entre les deux types de PE, qui est probablement induite par la différence de structure cristalline.

- Considérant n'importe quel type de source de rayonnement monochromatique ou polychromatique, l'approche expérimentale et numérique combinée proposée ici peut être adaptée aux prévisions de champ de température et aux mesures de température non invasives sur les thermoplastiques semi-cristallins et semi-transparents chauffés par rayonnement.

Recommandations et perspectives

Dans cette section, les points clés sur lesquels se concentrer pour des recherches futures sont énumérés en deux points principaux :

Détermination de la taille du diffuseur dans un thermoplastique semi-cristallin et des modifications du diffuseur et comportement de diffusion optique sous chauffage :

- D'autres méthodes de gravure / coloration chimique et l'utilisation d'autres techniques microscopiques, notamment l'AFM et le POM, peuvent être adoptées pour une meilleure visualisation des structures sphérolitiques.

- La vitesse de chauffage des mesures optiques dépendant de la température doit être synchronisée avec la vitesse de chauffage des analyses calorimétriques effectuées pour prédire la morphologie lamellaire. Dans cette thèse, la diffusion vers l'avant et la rétrodiffusion dépendante de la température ont été estimée dans une condition de chauffage par paliers, ce qui peut entraîner une réorganisation de la morphologie lamellaire. Alors que la morphologie lamellaire prédite était obtenue à une vitesse de chauffage constante. Bien qu'elle fournisse la plage de tailles de cristaux lamellaires à l'origine de la diffusion optique, la taille exacte ne peut être obtenue qu'en adoptant la même vitesse de chauffage que les mesures optiques dépendantes de la température et les analyses calorimétriques.

- La distribution spatiale de la lumière diffusée dépendante de la morphologie dans des milieux polymères semi-cristallins doit être analysée pour d'autres longueurs d'onde. Les analyses

inverses pour les analyses théoriques et expérimentales discutées dans la thèse peuvent être adoptées pour définir la taille de dispersion équivalente. L'incertitude concernant la forme du diffuseur (par exemple, la forme sphérique ou arbitraire) dans les polymères semi-cristallins non chargés peut être discutée lors de l'ajustement à la théorie de la diffusion de la lumière adoptée.

Modélisation du rayonnement thermique dans les thermoplastiques semi-cristallins non chargés et précision des méthodes de contrôle de la température :

- Le modèle développé dans cette thèse ne prend pas en compte la cinétique de fusion des thermoplastiques semi-cristallins. Compte tenu des divers types d'application de chauffage radiatif et de procédés de formage industriels, la vitesse de chauffage peut être différente. Par conséquent, le modèle peut nécessiter une amélioration concernant de la dépendance de la vitesse de chauffage des transitions de phase des polymères.

- Le transport de rayonnement peut être modélisé à l'échelle microscopique en considérant le phénomène de diffusion optique. Comme point de départ de cette modélisation, il peut être nécessaire de caractériser la taille du diffuseur dans un milieu semi-cristallin, en suivant la méthodologie inverse décrite dans cette thèse.

- En chauffage radiatif, les méthodes non invasives telles que la thermographie IR peuvent être l'une des méthodes les plus appropriées, comme proposé dans cette thèse. Toutefois, en ce qui concerne la nature semi-transparente d'un support analysé, tel que le PE, des solutions supplémentaires peuvent être nécessaires pour les évaluations des solutions numériques proposant une précision supérieure.

Bibliographie

[1] Biron M. Thermoplastics and Thermoplastic Composites: Technical Information for Plastics Users. Elsevier; 2007.

[2] Boisse P. Advances in Composites Manufacturing and Process Design. Woodhead Publishing; 2015.

[3] Heat Transfer in Polymer Composite Materials: Forming Processes, Ed: Nicolas Boyard, John Wiley & Sons, 2016.

[4] Burkhardt Gert, Hüsgen Ulrich, Kalwa Matthias, Pötsch Gerhard, Schwenzer Claus. Plastics Processing, 1. Processing of Thermoplastics. Ullmanns Encycl Ind Chem 2011.

[5] Poprawe R. Tailored Light 2: Laser Application Technology. Springer Science & Business Media; 2011.

[6] Klein R. Laser Welding of Plastics. John Wiley & Sons; 2012.

[7] Bhattacharyya D. Composite Sheet Forming. Elsevier; 1997.

[8] Gulmine J., Janissek P., Heise H., Akcelrud L. Polyethylene characterization by FTIR. Polym Test 2002;21:557–63.

[9] Kossack W, Papadopoulos P, Parkinson M, Prades F, Kremer F. IR transition moment orientational analysis on semi-crystalline polyethylene films. Polymer 2011;52:6061–5.

[10] Fratini CM. Study of the Morphology and Optical Properties of Propylene/Ethylene Copolymer Films 2006.

[11] Keane JJ, Stein RS. The scattering of light from thin polymer films. II. Scattering from polyethylene. J Polym Sci Part Polym Chem 1956;20:327–350.

[12] Wang L, Kamal MR, Rey AD. Light transmission and haze of polyethylene blown thin films. Polym Eng Sci 2001;41:358–372.

[13] Denis A, Dargent E, Lebaudy PH, Grenet J, Vautier C. Dependence on the spectral scattering coefficient on crystallinity into semicrystalline polyester. J Appl Polym Sci 1996;62:1211–8.

[14] Hakoume D, Dombrovsky LA, Delaunay D, Rousseau B. Spectroscopic diagnostics of morphological changes arising in thermal processing of polypropylene. Appl Opt 2014;53:2702.

[15] Kolesov I, Mileva D, Androsch R. Mechanical behavior and optical transparency of polyamide 6 of different morphology formed by variation of the pathway of crystallization. Polym Bull 2014;71:581–93.

[16] Ilie M, Kneip J-C, Matteï S, Nichici A, Roze C, Girasole T. Laser beam scattering effects in non-absorbent inhomogenous polymers. Opt Lasers Eng 2007;45:405–12.

[17] Mamuschkin V, Roesner A, Aden M. Laser Transmission Welding of White Thermoplastics with Adapted Wavelengths. Phys Procedia 2013;41:172–9.

[18] Hohmann M, Devrient M, Klämpfl F, Roth S, Schmidt M. Simulation of Light Propagation within Glass Fiber Filled Thermoplastics for Laser Transmission Welding. Phys Procedia 2014;56:1198–207..

[19] Wlochowicz A, Eder M. Distribution of lamella thicknesses in isothermally crystallized polypropylene and polyethylene by differential scanning calorimetry. Polymer 1984;25:1268–1270.

[20] Peacock AJ. Handbook of polyethylene: structures, properties, and applications. New York: Marcel Dekker; 2000.

[21] Keller B, Pfeifer R, Su W-N, Eyerer P. Temperature Dependent Optical Properties of Polymers as a Basis for Laser Process Modeling ,1998.

[22] Becker F, Potente H. A step towards understanding the heating phase of laser transmission welding in polymers. Polym Eng Sci 2002;42:365–374.

[23] Geiger M, Frick T, Schmidt M. Optical properties of plastics and their role for the modelling of the laser transmission welding process. Prod Eng 2009;3:49–55.

[24] Hawkins SW, Richards RB. Light transmission and the formation and decay of spherulites in polythene. J Polym Sci Part Polym Chem 1949;4:515–22.

[25] Schmidt F. Modelling of infrared heating of thermoplastic sheet used in thermoforming process. J Mater Process Technol 2003;143–144:225–31.
[26] Apetz R, Bruggen MPB. Transparent Alumina: A Light-Scattering Model. J Am Ceram Soc 2003;86:480–6.
[27] Berrocal E, Sedarsky DL, Paciaroni ME, Meglinski IV, Linne MA. Laser light scattering in turbid media Part I: Experimental and simulated results for the spatial intensity distribution. Opt Express 2007;15:10649–65.
[28] Humphrey A, Harman T, Berzins M, Smith P. A scalable algorithm for radiative heat transfer using reverse monte carlo ray tracing. Int. Conf. High Perform. Comput., Springer; 2015, p. 212–230.
[29] Agrawal BM, Mengüç MP. Forward and inverse analysis of single and multiple scattering of collimated radiation in an axisymmetric system. Int J Heat Mass Transf 1991;34:633–47.

ANNEX

ANNEX A.1

- Planck's constant: $h = 6.626*10^{34}$ J.s

- Boltzmanns's constant: $k_B = 1.38*10^{-23}$ J/K

- Derived constants: $C_1 = h.c_o^2$ and $C_2 = h.c_o / k_B$

- Planck's Law (Equation 2.3): $E_{\lambda b}(T) = \pi I_{\lambda b}(T) = \frac{2\pi h c_0^2}{n^2 \lambda^5 [\exp(\frac{hc_0}{nk_B \lambda T}) - 1]} = \frac{2\pi C_1}{n^2 \lambda^5 [\exp(\frac{C_2}{n\lambda T}) - 1]}$

A.1.1. Parametric constants and the derived auxiliary constants in the Planck's Law.

Step-by-step derivation between Gibbs-Thomson equation and Equation 2.16 is:

1 - $T_m = T_m^0(1 - \frac{2\sigma_e}{\Delta H_m l_c})$ (Eq. A.1.2 -1) written as: $l_c = \frac{T_m^0 K_o}{(T_m^0 - T_m)}$ with; $K_o = \frac{2\sigma_e}{\Delta H_m}$ (Eq. A.1.2 -2)

2 - Derivative of l_c with T_m: $dl_c = dT \frac{T_m^0 K_o}{(T_m^0 - T_m)^2}$ (Eq. A.1.2 -3) where also;

$$dM = \frac{dE}{dT}\frac{dT}{\Delta H_m} \quad \text{(Eq. A.1.2 -4)}$$

3 - Normalization of l_c distribution regarding to total mass of crystalline phase (M), using sample mass (m_{sample}) and X_c of the sample:

$$M = m_{sample} X_c \quad \text{(Eq. A.1.2-5)}$$

4 - Combining Eq. A.1.2 -3 and Eq. A.1.2 -4:

$$\frac{1}{M}\frac{dM}{dL} = \frac{dE}{dT}\frac{(T_m^0 - T_m)^2}{2\sigma_e T_m} \quad \text{(Eq. A.1.2 -6)}$$

A.1.2. Derivation between the Gibbs-Thomson equation and Alberola's approach (Equation 2.16) [55].

(a)

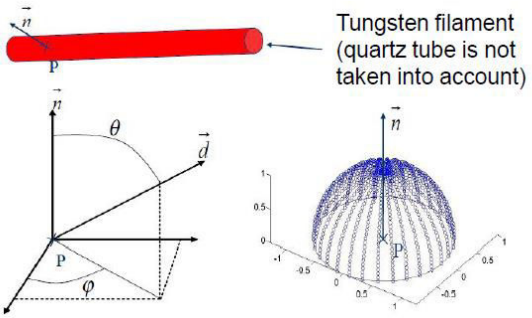

$$\begin{cases} \varphi = 2\pi R_1 \\ \theta = \arcsin\left(\sqrt{R_2}\right) \end{cases}$$

Each single filament is modeled by equivalent cylinders where its spiral form is neglected (a). The discretization of the rays emitted from the surface of IR lamp was performed adopting a stochastic approach. Hence, a numerous number of rays are released randomly from the modeled IR lamp. The total amount of energy emitted by the IR lamp is uniformly shared among all the rays.

(b)

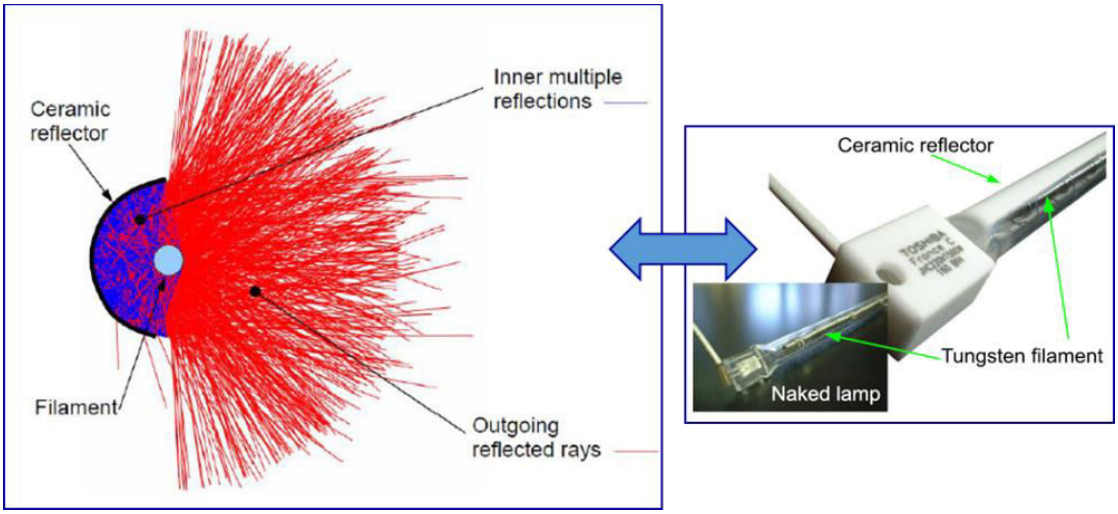

Either ceramic coated (b) or non-reflector (without coated with ceramic reflector) halogen emitters can be modeled in RAYHEAT.

$P_{reflected} = (1 - \rho_{sample})\ P_{incident}$ (Eq. A.1.2-7) where;

$P_{incident}$: Incident ray power before reflection from the sample surface

$P_{reflected}$: Ray power reflected from the sample surface

(c)

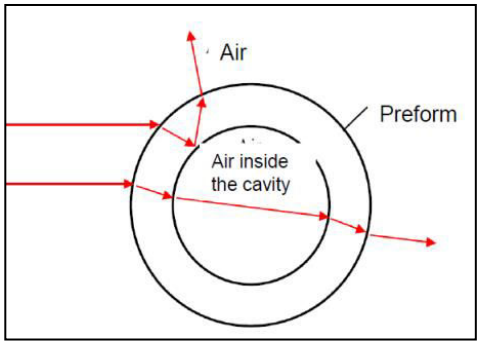

Once a ray intersects the polymer, some of the carried energy is reflected and the remaining part of the energy is transmitted through the medium, where the absorbed energy is computed. The change in the radiation direction due to refraction is taken into account based on Snell-Descartes Law (Equation 2.9). Considering a complex geometry of a heated component, refraction at each air-sample interface is modeled. Here it is given considering cylindrical preform geometry (c). $n_{polymer}$ in Eq. A.1.2-8 represent the mean n value of the heated polymer averaged over wavelength and used as input in the model.

$$n_{polymer}.\sin(\theta_{polymer}) = n_{air}.\sin(\theta_{air}) \quad \text{(Eq. A.1.2-8)}$$

A.1.3. Overview of the theoretical background and computation algorithm in RAYHEAT in terms of emitted radiation (a), reflection (b) and refraction / transmission / absorption (c) phenomena.

ANNEX A.2

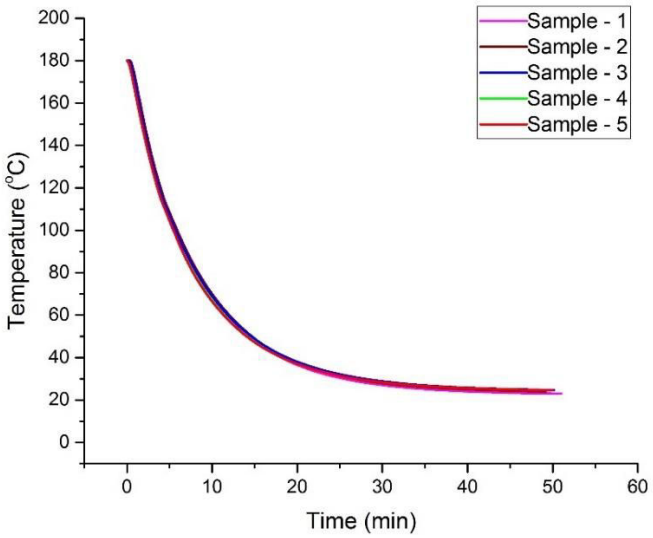

A.2.1. Cooling of the *SC* samples in still air condition.

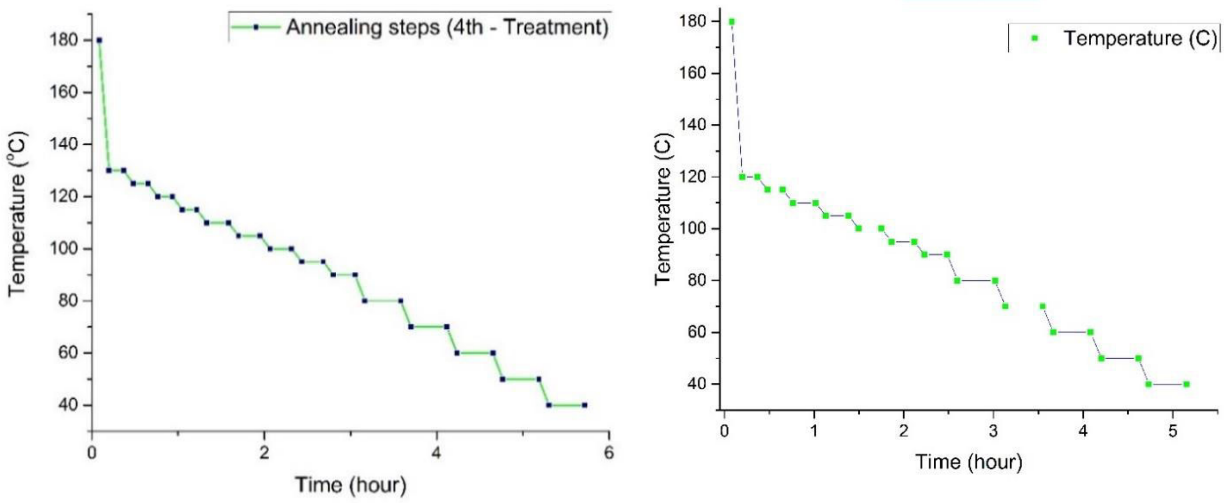

A.2.2. Thermal fractionation applied for PE-1 (a) and PE-2 (b) samples under stepwise cooling.

(a)

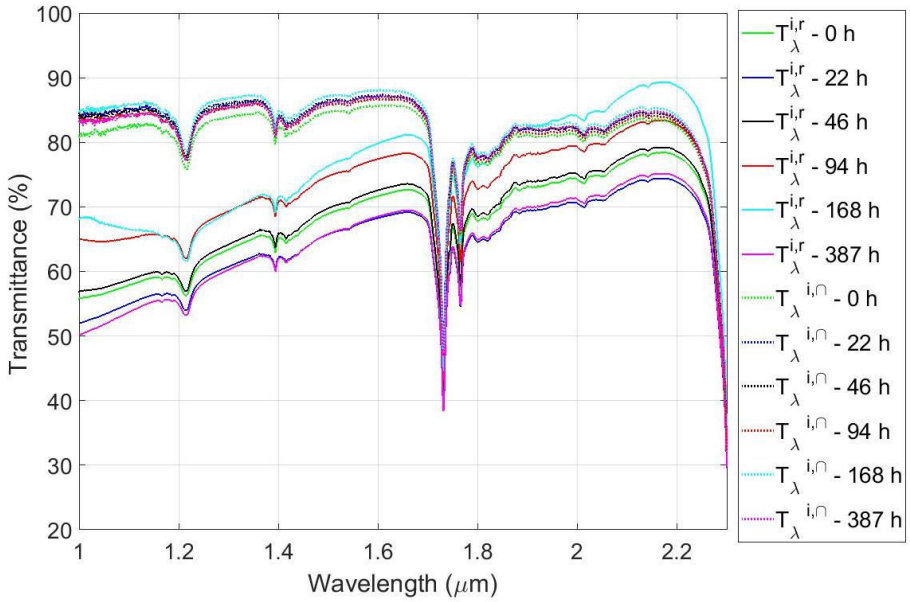

(b)

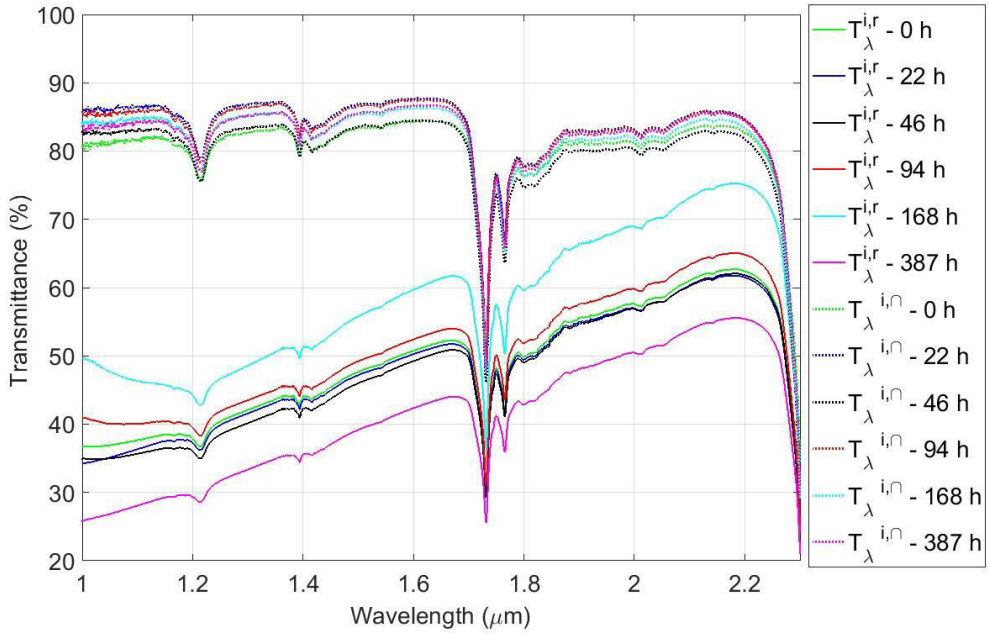

A.2.3. Time-dependent transmittance characteristics of PE-1 (a) and PE-2 (b) measured as $T_\lambda^{i,r}$ and $T_\lambda^{i,\cap}$ in NIR range. The results in NIR range does not give any consistency which is probably due to the change in the scattered and not detected light affected by the different orientation of the samples at each measurement.

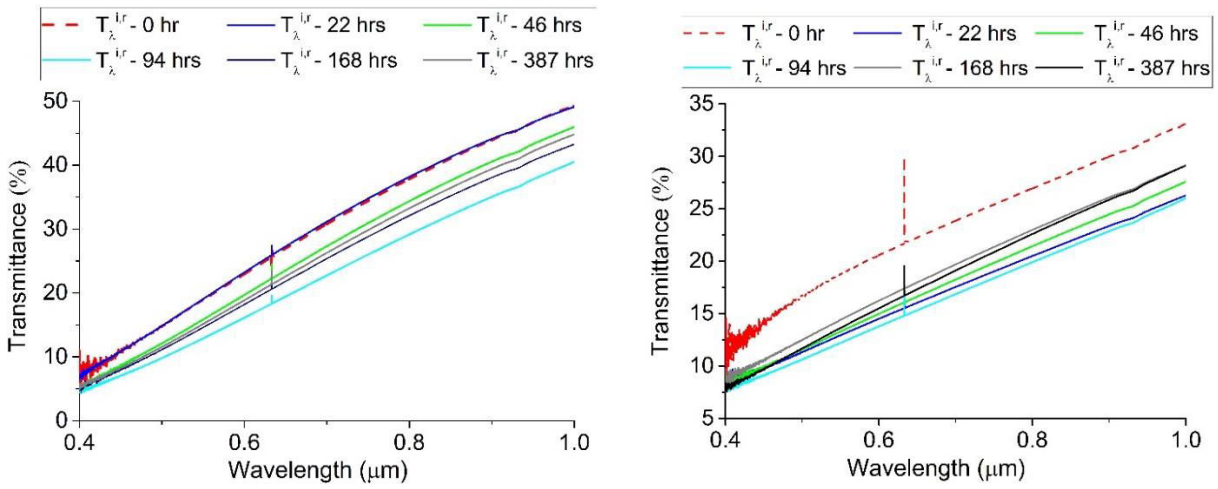

A.2.4. Time-dependent transmittance characteristics of the PE-1 (a) and PE-2 (b) samples measured as $T_\lambda^{i,r}$ in VIS range.

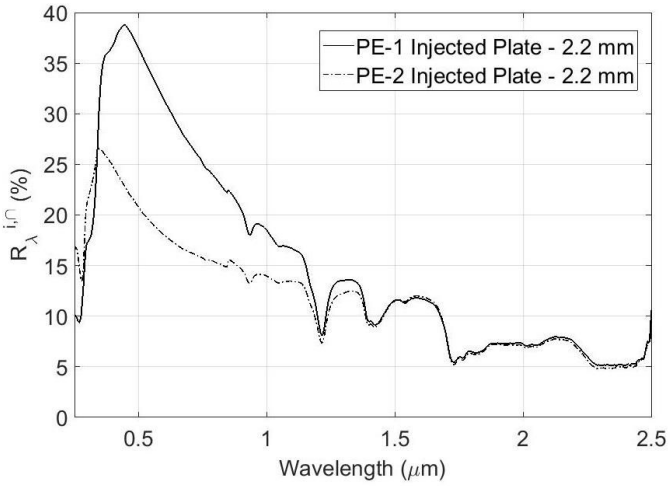

A.2.5. $R_\lambda^{i,\cap}$ of the injected PE-1 and PE-2 plates obtained at room temperature. The effect of PE morphology on the reflectance characteristics may be ignored NIR range, whereas its effect becomes more significant at shorter wavelengths in VIS range.

(a)

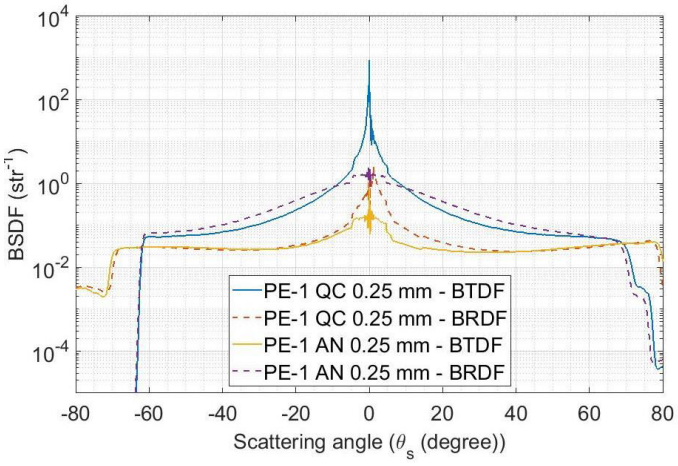

(b)

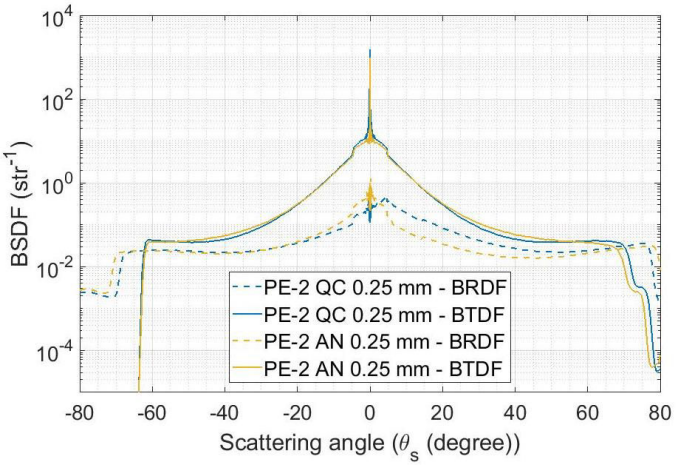

(c)

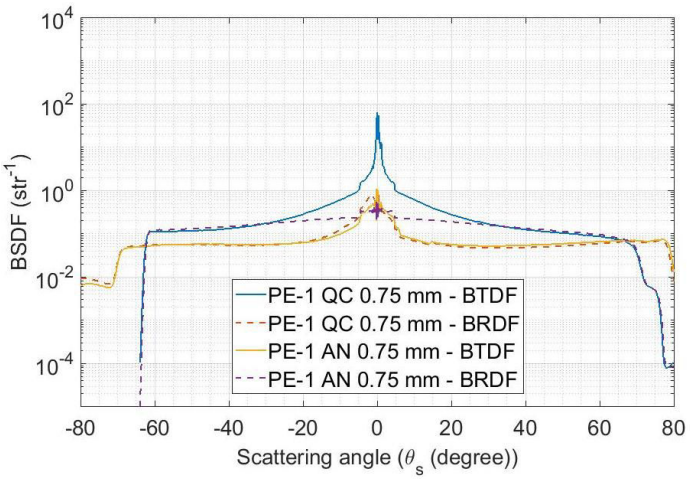

A.2.6. Spatial distribution of scattered light of 0.25mm thick PE-1 (a), PE-2 (b) and 0.75mm thick PE-1(c) samples which were measured as BRDF and BTDF at angles between 0 - 160° (λ=632.8 nm).

ANNEX A.3

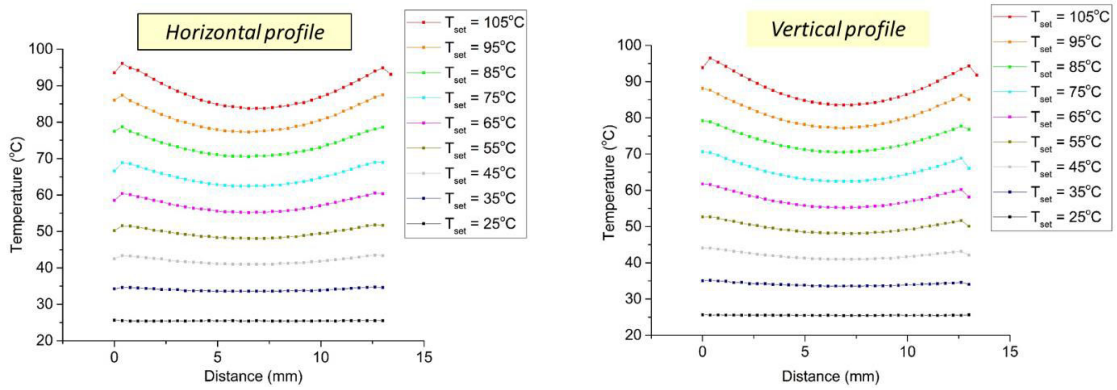

A.3.1. The horizontal and vertical temperature profiles obtained at each steady-state condition monitored at T_{set} values of the heating stage between 25°C and 105°C.

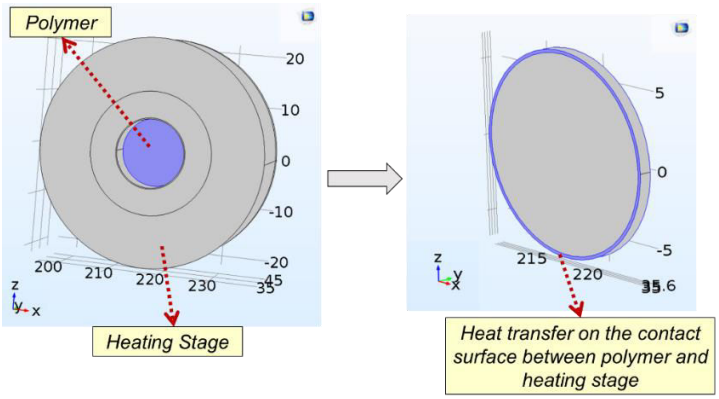

A.3.2. The schematical illustration of the modeled geometry and, the constant T_{set} values introduced at the contact interface between the polymer sample and heating stage.

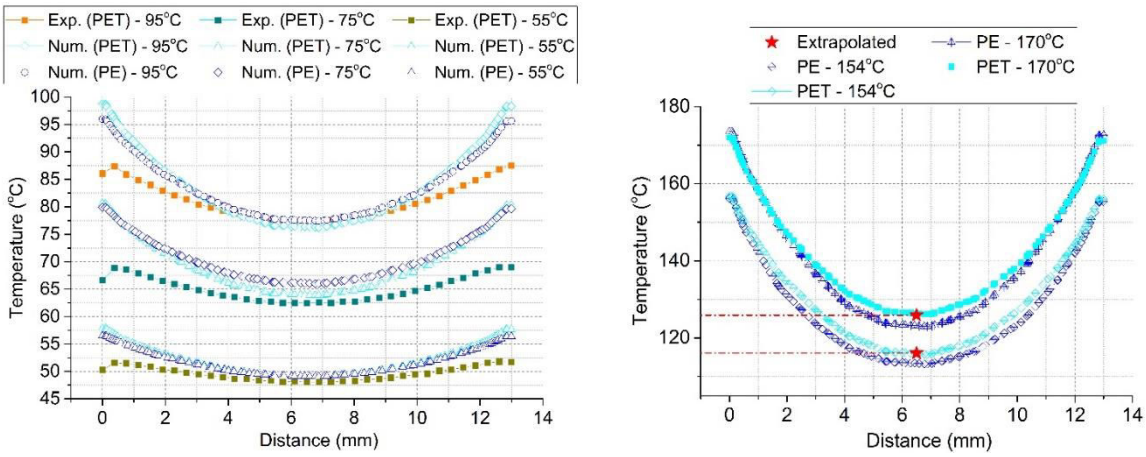

A.3.3. The comparisons between the measured / extrapolated values and numerical results simulated for 0.75mm thick PET and PE samples.

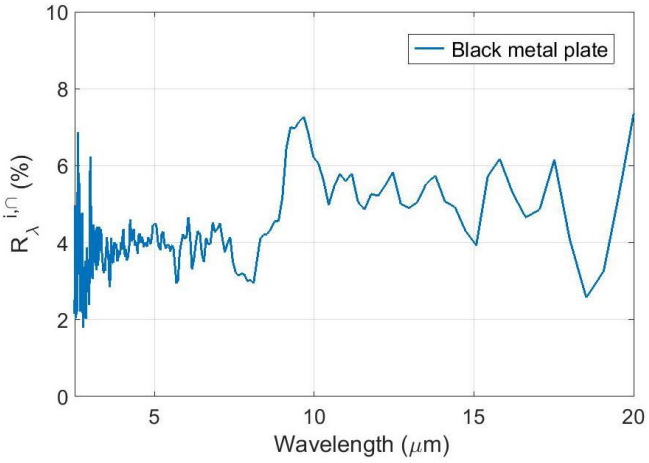

A.3.4. Reflectance characteristics of the black metal piece mounted below the back surface of the PE samples during the $R_\lambda^{i,\cap}(T)$ tests.

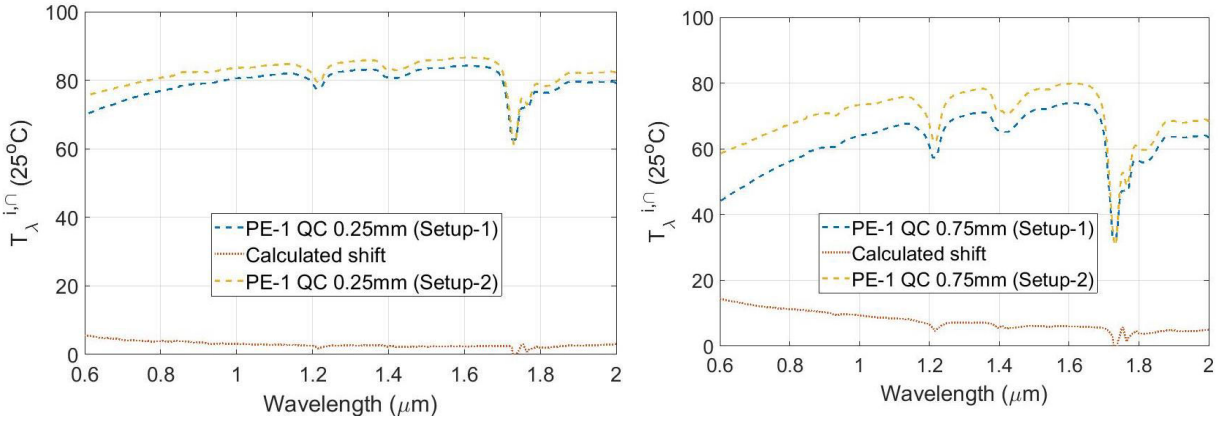

A.3.5. The missed amount of the detected forward-scattered light flux at large angles in the 0.25 mm and 0.75 mm thick PE-1 QC samples.

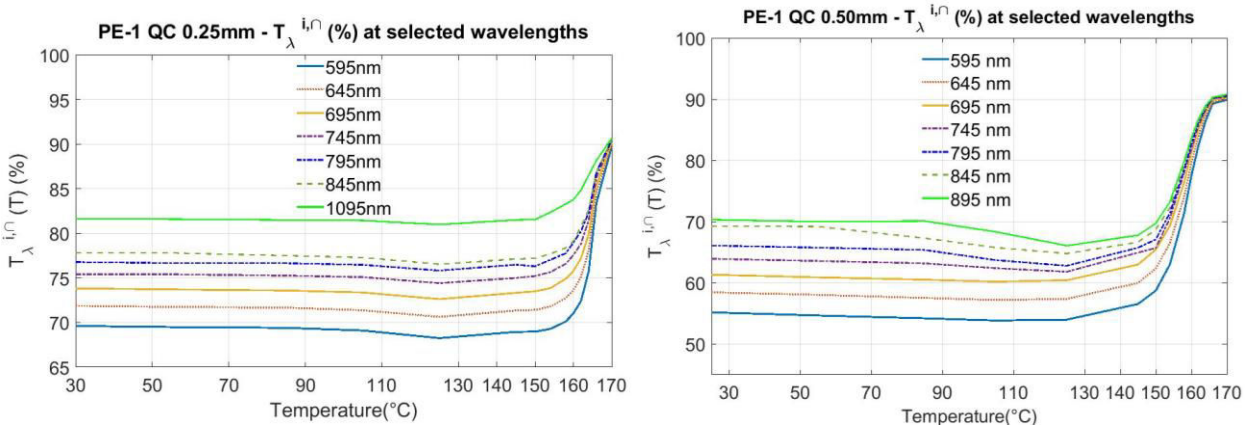

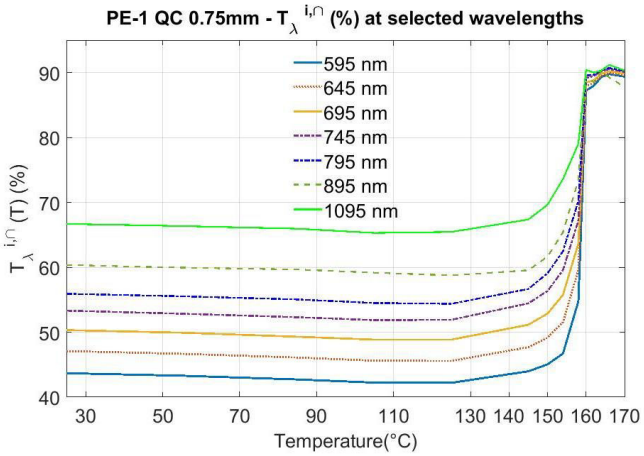

A.3.6. Exponential increasing trend in the $T_\lambda^{i,\cap}(T)$ of 0.25,0.50 and 0.75mm thick PE-1 QC samples at selected wavelengths between 595 – 1095nm.

$$\alpha(T=x)=\frac{T_\lambda^{i,n}(T=x)-T_\lambda^{i,n}(25°C)}{T_\lambda^{i,n}(128°C)-T_\lambda^{i,n}(25°C)} \text{ with; } \quad T_{\lambda,shift}^{i,n}(T)=T_{\lambda,shift}^{i,n}(25°C)*(1-\alpha(T))$$

A.3.7. The min-max normalization applied to the $T_\lambda^{i,\cap}(T)$ measurements of each sample and, the temperature-dependence rule defined for determining the shift-corrected $T_\lambda^{i,\cap}(T)$ values consideringthe fraction of the missed amount of forward-scattered light flux.

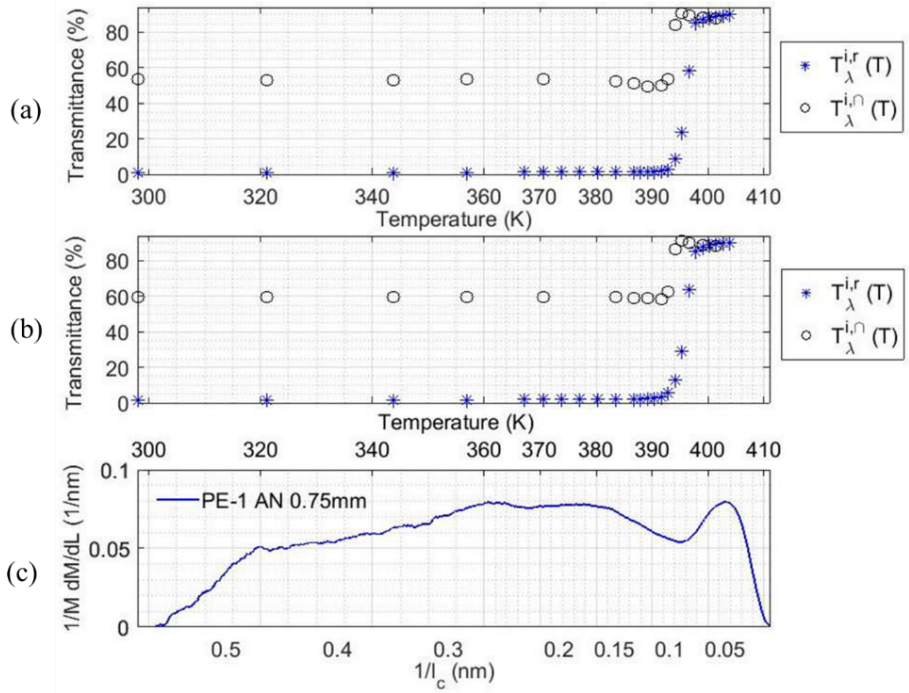

A.3.8. The temperature dependent increase in the $T_\lambda^{i,r}(T)$ and $T_\lambda^{i,\cap}(T)$ of 0.75mm thick PE-1 AN at λ=632.7nm (a) and 800nm (b) and, their correlations to the melting of most probable crystals (c).

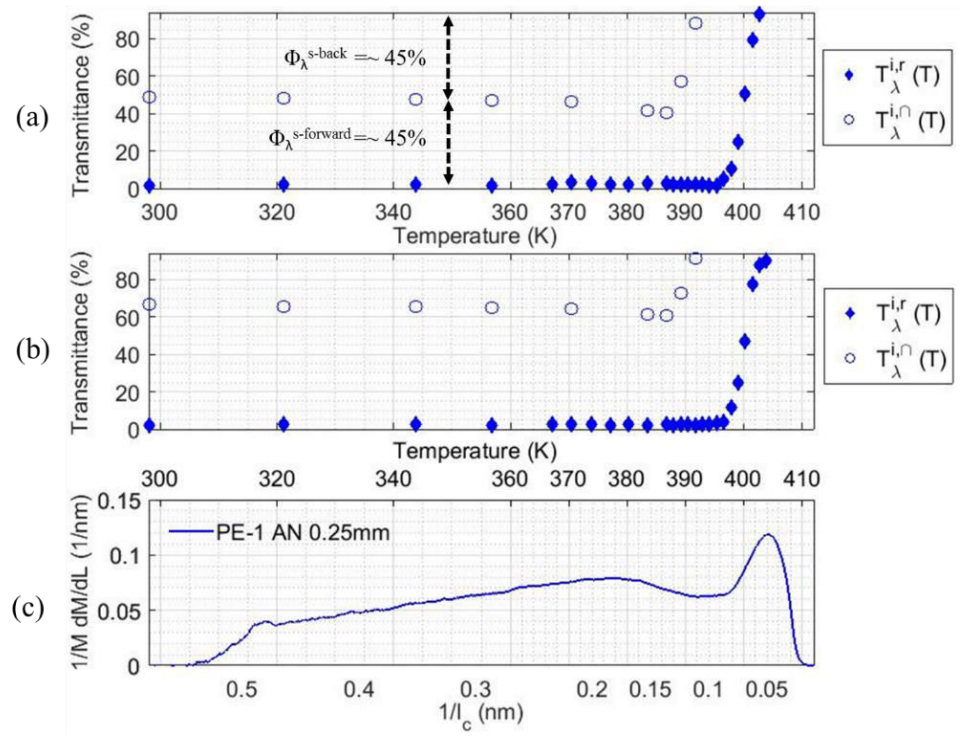

A.3.9. The temperature dependent increase in the $T_\lambda^{i,r}$ (T) and $T_\lambda^{i,\cap}$ (T) of 0.25 mm thick PE-1 AN at λ=330 nm (a) and 450 nm (b) and, their correlations to the melting of most probable crystals l_c (c).

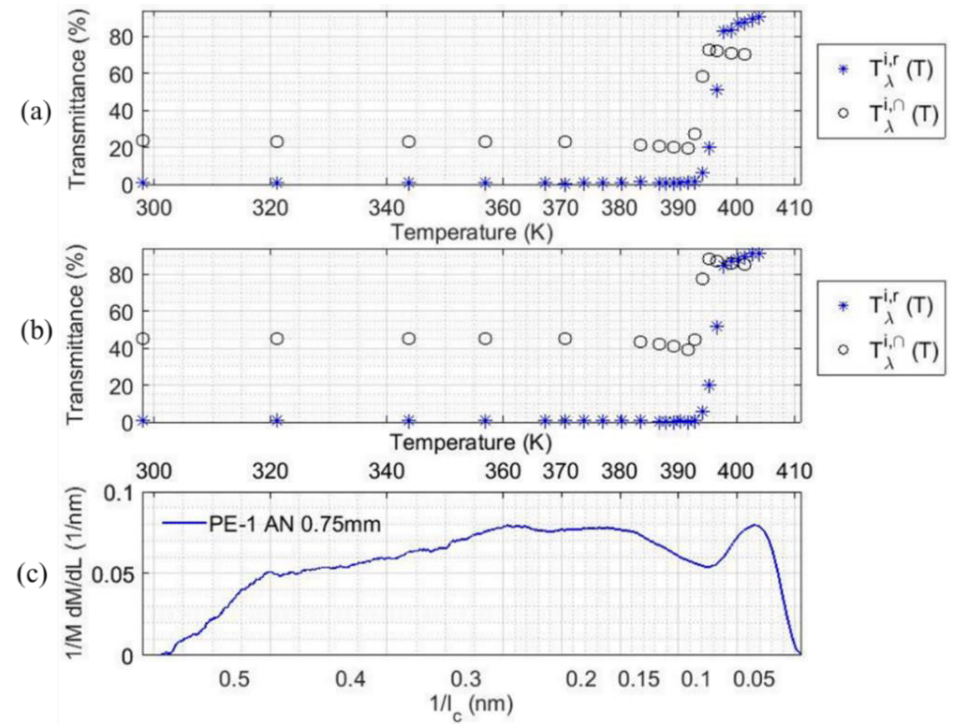

A.3.10. The temperature dependent increase in the $T_\lambda^{i,r}$ (T) and $T_\lambda^{i,\cap}$ (T) of 0.75 mm thick PE-1 AN at λ=330 nm (a) and 450 nm (b) and, their correlations to the melting of most probable crystals (c).

ANNEX A.4

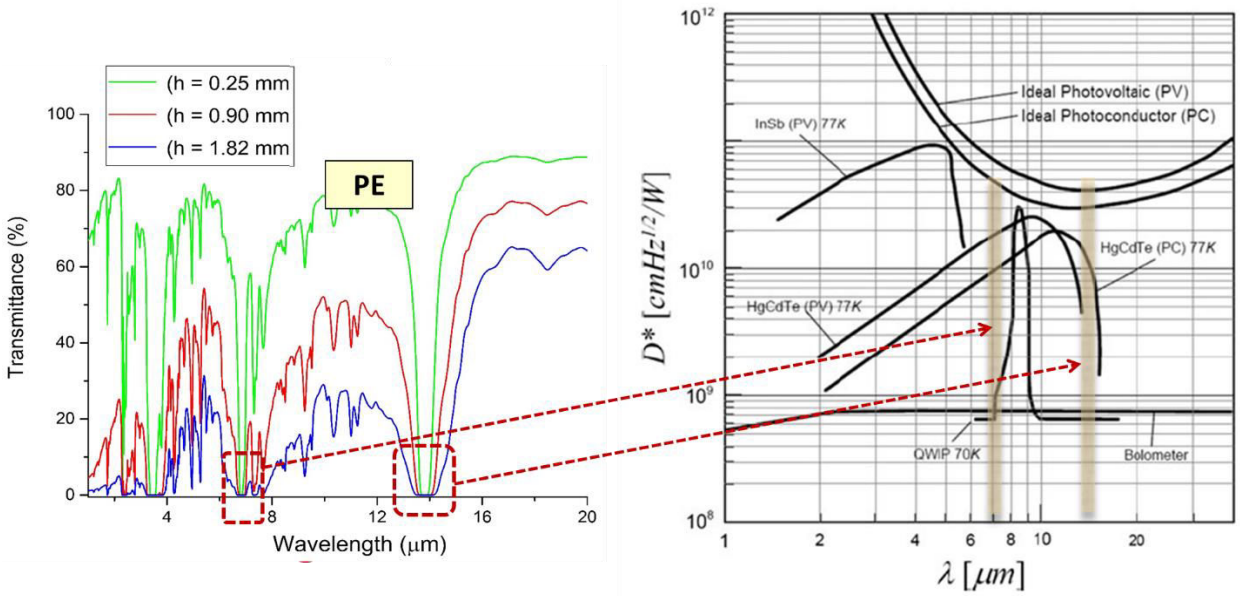

A.4.1. Necessity of usage of NBP optical filter for an accurate IR thermography on semi-transparent PE medium and, the spectral sensitivity of HgCdTe and bolometric detectors [25] in the absorption bands of PE. D* represents the infrared detector detectivities which was defined at a specific exposure time, as a function of λ. Hence, the higher D* indicates better performance.

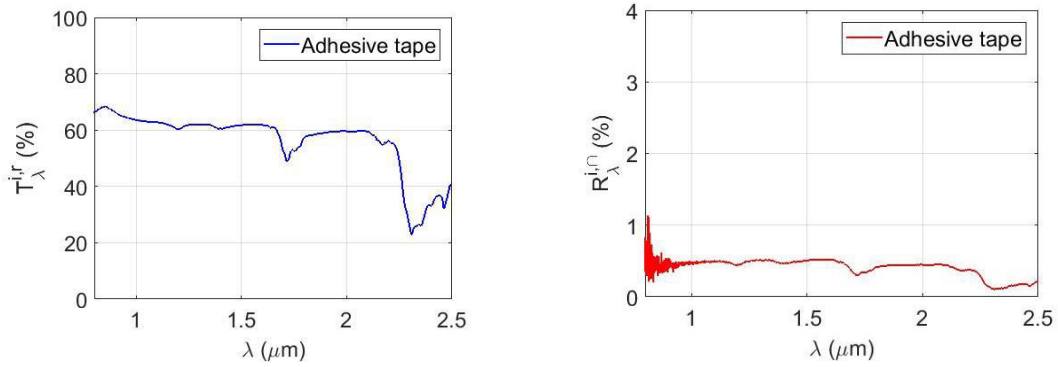

(a) (b)

A.4.2. $T_\lambda^{i,r}$ and $R_\lambda^{i,\cap}$ of the adhesive transparent tape used for positioning the TCs on the PE plate surface.

(a)

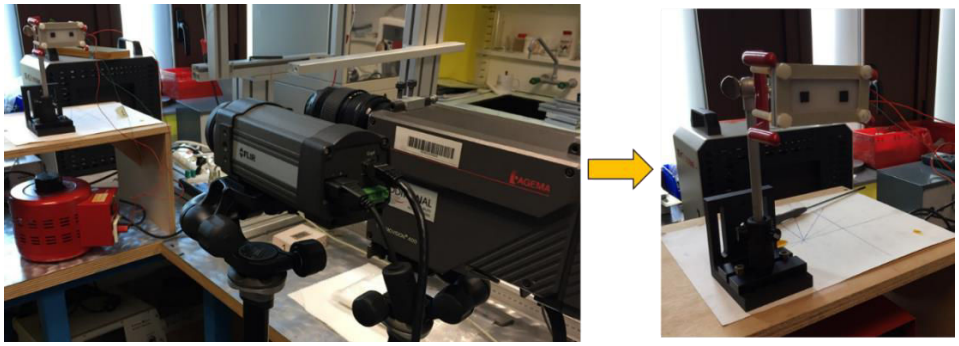

(b)

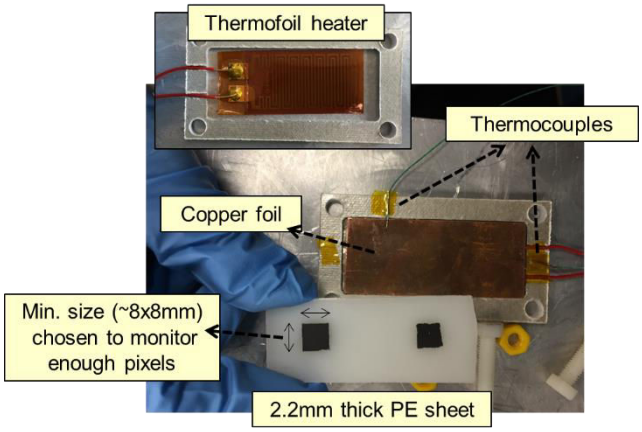

A.4.3. Overview of the test setup for IR thermography on PE sample heated by conduction on its back surface (a). The heating was done using an electric thermofoil heater (Minco). In order to secure a homogeneous heat transfer from the thermofoil heater throughout sample geometry a copper foil was embedded between the heater and sample (b).

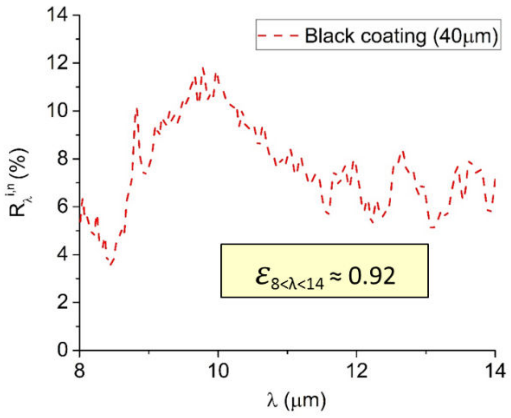

A.4.4. The $R_\lambda^{i,\cap}$(%) of 40 μm thick black coating measured in the operating spectral range of FLIR SC325 IR camera. The material showed zero transmittance in the corresponding range.

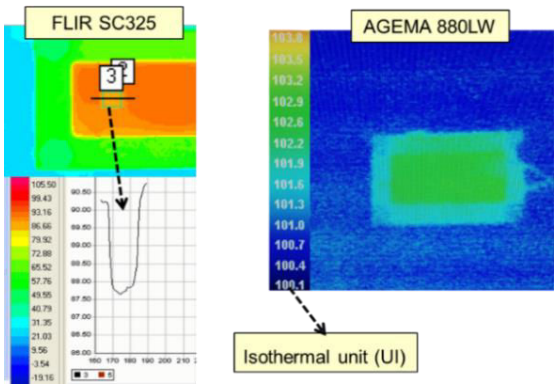

A.4.5. IR thermography of the black coated reference zones and the PE surface obtained via two different IR cameras.

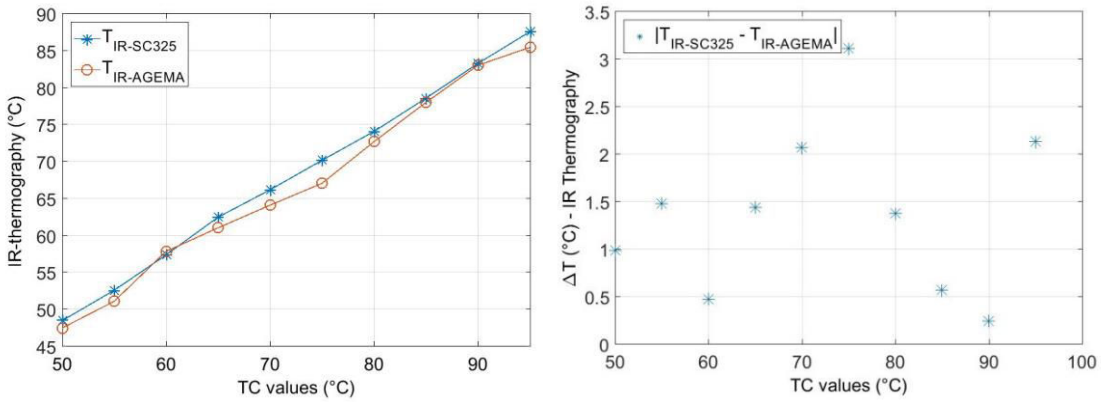

A.4.6. The comparisons between the temperature values read by two different IR camera on the black coated reference zones and on the PE surface, and their comparisons the TC values at each steady state temperature. Temperature difference read by the two IR camera is shown in (b).

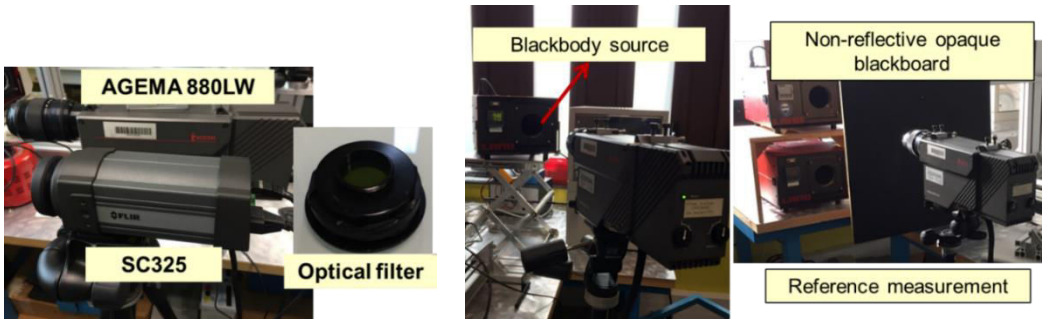

(a) (b)

A.4.7. Externally mounted optical filter (a) and the two-step IR thermographic measurements combined with actual measurements on the zone of interest and reference measurements (b). Here, the two-step measurements performed during the calibration of IR camera is displayed.

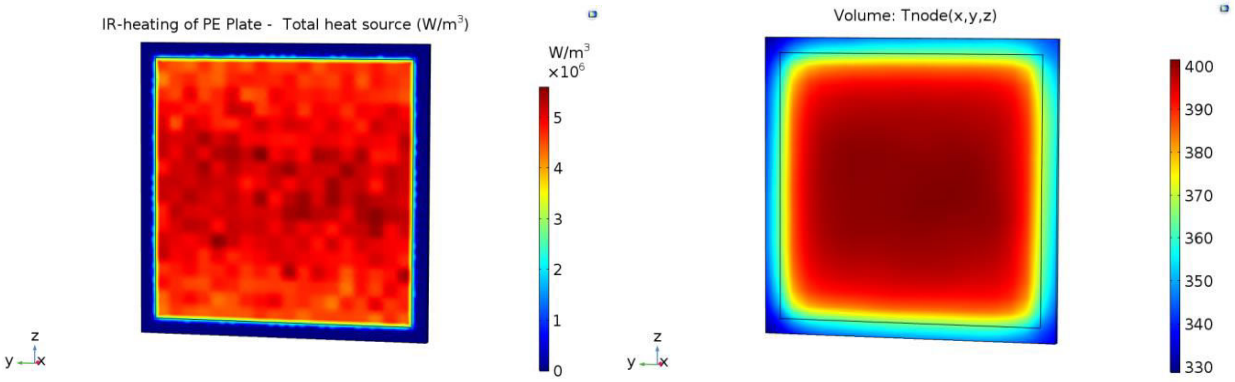

(a) (b)

A.4.8. Initial boundary conditions applied for the CFD computations on the PE plate. The $\nabla . q_r$ inside of PE medium at around 300 seconds of computational time (a) and, the node temperatures at the corresponding time step (b) were used as numerical input. Assuming a steady-state condition in the CFD computations, h was computed on the PE surface.

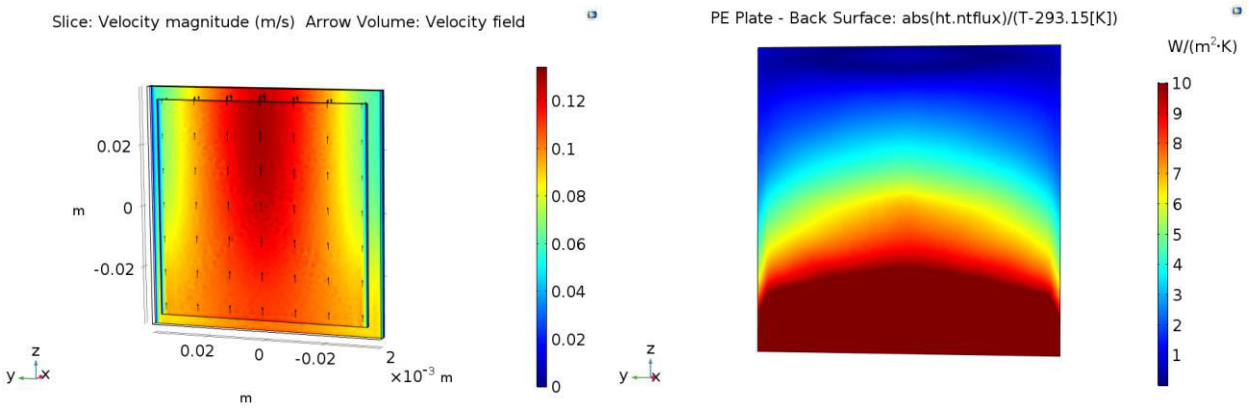

A.4.9. Velocity field and the vectors of buoyancy-driven air flow over the vertical surfaces of the PE plate (a) and, the computed h over the back surface of the plate.

$$Nu = 0.095 * (0.5 * \mathrm{Re}^2 + Gr)^{0.35}$$

A.4.10. Experimentally fitted equation proposed by Dropkin et al [44] for natural convection of rotating cylinders in still air.

This page intentionally left blank.

Publications

Journal articles

1. **S. Boztepe**, O. de Almeida, R. Gilblas, Y. Le Maoult, F. Schmidt, and C. Gerlach. A Combined Experimental and Numerical Approach for Radiation Heat Transfer in Semi-Crystalline Thermoplastics. *Int J of Therm Sci*, *142:142–55*, **2019**.

2. **S. Boztepe**, O. De Almeida, R. Gilblas, C. Gerlach, Y. Le Maoult and F. Schmidt. The role of microcrystalline structure on optical scattering characteristics of semi-crystalline thermoplastics and the accuracy of numerical input for IR-heating modeling. *Int J Mater Form, 11:717-727*, **2018**.

Conference proceedings

1. **S. Boztepe**, R. Gilblas, O. De Almeida, Y. Le Maoult and F. Schmidt. Cost-effective computational method for radiation heat transfer in semi-crystalline polymers. *21st International ESAFORM Conference on Material Forming, Palermo*, *Italy*, **2018.**

2. **S. Boztepe**, R. Gilblas, O. De Almeida, F. Schmidt and Y. Le Maoult. The role of microcrystalline structure on the temperature-dependent thermo-optical properties of semi-crystalline thermoplastics and non-invasive temperature measurements. *25ème Congrès Français de Thermique (SFT), Marseille, France,* **2017**.

3. **S. Boztepe**, R. Gilblas, O. De Almeida, Y. Le Maoult and F. Schmidt. A non-invasive experimental approach for surface temperature measurements on semi-crystalline thermoplastics. *20th International ESAFORM Conference on Material Forming, Dublin*, *Ireland*, **2017.**

4. **S. Boztepe**, O. De Almeida, Y. Le Maoult and F. Schmidt. Experimental analysis on the coupled effect between thermo-optical properties and microstructure of semi-crystalline thermoplastics. *19th International ESAFORM Conference on Material Forming, Nantes, France,* **2016**.

Conference without proceedings

1. **S. Boztepe**, O. De Almeida, Y. Le Maoult and F. Schmidt. Identification of the temperature-dependent relation between thermo-optical properties and morphology of semi-crystalline thermoplastics for thermoforming process. *32nd International Conference of the Polymer Processing Society, Lyon, France*, **2016.**

Compréhension de chauffage infrarouge de thermoplastiques semi-cristallins

Les thermoplastiques et les composites thermoplastiques sont généralement mis en œuvre par thermoformage et sont alors le plus souvent préchauffés en utilisant un chauffage IR. L'avantage du chauffage radiatif est qu'il permet de chauffer les polymères à cœur grâce au caractère semi-transparent des polymères. Néanmoins, dans le cas des polymères semi-cristallins, le chauffage radiatif est affecté par la structure cristalline et cette thèse a donc eu pour objectif d'améliorer la compréhension de l'interaction entre la structure cristalline et les propriétés optiques dans le but de proposer un modèle prédictif de chauffage de thermoplastiques semi-cristallins.

Cette étude répond à une problématique industrielle relative au contrôle de la température des thermoplastiques semi-cristallins dans les procédés recourant au chauffage radiatif. L'optimisation de ces procédés requiert un code de calcul suffisamment robuste pour permettre une bonne prédiction du champ de température tout en conservant des temps de calcul acceptables. Une approche combinée expérimentale et numérique a ainsi été proposée dans le but de modéliser la capacité d'absorption du rayonnement thermique de milieux polymères semi-cristallins et le transfert de chaleur par rayonnement avec changement des phases de cristaux/amorphe. Ces travaux se concentrent sur le PEHD, qui présente un intérêt particulier pour l'entreprise Procter&Gamble.

Dans cette thèse, après avoir établi une revue bibliographique mettant en avant les couplages existants entre les phénomènes de diffusion optique, la microstructure des polymères semi-cristallins et la température, une caractérisation et une analyse poussées des propriétés radiatives de deux polyéthylènes sont proposées. Les analyses morphologiques et optiques ont été réalisées à température ambiante et dans des conditions de chauffage afin d'identifier les formations cristallines à l'origine de la diffusion optique dans des polymères semi-cristallins et l'évolution de ce couplage au cours du chauffage. A travers ce travail de recherche, un coefficient d'extinction spectral thermo-dépendant a été proposé afin de décrire le caractère optiquement hétérogène du milieu semi-cristallin par un milieu homogène équivalent. Sur la base de la caractérisation de la capacité d'absorption du rayonnement thermique, un modèle thermique conducto-radiatif thermo-dépendant a été développé. Afin d'évaluer la précision de la modélisation, une méthodologie expérimentale spécifique a été proposée pour mesurer la température de surface par thermographie IR dans le cas du PEHD semi-transparent. L'étape finale a consisté à confronter les résultats issus des simulations numériques basées sur cette modélisation à plusieurs campagnes de mesures expérimentales. Les résultats de ces travaux démontrent la forte influence de la structure morphologique des polymères semi-cristallins sur les transferts de chaleur radiatifs.

Mots-clés: *Chauffage IR, Polymères semi-cristallins, Diffusion optique, Propriétés thermo-optiques, Morphologie cristalline, Transferts radiatifs, Thermographie IR.*

This page intentionally left blank.

Understanding of infrared heating for thermoforming of semi-crystalline thermoplastics

Thermoplastics and thermoplastic composites are promising candidates for manufacturing highly cost-effective and environmental-friendly components in terms of rapid forming and recyclability. Thermoforming is extensively used for the processing of thermoplastics where IR heating is widely applied. The major advantage of radiative heating is that the significant portion of radiation penetrates into the semi-transparent polymer media.

This thesis focuses on understanding of IR heating of semi-crystalline thermoplastics which aims to analyze the driven mechanisms for radiation transport in optically heterogeneous unfilled semi-crystalline polymer media. Considering the relatively narrow thermoforming window of semi-crystalline thermoplastics, accurate temperature control and close monitoring of temperature field is crucially important for successful forming process. It is thus required to build a numerical model robust enough to allow a good prediction of the temperature field while maintaining acceptable calculation times. In this research work, a combined experimental-numerical approach has been proposed which enables both to characterize the radiation absorption capacity of semi-crystalline polymer media and, to model the radiation heat transfer considering the crystalline/amorphous phases change under heating. This research focuses on a particular polymer - highly crystalline HDPE- which is supported by Procter & Gamble.

In this thesis, the literature was reviewed at first for highlighting the existing coupled relation between the optical properties and the crystalline structure of semi-crystalline polymers. The role of crystalline morphology on the optical properties and optical scattering of two type of polyethylene, namely HDPE and LLDPE, were addressed. More specifically, the morphological and optical analyses were performed at room temperature and under heating to determine: *which crystalline formations are responsible for optical scattering in semi-crystalline polymer media and, how does their coupled relationship evolve under heating conditions?* Hence, one of the key contributions of this research is on establishing a temperature-dependent spectral extinction coefficient of HDPE allowing to describe temperature-dependent radiation absorption capacity of its semi-crystalline medium and, to model radiative transfer considering an equivalent homogeneous medium. Based on the characterization of radiation absorption capacity of semi-crystalline media, a temperature-dependent conduction-radiation model was developed. In order to assess the modeling accuracy, an experimental methodology was proposed for non-invasive surface temperature measurements via IR thermography on semi-transparent polymer media. The final step was to compare the results of numerical simulations with the several IR heating experiments to prove the strong influence of the crystalline morphology on heat transfer.

Keywords: *IR heating, Semi-crystalline thermoplastics, Optical scattering, Crystalline morphology, Thermo-optical properties, Radiation heat transfer, IR thermography.*